Università degli Studi di Genova

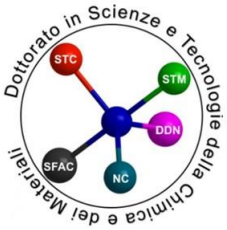

Doctorate School in Sciences and Technologies of
Chemistry and Materials

Doctorate in Chemical Sciences and Technologies
XXXIII CYCLE

Thermodynamic modelling and experimental validation of High Entropy Alloys containing Al, Co, Cr, Fe, Mo, Ni, Ta and W for high -temperature applications

Marlena Ostrowska

Tutor: Prof. Gabriele Cacciamani

Thesis abstract

The aim of the current project is to contribute to the design of novel High Entropy Alloys (HEAs) which meet targeted industrial needs, for instance the request for new high-temperature alloys.

HEAs attracted a lot of attention due to their promising high temperature mechanical performance. Taking into account a very wide range of alloys that fall into this group of materials, using only experimental investigations would be insufficient in finding new compositions with attractive properties.

The objective is achieved by thermodynamic modelling of the Al-Co-Cr-Fe-Mo-Ni-Ta-W system, through the CALPHAD method, in order to predict the best candidate elements and compositions which can give the required structure.

The reliable and self-consistent database is obtained by assessing several important ternary systems and by adopting published assessments, if they were compatible with the models selected in this work.

The reliability of the database is verified with experimental measurements performed during this work regarding the reference system Al-Co-Cr-Fe-Ni, as well as the critically selected published experimental data regarding several other multicomponent systems containing Mo and W.

The synergy between modelling and experimental validation produce a highly reliable thermodynamic database which allows to screen and quickly identify high performance compositions, with a significant reduction in time and costs with respect to traditional trial and error experiments.

Acknowledgements

This work was performed during my PhD study at the University of Genoa at the Department of Chemistry and Industrial Chemistry. I would like to acknowledge all people who made it possible and contributed to this work.

Firstly, I would like to thank my supervisor Prof. Gabriele Cacciamani for his commitment to my work and constant support. I could profit from his broad knowledge and experience during the discussion of the results. I should also mention his great humour which made my PhD thesis very enjoyable.

I would like to express my gratitude to Prof. Zi-Kui Liu, for giving me the opportunity to visit his group Phases Research Lab at the Pennsylvania State University and to all members of the group in particular Brandon Bocklund for instructing me on how to use ESPEI and helping with solving problems.

I also want to thank Prof. Paola Riani for the guidance and help during the experimental part of my research.

I cannot forget about my colleagues from COMAT research group, Giacomo Roncallo, Saverio Sitzia and Yao Wang, and all the other members of the Inorganic Materials group. They were always helpful and created a very friendly atmosphere at work.

Finally, I would like to thank my boyfriend Christopher Ramsauer and my whole family for being a source of motivation and support.

Contents

1. Introduction

1.1 General introduction

High Entropy Alloys (HEA) introduced in **chapter 1.2,** have been intensively studied in the recent years with the hope to find among them new materials with improved properties with respect to the classical alloys [1]. HEAs based on 3d transition metals and in particular on Co, Cr, Fe and Ni, are especially being investigated as a possible replacement of classical superalloys for high temperature applications [2–6]. With the aim of improving high temperature performance of the alloys, refractory metals can be added, such as Hf, Mo, Nb, Ta, Ti, V, W and Zr. However, due to their very wide range of properties, it is very difficult to predict the results of their addition to the base elements in approximately equimolar quantity.

Another element to be taken into account is Al, already included in classical superalloys for many reasons, such as formation of the gamma prime phase in the alloy bulk and the thermal grown oxide (TGO) on the alloy surface, stabilisation of A2 phase, as well as reduction of density.

The CALPHAD approach [7], introduced in **chapter 1.3,** is the main methodology used in this work to accelerate the research on HEAs for high temperature applications. CALPHAD is a very powerful method for designing new materials, because it allows to predict stable phases as a function of thermodynamic conditions in complex multicomponent materials, such as HEAs, once thermodynamic functions for the phases in lower order systems have been defined. Such method has several advantages over the traditional experimental investigation, which are described in more details in chapter 1.3. Though the classical CALPHAD approach can be considered a mature methodology, new developments are in progress, especially at the Pennsylvania State University, in the laboratory of prof. Zi-Kui Liu, where the very powerful tool - ESPEI infrastructure (Extensive Self-optimizing Phase Equilibria Infrastructure) [8] is under development. ESPEI is briefly introduced in section 1.3.2. During my thesis I had the opportunity to visit this laboratory and this made it possible to adopt such new techniques to the assessment of the most complex systems considered in this thesis.

The main aim of this thesis is the development of a thermodynamic database able to simulate HEAs based on a combination of basic alloy elements (Co, Cr, Fe and Ni) with refractory metals (Mo, Ta, W) and Al, in order to provide a reliable thermodynamic background to support the design of novel HEAs for high temperature applications.

The first step in implementing a new thermodynamic database is the selection of the most appropriate thermodynamic model for the representation of the thermodynamic functions of

each phase. This is crucial for a successful calculation of multi-component systems. Thermodynamic models adopted in this work are introduced in **chapter 2**.

Many attempts to predict thermodynamic properties and phase equilibria of HEAs by means of CALPHAD modelling have already been presented in the literature [9–12]. However, the available multicomponent databases, which have been often developed as an extension of the already existing databases for superalloys, are seldom reliable outside limited ranges of composition and temperature. It is then necessary to develop self-consistent multi-component databases where the different binary and ternary subsystems are reliably assessed in the full composition and temperature ranges.

In view of implementing a new multi-component database all assessment works already available in literature must be duly considered. They are usually concerning binary or ternary systems and are hardly consistent with each other, especially about the thermodynamic models adopted for the solid solution phases. Actually, different authors assessing different systems often select different models for the same phase, because their choice is based on different criteria. This makes it impossible to merge their lower order databases in the same multi-component database without reassessing selected phases or, in the worse cases, the entire system. From this point of view, one of the main challenges is the modelling of TCP phases, commonly occurring in systems formed by transition elements. Simplified thermodynamic models are often used to describe such phases and different authors applied different simplification criteria. The models chosen in this work are presented and discussed in **chapter 2.2**. In particular, the extended review of different models applied in the literature for the μ and σ phases can be found in sections 2.2.5-2.2.6. The correct prediction of the stabilities of the TCP phases is essential for industrial applications, therefore, in this work particular attention was paid to the modelling of such phases, in particular, μ and σ, present in several ternary systems [13]. Due to the high complexity of the modelling of TCP phases (high number of parameters to be evaluated), the very powerful tool - ESPEI [8] was often applied for the optimisation process.

Binary and ternary systems that have been partially or completely assessed in this thesis are presented and discussed in **chapter 3.1.**

According to the CALPHAD method, once binary and ternary subsystems are assessed, higher order phase diagrams may be reliably calculated by ideal extrapolation of the lower order ones. During this work I verified that this assumption is only approximately correct. In fact, I found that, when experimental results are available for quaternary or quinary systems, the introduction and evaluation of quaternary interaction parameters may be needed to better reproduce experimental equilibria. In some cases, metastable binary and ternary parameters turned out to

have an influence on equilibria in the multicomponent systems and were evaluated on the basis of multicomponent equilibria.

During my thesis I focused on the Al-Co-Cr-Fe-Ni system. Despite the fact that this system is the most frequently investigated HEA, the experimental information on the influence of single elements (such as Co, Cr and Fe) on the quinary phase stabilities is still very limited and validation of such system based purely on the literature data would be insufficient. This is also the reason why I decided to synthesize and analyse a few selected quinary samples. The results of this experimental investigation are reported in **chapter 4**, while experimental methods employed are briefly described in section 4.1. Microstructure and phase compositions of the tested samples were investigated after prolonged annealing to ensure attainment of equilibrium. Indeed, there were some appreciable discrepancies between the experimentally observed phase equilibria and those predicted by calculations. Then structural information and measured phase compositions obtained experimentally were used for the improvement of the database by a revision of metastable binary and ternary parameters and evaluation of quaternary interaction parameters.

The synergy between experiments and calculations is very important in the computational simulations in order to verify the reliability of the database. The available literature of the multicomponent systems of interest has been critically reviewed and the reported experimental information was used for further improvement of the quinary Al-Co-Cr-Fe-Ni system and several quaternary systems containing refractory metals, such as Mo and W. This is reported in **chapter 5**.

Finally, in **chapter 6,** the thermodynamic database was used for the simulations of phase stabilities in various multicomponent systems, with the scope of finding materials with solid solution structure suitable for high temperature applications. The behaviour of HEAs cannot be easily predicted, due to many factors that are described in the following section, therefore, CALPHAD modelling plays a very important role in accelerating the research on such alloys. The simulations provided a lot of valuable information on liquidus and solidus temperatures, the formation of intermetallic phases, eutectic reactions, phase compositions and the primary solidified phases in several multicomponent systems.

1.2. High Entropy Alloys

The concept of High Entropy Alloys (HEA) also called Multi-Principal Element Alloys (MPEA) is based on the relation between the configurational entropy and phase stability. Multiplicity of principal elements is the main factor that distinguishes them from conventional alloys, which composition is usually based on one or two principal components with other elements added in small quantities.

There is no strict definition of these systems, however, there are some general concepts. From the composition point of view HEAs have to be composed of at least 5 different elements in the nearly equimolar ratio [14]. It has been later extended by the same author, allowing addition of minor elements in order to tune the properties of the HEAs [15].
The entropy-based definition assumes that the ideal entropy of the system ΔS_{mix} should be higher or equal to 1.61R [15], where R is the gas constant (R=8.314 J/molK).
The value of ideal configurational entropy ${}^{id}_{\Delta}S$ can be quickly estimated from the Boltzmann equation:

$$\Delta^{id}S = -R\sum_{i=1}^{n} c_i \ln(c_i), \qquad \text{eq. (1)}$$

where n is number of components and c_i is concentration of the i-component.
The equation reaches a maximum value when all c_i are equal. For n=5 (compositional definition of HEAs), $\Delta^{id}S = 1.61R$. This number is a very simple approximation for an ideal system, where all of the atoms are relocated randomly, which is never the case of a real system. It is important to remember that the entropy is dependent on the temperature. It is assumed that the highest possible configurational entropy can be obtained at the elevated temperature when the atoms occupy nearly random positions. That is why the mentioned definitions should not be treated very strictly.
In fact, the ideal configurational entropy is only one of the contributions to the total mixing entropy $\Delta^{mix}S$, which also consists of the excess entropy $\Delta^{ex}S$, vibrational entropy $\Delta^{vib}S$, electronic ramdomness entropy $\Delta^{elec}S$ and magnetic dipole entropy $\Delta^{magn}S$.

$$\Delta^{mix}S = \Delta^{id}S + \Delta^{ex}S + \Delta^{vib}S + \Delta^{elec}S + \Delta^{magn}S \qquad \text{eq. (2)}$$

As the ideal and excess configurational entropy ($\Delta^{id}S + \Delta^{ex}S$) have a dominant influance on the total value of $\Delta^{mix}S$, the other contributions are often neglected in order to simplify calculations.

Maximizing configurational entropy can promote formation of single phase solid solutions instead of intermetallic compounds and this fact makes them attractive. Moreover, it can favor their mechanical and physical properties over conventional alloys. Another very important feature of HEAs is lattice distortion. Atoms with often very different atomic radius and electronic environments are randomly occupying different crystallographic sites (Wyckoff positions). As a consequence, every atom has different surroundings with different bonding energies. It leads to the various distortions of the lattice. The internal stresses that are accumulated due to the distortions can increase hardness and strength of the material. Nanoprecipitates that are formed during solidification are believed to be the main reason for the sluggish diffusion. It is the next characteristic that distinguishes HEAs from other alloys. Slower diffusion provides higher thermal resistance and allows for the better microstructure control [16]. All of these features have driven the scientific community to thoroughly explore such alloys in the search of a new material with excellent mechanical properties.

The enormous amount of possible alloy compositions that can be classified as HEAs or variation of HEAs makes it very challenging to compare the data or make any predictions.

Miracle and Senkov [1] divided HEAs into seven groups. In the first group there are 9 elements: Al, Co, Cr, Cu, Fe, Mn, Ni, Ti and V, most of them belong to the 3d transition metals. Alloys from this group are the most widely investigated (around 85% of all studies about HEA systems). They can be considered an extension of superalloys and stainless steels. The second group comprises alloys containing at least four refractory metals, however, often non-refractory elements are added, such as Al or Si. Such alloys are considered potential candidates for new generation high temperature structural alloys. Refractory metals represent very wide set of physical, mechanical and electrical properties. Light metals, such as Al, Be, Li, Mg, Sc, Si, Sn, Ti and Zn belong to the third family of low density materials. They could find application in the aerospace and transportation industry. The next groups consist of: lanthanides exhibiting single phase hcp structure; brasses and bronzes with elevated strength; precious metals that could be used as catalysts and interstitial compounds containing 3d transition and refractory metals with addition of B, C or N in the form of thin films.

The field of High Entropy Alloys (HEAs) is relatively new. First papers referring to HEAs were published in 2004 [14,17–20]. HEAs gained a lot of attention, when in 2011, Senkov et al. noticed that some refractory HEAs, namely NbMoTaW and VNbMoTaW can maintain superior mechanical properties to Ni-based superalloys, such as Inconel718 or Haynes230, at elevated temperatures [21]. Their yield strength as a function of temperature is compared in Fig. 1.

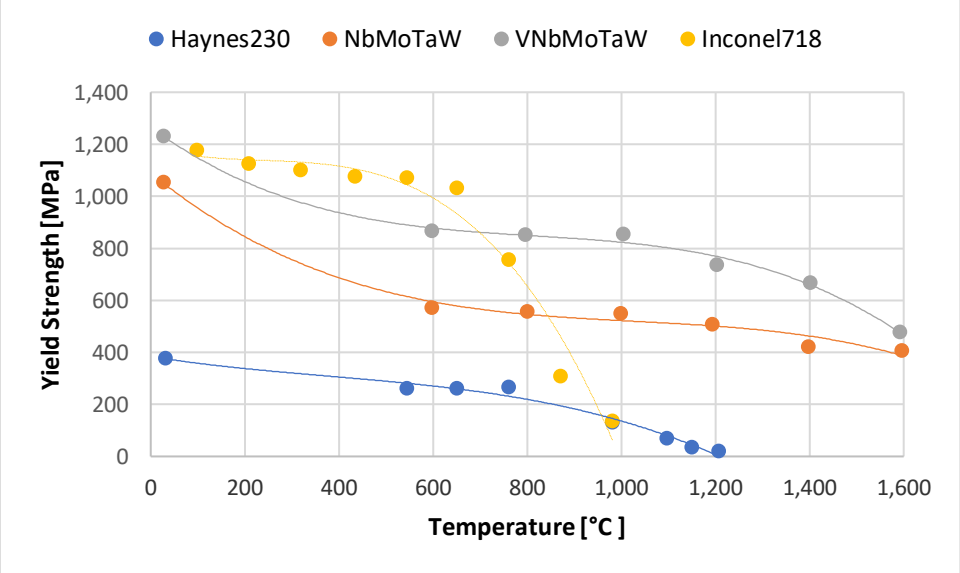

Fig. 1 *The yield strength as a function of temperature of selected superalloys and HEAs* [21].

As already mentioned, in this work I was particularly interested in the alloys for high temperature applications combining elements from the first and second family (3d transition metals and refractory metals). There is a huge amount of literature reporting microstructure, mechanical or corrosion behavior of alloys containing a mixture of 3d and refractory elements.

Among the most recent publications, the influence of Mo in the Co-Cr-Fe-Mo-Ni system was experimentally studied by Wu et al. [22], in particular the formation of μ and σ phases, which

were correlated with the addition of Mo and Cr, respectively. Shang et al. [23] studied the effect of Mo on the corrosion behavior. The Mo was found to be beneficial for the corrosion resistance, as long as the formation of σ phase is limited. Wang et al. [24] additionally examined the influence of annealing temperatures on the microstructure and corrosion resistance. Gasan and Ozcan [25] synthesized selected compositions from the Al-Co-Cr-Fe-Mo-Ni system examining their microstructure. They observed that the samples were composed of the soft solid solution A1 phase with precipitates of harder B2 phase and such mixture exhibited very good mechanical properties. Juan et al. [26] studied the influence of Mo in the same system on the laser-clad coatings. Beside the experimental measurements of microstructure, microhardness and wear resistance, the authors proposed criterions for phase predictions, such as atomic size difference, the mixing enthalpy, the mixing entropy and the specific laser energy. Zhuang et al. [27,28] investigated the influence on Mo and annealing on the microstructure and mechanical properties of $Al_{0.5}CoCrFeMo_xNi$ alloys. By the addition of 0.3 and 0.4 mol of Mo, the best balance between compressive strength and ductility was obtained.

The effect of Ta on the microstructure and mechanical properties of as-cast Co-Cr-Fe-Ni-Ta_x samples were investigated by several authors [29–32]. Fan et al. [33] examined the influence of annealing temperature on phase stabilities of the CoCrFeNiTa samples. They noticed that several intermetallic phases result stable at the equimolar composition, among which the Laves C14 phase is dominant.

Niu et al. [34] studied the influence of W on the microstructure, mechanical properties and corrosion resistance in the Co-Cr-Fe-Ni-W system. They reported that the addition of W creates lattice distortions and stabilizes the μ phase. The grain size decreases with the increasing amount of W which has a positive effect on microhardness, yield strength and pitting resistance. Dong and Lu investigated the microstructure and mechanical properties of the as-cast samples in the $AlCoCrFeNi_2W$ system by changing the amount of W [35] and the molar ratio between Al and W [36]. Only two phases resulted stable, A1 and A2 and their existence was correctly predicted by empirical parameters, such as the atomic radius difference, the mixing enthalpy, valence electron concentration and geometrical parameters. The increased amount of W improved the yield strength and hardness, however, it reduced the ductility. Among tested compositions, the $AlCoCrFeNi_2W_{0.2}$ showed the most promising results. In case of changing the Al:W molar ratio, the increased amount of W had a negative effect on mechanical performance.

A comprehensive review of high entropy alloys with promising high temperature applications was written by Chen et al. [2]. The authors noticed that the mechanical performance of refractory high entropy alloys is elevated in respect to the traditional refractory alloys. Additionally, they observed that the addition of other elements such as 3d metals or Al can be beneficial, due to the inhibition of formation of intermetallic phases or reduction of density. Addition of Cr and Al can further improve high temperature oxidation resistance. However, it has been underlined, that more work is needed in order to find compositions that provide good balance between high temperature strength and high ductility at room temperature, keeping the alloy density low. The same observation was made in the review by Senkov et al. [37]. The

proposed approach to deal with this problem is designing a structure with a well-distributed strengthening phase in a ductile matrix. As the authors noticed, controlling the microstructure in the meaning of size, volume fraction and distribution of a strengthening phase by means of heat treatment is essential in obtaining good balance between strength and ductility. The authors encourage to explore the broad range of compositions rather than study alloys that are already known. Development of universal strategies and criteria that could help in understanding the connection between the HEA's composition and its properties is vital. The detailed review of mechanical properties and deformation mechanisms of HEAs was recently published by George et al. [38]. They highlighted the importance of characterizing and controlling the microstructure of investigated alloys.

1.3 Introduction to CALPHAD

The first step in designing a new material is investigating its microstructure, because this is the origin of mechanical properties, and consequently the performance. Gathering raw experimental data is a very time-consuming and expensive process. Additionally, experimental measurements are restricted to small systems, with increasing amount of elements the alloys become very complicated to analyze. Due to this fact it would not meet the present requirements of the industry. There was a need for more powerful tool that could support experimental measurements and accelerate the new material development.
The obvious solution was to implement numerical calculations. Every system at its equilibrium is described by thermodynamic functions, which determine phase equilibria, therefore are crucial in understanding its behavior at different conditions. The main challenge was to create a model that can link the experimentally obtained properties with mathematical calculations. The lack of data can be compensated by estimates. Verifying the calculations with experimental data creates very good and productive synergy, accelerating the research and at the same time controlling the reliability of the results. However, the high emphasize should be put on the critical evaluation of the data. It may be problematic to estimate if the samples have reached the equilibrium state, whereas thermodynamic calculations require equilibrium conditions [39].

As already mentioned before, thermodynamics determine phase equilibria at certain conditions, which allows for constructing phase diagrams. First attempts to calculate phase diagrams took place at the beginning of ninetieth century [40], however, a lot of time has passed until they started being used for real applications [41,42].

1.3.1 Classic CALPHAD

The CALPHAD method (CALculation of PHAse Diagrams) was first described in 1970 by Kaufman and Bernstein [7]. Initially, the method did not reflect all of the real systems due to using regular and stoichiometric models. It underwent a very fast development and improvement due to very high potential of application and simplicity that it offers [43]. In fact, it is the simplest and most efficient way to calculate phase diagrams for multicomponent

systems [44].

The CALPHAD approach is based on mathematical models that allow to calculate the molar Gibbs free energy (G_m) of individual phases α. Presenting G_m^α as a function of state variables (temperature T, pressure p, chemical composition x_i, etc.) allows to calculate thermodynamic equilibrium by finding its global minimum (eq. 3) [45]. This is the basis for finding stable phases and their compositions at the certain conditions in every system and constructing their phase diagrams.

$$\min(G) = \min\left(\sum_\alpha m^\alpha G_m^\alpha\left(T, p, x_i^\alpha or\ y_k^{(l,a)}\right)\right) \quad \text{eq. (3)}$$

By knowing the value of the Gibbs free energy it is possible to derive other thermodynamic quantities, some relations are presented below:

Entropy: $S = \left(\frac{\partial G_m}{\partial T}\right)_{p,N_i}\ [\frac{J}{K}]$ eq. (4)

Enthalpy: $H = G + TS = G - T\left(\frac{\partial G}{\partial T}\right)_{p,N_i}\ [J]$ eq. (5)

Heat capacity: $C_p = -T\left(\frac{\partial^2 G}{\partial T^2}\right)_{p,N_i}\ [\frac{J}{K*mol}]$ eq. (6)

In the CALPHAD method every phase is represented as a set of thermodynamic functions describing Gibbs free energy containing adjustable parameters, that can be optimized with help of experimental data and first-principle calculations based on density functional theory (DFT) [46]. Experimental data can regard phase equilibria (equilibrated alloys, diffusion couples) as well as thermodynamic quantities measured using calorimetry, such as enthalpy of formation ΔH_f, enthalpy of mixing ΔH_{mix} or heat capacity C_p. Gibbs free energy cannot be measured directly, but can be derived from other quantities, the relations were shown in eq. 4-6. DFT-based first-principle calculations can also provide very valuable information on thermodynamic properties, not only of stable phases but also unstable and metastable, which can play very important role during extrapolation to higher order systems. The integration of CALPHAD modelling and the DFT calculations is more and more common and significantly increases the robustness of the CALPHAD method.

Very powerful feature of CALPHAD modelling is the fact that binary and ternary parameters can be extrapolated to the multicomponent systems with sufficient accuracy. The obvious limitation of such approach is inability to predict the formation of phases that are present only in higher order systems (at least 4 elements). What is more, any changes in the description of lower order system have an influence on related higher order systems and as a consequence their description has to be adjusted.

Nowadays there is a big number of software suitable for thermodynamic calculations being used for the academic and industrial purposes (for instance PANDAT [47], Thermo-Calc [48], FactSage [49], PyCalphad [50] and many other).
In the present work Thermo-Calc software was used for calculating of phase diagrams. Optimisations have been carried out using different procedures: Parrot module in Thermo-Calc

[48], where the parameters' values are fitted to the experimental data by the least-squares method (eq. 7), and by ESPEI [8], described in the following section.

$$F = \sum_j \left(\frac{a_j^{exp} - a_j^{model}(vi)}{\sigma_j} w_j\right)^2 \qquad \text{eq. (7)}$$

Where σ_j is the uncertainty of the experiment a_j^{exp}, w_j is a weight assigned to the set of data (default 1) and $a_j^{model}(vi)$ is the value calculated using the model parameters, v_i. During the optimization by the least-squares method the model parameters v_i are modified in order to minimize the value of F.

Many researchers have already successfully applied CALPHAD modelling to the exploration of HEAs. As an example, Zhang et al. [51] developed a thermodynamic database of the Al-Co-Cr-Fe-Ni system and studied the primary solidified phases and the effect of each element on the stabilities of solid solution phases. Choi et al. [12] thermodynamically described the Co-Cr-Fe-Ni-V system. However, their database is limited to the phases stable in the quinary system and many intermetallic phases stable in the binary sub-systems were omitted. Muller et al. [52] created a database containing Al, Cr, Mo, Nb, Ta and Ti and confirmed its reliability by experimental measurements. What is more, several software released commercial databases dedicated for high entropy alloys, such as PanHEA (Pandat) containing 15 elements or TCHEA4 (Thermo-Calc) with 26 elements.

1.3.2 New developments

Nowadays, CALPHAD is a well-established method, however, it is still being developed. New experimental or calculated information about low order (1, 2 or 3-component) systems is being constantly published and updating the already existing multicomponent databases is one of the main challenges of CALPHAD modelling. Any small modification of parameters in a low-order system creates a domino effect: a need of revision of all related systems. In the recent years a lot of effort has been made to automate the development of thermodynamic databases by applying advanced algorithms and machine learning approach.

The high-throughput ML-HEA approach has been developed by Kaufmann and Vecchio [53] in which the random forest machine learning model is applied to predict which solid solution will form in a multicomponent high entropy alloy which is a very useful information prior modelling. Zomorodpoosh et al. proposed an automated model for weighting datasets used for parameters optimization [54]. This method is based on Unequal K-Fold Cross-Validation (UKFCV) approach. Usually, the weight of experimental datasets is assigned manually by a researcher which is linked to a large uncertainty. Applying UKFCV can contribute to the improved quality of the optimization process. Krajewski et al. implemented machine learning techniques in a development of a tool for predictions of formation energies - SIPFENN (Structure-Informed Prediction of Formation Energy using Neural Networks) [55]. The neural

networks were trained with the DFT calculation results published in the Open Quantum Materials Database (OQMD) [56].

Another example of a very powerful, new generation software tool is ESPEI (Extensive Self-optimizing Phase Equilibria Infrastructure) [8], an open-source Python library for an automated database optimization. It uses PyCalphad [50] for calculations of Gibbs Free energy. In the first step, the models for each phase and parameters are generated based purely on the thermochemical data. Afterwards, the parameters generated in the first step are optimized based on all provided experimental data simultaneously by means of Bayesian optimization [57] determined numerically by Markov Chain Monte Carlo (MCMC). Unlike any other tool for CALPHAD modelling, ESPEI allows for the uncertainty quantification. What is more, thanks to the high level of automation, database can be quickly refined when new data are available.

In this work, beside the classical CALPHAD approach, the new solutions, such as ESPEI tool, were applied for optimization of selected complex ternary systems.

2. Thermodynamic models

2.1. Introduction to thermodynamic models

A CALPHAD thermodynamic database contains a list of thermodynamic functions describing Gibbs Free Energy of every stable phase in a given system.
The Gibbs energy is expressed according to the "Compound Energy Formalism" (CEF) [58], a general approach which allows to select the most appropriate model for each phase in the framework of the same formalism. According to the CEF, the different constituents of a phase (neutral atoms, ions, vacancies, etc.) are distributed in one or more thermodynamic sublattices where they mix according to the classical solution theory (adopting ideal, regular, subregular, etc. behavior) with different interaction parameters in different sublattices.

The total Gibbs energy can be expressed as the sum of three main terms: the reference term (${}^{\mathrm{ref}}\mathrm{G}^{\varphi}$), one ideal mixing term (${}^{id}\mathrm{G}^{\varphi}$) and an excess term (${}^{ex}\mathrm{G}^{\varphi}$). They can be followed by further terms in case further physical interactions (such as magnetic, electrical, etc.) occur (${}^{phy}\mathrm{G}^{\varphi}$):

$$G^{\varphi} = {}^{\mathrm{ref}}\mathrm{G}^{\varphi} + {}^{id}\mathrm{G}^{\varphi} + {}^{ex}\mathrm{G}^{\varphi} + {}^{phy}\mathrm{G}^{\varphi} \qquad \text{eq. (8)}$$

The molar reference Gibbs energy of a phase φ can be easily calculated by summing the reference Gibbs energies for pure elements (taken from SGTE Pure Element Database version 5.0, 2009 (unary database [59])) multiplied by their molar fractions.

$${}^{\mathrm{ref}}\mathrm{G}^{\alpha}{}_{\mathrm{m}} = \sum_x y_x \, (a_x + b_x T + GHSERXX) \qquad \text{eq. (9)}$$

where y_x is mole fraction of the element x in the α phase, GHSERXX is the function describing its Gibbs energy in the reference state and a+bT is its lattice stability in the phase. The set of functions describing the reference Gibbs energy consists of so called “endmembers”, where each sublattice is occupied by only one element.

The configurational Gibbs energy is dependent on the number of sites in each sublattice, assuming the random mixing of the constituents. It takes into account only long range ordering (LRO).

Excess Gibbs energy can be expressed by the following polynomial equation, that was used for the first time by Redlich and Kistler [60]:

$$G_m^E = x_1 x_2 \sum_{k=0}^{n} L_{12}^k (x_1 - x_2)^k \qquad \text{eq. (10)}$$

2.1.1. Pure elements

In case of a pure element, second and third terms are missing and any dependence on

composition of course disappears. Eq. (8) becomes:

$$G^{\varphi} = {}^{\mathrm{ref}}\mathrm{G}^{\varphi} + {}^{magn}\mathrm{G}^{\varphi} \qquad \text{eq. (11)}$$

with:

$${}^{\mathrm{ref}}\mathrm{G}^{\varphi} - H_{298}^{SER} = \mathrm{A} + \mathrm{BT} + \mathrm{CT}\ln(\mathrm{T}) + DT^{2} + ET^{-1} + \cdots \qquad \text{eq. (12)}$$

and

$${}^{magn}\mathrm{G}^{\varphi} = RT \cdot f(\tau) \cdot ln(\beta(x) + 1) \qquad \text{eq. (13)}$$

where *A*, *B*, *C*, *D*,… are empirical parameters taken from the PURE database by SGTE [59]. They are referred to the Standard Element Reference (SER) state, i.e. the stable phase at 1 10^{-5} Pa and 298.15 K.

The magnetic term (eq. 13) is based on the model introduced by Inden [61] and subsequently adapted by Hillert and Jarl [62]. β is the average magnetic moment per mole of atoms in Bohr magnetons, τ is the ratio T/T_C (T_C= critical temperature for magnetic ordering), and $f(\tau)$ is a polynomial expression obtained by expanding Inden's description of the magnetic heat capacity into a power series of τ.

2.1.2. Substitutional random solutions

In the simplest case of random mixing, as in the liquid phase or in the fcc, bcc and hcp solid solutions, only one sublattice is needed and it can be occupied by each element with the equal probability. The three main terms of eq. (8) are:

$$\begin{aligned} {}^{\mathrm{ref}}\mathrm{G}^{\varphi} &= \sum_{i} x_i G_i^{\varphi}(T) \\ {}^{id}\mathrm{G}^{\varphi} &= RT \textstyle\sum_i x_i ln x_i \\ {}^{ex}\mathrm{G}^{\varphi} &= {}^{\mathrm{ex}}\mathrm{G}^{\varphi}_{2} + {}^{\mathrm{ex}}\mathrm{G}^{\varphi}_{3} + \ldots \end{aligned} \qquad \text{eq. (14)}$$

where: x_i is, at the same time, the site fraction in the unique sublattice and the overall mole fraction of component *i*. $G_i^{\varphi}(T)$ is the Gibbs energy of the pure component *i* in the φ phase (eq. (12)), and ${}^{\mathrm{ex}}\mathrm{G}^{\varphi}_{2}$ and ${}^{\mathrm{ex}}\mathrm{G}^{\varphi}_{3}$ are the binary and ternary excess terms, respectively. They are expressed as:

$${}^{\mathrm{ex}}\mathrm{G}^{\varphi}_{2} = \textstyle\sum_{i=1}^{n-1}\sum_{j=i+1}^{n} x_i x_j \sum_{\nu} L_{i,j}^{\varphi}(T)\left(x_i - x_j\right)^{\nu} \qquad \text{eq. (15)}$$

and

$${}^{\mathrm{ex}}\mathrm{G}^{\varphi}_{3} = \textstyle\sum_{i=1}^{n-2}\sum_{j=i+1}^{n-1}\sum_{k=j+1}^{n} x_i x_j x_k \left(u_i L_i^{\varphi}(T) + \mathrm{u}_j L_j^{\varphi}(T) + \mathrm{u}_k L_k^{\varphi}(T)\right) \qquad \text{eq. (16)}$$

respectively, with:

$$u_i = x_i + \frac{1 - x_i - x_j - x_k}{3}, \quad u_j = x_j + \frac{1 - x_i - x_j - x_k}{3}, \quad u_k = x_k + \frac{1 - x_i - x_j - x_k}{3} \qquad \text{eq. (17)}$$

according to the Muggianu ternary extrapolation formula [63].

$L^{\varphi}(T)$ in eqs. (15) and (16) are empirical parameters whose temperature dependence is similar to that of $G^{\varphi}(T)$ given in eq. (12), i.e.:

$$L^{\varphi}(T) = A^{\varphi} + B^{\varphi}T + C^{\varphi}TlnT + D^{\varphi}T^2 + \ldots \qquad \text{eq. (18)}$$

For a binary phase with magnetic ordering the composition dependence of ${}^{magn}G^{\varphi}$ (eq. (13)) results from the composition dependence of T_C and β, which are expressed by a Redlich–Kister series expansion:

$$\begin{aligned} T_C^{\varphi}(x) &= x_A T_C^{\varphi}(A) + x_B T_C^{\varphi}(B) + x_A x_B \sum_{i=0..n} T_C^{\varphi} \cdot (x_A - x_B)^i \\ \beta^{\varphi}(x) &= x_A \beta^{\varphi}(A) + x_B \beta^{\varphi}(B) + x_A x_B \sum_{i=0..n} \beta^{\varphi} \cdot (x_A - x_B)^i \end{aligned} \qquad \text{eq. (19)}$$

where T_C^{φ} and β^{φ} are expansion parameters to be evaluated on the basis of the experimental information available.

2.1.3. Stoichiometric phases

Stoichiometric phases or compounds are modelled by an n-sublattice model with each sublattice occupied by only one element. As in the case of pure elements, the ideal mixing ${}^{id}G^{\varphi}$ and excess energy ${}^{ex}G^{\varphi}$ contributions are equal to zero. In this case eq. (8) reduce to:

$${}^{ref}G^{\varphi} = \sum_i x_i G_i^{SER}(T) + {}^{form}G^{\varphi}(T) \qquad \text{eq. (20)}$$

where $G_i^{SER}(T)$ is the Gibbs energy of the pure component *i* in its standard element reference state (SER) and ${}^{form}G^{\varphi}(T)$ is the Gibbs energy of formation of the considered compound, expressed as a function of temperature, according to eq. (9).

2.1.4. Ordered solutions

Ordered solutions are intermetallics with a reference stoichiometry, but characterised by more or less extended solubility ranges. The solubility mechanism is generally due to the reciprocal substitution between components in their crystallographic sites. In this case each component can occupy two or more (possibly all) sublattices. A typical example may be an ordered binary solution represented by a two-sublattice model where each sublattice is mainly occupied by one component but its substitution by the other element is allowed. Then both elements can occupy both sublattices.
In case of mixing between constituents, the term "site fraction" $y^{(s)}_i$ is introduced, which is the mole fraction of the component i in the sublattice s. Site fractions obey the conditions:

$$\sum_i y_i^{(s)} = 1$$
$$\frac{\sum_s n^{(s)} y_i^{(s)}}{\sum_s n^{(s)}(1-y_{VA})} = x_i \qquad \text{eq. (21)}$$

where $n^{(s)}$ are the stoichiometric coefficients relating the sublattices. Notice that eqs. (21) have been formulated assuming that vacancies (Va) can also be included in one or more sublattices. This accounts for a second solubility mechanism, namely vacancy formation in one or more sublattices.
Equations (14) become:

$$^{ref}G^{\varphi} = \sum_i \sum_j \dots \sum_k y_i^{(1)} y_j^{(2)} \dots y_k^{(s)} G^{\alpha}_{i,j..k}$$
$$^{id}G^{\varphi} = \frac{1}{\sum_s n^{(s)}} RT \sum_s \sum_i n^{(s)} y_i^{(s)} \ln y_i^{(s)} \qquad \text{eq. (22)}$$
$$^{ex}G^{\varphi} = {}^{ex}G^{\varphi}_2 + {}^{ex}G^{\varphi}_3 + \dots = \sum_s \sum_i \sum_j y_i^{(s)} y_j^{(s)} \sum_{r \neq s} \sum_k y_k^{(s)} L^{\alpha}_{i,j..k}(T) + \dots + {}^{ex}G^{\varphi}_3 + \dots$$

where $G^{\varphi}_{i:j:\dots:k}$ in $^{ref}G^{\varphi}$ are the Gibbs energies of all the so-called "end members", the stoichiometric compounds (either stable, metastable or unstable) formed when only one constituent is present in each sublattice. $L^{\varphi}_{I,j:\dots:k}(T)$ in $^{ex}G^{\varphi}_2$ are the parameters describing interaction between two mixing elements i and j in the sublattice s (interaction parameters), while the other sublattices are singly occupied. More terms can be added to $^{ex}G^{\varphi}_2$, corresponding to simultaneous mixing on two sublattices while the remaining sublattices are singly occupied. $^{ex}G^{\varphi}_3$ accounts for the possible interactions of three elements in a given sublattice.

2.1.5. Solid solutions with an order/disorder relation

A special case, relatively frequent in intermetallic systems, are the ordered phases which may be related to a disordered one. This is the case of the B2 phase (cP2, CsCl type) related to the disordered bcc structure A2 (cI2, W-type), and the $L1_2$ phase (tP2, $AuCu_3$ type) related to the disordered fcc structure A1 (cF4, Cu-type).
Ordered and disordered structures can transform to each other by a first order as well as a second order transformation. Such a behavior may be modeled by introducing one single Gibbs energy expression for both ordered and disordered phases. The ordering state will depend on the occupation of the different sublattices. This means that, in the case of A2/B2 ordering in Al-Fe, taken as an example, we can assume for B2 a two-sublattice model, $(Al,Fe)_{0.5}$ $(Al,Fe)_{0.5}$, which become equivalent to the single sublattice model of A2, $(Al,Fe)_1$, when the two sublattices have identical occupation and, consequently, become indistinguishable. This is realized by introducing the following expression for the Gibbs energy:

$$G^{A2/B2} = G^{A2}(x) + G^{B2}(y_1, y_2) - G^{B2}(x, x) \qquad \text{eq. (23)}$$

where $G^{A2}(x)$ is the Gibbs energy of the disordered phase calculated at the concentration *x*

according to the one sublattice model (eq. 14), while $G^{B2}(y_1, y_2)$ and $G^{B2}(x, x)$ are the Gibbs energies of the ordered phase (eq. 22) calculated first at the site fractions y_1, y_2 (ordered state) and then at the site fractions x, x (disordered state). So, the difference $G^{B2}(y_1, y_2) - G^{B2}(x, x)$ is the Gibbs energy of ordering.

2.2. Models selected in this work

In the following chapter the phase models used in this work will be presented together with the main criteria, based on which the models have been chosen. A special attention will be given to the modelling of the σ and μ phases, due to their complexity and a big variety of models used in the literature and, as a consequence, lack of compatibility between different published assessments.

For ordered phases the crystallographic structure is a dominant factor in choosing the right model. The thermodynamic sublattices should correspond to crystallographic sites. What is more, in the case of multi-component databases, it is important to use the minimum number of sublattices for the purpose of limiting the number of parameters to be evaluated while keeping the ability to satisfactorily reproduce the phase solubility observed experimentally. For that reason, crystallographic sites that are occupied by atoms of similar size and coordination number, can be merged together in a single sublattice.

All sublattices in a single model follow the order of decreasing coordination of the corresponding crystallographic sites. By way of illustration, in the structure of μ phase there are 5 different atomic positions. In the model adopted in the present work, two of atomic positions with the highest coordination number are merged, which generates 4 sublattices: (CN15-16, $6c^{I}+6c^{II})_{12}$ (CN14, $6c^{III})_6$ (CN12, 3a)$_3$ (CN12, 18h)$_{18}$. Finally, the model can be simplified as (A)$_4$ (A,B)$_2$ (A,B)$_1$ (A,B)$_6$.

The names of the phases were usually selected following a few rules. The most common phases are named after their Strukturbericht, e.g. A1, A2, A3, etc. If the model was chosen based on the crystallographic structure, the name of the prototype is used followed by '_type'. On the other hand, if the model is related to the stoichiometry of the phase, the name is simply the stoichiometric composition.

The detailed discussion of model selection for each type of phases can be found in the following sections of this chapter.

2.2.1. Disordered phases: fcc (cF4 – Cu), bcc (cI2 – W) and hcp (hP2 – Mg)

In the disordered phases, such as fcc – A1, bcc – A2 and hcp - A3 the single crystallographic site can be occupied by each element with the same probability, hence only one sublattice is needed. Their unit cells are presented in Fig. 2. An additional sublattice containing only vacancies (Va) is added, to represent the octahedral interstitial sites, possibly occupied by small atoms such as C, O, etc.

Point defects can be present in the crystallographic structure, such as vacancy formation, therefore Va is added together with all elements to the first sublattice. This means that endmembers and interaction parameters involving vacancies must be added for more accurate modelling, especially in the systems where they are present in significant amounts. As observed by [64], assuming the value of zero for the Va endmembers G(XX,Va:Va) can lead to unwanted stability. With the zero value, the increase amount of vacancies lowers the Gibbs energy in respect to the pure metal. The opposite tendency can be observed with the positive value of Gibbs energy for the pure vacancies, increasing the Gibbs energy with the increasing fraction of vacancies. What is more, for the low amount of vacancies, the sum of Gibbs free energy G_{Va} and interaction parameter between vacancies and other atoms or vacancies L was important rather than G_{Va} alone, which means that G_{Va} can have a general value that in different systems can be modified using L parameter. This requires that the Gibbs energy of the empty bcc sublattice, G(A2,Va:Va), is evaluated even if this value is not experimentally accessible: Stein et al. [65] suggested G(A2,Va:Va)=30T and this assumption was subsequently confirmed by Dinsdale [64]. Guan and Liu proposed a new approach of modelling vacancies in solids [66] where the value of the Gibbs Energy of vacancies is related to their molar volume and pressure (G_{va} =G_{Va}^{0}+PV_{Va}). While this approach has certainly more physical meaning compared to the previous works, it would require a lot of modifications in the multicomponent database, in which the value proposed by Stein et al. (30T) has been applied.

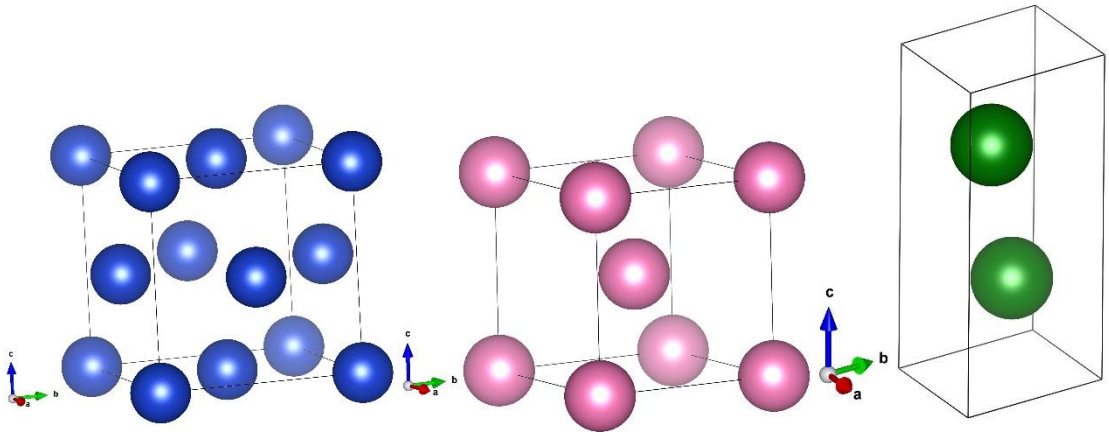

a) fcc **b)** bcc **c)** hcp

Fig. 2 *The unit cell of the a) fcc, b) bcc and c) hcp phase.*

About the binary parameters for the atom/vacancy interactions in the A2 phase, the literature data has been rearranged by introducing the new functions G8CXXVA and G6OXXVA. This takes into account that the first coordination sphere includes 14 positions: 8 closer to the central atom, with cubic geometry, and 6 a little more distant, with octahedral geometry. In this way vacancies placed in the 8 cubic position are distinguished from vacancies placed in the 6 octahedral position. This description, though mathematically equivalent to the previous one, should be more chemically significant.

2.2.2. Ordered bcc – B2 (cP2 – CsCl type)

In the ordered bcc structure (B2), 2 crystallographic sites can be distinguished: 1a and 1b, as shown in Fig. 3. Two sublattices were used to model ordered bcc (B2) phase, each of them containing vacancies in addition to all of the elements present in the system. In principle a 4-sublattice model would be more appropriate, because it would be able to describe also the $D0_3$ and B32 bcc-related ordered structures observed in some systems. However, for simplicity in a large multi-component alloy database, the simpler 2-sublattice model has been preferred.

$$\boldsymbol{(A,B,Va)_{0.5}\ (A,B,Va)_{0.5}(Va)_3}$$

The sublattices being equivalent, a series of constraints between Gibbs energy terms must be fulfilled, as suggested by Dupin and Ansara [67]: in particular the Gibbs energy cannot change when constituents are exchanged from first to second sublattice:

$$G^{BCC2}_{A:B} = G^{BCC2}_{B:A}, \qquad L^{BCC2}_{A,B:C} = L^{BCC2}_{C:A,B}, \text{ etc.}$$

Such relations are very effective in reducing the overall number of independent interaction parameters to be evaluated.

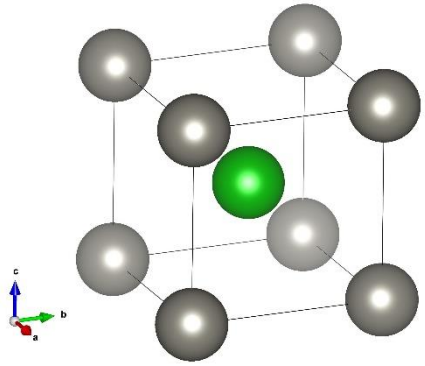

Fig. 3 *The unit cell of the B2 phase. Different colours correspond to different Wyckoff positions.*

2.2.3. Ordered fcc – $L1_2$ (cP4 - Cu_3Au type)

In the ordered $L1_2$ lattice there are two Wyckoff positions 1a and 3c (Fig. 4). In the literature, four sublattices $(A,B)_{0.25}(A, B)_{0.25}(A, B)_{0.25}(A,B)_{0.25}$ are sometimes used to describe different types of ordering of the fcc phase, such as $L1_2$ and $L1_0$ by a single phase model. As the $L1_2$ structure is more common in the systems considered in this work, for simplicity the two-sublattice model is applied:

$$\mathbf{(A,B)_{0.75}\ (A,B)_{0.25}(Va)_1}$$

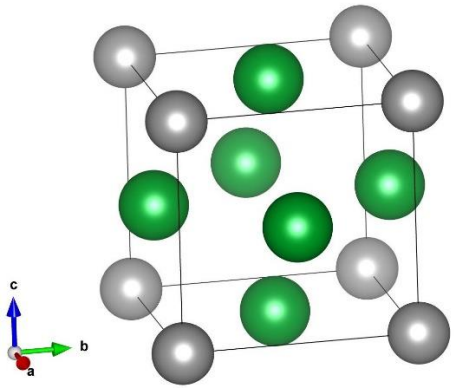

Fig. 4 *The unit cell of the $L1_2$ phase. Different colours correspond to different Wyckoff positions.*

2.2.4. Stoichiometric intermetallic phases

The models describing stoichiometric binary and ternary intermetallic phases contain n sublattices and each of them is occupied by only one element (or more elements if the same phase is present in more than one system). They do not show any solubility ranges in binary systems, while binary stoichiometric phases can show some line solubility in ternary systems. The model can be related to their crystal structure if it is known or to the composition that was experimentally observed, which is more often the case. The phases modelled as stoichiometric are listed in Table 1.

Table 1 *The stoichiometric phases, their structural information and model used in the database.*

Phase	Structure information	Model
$FeAl_2$_type	aP18 – $Fe_5(Fe_{0.5}Al_{0.5})_3Al_{10}$ -P1	$(Co,Cr,Fe,Mo,Ni)_1(Al,Ta)_2$
WAl_2		$(W)_1(Al)_2$
$CoAl_3$	mS36 – $(Co_{.88}Ni_{.12})_4Al_{12.1}$	$(Co,Ni)_{0.255}(Al)_{0.745}$
$MoAl_3$	mC32 – Cr_3Si– Cm	$(Fe,Mo)_1(Al)_3$
$NiAl_3$_type	oP16 – Fe_3C	$(Co,Fe,Ni)_1(Al)_3$
$CrAl_4$	oS584 - $Cr_{23.76}(Cr_{0.23}Al_{0.77})_{21}Al_{96.10}$	$(Cr,Fe)_1(Al,Va)_4$
$MoNi_4$_type	*tI*10 – $MoNi_4$ - *I*4/*m*	$(Al,Mo,W)_1(Ni)_4$
WAl_4_type	mC30 - WAl_4 - Cm	$(Fe,Mo,W)_1(Al)_4$
$CrAl_5$	*mP*48 – $CrAl_5$ - *P2*	$(Cr,Fe)_1(Al)_5$
WAl_5_type	hP12 - WAl_5 – $P6_3$	$(Fe,Mo,W)_1(Al)_5$
$NbNi_8$_type	*tI**	$(Mo,Ta,W)_1(Ni,W)_8$
$MoNi_8$	Pt_8Ti – 4/m2/m2/m	$(Mo)_1(Ni)_8$
WAl_{12}_type	cI26 - WAl_{12} – $Im\bar{3}$	$(Fe,Mo,W)_1(Al)_{12}$
W_2Ni	*tI*96 – W_2Ni - *I4*	$(W)_2(Ni)_1$
Co_2Al_5	hP28 - Co_2Al_5	$(Co,Fe,Ni)_2(Al)_5$
Fe_2Al_5	oS24 – $FeAl_{2.8}$ - Cmcm	$(Co,Cr,Fe,Mo,Ni)_2(Al)_5$

Ta_2Co_7_type	*hR*36 – Ta_2Co_7 - *R*-3*m*	$(Ta,W)_2(Co,Cr,Ni)_7$
Co_2Al_9	mP22 - Co_2Al_9	$(Co,Fe,Ni)_2(Al)_9$
Ni_3Al_4	cI112 - Ni_3Ga_4	$(Co,Ni)_3(Al)_4$
Mo_3Al_8	mC22 - - c2/m	$(Fe,Mo)_3(Al)_8$
Cr_4Al_{11}	*aP*15 – Mn_4Al_{11} - *P-1*	$(Cr)_4(Al)_{11}$
O-Co_4Al_{13}	oP102 - Co_4Al_{13}	$(Co)_{0.24}(Al)_{0.76}$
Y-Co_4Al_{13}	m* - ??? *C2/m*	$(Co,Ni)_{0.245}(Al)_{0.755}$
Mo_4Al_{17}_type	mC84 - -C2	$(Fe,Mo)_4(Al)_{17}$
Ni_5Al_3	oS16 – Pt_5Ga_3	$(Ni)_5(Al)_3$
Mo_5Al_{22}	oF216 - -Fdd2	$(Fe,Mo)_5(Al)_{22}$
Cr_7Al_{45}	*mC*104 – V_7Al_{45} - *C2/m*	$(Cr,Fe,Ni)_7(Al)_{45}$
$Mo_{37}Al_{63}$	- -	$(Fe,Mo)_{37}(Al)_{63}$
$TaCo_2Al$	cF16 -BiF_3 - Fm-3m	$(Ta)_1(Co)_2(Al)_1$
$TaNi_6Al$	hP16 -$TiNi_3$ - $P6_3/mmc$	$(Ta)_1(Ni)_6(Al)_1$
$Fe_5Ni_{24}Al_{71}$		$(Fe)_{0.5}(Ni)_{0.24}(Al)_{0.71}$
EPSILON3	oP - $Cr_{20}Fe_{2.5}Al_{77.5}$	$(Cr)_{0.21}(Fe)_{0.02}(Al)_{0.77}$
$Ni_{14}Al_{75}Mo_{11}$		$(Al)_{0.75}(Mo)_{0.11}(Ni)_{0.14}$

2.2.5. Nonstoichiometric intermetallic phases

Nonstoichiometric intermetallic phases exhibit a certain homogeneity range, usually around a reference stoichiometry. The solubility is generally caused by substitution between elements in one or more crystallographic sites and it can be represented in the thermodynamic model by allowing exchange between various components (placing more than one element in one or more sublattices). Solubility can be also attributed to the formation of vacancies, reproduced by adding Va to one or more sublattices. The phases modelled as nonstoichiometric are listed in Table 2.

Table 2 *The nonstoichiometric phases, their structural information and model used in the database.*

Phase	Structure information	Model
MoNi_type	oP56 - MoNi – $p2_12_12_1$	$(Mo,Ta,W)_{12}(Al,Co,Cr,Fe,Mo,Ni,Ta,W)_{20}(Co,Cr,Fe,Ni)_{24}$
$MoPt_2$_type	oI6 - $MoPt_2$ - Immm	$(Cr,Mo,Ni)_1(Cr,Ni)_2$
$MoSi_2$_type	tI6 – $MoSi_2$ – I4/mmm	$(Al,Co,Cr,Ni,Ta)_1(Al,Co,Cr,Ni,Ta)_2$
$D0_{19}$	hP8 – Mg_3Cd – $P6_3/mmc$	$(Al,Co,Cr,Mo,Ni,Ta,W)_1(Al,Co,Ni,Ta,W)_3(Va)_2$
$TiAl_3$_type	tl8 – $TiAl_3$ – I4/mmm	$(Al,Fe,Mo,Ta)_1(Al,Fe,Ni)_1(Al,Fe,Ni)_2$
$NbPt_3$_type	mP16 – $NbPt_3$ – $P2_1/m$	$(Mo,Ni,Ta)_1(Mo,Ni,Ta)_3$
$TiCu_3$_type	$D0_a$ - Cu_3Ti - pmmn	$(Mo,Ni,Ta,W)_4(Ni)_2(Al,Mo,Ni,Ta,W)_2$
Al_2Cu_type	tI12 – Al_2Cu – I4/mmc	$(Co,Cr,Ni,Ta,W)_2(Al,Co,Cr,Ni,Ta,Va)_1$

Ni_2Al_3	hP5 – Ni_2Al_3 -	$(Al)_3(Al,Co,Cr,Fe,Ni)_2(Co,Ni,Va)_1$
Mo_3Al	cP8 – Cr_3Si -	$(Al,Fe,Mo)_{.75}(Al,Fe,Mo)_{.25}$
Ta_3Fe_2		$(Al,Fe,Ta)_2(Al,Fe,Ta)_3$
M_4Al_{13}_type	mS102 – Fe_4Al_{13} – C2/m	$(Co,Cr,Fe,Mo,Ni)_{.235}(Al)_{.6275}(Al,Ta,Va)_{1375}$
γ-HT	cI52 – Cu_5Zn_8 – I4-3/m	$(Al,Cr,Fe,Mo)_2(Al,Cr,Fe,Mo,Ni)_3$ $(Cr,Fe,Ni)_2(Al,Fe)_6$
γ-LT		$(Al,Cr)_{12}(Al,Cr,Fe,Ni)_5(Al,Cr,Fe,Ni)_5$ $(Al,Cr,Fe)_4$
$Ta_{39}Al_{69}$_type	cF432 – $Ta_{39}Al_{69}$ -	$(Al,Fe,Ta)_{39}(Al,Fe,Ta)_{69}$
$Ta_{48}Al_{38}$_type	mP86 - - $P2_1/c$	$(Al,Fe,Ta)_{48}(Al,Fe,Ta)_{38}$
$Al_{60}Fe_{35}Mo_5$	structure unknown	$(Al,Fe,Mo)_1(Va)_3$
DAlCoNi	P10/mmm	$(Al)_{14}(Al,Co,Ni)_1(Co,Ni)_5$
XAlCoNi	mS26 - - C2/m	$(Al)_9(Co)_2(Co,Ni)_2$
Y_2AlCoNi	oI96 - - Immm	$(Al)_3(Co,Ni)_1$
Fe_3NiAl_{10}	mP22 – Co_2Al_9 – $P2_1/a$	$(Fe,Ni)_2(Al)_5$
$FeNiAl_9$	P10/mmm	$(Fe,N)_2(Al)_9$
O1	oI366 - - Immm	$(Al,Cr,Fe)_{.28}(Al)_{.72}$
$Cr_{16}Fe_{12}Al_{72}$		$(Al,Cr,Fe)_{.28}(Al)_{.72}$
$Cr_{11.5}Fe_6Al_{82.5}$	hR1389 - - R-3	$(Cr)_{0.9}(Al,Cr,Fe)_{.22}(Al)_1$

2.2.6. μ phase (hR13 – W_6Fe_7)

The μ phase (Strukturbericht designation $D8_5$) has rhombohedral structure (hR13, W_6Fe_7 type, R-3m space group). There are 5 different atomic positions: 3a, 6c', 6c'', 6c''' and 18h. Position 18h, with CN=12, is occupied by smaller (B-type) atoms (typically Fe, Co, Ni, Zn). Sites 6c', 6c'' and 6c''' with CN =15, 16 and 14, respectively, are usually occupied by A-type atoms belonging to the groups 5 or 6. The 3a site, however, with CN 12, can be occupied by either atom types, A or B, resulting in the two stoichiometric compositions of the μ phase, A_7B_6 or A_6B_7 [68]. The μ unit cell is shown in Fig. 5. and crystal structure data are summarised in Table 3.

The formation of the μ phase is very frequent in several binary and ternary systems involved in multi-component alloys such as superalloys or high entropy alloys where A-type refractory elements such as Mo, Ta and W are present together with B-type late transition elements such as Fe, Co, and Ni.

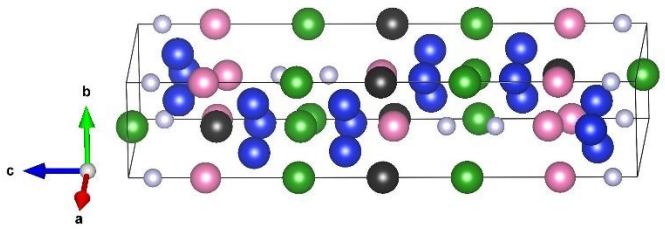

Fig. 5 *The unit cell of the μ phase. Different colours correspond to different Wyckoff*

positions.

Table 3 *Crystal structure data for the μ phase (W6Fe7 prototype)*

Pearson Symbol			hR13	
Prototype			W_6Fe_7	
Strukturbericht			$B8_5$	
Space group			R-3m 166	
Lattice parameters for W_6Fe_7			a = 0.4766 nm, c = 2.58731 nm	
Wyckoff position	*Coordinate (x,y,z)*	*CN*	*Occupation (mol%Ta) in μ TaNi at 51.8, 53.2, 55.1 mol% Ta* [68]	*Occupation (mo%lMo) in μ MoCo at 40.7, 45.3, 48.1 mol%Mo* [68]
3a	(0, 0, z) z = 0.5	12	89, 81, 77	3, 20, 64
6c'	(0, 0, z) z = 0.33333	15	95, 96, 100	87, 95, 91
6c''	(0, 0, z) z = 0.154	16	90, 97, 97	100, 98, 100
6c'''	(0, 0, z) z = 0.052	14	77, 86, 95	76, 88, 72
18h	(x, x, z), x = 0.5, z = 0.09	12	10, 9, 9	0, 1, 6

In order to simplify the description of the μ phase in different systems, a number of models were proposed by different authors. Bolcavage and Kattner [69] described the μ phase using a $(Nb,Ni)_{21}(Nb)_{18}$ 2-sublattice model in their assessment of Nb-Ni. Davydov and Kattner [70] used a similar model in the optimisation of Co-Mo system, but mixing of the elements was allowed in both sublattices. Such a 2-sublattice model seems too simple to correctly reproduce interactions in the relatively complex structure of the phase; moreover it combines in the same sublattice the two sites with CN12, which is wrong, as explained by Joubert and Crivello [71]. The sites 3a and 18h, despite having the same coordination, can have different occupation: site 3a can be occupied by both A and B-type metals, whereas site 18h is mainly occupied by the B-type element.

A 3-sublattice model $(B)_{21}(A,B)_{12}(A)_6$ was used by Guillermet [72] to describe Fe-Mo binary system. In this case not only 3a and 18h were considered in the same sublattice, but also the mixing of elements was not allowed, while it is known that 3a site can be occupied by both A and B elements. This model was modified by Kumar et al. [73] in the assessment of Co-Nb system, where mixing in the first sublattice was also allowed. Nevertheless, it did not took into account the fact that 3a and 18h positions show different behaviour. The authors compared that model with a 4-sublattice model $(A,B)_3(B)_{18}(A)_{12}(A,B)_6$, in the already mentioned work [73] and they obtained better results. Davydov and Kattner [70] used 3 different models in the assessment of Co-Mo system: the already mentioned $(A,B)_{21}(A,B)_{18}$, $(A,B)_{21}(A,B)_{12}(A)_6$ and

$(A,B)_3(B)_{18}(A)_{12}(A,B)_6$. As expected, the last one was able to describe the phase in the best way. However, using this model still did not allow to reproduce the whole solubility range of μ phase in other systems. Therefore, Joubert and Dupin [68] proposed a new model with four sublattices and mixing allowed in 3 of them $(A,B)_3(A,B)_{18}(A)_{12}(A,B)_6$. This model seems to be the most accurate: it is able to reproduce all the solubility ranges that were found in different systems as well as the experimentally determined lattice occupancies as a function of the phase composition. The sublattice models used in literature are summarised in Table 4.

The 4-sublattice model

$$\mathbf{(CN15\text{-}16,\ 6c^{I}+6c^{II})_{12}\ (CN14,\ 6c^{III})_6\ (CN12,\ 3a)_3\ (CN12,\ 18h)_{18}}$$
$$\mathbf{(A)_{12}\ (A,B)_6\ (A,B)_3\ (A,B)_{18}}$$
simplified as
$$\mathbf{(A)_4\ (A,B)_2\ (A,B)_1\ (A,B)_6}$$

was then adopted in the present database. Notice that sublattices are sorted according to the decreasing value of the coordination. Then, in general, A-type atoms will prefer first sublattices, while B-type atoms will prefer last ones. For the simplicity the stoichiometry has been divided by 3 in this assessment, resulting in the model $(A)_4(A,B)_2(A,B)_1(A,B)_6$. Therefore, all assessed μ parameters will be referred to 13 moles of atoms.

Table 4 *Summary of sublattice models used in literature for the μ phase.*

Model	Ref.	Remarks
$(3a+18h)_{21}(6'+6''+6''')_{18}$		
$(A,B)_{21}(A)_{18}$	[69]	Sites 3a and 18h exhibit different behaviour and should not be put together in the same sublattice
$(A,B)_{21}(A,B)_{18}$	[70]	Sites 3a and 18h exhibit different behaviour and should not be put together in the same sublattice
$(3a+18h)_{21}(6'+6'')_{12}(6''')_6$		
$(B)_{21}(A,B)_{12}(A)_6$	[72]	3a site can be occupied by either A or B element
$(A,B)_{21}(A,B)_{12}(A)_6$	[73]	sites 3a and 18h should not be put together
$(3a)_3(18h)_{18}(6'+6'')_{12}(6''')_6$		
$(A,B)_3(B)_{18}(A)_{12}(A,B)_6$	[73]	This cannot describe the whole solubility range of μ phase
$(A,B)_3(B)_{18}(A,B)_{12}(B)_6$	[73]	This cannot describe the whole solubility range of μ phase

$(A,B)_3(A,B)_{18}(A)_{12}(A,B)_6$	[68]	This can describe the whole solubility range of μ phase
$(3a)_3(18h)_{18}(6')_6(6'')_6(6''')_6$ $(A,B)_3(A,B)_{18}(A)_6(A)_6(A,B)_6$	[68]	

2.2.7. σ phase (tP30 – CrFe)

The σ phase (Strukturbericht designation $D8_b$) was first recognised in the Cr-Fe system by Treischke and Tamman in 1907 [74], but its crystal structure was first determined many years later by Bergman and Shoemaker [75].
It belongs to the group of topologically close-packed (TCP) phases, with a space filling of 73.1% in case of the CrFe prototype. It also belongs to the Frank-Kasper (FK) phases, due to the geometry of the coordination polyhedra.

The σ phase has a tetragonal structure (tP30, CrFe type, $P4_2/mnm$ space group) with 30 atoms in the unit cell. They are distributed in 5 different Wyckoff positions: 2a, 4f, 8i', 8i" and 8j. About coordination there are 10 atoms (positions 2a and 8i") with CN 12, 16 atoms (positions 8i' and 8j) with CN 14 and the remaining 4 atoms (position 4f) with CN 15. The unit cell is shown in Fig. 6 and the crystal structure data are summarised in Table 5.

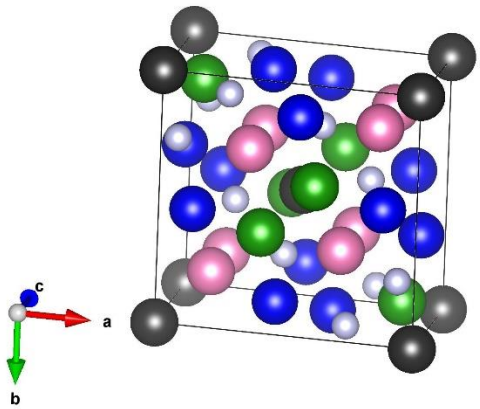

Fig. 6 *The unit cell of the σ phase. Different colours correspond to different Wyckoff positions.*

Table 5 *Crystal structure data for the σ phase (CrFe prototype)*

Pearson Symbol	tP30
Prototype	CrFe
Strukturbericht	$D8_b$

Space group		$P4_2/mnm$ 136			
Lattice parameters for CrFe		a = 0.87995 nm, c = 0.45442 nm			
Wyckoff position	*Coordinate (x,y,z)*	*CN*	*average N-N distance (nm)* [75]	*Occupation (mol% Fe) in σ CrFe at 50 mol%Fe* [76]	*Occupation (mol% Re) in σ WRe at 46, 56, 66 mol%Re* [77]
2a	(0, 0, 0)	12	2.508	86	84, 93, 95
4f	(x, x, 0), x = 0.398	15	2.701	24	8, 28, 40
8i'	(x, y, 0), x = 0.463, y = 0.131	14	2.652	36	25, 38, 54
8i”	(x, y, 0), x = 0.739, y = 0.066	12	2.526	88	94, 92, 98
8j	(x, x, z), x = 0.183, z = 0.250	14	2.638	28	30, 44, 53

The larger and electron-poor atoms (A-type atoms such as V, Nb, Ta, Mo, W, U) prefer the higher coordination positions (CN15), while smaller and electron-rich atoms (B-type atoms such as Mn, Fe, Ru, Os, Co, Rh, Ir, Ni, Pd, Pt, Au, Al) prefer the lower coordination ones (CN12). In this scheme Cr, Tc and Re can assume either A or B behaviour, depending on the partner element. Then A-type elements occupy 4f site with CN 15, whereas smaller B-type elements tend to take 2a and 8i” positions with CN 12. The remaining 8i’ and 8j sites will rather have a mixed occupancy [78].

According to an extensive analysis of the site occupation in different systems Joubert [79] found that actually sites with the same coordination have similar occupation and sites with CN 12 or 15 are more ordered (are more typically occupied by one type of atom), while sites with CN 14 are more disordered (i.e. more typically occupied by a mix of A and B atoms). Anyway it appears that this phase is never completely ordered or completely disordered.

According to the exhaustive review published by Joubert [79], the σ phase can be stabilised in a very large composition range, going from 10 to 100 at% of the A-type element and, depending on the system, it can shows either large or narrow solubility ranges. However, if the average electron concentration (e/a) is considered, it results that the σ phase is generally stabilised at e/a between 6 and 7.

Over the years many different models were used by researches to thermodynamically describe the σ phase: they are summarised in Table 6 and briefly discussed in the following.
In some old assessments [80]-[81] the σ phase was considered stoichiometric, which might reproduce correctly equilibria in some specific systems, where σ phase has very limited homogeneity, but definitely cannot be used for multicomponent systems, as σ is a non-stoichiometric phase.

The sublattice model most commonly used in older literature, $(A)_4(A,B)_{18}(B)_8$, was introduced by Andersson and Sundman [82]. This model assumes that the first sublattice is only occupied

by atoms with CN 15, the third one corresponds to CN 12, whereas the second one is a mixture of CN14 and CN12. There are no experimental data that could support such choice. However, this way the composition range of σ phase that can be described by the model is extended and this might be convenient during modelling of some systems where σ has large homogeneity range. Joubert [79] underlined that the main drawback of using such model is the fact that σ does not order at the composition A_2B, as it should. Even though, several authors still use this description in order to stay consistent with older assessments present in the literature.

A more crystallographically correct model $(A)_4(A,B)_{16}(B)_{10,}$ where atoms with the same coordination number are collected in the same sublattice, was introduced by the same authors one year earlier [83]. However, the homogeneity range that could be described by this model is very limited and not suitable for some systems; for this reason this model was quickly abandoned. It was subsequently modified by Servant et al. [84] during the assessment of Al-Nb system. The A-type atom was added to the last sublattice resulting in the $(A)_4(A,B)_{16}(A,B)_{10}$ model. However, Watson and Hayes were not able to obtain good agreement with the experimental data using this model in the assessment of Ni-V [85]. Then, in the same assessment work, the authors performed another optimisation using the model $(A,B)_4(A,B)_{16}(A,B)_{10}$, where mixing of all atoms in all sublattices was allowed. This model was later recommended by Joubert [79] and Ferro and Cacciamani [86].

Joubert [79] also proposed a simpler two-sublattice model allowing mixing between elements with different coordination in both sublattices $(A,B)_2(A,B)_1$ that was later applied e.g. by Farzadfar et al. [87] in the assessment of Mo-Re. This model does not distinguish between A and B type elements, covers the whole homogeneity range and generates a low number of end-members, but, due to this, it might not be suitable for describing more complex equilibria with the sigma phase.

A 5-sublattice model was applied by Fries and Sundman [88] to describe σ phase in Re-W binary system. Each lattice site was associated with a separate sublattice, which directly corresponds to the crystallographic structure. Additionally, mixing of elements was allowed in each sublattice, which generated a huge number of end-members. Though crystallographically more consistent, this model can be very problematic for calculations of equilibria in multicomponent systems.

An order-disorder model was also proposed for the σ phase by Hallstedt et al. [89] and used in the assessment of selected systems such as Cr-Re [90] and Co-Cr [91]. In this case the ordered configurations were described with 5 sublattices and end-members were evaluated by DFT calculations, while disordered mixing parameters were assessed on the basis of the experimental information. In both cases the authors were able to well reproduce the experimental and calculated data.

After this short review of sublattice models used in literature it is concluded that the 5-sublattice models should be preferred, however, in view of creating a multicomponent database it is essential to precisely reproduce all phase equilibria while keeping the number of sublattices as

low as possible, in order to limit the overall number of parameters to be evaluated. Therefore, the best compromise is the model:

$$\mathbf{(CN15,\ 4f)_4\ (CN14,\ 8i^{I}+8j)_{16}\ (CN12,\ 2a+8i^{II})_{10}}$$
$$\mathbf{(A,B)_4\ (A,B)_{16}\ (A,B)_{10}}$$
simplified as
$$\mathbf{(A,B)_2\ (A,B)_8\ (A,B)_5}$$

It associates in the same thermodynamic sublattice crystallographic sites having the same coordination and, more important, having similar occupation as a function of the phase composition [79]. On the other hand, to reproduce all σ composition ranges according to the systematic site occupation analysis conducted by Joubert, it is not possible to exclude any element from any sublattice.

Notice that as a criterion for the ordering of sublattices I selected the decreasing value of the coordination number. Then, in general, A-type atoms will prefer first sublattices with higher coordination, while B-type atoms will prefer last ones. For the simplicity the stoichiometry has been divided by 2 in this assessment, resulting in the model $(A,B)_2(A,B)_8(A,B)_5$. Therefore, all assessed σ parameters will be referred to 15 moles of atoms.

Of course, as underlined by Watson and Hayes [85], implementing this model creates problem of incompatibility with commonly used $(A)_4(A,B)_{18}(B)_8$ model and the need of reassessment of σ phase in many systems.

Table 6 *Summary of sublattice models used in literature for the σ phase.*

Model	**Ref.**	**Remarks**
$(4f+8i'+8j+2a)_2(8i'')_1$		
$(A)_2(B)_1$	[80]	Stoichiometric description is inconsistent with the non-stoichiometric character of σ phase
$(A,B)_2(A,B)_1$	[87]	Not suitable for describing complex equilibria
$(4f)_4(8i'+8j+2a)_{18}(8i'')_8$		
$(A)_4(A,B)_{18}(B)_8$	[82]	Atoms with CN12 are separated into two different sublattices
$(4f)_4(8i'+8j)_{16}(2a+8i'')_{10}$		
$(A)_4(A,B)_{16}(B)_{10}$	[83]	Very limited homogeneity range
$(A)_4(A,B)_{16}(A,B)_{10}$	[84]	Small improvement, mismatch with exp data

$(A,B)_4(A,B)_{16}(A,B)_{10}$	[85]	Better results, difficult to optimise
$(4f)_4(8i')_8(8j)_8(2a)_2(8i'')_8$ $(A,B)_4(A,B)_8(A,B)_8(A,B)_2(A,B)_8$	[88]	Crystallographically consistent but high number of end-members
order-disorder disordered: (A,B) ordered:$(A,B)_4(A,B)_8(A,B)_8(A,B)_2(A,B)_8$	[89]	High number of end-members

2.2.8. R phase (*hR*159 – $Co_5Cr_2Mo_3$)

The R phase was first observed by Rideout et al. [92]. Its crystal structure was determined a few years later by Komura et al. [93] by single-crystal X-ray diffraction analysis. Its composition in Co-Cr-Mo system was found to be 51.3 at% Co - 18.3 at% Cr - 30.4 at% Mo. It has a complex structure where atoms can occupy 11 Wyckoff positions: $6c^{II}$ and $18f^{VIII}$ with coordination 16, $18f^{VII}$ with CN 15, $18f^{V}$ and $18f^{VI}$ with CN 14 and the remaining sites 3b, $6c^{I}$, $18f^{I}$, $18f^{II}$, $18f^{III}$ and $18f^{IV}$ with CN 12. Atoms are arranged in a hexagonal unit cell, as presented in Fig. 7.

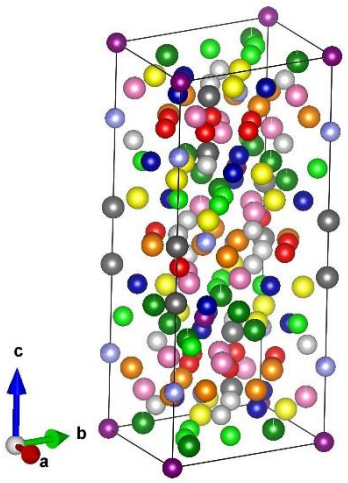

Fig. 7 *The unit cell of the R phase. Different colours correspond to different Wyckoff positions.*

The R phase is stable in Fe-Mo binary system and extends to the ternary Cr-Fe-Mo, Fe-Mo-Ni and Fe-Mo-W systems. What is more, it precipitates as a ternary phase in Co-Cr-Mo.

The sites with CN 15 and 16 can be occupied by large elements such as Mo and W, additionally, as suggested by Komura et al. [93] Mo can be replaced by Cr. The site with the medium CN (14) will have a mixed occupancy. Small elements, such as Co, Fe, Ni will preferentially take the third sublattice with CN 12, however, as experimental work suggests [94], Cr and Mo can exchange with each other. Therefore, the R phase is described with the following 3-sublattice model, which has been adopted by many authors [72,94–96]:

(CN16-15, $6c^{II}$+$18f^{VIII+}18f^{VII}$)$_{42}$(CN14, $18f^{V}$+$18f^{VI}$)$_{36}$ (CN12, 3b+$6c^{I}$+$18f^{I}$+$18f^{II}$+$18f^{III}$+$18f^{IV}$)$_{81}$
(A)$_{42}$ (A,B)$_{36}$ (A,B)$_{81}$
simplified as
(A)$_{14}$ (A,B)$_{12}$(A,B)$_{27}$

2.2.9. χ phase (cI58 – α-Mn)

Among all included systems in the multicomponent database developed in this work, the χ phase is stable in two of them as a purely ternary compound – in Cr-Fe-Mo and Cr-Fe-W. The ternary χ phase was first observed in the Cr-Fe-Mo system by Andrews and Brookes [97] with the composition $Cr_{12}Fe_{36}Mo_{10}$. Subsequently, Kasper [98] investigated its structure by means of X-rays and neutron diffraction. The structure of the χ phase is strongly related to other TCP phases such as μ, σ and R phases. It has a bcc structure where 58 atoms are distributed on four different Wyckoff positions 2a and 8c with CN16, $24g^{I}$ with CN13 and $24g^{II}$ with CN12. The presence of a coordination polyhedron with CN13 is unusual for Frank-Kasper phases [99]. The unit cell is presented in Fig. 8.

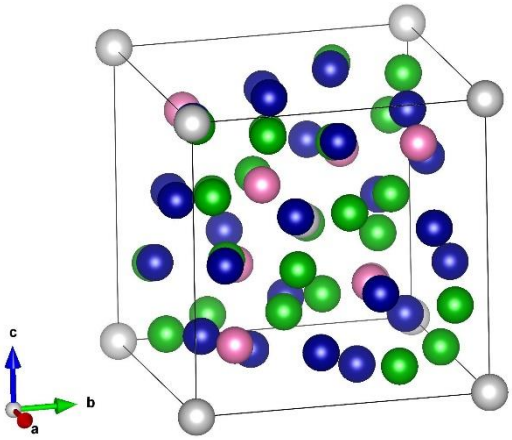

Fig. 8 *The unit cell of the χ phase. Different colours correspond to different Wyckoff positions.*

Based on experimental data, Joubert and Phejar [99] concluded that the occupancies on two sites with the same CN16 (2a and 8c) are similar and can be merged in one sublattice. Therefore, the structure of the χ phase can be thermodynamically described with a 3-sublattice model, each corresponding to a different CN. In the same article, the authors defined two ordered compositions of this phase: A_5B_{24} and $A_{17}B_{12}$. Kasper [98] observed that in the compound $Cr_{12}Fe_{36}Mo_{10}$ only Mo occupies the first sublattice with CN16 while the remaining two sublattices have mixed occupancy of Cr and Fe. However, Andersson and Lange [95] investigated the Cr-Fe-Mo system experimentally and notice, that the χ phase has a certain homogeneity range at lower temperature with Mo varying between 14 and 19at%, which implies that Mo can also enter the sublattice with CN13. This phase was also observed in the Cr-Fe-W ternary [100], where W takes crystallographic position of Mo due to their chemical

similarities. What is more, Yang et al. [101] confirmed the presence of this phase in the quaternary system Cr-Fe-Mo-Ni, with up to 7at% of Ni, hence Ni has been added to the second and third sublattice. As a conclusion, the model selected in this work is:

$$\mathbf{(CN16,\ 2a+8c)_{10}(CN13,\ 24g^{I})_{24}(CN12,\ 24g^{II})_{24}}$$
$$\mathbf{(A,B)_{10}\ (A,B)_{24}\ (B)_{24}}$$

2.2.10. Laves phases: C14 (*hP*12 – $MgZn_2$), C15 (*cF*24 – $MgCu_2$) and C36 (*hP*24 – $MgNi_2$)

The Laves phases are named after Dr. Fritz Laves who pioneered their study and described their structure [102]. They belong to TCP Frank-Kasper phases with composition AB_2, where A is a large electropositive element, while B is less electropositive and smaller. C14 and C36 phases have hexagonal structure, while C15 phase is cubic. Their crystallographic structure is closely related, it only differs by stacking layers of atoms, as shown in Fig. 9.

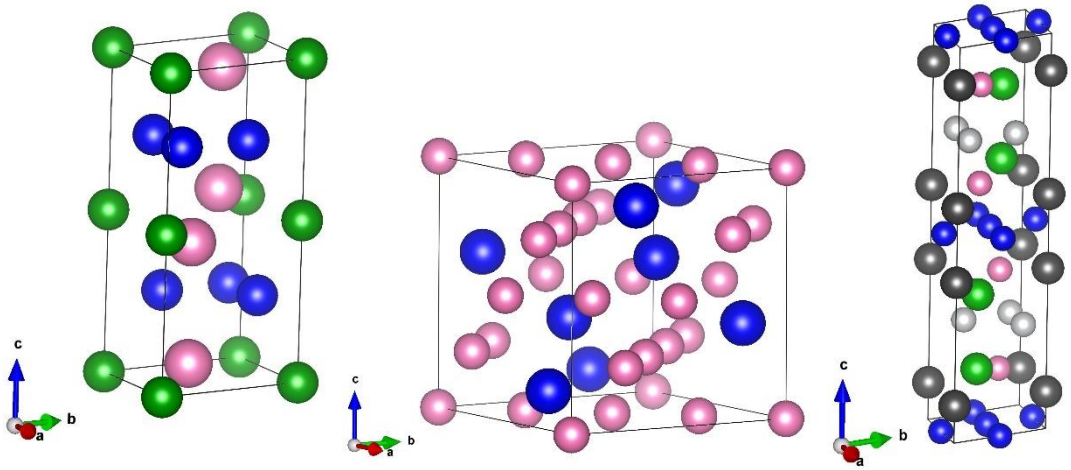

a) C14 **b)** C15 **c)** C36

Fig. 9 *The unit cell of the a) C14, b) C15 and c) C36 phase. Different colours correspond to different Wyckoff positions.*

All three Laves phases are described with a 2-sublattice model $(A,B)_1(A,B)_2$. All elements can occupy both sublattices, however, bigger elements such as Mo, Ta, and W with high CN will rather occupy the first sublattice, whereas smaller elements with lower CN tend to take the second sublattice. C14 has 3 Wyckoff positions, the first sublattice corresponds to the 4f site and CN=16, while the second sublattice to the 2a and 6h sites and CN=12. In the C15 phase, they are related to the 8b and 16c crystallographic positions, respectively. The structure of the C36 phase is represented by 5 different sites, where the positions with similar geometry and the same CN are merged and result in 2 sublattices $4e+4f^{I}$ with CN=16 and $4f^{II}+6g+6h$ with CN=12.

$$\mathbf{C14:\ (CN16,\ 4f)_4\ (CN12,\ 2a+6h)_8}$$

$(A,B)_4$ $(A,B)_8$
simplified as
$(A,B)_1$ $(A,B)_2$

C15: $(CN16, 8b)_8$ $(CN12, 16c)_{16}$
$(A,B)_8$ $(A,B)_{16}$
simplified as
$(A,B)_1$ $(A,B)_2$

C36: $(CN16, 4e+4f^{I})_8$ $(CN12, 4f^{II}+6g+6h)_{16}$
$(A,B)_8$ $(A,B)_{16}$
simplified as
$(A,B)_1$ $(A,B)_2$

2.2.11. P phase (oP56)

P phase results stable as a ternary compound in two ternary systems included in the present multicomponent database, Cr-Mo-Ni and Fe-Mo-Ni. The phase $Cr_{18}Mo_{42}Ni_{40}$ was first observed by Rideout et al. [103] and its crystal structure was later determined by Shoemaker et al. [104,105]. 56 atoms are distributed over 12 different Wyckoff positions in a primitive orthorhombic unit cell. The atoms form 4 different coordination polyhedra, namely CN16 ($4c^{VI}$), CN15 ($4c^{V}+4c^{X}$), CN14 ($4c^{IV}+4c^{VII}+4c^{IX}+8d^{II}$) and CN12 ($4c^{I}+4c^{II}+4c^{III}+4c^{VIII}+8d^{I}$). Its unit cell can be seen in Fig. 10.

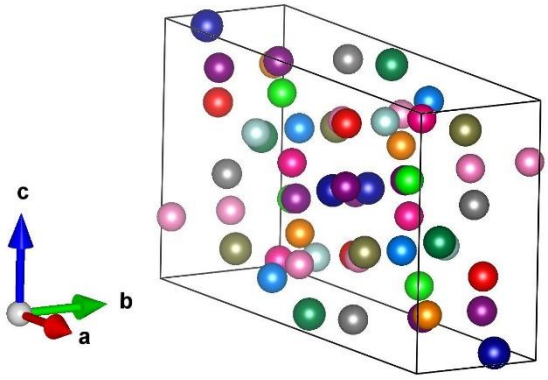

Fig. 10 *The unit cell of the P phase. Different colours correspond to different Wyckoff positions.*

The structural information determined by Shoemaker et al. indicates that the atomic sites with CN 15 and 16 (first sublattice) are mainly occupied by large A-type elements, the B-type elements will be placed at positions with the smallest CN = 12 (third sublattice). The second sublattice can be occupied by both types of elements, this way the model is able to reproduce the homogeneity range of the P-phase in both ternary systems.

$$(CN15{+}16,\ 4c^{VI}{+}4c^{V}{+}4c^{X})_{12}(CN14,\ 4c^{IV}{+}4c^{VII}{+}4c^{IX}{+}8d^{II})_{20}$$
$$(CN12,\ 4c^{I}{+}4c^{II}{+}4c^{III}{+}4c^{VIII}{+}8d^{I})_{24}$$
$$(A)_{12}(A,B)_{20}(B)_{24}$$

3. **Thermodynamic assessments**

3.1. Binary and ternary sub-systems.

The system Al-Co-Cr-Fe-Ni-(Mo,Ta,W) contains 28 binary and 56 ternary sub-systems that are needed in the multi-component database. In general the parameters were adopted from published assessments, if they were compatible with the models selected in this work. Otherwise, some modifications were needed in order to be consistent with the models adopted in the present database.

A few important ternary systems have been completely assessed in this work. If the assessment is based on only one source of data, the evaluation of the data was limited to the verification if the reported measurements are reliable. The ternary systems about which there is no published experimental or theoretical information, were described by the ideal extrapolation of the binary parameters. The summary of all inserted binary and ternary subsystems is shown in Fig. 11.

Parameters were adopted from published assessments

- Al-Cr, Al-Fe, Al-Mo, Al-Ni, Al-Ta, Al-W, Co-Fe, Co-Ni, Co-W, Cr-Fe, Cr-Mo, Cr-Ni, Cr-Ta, Cr-W, Fe-Ni, Fe-W, Mo-Ta, Mo-W, Co-Fe-Mo, Al-Ni-W, Mo-Ni-W

Parameters were adopted from published assessments with modifications due to inconsistent models

- Al-Co, Co-Cr, Co-Mo, Co-Ta, Fe-Mo, Fe-Ta, Mo-Ni, Ni-Ta, Ni-W, Ta-W, Al-Co-Cr, Al-Co-Ni, Al-Co-W, Al-Cr-Fe, Al-Cr-Ni, Al-Fe-Ni, Co-Cr-Ni, Al-Fe-Mo, Al-Mo-Ni, Co-Mo-Ni, Co-Mo-W, Co-Cr-Ta, Co-Cr-W, Co-Ni-W, Cr-Ni-W, Al-Co-Ta, Al-Fe-Ta, Cr-Ni-Ta, Fe-Ni-Ta, Mo-Ni-Ta

Systems were assessed in this work

- Al-Co-Fe, Al-Ni-Ta, Co-Cr-Fe, Co-Fe-Ni, Cr-Fe-Ni, Al-Co-Mo, Co-Cr-Mo, Cr-Fe-Mo, Cr-Mo-Ni, Fe-Mo-Ni , Co-Fe-W, Cr-Fe-W, Fe-Ni-W, Co-Ni-Ta

Ideal extrapolation from binary parameters

- Al-Cr-Mo, Al-Cr-W, Al-Fe-W, Al-Cr-Ta, Co-Fe-Ta, Cr-Fe-Ta, Al-Mo-Ta, Al-Mo-W, Al-Ta-W, Co-Mo-Ta, Co-Ta-W, Cr-Mo-Ta, Cr-Mo-W, Cr-Ta-W, Fe-Mo-Ta, Fe-Mo-W, Fe-Ta-W, Ni-Ta-W, Mo-Ta-W

Fig. 11 *All the binary and ternary sub-systems included in the present multicomponent database, adopted from other assessments, modified in this work, completely assessed in this work or extrapolated from binary parameters.*

Inclusion of many elements in the same database generates a lot of end-members, especially for the phases that are commonly present in various systems, such phases are summarised in Table 7 together with the model applied in the present multicomponent database and the number of generated end-members. If C components occupy Ns sublattices the model generates C^{Ns} endmembers, most of which do not correspond to stable compositions for the phase. Defining stable parameters can be very problematic in some cases, as illustrated in my previous work [13] for μ and σ phases. Due to such high number of parameters to be evaluated it is essential

to find a way to estimate values for metastable and unstable parameters, leaving only stable parameters for optimisation and fitting to the experimental data.

Some of the concepts applied in this work are as follows:

- The parameters describing the ordered fcc phase were evaluated according to the relations proposed by Dupin and Sundman [106] in all binary, ternary and quaternary systems

- If available, the values of metastable parameters regarding intermetallic binary phases were taken from the published DFT calculations [107]

- The end-members of μ, σ, χ, C14 and C15 phases, for which calculated energy of formation is not available in the literature, are referred to the lattice stability of the pure elements in a certain structure calculated ab-initio by Sluiter [108,109]

- Finally, metastable parameters that appeared to have an influence on the equilibria in multicomponent systems were evaluated based on the equilibrium data in the quaternary and quinary systems of interest using Parrot module in Thermo-Calc [48] or ESPEI (Extensive Self-optimizing Phase Equilibria Infrastructure)[8].

Table 7 *The common phases present in the Al-Co-Cr-Fe-Mo-Ni-Ta-W system, the applied model and number of generated end-members*

Phase – prototype- Pearson symbol	**Applied model**	**Number of endmembers**
μ - W_6Fe_7 – hR13	$(Al,Co,Mo,Ta,W)_4(Al,Co,Cr,Fe,Mo,Ni,Ta,W)_2$ $(Al,Co,Cr,Fe,Mo,Ni,Ta,W)_1(Al,Co,Cr,Fe,Mo,Ni,Ta,W)_6$	2560
σ – CrFe – tP30	$(Al,Co,Cr,Fe,Mo,Ni,Ta,W)_2(Al,Co,Cr,Fe,Mo,Ni,Ta,W)_8$ $(Al,Co,Cr,Fe,Mo,Ni,Ta,W)_5$	512
χ - α-Mn - cI58	$(Cr,Fe,Ni,W)_{24}(Cr,Fe,Mo,Ni,Ta,W)_{10}(Cr,Fe,Mo,Ta,W)_{24}$	120
γ-HT - Cu_5Zn_8 - cI52	$(Al,Cr,Fe,Mo)_2(Al,Cr,Fe,Mo,Ni)_3(Cr,Fe,Ni)_2(Al,Fe)_6$	120
γ-LT - Cu_5Zn_8 - cI52	$(Al,Cr)_{12}(Al,Cr,Fe,Ni)_5(Al,Cr,Fe,Ni)_5(Al,Cr,Fe)_4$	96
R– $Co_3Cr_2Mo_3$ – hR159	$(Cr,Mo,W)_{14}(Co,Cr,Fe,Mo,Ni,W)_{12}(Co,Cr,Fe,Mo,Ni)_{27}$	90
C14 - $MgZn_2$ – hP12	$(Al,Co,Cr,Fe,Mo,Ni,Ta,W)_1(Al,Co,Cr,Fe,Mo,Ni,Ta,W)_2$	64
C15 - $MgCu_2$ – cF24	$(Al,Co,Cr,Fe,Ni,Ta,W)_1(Al,Co,Cr,Fe,Ni,Ta,W)_2$	49
P - - oP56	$(Mo,W)_{12}(Cr,Fe,Mo,Ni,W)_{20}(Cr,Fe,Ni)_{24}$	30

C36 - $MgNi_2$ – hP24	$(Co,Cr,Ni,Ta,W)_1(Co,Cr,Ni,Ta)_2$	20

3.1.1. Binary systems

Parameters describing all 28 binary sub-systems present in the Al-Co-Cr-Fe-Ni-(Mo, Ta, W) have been added to the multicomponent database. The calculated phase diagrams can be found in Appendix A.

Re-assessment of the **Al-Co** system, developed during this thesis [110], is based on parameters from [65] with modifications regarding vacancies in the A2 and B2 and re-assessment of bundle of phases close to 4:13 stoichiometry which were experimentally investigated by [111]. The binary parameters describing the **Co-Cr** system were adopted from [112]. The original σ parameters were slightly modified in order to compensate the differences in functions describing stability of pure elements in σ structure. For the **Co-Fe** system, the description from [113] was used together with parameters concerning magnetic ordering (TC) from [114]. The assessment of the **Co-Mo** system by [115] was implemented in the database with a small adjustment of phase models regarding σ, μ and $D0_{19}$ phases, where Co was added to the first sublattice in order to stay consistent with the models used in other systems where these phases are present. In the **Co-Ta** system the parameters describing the liquid phase were taken from [116] whereas all other phases were reassessed in this work. The parameters considering the **Fe-Mo** system were adopted from [117], however, the models used to describe the R and σ phases were not consistent with the models implemented in the present database. Therefore, these phases had to be re-assessed in the present work. The parameters related to the R phase were based on the previous assessment by Andersson and Lange [95]. The description of the **Fe-Ta** system is entirely taken from [118], with a small modification (Ta was added to the last sublattice in μ). The thermodynamic parameters of the **Mo-Ni** system were taken from [119], a positive mixing parameter was added to the $MoPt_2$ phase due to differences in the implemented model. The **Ni-Ta** assessment by Zhou et al. [120] was adopted with the μ phase completely re-assessed due to the inconsistent model. The **Ni-W** parameters assessed by Guillermet and Ostlund [121] were implemented in the database. The description of the $MoNi_4$ phase was modified to stabilize the phase at lower temperature. For the **Ta-W** system the interaction parameters by Guo et al. [122] for liquid and A2 have been adopted, together with B2 parameters from [123].

The remaining binary sub-systems were entirely adopted from the available assessments: Al-Cr [124], Al-Fe [125], Al-Mo [126], Al-Ni [124], Al-Ta [127], Al-W [128], Co-Ni [129], Co-W [128], Cr-Fe [130], Cr-Mo [131], Cr-Ni [132], Cr-Ta [133], Cr-W [132], Fe-Ni [134], Fe-W[135], Mo-Ta[136] and Mo-W [137].

3.1.2. Ternary systems

From a total of 56 ternary sub-systems, 37 systems have been described with ternary parameters and 19 are described by an ideal extrapolation from binary parameters, no data being available in the literature. Parameters for most of the ternary sub-systems were taken from the literature, however, very rarely they did not require modification. The main incompatibilities were related to thermodynamic models used to describe TCP phases, such as μ and σ, as well as to the parameters used to describe binary sub-systems, especially in case of less recent assessments. The detailed description of model selection for μ and σ phases and application of these models in modelling of a series of selected ternary systems can be found in my previous work [13]. The ternary systems for which the parameters were adopted from the literature or underwent small modifications are discussed below. The systems which required more adjustments are presented in details in the following sections (3.2.-3.11.).

The most recent assessment of **Al-Co-Cr** system by Liu et al. [138] is incompatible with the present database due to differences in binary parameters and models describing the σ phase. Therefore, the system Al-Co-Cr was completely reassessed in this work based on the experimental data from [138–140]. The **Al-Co-Fe** system was assessed in our previous work [110]. The stabilities of intermetallic phases rich in Al, namely Co_2Al_9 and $FeAl_2$, were recently revised, after the publication of new experimental data by Zhu et al [141]. The parameters describing the **Al-Co-Ni** system were taken from the assessment by Wang and Cacciamani [142] however, the A1, A2 and B2 parameters were reoptimized using ESPEI [8]. The parameters from Wang and Cacciamani were the starting values for the optimization. The slight improvement of equilibria between the fcc and bcc phases was obtained. The description of the **Al-Cr-Fe** system was based on the assessment by Wang et al. [143], however, due to differences in binary parameters the assessment had to undergo considerable modifications in major phases, such as liquid, bcc, fcc, γ-LT and γ-HT. The parameters regarding the **Al-Cr-Ni** system assessed by Wang and Cacciamani [124] were adopted in this work. The **Al-Fe-Ni** assessment by Zhang et al. [144] was implemented in the database. Due to the discrepancies in binary parameters the equilibria between fcc and bcc phases were revised and adjusted to the available experimental data. The **Co-Cr-Fe** system was assessed in this work using ESPEI [8] for optimization process and the experimental data from Dombre et al. [145], who determined various isothermal sections at temperatures ranging from 800 to 1300˚C. The resulted isothermal sections compared with the experimental data were presented in our previous publication [13]. The parameters describing the **Co-Cr-Ni** system were adopted from Cacciamani et al. [146]. Due to differences in Co-Cr binary parameters, the A1, A2 and σ phases were revised. The **Co-Fe-Ni** system was assessed in this work based on the available experimental information regarding the equilibria between A1 and A2 phases in the temperature range 500-800˚C determined by Koester and Haehl [147], as well as data regarding magnetic transition investigated by Kase [148]. The **Cr-Fe-Ni** thermodynamic database reported by Franke and Seifert [134] combined with bcc parameters from Miettinen [149] was used as a base for this assessment. However, in both publications, the model used to describe the σ phase is not compatible with this work, therefore the σ phase was reassessed in this work, which also required small modifications of A1 parameters.

The only available experimental data regarding the **Al-Co-Mo** system were published by Zhu

et al. [150] and are related to the compositions rich in Co (above 50at%) at 800 and 900˚C. Based on this information the ternary parameters describing the μ and $D0_{19}$ phases were optimised. The **Al-Fe-Mo** assessment by Du et al. [151] was adopted in this multicomponent database. The $TiAl_3$, γ-HT and μ phases were reassessed, due to differences in applied models. Moreover, the ternary AlFeMo phase became stable in the Al-Mo and Al-Fe binary systems, so the parameters from the literature had to be modified. The parameters regarding **Al-Mo-Ni** system were taken from the assessment by Peng [126] with the exception of parameters describing the ternary $TiAl_3$ and $Ni_{14}Al_{75}Mo_{11}$ phases, which were adopted from the assessment by Zhou et al. [152]. In the present database the ordered fcc phase is described using the relations proposed by Dupin and Sundman [106], therefore the parameters of the $L1_2$ phase could not be adopted from [126] and were readjusted in order to reproduce the measured equilibria correctly. The assessment of the **Co-Cr-Mo** system was based on the parameters published by Wang et al. [94], however, the differences in models used for μ and σ phases, as well as some discrepancies in binary Co-Cr parameters required a thorough reassessment of the system. The results of the assessment can be found in our previous publication [13]. The parameters for the **Co-Fe-Mo** system modelled by Povoden et al. [153] were implemented in this database without any modifications. The thermodynamic description of the **Co-Mo-Ni** system by Zhang et al. [154] was adopted. The μ phase was re-optimized due to an incompatible model, and the hcp phase became stable at wrong composition and therefore had to be re-assessed. The parameters for the **Cr-Fe-Mo** system were entirely re-optimised, and the results of the assessment can be found in our recent publication [13]. The models used in an available **Cr-Mo-Ni** assessment by Frisk [155], in particular the σ model, were not compatible with the model selected in this work, and as a consequence the system have been remodelled in the present work based on the available experimental data compiled in [155]. The only published assessment of the **Fe-Mo-Ni** system by Frisk [96] is not compatible with this database, due to different models used for μ and σ phases. Therefore, the description of these phases was remodelled in this work, and consequently the parameters related to other stable phases in this system had to be adjusted. The parameters of the **Al-Co-W** and **Al-Ni-W** systems were adopted from the assessments by Wang et al. [128], and Zhu et al. [156], respectively. The thermodynamic description of the **Co-Cr-W** by Kaplan et al [157] was adopted in this work. The μ and σ phases were reassessed with the present models.

The experimental information on the equilibria present in the **Co-Fe-W** system is very limited, therefore the available assessment by Guillermet [158] is based on ideal extrapolation from binary parameters. The ternary parameters were assessed only for liquid and μ phases. The liquid interaction parameter was added to the present database, whereas the parameters of the μ phase were re-optimised in this work, because of different model used by Guillermet. The parameters of the **Co-Ni-W** system assessed by Zhu et al. [156] were implemented in the present database, except for μ parameters, which were re-assessed in this work. The **Cr-Fe-W** system was completely reassessed in the present work due to model inconsistences with the published assessment by Gustafson [100]. The resulted isothermal sections at the temperatures between 1000 and 1400°C were compared with the experimental tie lines in our previous publication [13]. The assessment of the **Cr-Ni-W** system by Gustafson [132] was used in this database. The σ phase was remodelled to match the experimental data reported by Gustafson.

The **Fe-Ni-W** system was remodelled in the present work, in order to reproduce the experimental data by Guillermet and Östlund [121]. In the **Al-Co-Ta** system, the ternary $TaCo_2Al$ phase experimentally observed by Zhu et al. [150] at 900˚C was included in the present database. It was impossible to assess other phases in this system due to the lack of experimental data. The thermodynamic description by Witusiewicz et al. [127] was adopted in this work to describe equilibria present in the **Al-Fe-Ta**. The parameters of the μ phase were re-assessed in this work due to differences in model.

The **Al-Ni-Ta** and **Co-Ni-Ta** systems were assessed in the present work based on the available experimental data: [159] (Al-Ni-Ta) and [160–163] in case of **Co-Ni-Ta**. The parameters regarding **Co-Cr-Ta** system were adopted from the assessment by Cacciamani et al. [146] with a modification of the σ phase, due to differences in the Co-Cr binary system. The parameters for the **Co-Mo-W** system were adopted from the assessment by Wang et al. [164], however, due to the different model applied for the μ phase, the description of this phase had to be reassessed. The **Co-Ta-W** system has been assessed in this work in order to reproduce the data measured by Asrar et al. [165] at 1000°C. The **Cr-Ni-Ta** parameters assessed by Dupin and Ansara [166] were implemented in the present database. They were modified according to the recently published data by Wang et al. [167]: the ternary parameters of the μ, $MoSi_2$ and Al_2Cu phases were added, liquid was destabilized. The models describing μ and σ phases in the **Fe-Mo-W** system applied by Gustafson in his assessment [137] are inconsistent with the models selected in the present database, therefore the Fe-Mo-W system was entirely reassessed in this work. The parameters describing the **Fe-Ni-Ta** system were added in order to reproduce the experimental isothermal section at 1100 ˚C constructed by Tang et al. [168]. The assessment of the **Mo-Ni-Ta** system by Zhou et al. [120] was used in the present database. The μ phase had to be slightly destabilized. Finally, the parameters assessed by Wang et al. [169] were adopted for the **Mo-Ni-W** system.

Due to the lack of experimental or theoretical data regarding the following ternary systems: Al-Cr-Mo, Al-Cr-W, Al-Fe-W, Al-Cr-Ta, Co-Fe-Ta, Cr-Fe-Ta, Al-Mo-Ta, Al-Mo-W, Al-Ta-W, Co-Mo-Ta, Cr-Mo-Ta, Cr-Mo-W, Cr-Ta-W, Fe-Mo-Ta, Fe-Ta-W, Ni-Ta-W and Mo-Ta-W, it was impossible to evaluate ternary parameters and the ternary equilibria are described as ideal extrapolation from respective binary systems.

The thermodynamic assessment of the selected ternary systems is presented in the following sections. The systems have been chosen based on their complexity and the availability of experimental data. The assessment procedure began with the formation of a starting database, based on the parameters from all the binary subsystems. Then, ternary end-members and interaction parameters were introduced and carefully selected in order to keep the balance between the quality of fitting and reduction of the number of parameters. The optimization process was done by means of Parrot module in Thermo-Calc [48] or ESPEI (Extensive Self-optimizing Phase Equilibria Infrastructure)[8].

3.2. Al-Co-Fe

3.2.1. Literature review

The Al-Co-Fe phase diagram is characterized by a large central region where the ordered B2 phase is stable over a wide temperature range, resulting from the combination of the corresponding B2 stability areas present in all the binary subsystems. In the Fe-rich corner complex equilibria appear due to the combination of magnetic and chemical ordering in the bcc phases, while the Co-rich corner is dominated by equilibria between bcc and fcc phases. The Al-rich corner, however, is characterized by the equilibria between the different Al-rich binary phases stable in both Al-Fe and Al-Co subsystems.

Phase equilibria of the Al-rich part were first investigated by Raynor and Waldron [170] using X-ray diffraction and thermal analysis methods. Isothermal sections in the aluminum corner (> 89 wt.% Al) were established at 550, 600 and 640 °C as well as the vertical sections at high aluminum content (at 98.75, 98.5, and 97.5 wt% Al). Moreover, the liquidus surface was determined in the Al-rich corner (97.5 to 100 wt% Al) and the temperature of the ternary eutectic liquid=>A1 + Co_2Al_9 + m$(Co,Fe)_4Al_{13}$ was estimated to be 653.9±0.3 °C with the liquid composition: 1.55Fe - 0.35Co - 98.1Al (wt%). Kozakai et al. [171] investigated the Al-rich corner to the higher extent, using diffusion couples and EDS analysis, constructing the isothermal diagram at 650 °C. More recently, Grushko et al. [172] examined series of samples annealed at higher temperatures (800 and 1070 °C) by XRD and SEM techniques, whereas phase compositions were measured by EDX. The study revealed that monoclinic Co_4Al_{13} and Fe_4Al_{13} (sometimes identified as $FeAl_3$) form a continuous solid solution region, which was not considered in the previous investigations due to lack of information about the different phases stable close to the Co_4Al_{13} composition.

In the Co-corner equilibria between disordered fcc (A1), ordered (B2) and disordered (A2) bcc phases are present. Edwards [173] defined the single and two-phase regions at 800°C using X-ray diffraction. Afterwards, Ackermann [174] determined phase boundaries using diffusion couples at temperatures ranging from 800 up to 1200°C. Kozakai et al. [171] measured phase equilibria at 650°C in the whole composition range, as well as the Curie Temperature as a function of composition in the Fe-rich region. Moreover, they performed thermodynamic calculations of the A2/B2 phase equilibria in the ternary system assuming the Bragg-Williams-Gorsky approximation. Afterwards, they continued the investigation of this system [175], [176] to evaluate the precipitation limit of A2 particles using TEM and the composition gradient method. Kamiya et al. [177] carried out similar research in a wider temperature range (900-1200°C) by EPMA and DSC measurements. They obtained a more detailed description including chemical and magnetic ordering. The Curie temperatures and the temperatures of the second order A2/B2 transition were determined in their studies.

In the Fe-rich corner the bcc phase separation was determined by Miyazaki et al. [178] by magnetization measurements and SEM in the temperature range 450-700 °C. Two kinds of

separations were observed: between ordered and disordered forms as well as between two ordered forms having different chemical compositions. The studies continued [179] using TEM and DTA. In these works the Bragg-Williams-Gorsky model was adopted in calculations of the A2/B2 two phase field.

The relationship between liquidus and solidus was first studied by Koester [180] in the composition range up to 40 wt% Al by thermal methods. Afterwards, Raynor and Waldron [170] established the liquidus surfaces in the Al-rich corner (>97.5 wt% Al). There are no data concerning the remaining ternary compositions.

Yin et al. [181] and [182] measured enthalpies of formation of the various Co_2YZ and Fe_2YZ Heusler compounds, including $AlFeCo_2$ and $AlFe_2Co$.

3.2.2. Solid phases

The sublattice models adopted for the solid phases present in the Al-Co-Fe are summarized in Table 8.

Table 8 *Solid phases stable in the Al-Co-Fe system.*

Phase name	Struktur-bericht	Pearson symbol	Prototype	Space group
A1	A1	cF4	Cu	$Fm\bar{3}m$
A2	A2	cI2	W	$Im\bar{3}m$
A3	A3	hP2	Mg	$P6_3/mmc$
Co_2Al_9		mP22	Co_2Al_9	$P2_1/c$
o-Co_4Al_{13} HT **o'-Co_4Al_{13} LT**		oP102	Co_4Al_{13}	$Pmn2_1$ $Pnma$
M_4Al_{13}_type		mS102	Fe_4Al_{13}	$C2/m$
y-Co_4Al_{13}				$C2/m$
$CoAl_3$		mS36	$(Co_{.88}Ni_{.12})_4Al_{12.1}$	P2/m
Co_2Al_5	$D8_{11}$	hP28	Mn_2Al_5	$P6_3/mmc$
B2	B2	cP2	CsCl	$Pm\bar{3}m$
Fe_2Al_5		oC24	Fe_2Al_5	$Cmcm$
$FeAl_2$_type		aP18	$FeAl_2$	$P1$
Fe_5Al_8 (γ-HT)	$D8_2$	cI52	Cu_5Zn_8	$I4\bar{3}m$
Fe_3Al	$D0_3$	cF16	BiF_3	$Fm\bar{3}m$

3.2.2.1. Solid solutions

Several phases which are stoichiometric in binary systems dissolve the third element, as cobalt and iron can substitute each other. The phases: Fe_2Al_5 (oC24 – Fe_2Al_5 type), $FeAl_2$ (aP18 – $Fe_5(Fe_{0.5}Al_{0.5})_3Al_{10}$ type) and Co_2Al_5 (hP28 – Co_2Al_5 type) at 1070 °C dissolve up to 5.8 at.% Co, 6.5 at.% Co and 19.7 at.% Fe respectively, whereas at 800 °C, Co_2Al_9 (mP22 – Co_2Al_9 type) dissolves up to 5 at.% Fe at the constant concentration of aluminum [172]. Their models correspond to the primary stoichiometric phases with addition of the third element (Co or Fe)

in the first sublattice. As a consequence, there are two additional terms describing the Gibbs free energy: the end-member containing the additional element (B) and the interaction parameter with Co and Fe in the first sublattice:
$G^{\alpha}_{A:Al}$, $G^{\alpha}_{B:Al}$, $L^{\alpha}_{A,B:Al}$

3.2.2.2. m-(Co,Fe)$_4$Al$_{13}$

The monoclinic phases Co_4Al_{13} and Fe_4Al_{13} have the same crystallographic structure (mS102-Fe_4Al_{13} type) and create a continuous solid solution at around 76 at.% of Al. Two different models had been used in literature for Co_4Al_{13} and Fe_4Al_{13}. In this work, consistently with Sundman et al. [125], the model $(Co,Fe)_{.235}(Al)_{.6275}(Al,Va)_{.1375}$ has been adopted because it seems in better agreement with the crystal structure description of the phase, which binary solubility range seems related to vacancies in selected Al sublattices. In this way it was possible to reproduce both the small solubility range in Al-Fe and the nearly stoichiometric behavior in Al-Co.

3.2.3. Assessment procedure.

The Parrot module of Thermo-Calc software was used for optimization process, based on critically selected experimental data illustrated above.

In particular, tie lines describing equilibria between A1 and B2 phases at temperatures ranging from 650°C to 1200°C where taken from Kozakai et al. [171], Grushko et al. [172] and Ackermann [174]. Moreover, work of Kamiya et al. [177] provided very valuable information about Curie temperatures and temperatures of ordering transition of bcc phase, which allowed for optimization of TC and A2 parameters respectively. The parameters for solid solution phases present in the Al-rich corner were calculated according to the data from Kozakai et al. [171] and Grushko et al. [172]. However, taking into account some inconsistencies between the two publications, the higher weight was given to the most recent work [172].
In order to reproduce solubilities of the binary intermetallic compounds rich in Al, such as m-$(Co,Fe)_4Al_{13}$, Fe_2Al_5, $FeAl_2$, Co_2Al_9 and Co_2Al_5, negative parameters were added for the metastable binary end members as well as for the Co-Fe interaction in the first sublattice.
In order to reproduce the equilibria between disordered A1, A2 and ordered B2 phases, the mixing parameters were introduced. The disordered phases were described with the symmetric ternary parameters containing temperature-dependent and temperature-independent variables, whereas parameters describing interaction between Al-Co, Co-Fe and Al-Fe were added to the description of B2 phase. Functions related to the same interaction in the first and second sublattice of B2 phase have the same value, due to the symmetry between them.
Unfortunately, experimental information about the liquid is very limited and not enough to evaluate ternary interaction parameters for this phase, which was then described as ideal extrapolation of the binary ones.
All assessed Al-Co-Fe parameters can be found in my previous work [110].

3.2.4. Results and discussion

3.2.4.1. Isothermal sections

Different isothermal sections were calculated using the optimized parameters and the results are compared with the experimental data.

Fig. 12 shows phase diagrams of Al-rich corner (x(Al) > 0.5) calculated at 800 °C and 1070 °C in comparison with the experimental tie lines from Grushko et al. [172]. The solubilities of the phases: Fe_2Al_5, Co_2Al_5 and $FeAl_2$ at 1070 °C and Co_2Al_9 at 800 °C are reproduced in a satisfactory way, although, the small discrepancies in their homogeneity ranges can be observed due to the fact, that they have been approximated as line phases in this work. As expected, the isostructural m-Co_4Al_{13} and Fe_4Al_{13} create a continuous solid solution m-$(Co,Fe)_4Al_{13}$ at around 76 at% Al at both temperatures. It was not possible to reproduce the large Al solubility (~55 at% Al) of the B2 phase detected by Grushko et al. [172]. On the other hand it can be observed that results by Grushko et al. are in conflict with the more limited binary solubilities previously accepted for Al-Fe and Al-Co.

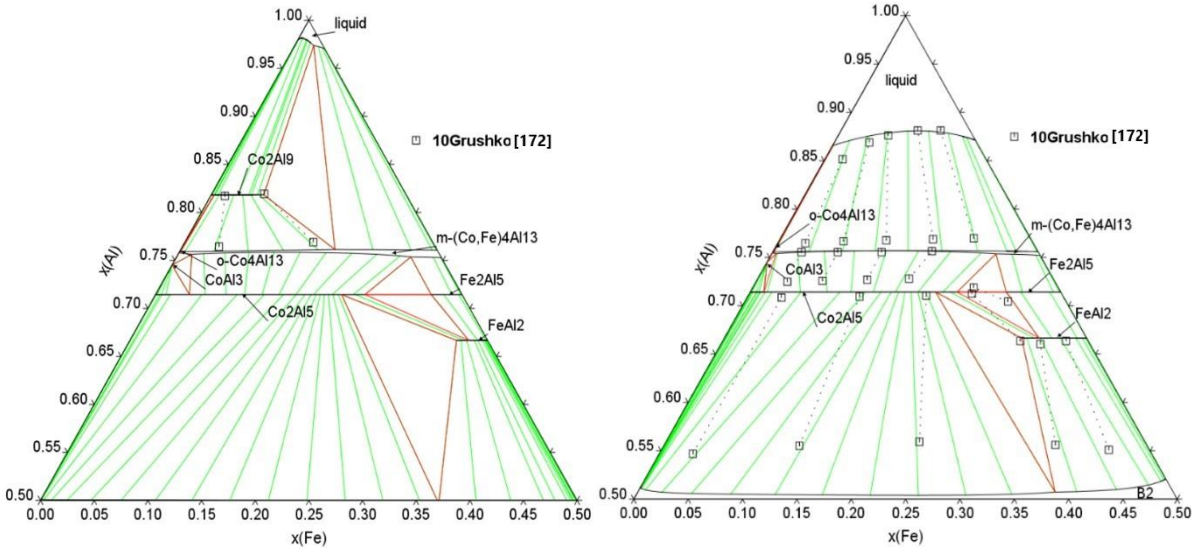

a) 800°C **b)** 1070°C

Fig. 12 *Isothermal section of Al-rich corner of Al-Co-Fe system calculated at 800°C and 1070°C compared with the experimental data from* [172].

The present equilibria between fcc and bcc phases are shown in Fig. 13 and Fig. 14 for temperatures ranging from 650 up to 1200 °C. The calculated diagrams are compared with experimental data from Kozakai et al. [171] (Fig. 13) and Ackermann [174] and Kamiya et al. [177] (Fig. 14). Calculated A2/B2 2nd order transitions are also reported in the isothermal sections.

At 650 °C most of the experimental points from Kozakai et al. [171] are well reproduced, especially the two phase field A2+B2 and the A2/B2 ordering transition. However, the solubility of A1 in the Co corner should be higher, as suggested by experimental tie lines.
Moreover, according to the calculation, a demixing between two different ordered B2 phases (denoted as B2 and B2') appears. As a consequence, there can be found a two-phase field B2+B2' and a three-phase field A1+B2+B2' which does not appear in the experimental section. According to calculations by Colinet et al. [183] in the composition area of the B2+B2' field, the $D0_3$ ordering (not reproducible in the calculations) should be stable.
In the calculated vertical sections which will be discussed later, it appears that B2 and B2' correspond to the ferro- and para-magnetic ordering of the B2 phase.

The first-order transition between A2 and B2 in the Fe rich corner at 900 °C was not observed in any experimental work: it can be an artifact of the calculation or it has not been observed due to experimental difficulties. However, at higher temperature, the computed transition is 2nd order, in good agreement with experiments. The tie lines in the two phase field A1+B2 are fitted in a satisfactory way, taking into account small discrepancies between the two authors: Ackermann [174] and Kamiya et al. [177]; a better agreement is obtained at temperatures above 900 °C.
At temperatures above 1070 °C no data are available for the equilibria in the Al-rich part of the diagram and equilibria calculated in these conditions may be considered as predictions obtained in this work.

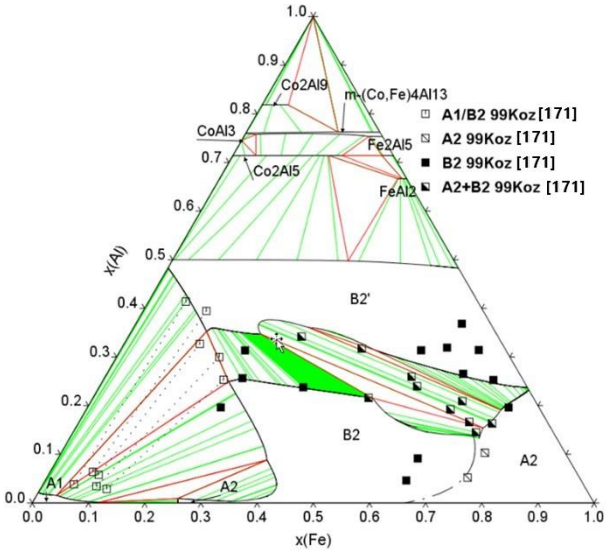

Fig. 13 *Isothermal section of Al-Co-Fe system calculated at 650°C compared with the experimental data from* [171].

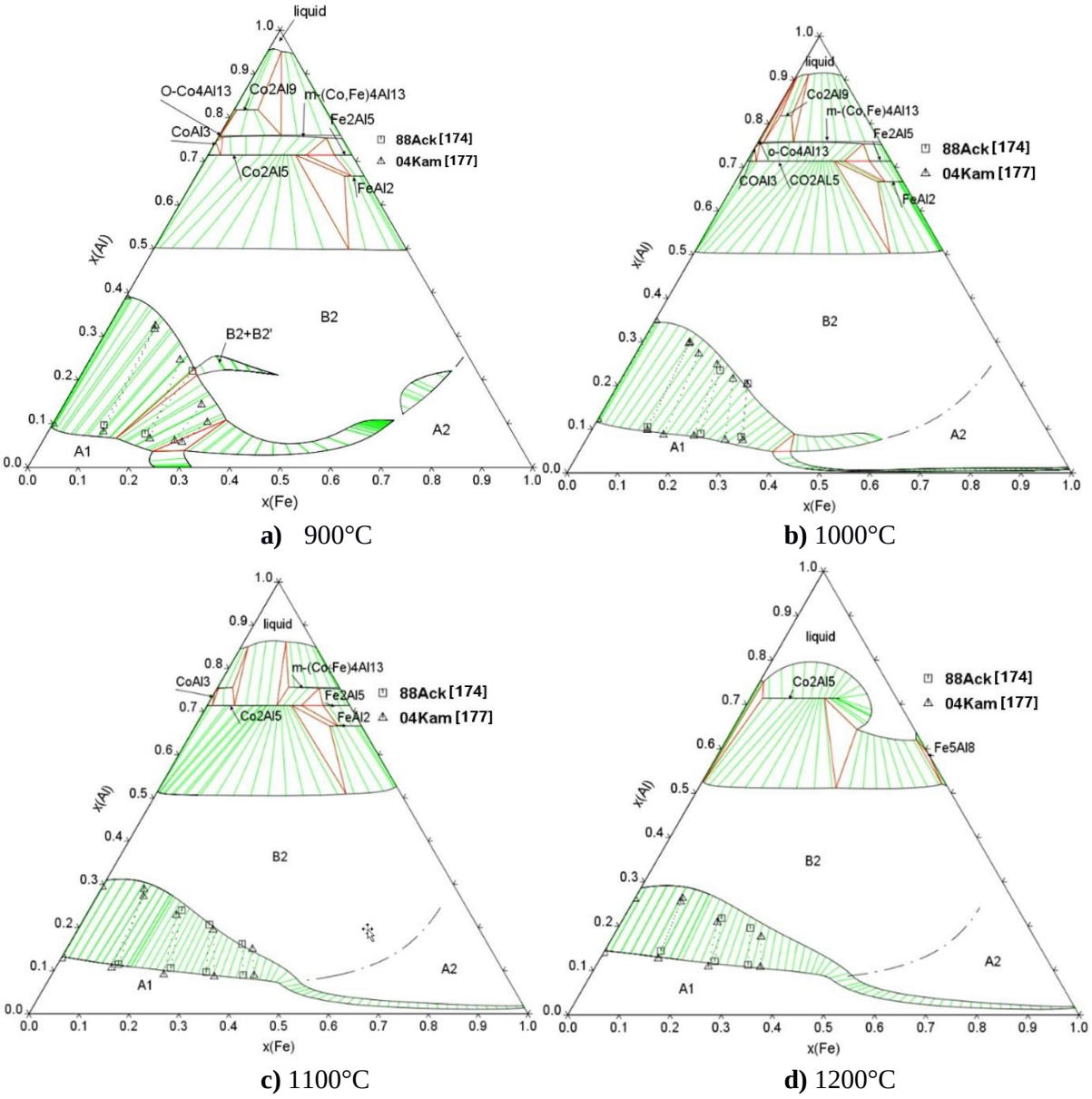

Fig. 14 *Isothermal sections of Al-Co-Fe system calculated at a) 900°C, b)1000°C, c) 1100°C and d) 1200°C compared with the experimental data from* [174] *and* [177].

3.2.4.2. Liquidus surface

The calculated liquidus projection with isotherms for Al-Co-Fe system is shown in Fig. 15. The monovariant liquidus lines are marked in blue. The computed surface is in good agreement with the partial experimental data available: by Koester [180] (in the 0-40 wt% Al area) and Raynor and Waldron [170] (in the Al-rich corner, at > 97.5 wt% Al).

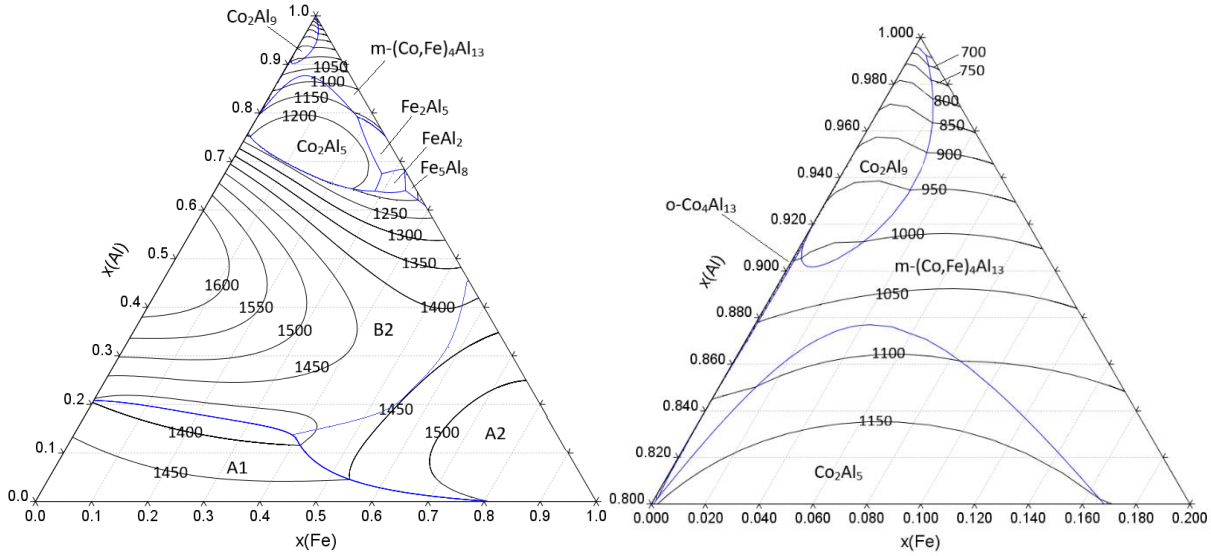

a) **b)**

Fig. 15 *Calculated liquidus projection with isotherms and monovariant liquidus lines (blue) a) in the whole composition range b) in the Al-corner (>80 at% Al).*

3.2.4.3. Vertical sections

Several vertical Al-Co-Fe sections have been reported in literature, mainly placed in the Al-rich corner or in the Co-Fe side up to about 30 at% Al. In the following they will be discussed in detail.

The vertical sections calculated at high aluminium content (97.5 wt%, 98.5 wt% and 98.75 wt% Al) are shown in Fig. 16 together with experimental results. The equilibria between liquid and intermetallic phases: m-$(Co,Fe)_4Al_{13}$ and Co_2Al_9 were investigated by Raynor and Waldron [170]. Solidus and liquidus temperatures were also determined in this work.
The equilibria between liquid, m-$(Co,Fe)_4Al_{13}$ and Co_2Al_9 are well reproduced (the difference is about 0.2 wt% Co). The predictions for the liquidus temperatures does not vary more than 20°C from the measurements. The solidus temperatures are fitted to the experiments with higher precision, however, for the section at 98.5 wt% Al, the experimental invariant temperature is slightly lower than calculated, due to the differences in binary Al-Fe system.

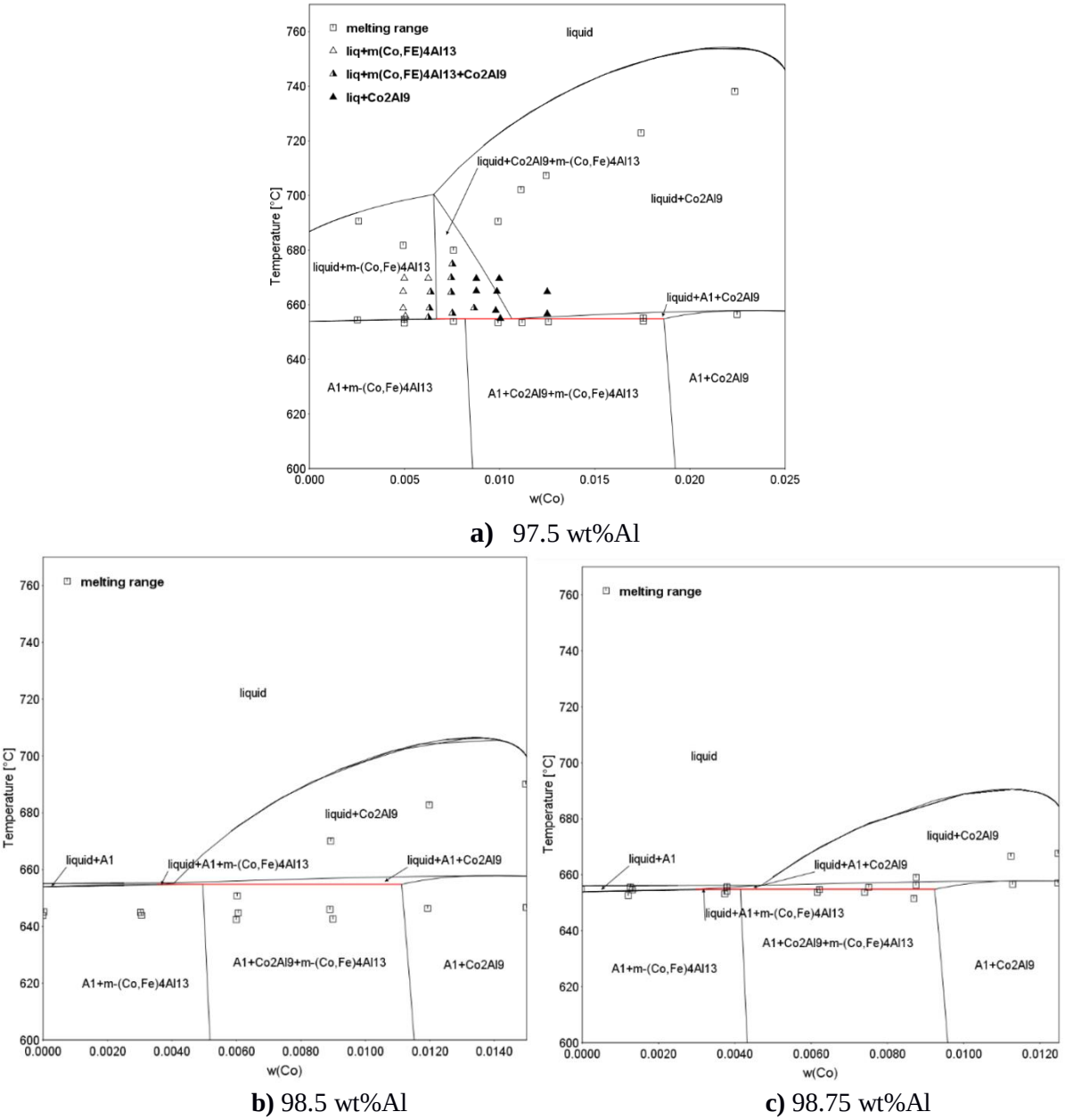

a) 97.5 wt%Al

b) 98.5 wt%Al

c) 98.75 wt%Al

Fig. 16 *Vertical sections for a) 97.5 wt% Al, b) 98.5 wt% Al and c) 98.75 wt% Al compared with experimental results from* [170].

Fig. 17 presents vertical sections calculated for 10, 20 and 40 wt% Fe and up to 30 wt%Al. They are compared with the experimental data from Koester [180] regarding liquidus temperatures and equilibria between fcc and bcc phases. Additionally, the magnetic transition in the bcc phase was calculated for 40 wt% Fe and compared with data from Koester [180].

The two phase field A1+B2 extends to an Al content higher than measured in [180], the difference being lower than 5 wt% Al. All of the liquidus temperatures reported by Koester are located between solidus and liquidus in the diagrams or in a very short distance from them. The measured magnetic ordering temperatures for 40 wt% Fe differ from these predictions, however, it should be taken into account that the data derive from very old measurements and they were not considered during optimization of TC parameters in this assessment.

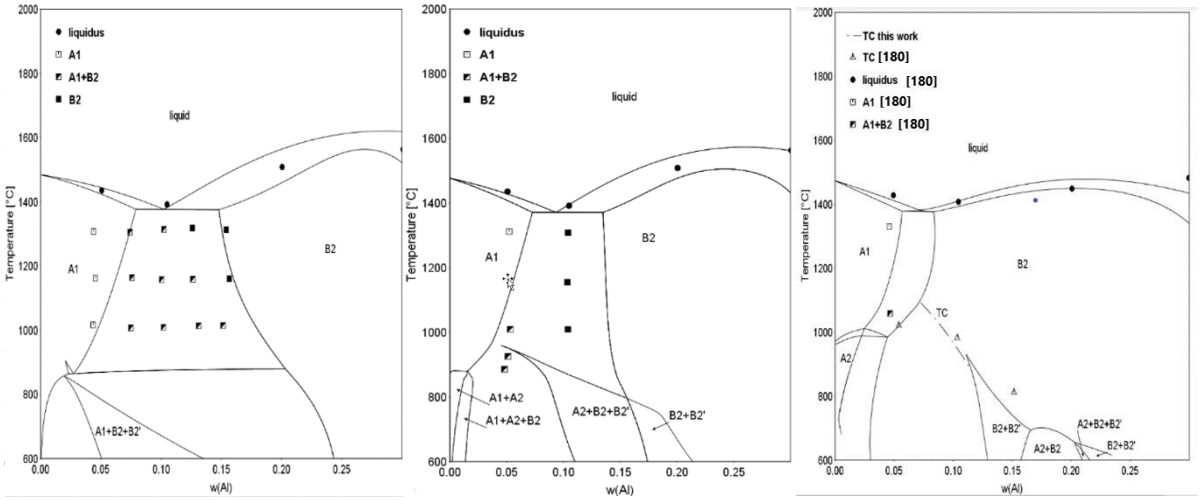

a) 10 wt% Fe **b)** 20 wt% Fe **c)** 40 wt% Fe

Fig. 17 *Vertical sections for a) 10 wt% Fe, b) 20 wt% Fe and c) 40 wt% Fe compared with experimental results from* [180].

The calculated vertical diagrams with 30, 40 and 50 at% Fe are shown in Fig. 18 The magnetic transition temperatures in the bcc phase and the transition between A2 and B2 (for 50 at% Fe) are added to the plots. Experimental data regarding A2+B2 equilibria and A2/B2 2nd order transition were taken from Kamiya et al. [177], whereas data regarding TC from Kamiya et al. [177] and Kozakai et al. [179] and are juxtaposed with the present calculations in Fig. 18.
The two phase field recognized by Kamiya as A2+B2 turned out to be A1+B2 in the present calculations. The possible explanation could be that A2+B2 field found in Kamiya et al. [177] is metastable and A2 phase transforms into A1.

The magnetic ordering temperatures are well fitted taking into account discrepancies between Kamiya et al. [177] and Kozakai et al. [179]. The big disagreement with literature data can be observed for A2/B2 transition in Fig. 18c. This difference can result from the lack of parameters describing A2 phase in Al-Co, where the metastable A2+B2 field was detected by several authors: Kozakai et al. [175], Kamiya et al. [177], Ohtani et al. [184] and Niitsu et al. [185] within the stable A1+B2 field.

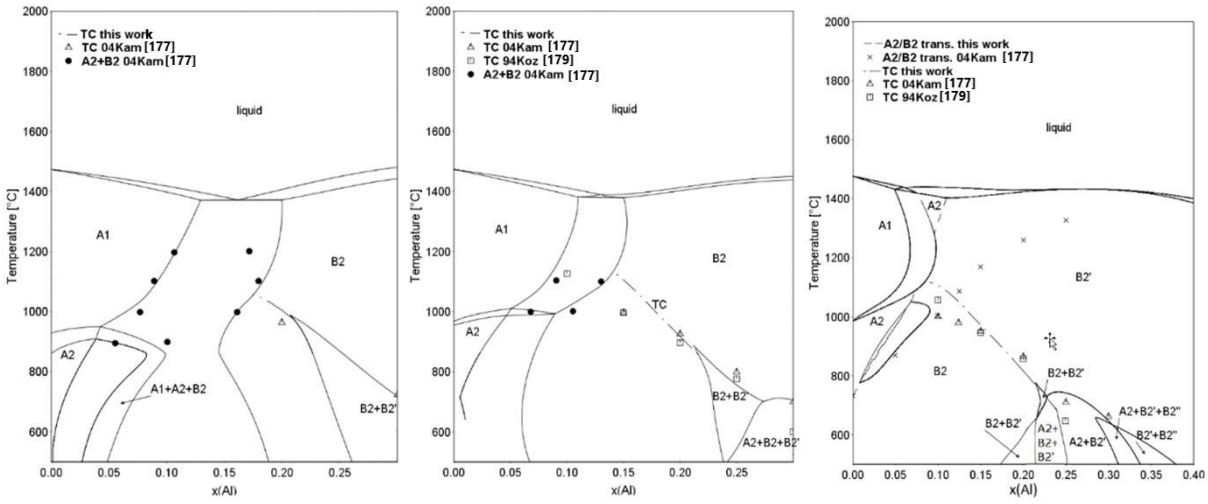

a) 30 at% Fe **b)** 40 at% Fe **c)** 50 at% Fe

Fig. 18 *Vertical sections for a) 30 at% Fe, b) 40 at% Fe and c) 50 at% Fe with calculated magnetic transition of bcc phase compared with experimental results from* [177] *and* [179].

3.3 Al-Fe-Mo

3.3.1. Literature review

One of the first experimental investigations of the Al-Fe-Mo system was performed by Markiv et al. [186]. They established the isothermal sections at 800 and 1050 °C rich in Al (up to 46 at% Fe and 60 at% Mo) using equilibrated alloys method. The samples were annealed at 800 and 1050°C for 800 and 8h, respectively. The samples were examined by means of XRD. Two ternary phases (called 'N' and 'S') were identified at 1050°C. Afterwards, the composition of the 'N' phase was determined by Villars et al. [187] Al_8FeMo_3. Sokolovskaya et al. [188] constructed isopleths along compositions $FeAl_3$-$MoAl_{12}$ and Fe_3Mo_1-Al. Wang et al. [189] studied the equilibria between the A2 and μ phases at 800°C by means of EDS and EPMA. More recently, Eumann et al. [190,191] determined isothermal sections at 800, 1000 and 1150 °C by means of equilibrated alloys studied by EPMA and XRD. They confirmed the presence of the ternary N-phase, previously observed by Markiv et al. Two additional ternary phases were found, one with a W-type structure and a very large homogeneity field, the second one with a hexagonal Al_8Cr_5-type structure. Another ternary phase, with the composition $Al_{0.25}Fe_{4.75}Mo_9$ was reported by Stepien-Damm et al. [192]. The phase forms at around 1650°C.

Du et al. thermodynamically described the Al-Fe-Mo system [151]. They used the $(Al,Fe)_7Mo_2(Fe,Mo)_4$ model to describe the μ phase. Eumann et al. [191] suggested that the binary Al_5Fe_4 phase transforms into the ternary phase with the hexagonal Al_8Cr_5-type structure through the second order transition. However, the composition where the transition takes place has not been established and Du et al. modelled them as a single Al_5Fe_4 phase.

3.3.2. Solid phases

The bcc phase undergoes ordering transition at the Al-Fe side. The μ phase is stable in the Fe-Mo binary system and dissolves a considerable amount of Al (up to 16at% at 1000°C). Numerous intermetallic phases stable in the Al-Fe and Al-Mo binary sub-systems are present. Four ternary phases were observed in this system. The first one with composition Al_8FeMo_3, the second one having the W-type structure and a large solubility, the third one with a hexagonal Al_8Cr_5-type structure and the last one with the composition $Al_{0.25}Fe_{4.75}Mo_9$ formed at around 1650 °C. All stable solid phases are gathered in Table 9.

Table 9 *Stable solid phases in the Al-Fe-Mo system.*

Phase name	Struktur-bericht	Pearson symbol	Prototype	Space group
A1	A1	cF4	Cu	$Fm\bar{3}m$
A2	A2	cI2	W	$Im\bar{3}m$
B2	B2	cP2	CsCl	$Pm\bar{3}m$
M_4Al_{13}_type		mS102	Fe_4Al_{13}	$C\ 2/m$
Fe_2Al_5		oC24	Fe_2Al_5	$Cmcm$
$FeAl_2$_type		aP18	$FeAl_2$	$P1$
Fe_5Al_8 (γ-HT)	$D8_2$	cI52	Cu_5Zn_8	$I4\bar{3}m$
Fe_3Al	$D0_3$	cF16	BiF_3	$Fm\bar{3}m$
C14		hP12	$MgZn_2$	$P\ 6_3/m\ mc$
μ		hR36	W_6Fe_7	$R\bar{3}m$
WAl_{12}_type		cI26	WAl_{12}	$Im\bar{3}$
WAl_5_type		hP12	WAl_5	$P6_3$
Mo_5Al_{22}		oF216		$Fdd2$
Mo_4Al_{17}_type		mC84		C2
WAl_4_type		mC30	WAl_4	Cm
$MoAl_3$		mC32	Cr_3Si	Cm
Mo_3Al_8		mC22		c2/m
$Mo_{37}Al_{63}$				
γ-HT		cI52	Cu_5Zn_8	
$TiAl_3$_type	$D0_{22}$	tI8	$TiAl_3$	I4/mmm
$Al_{12}Fe_7Mo$				

3.3.3. Results and discussion

The assessment by Du et al. [151] was adopted in this work. Due to the model inconsistencies, μ, γ-HT, $Al_{12}Fe_7Mo$ and $TiAl_3$ phases were reassessed in this work. The ternary phase $Al_8Fe_5Mo_3$ is isostructural with the $TiAl_3$ phase and was described with the same model in the present database. The name $Al_{12}Fe_7Mo$ was assigned to the second ternary phase. The most stable μ endmember parameters are *G(μ,Mo:Al:Al:Fe)=-243000, G(μ,Mo:Mo:Fe:Al)=-180000* and *G(μ,Mo:Al:Fe:Fe)=-170000*, three interaction parameters were added allowing mixing between Al and Fe in the last sublattice and all three elements in the second sublattice. The γ-HT phase is described with 7 end-member and 2 interaction parameters. The end-members in which Al occupies the first sublattice have a positive value (are unstable). The

interaction parameters contain the temperature-dependent coefficient: *G(γ- HT,Al,Mo:Fe:Fe:Al)= -94250-250*T and G(γ-HT,Al:Fe,Mo:Fe:Al)= -130750-250*T.* In the $TiAl_3$ phase Al can replace Fe in the second sublattice which is represented by the addition of *G($TiAl_3$,Mo:Al,Fe:Al)= -137166.67* parameter. The model describing $Al_{12}Fe_7Mo$ phase contains only one sublattice and is described with several ternary and metastable binary interaction parameters.

The calculated isothermal sections are shown in Fig. 19 together with the experimental datapoints from [190,191]. The good agreement with the experimental data has been obtained. the homogeneity ranges of the μ and the ternary $Al_{12}Fe_7Mo$ phase is well reproduced. The data at 1000 °C suggest that the A2 phase AlFe dissolves too much Mo, however, in the remaining figures the solubility of the A2 phase is in agreement with the experimentally observed phase boundaries. The $TiAl_3$ and $Al_{12}Fe_7Mo$ phases are not stable at 800°C

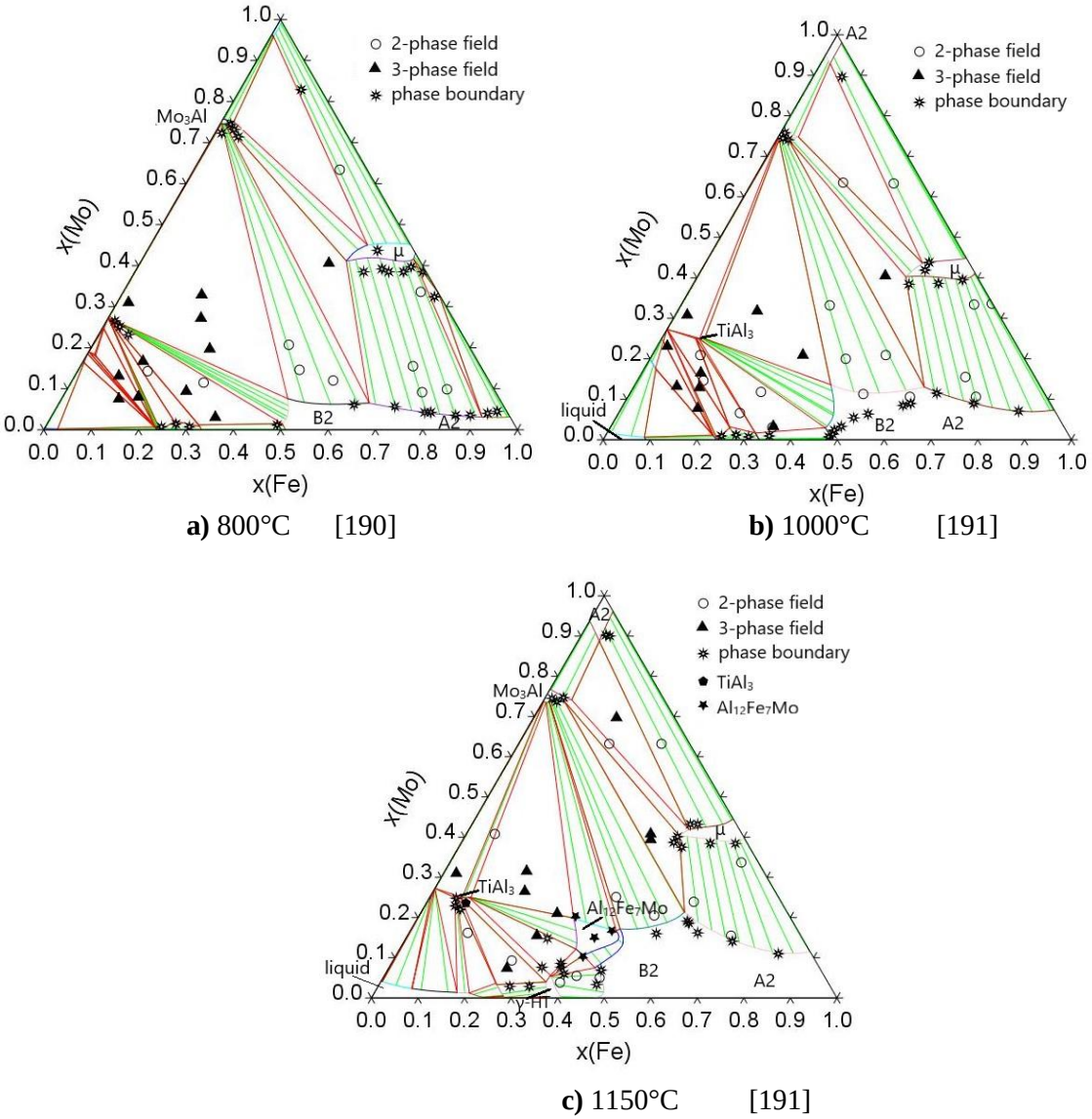

a) 800°C [190] **b)** 1000°C [191]

c) 1150°C [191]

Fig. 19 *Isothermal section of Al-Fe-Mo system calculated at a) 800°C, b) 1000°C and c)*

1150°C compared with the experimental data from [190,191].

3.4 Al-Fe-Ni

3.4.1. Literature review

The Al-Fe-Ni system has been extensively studied. In this section I will present the most relevant experimental information that has been used for the optimisation of the parameters. The full review of the literature data up to 2005 was published by Eleno et al. [193].
The first detailed investigation of the phase stabilities in the whole composition range by means of XRD was published by Bradley and Taylor [194,195].

The phase equilibria in the Al-rich region were studied by numerous authors. Schrader and Hanemann [196] investigated the phase equilibria at 620°C, Raynor and Pfeil [197] studied the Al-rich corner (>95wt% Al) at 550 and 600 °C. Khaidar et al. [198,199] constructed the isothermal section in the whole compositions range at 950 and 1050 °C by means of XRD, EPMA and DTA. More recently, Chumak and Richter [200] determined the partial isothermal section at 850 °C and invariant reactions. Zhang et al. [201] established the phase equilibria above 50 at% Al at 627 and 850 °C using XRD, SEM, EDX and EPMA techniques.

The Fe-rich region was investigated by Hao et al. [202] using the diffusion couple method and EPMA measurement at the temperature ranging from 750 up to 1150 °C. The miscibility gap in the bcc phase was determined in the same work.

In the Ni-rich region, the equilibria between A1, $L1_2$ and B2 were investigated by Jia et al. [203], Himuro et al. [204] and Bramfitt and Michael [205]. Additionally, the ordering of the fcc phase was studied by Masahashi et al. [206] and Himuro et al. [207]. Chumak et al. [208] constructed the vertical section along 75 at.% Ni and investigated phase equilibria close to the Fe-Ni side [209].

The solidus temperatures of the B2 phase were measured by Bitterlich et al. [210] at 50 at.% Al and Chumak et al. [200] at 60 at% Al.

The Al-Fe-Ni system was thermodynamically described by Zhang and Du [211] and the parameters for ternary phases $FeNiAl_9$ and Fe_3NiAl_{10} were reassessed 2 years later by Zhang et al. [212] after publication of the new experimental information [200,208,209].

3.4.2. Solid phases

The two bcc ordered phases AlFe and AlNi create a continuous solid solution in the whole temperature range. Its ordering transformation takes place in the Fe-rich corner, while the ordering of the fcc lattice takes place in the Ni-rich side. Intermetallic compounds are present in the Al-rich corner. Some of them, such as: $FeAl_2$, Fe_2Al_5, Fe_4Al_{13}, Al_3Ni and Al_3Ni_2 dissolve

the third element forming solid solution in the ternary system. Additionally, three ternary compounds are formed: $FeNiAl_9$, Fe_3NiAl_{10} and $Fe_5Ni_{24}Al_{71}$.

The stable solid phases together with their crystallographic structures are presented in Table 10.

Table 10 *Stable solid phases in the Al-Fe-Ni system.*

Phase name	Struktur-bericht	Pearson symbol	Prototype	Space group
A1	A1	cF4	Cu	$Fm\bar{3}m$
A2	A2	cI2	W	$Im\bar{3}m$
B2	B2	cP2	CsCl	$Pm\bar{3}m$
$L1_2$	$L1_2$	cP4	Cu_3Au	$Pm\bar{3}m$
M_4Al_{13}_type		mS102	Fe_4Al_{13}	$C\,2/m$
Fe_2Al_5		oC24	Fe_2Al_5	$Cmcm$
$FeAl_2$_type		aP18	$FeAl_2$	$P1$
Fe_5Al_8 (γ-HT)	$D8_2$	cI52	Cu_5Zn_8	$I4\bar{3}m$
Fe_3Al	$D0_3$	cF16	BiF_3	$Fm\bar{3}m$
$NiAl_3$_type		oP16	Fe_3C	$Pnma$
Ni_2Al_3		hP5	Ni_2Al_3	$P\bar{3}m1$
Ni_5Al_3		oS16	Pt_5Ga_3	
$FeNiAl_9$		mP22	Co_2Al_9	$P2_1/a$
Fe_3NiAl_{10}		hP28	Co_2Al_5	$P6_3/mmc$
$Fe_5Ni_{24}Al_{71}$				

3.4.3. Results and discussion

The assessment is based on the parameters determined by Zhang et al. [212]. A few modifications were applied to the description Zhang et al. The parameter *G(B2,Al,Ni:Al:Va)= +300* was added to the B2 phase in order to avoid formation of the miscibility gap. What is more, the ternary A1 and A2 parameters were reoptimized, due to significant differences caused by the inclusion of the additional sublattice for vacancies in the A2 phase, which is missing in the description by Zhang et al.

The results of calculations of the isothermal section at 850-1250 °C are shown in Fig. 20 together with the experimental data from [213,214]. As it can be seen, the experimental data can be well reproduced. The miscibility gap between two bcc phases can be observed in the calculations from this work, which can result from the slight difference in the model for bcc phase, as explained before. Fig. 21 represents vertical sections at 50 at% and 60 at% Al in comparison with the experimental data regarding liquidus and solidus temperatures [200,210]. The satisfactory agreement with the experimental data has been obtained.

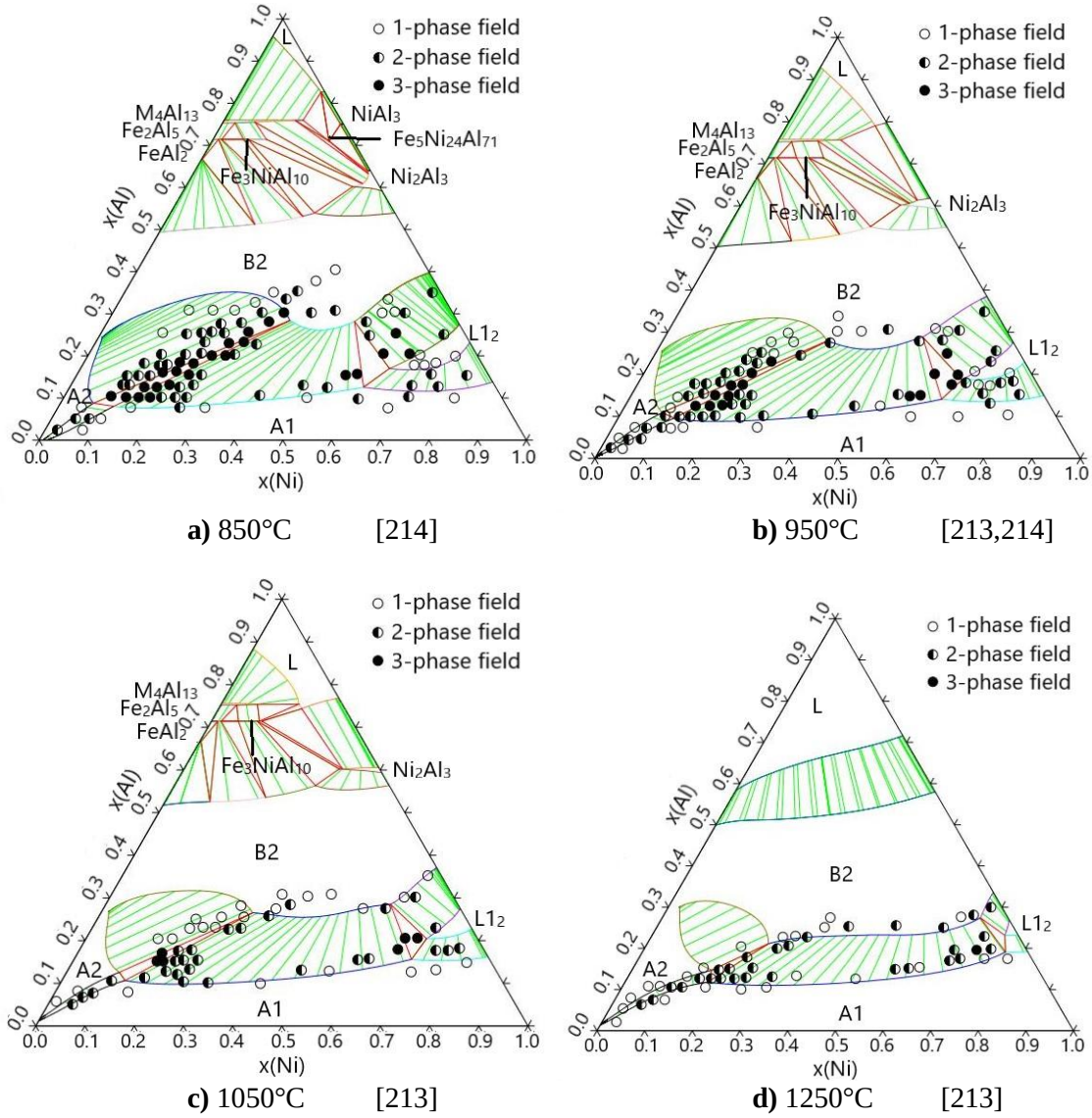

a) 850°C [214] **b)** 950°C [213,214]

c) 1050°C [213] **d)** 1250°C [213]

Fig. 20 *Isothermal section of Al-Fe-Ni system calculated at a) 850°C, b) 950°C, c) 1050°C and d) 1250°C compared with the experimental data from* [213,214].

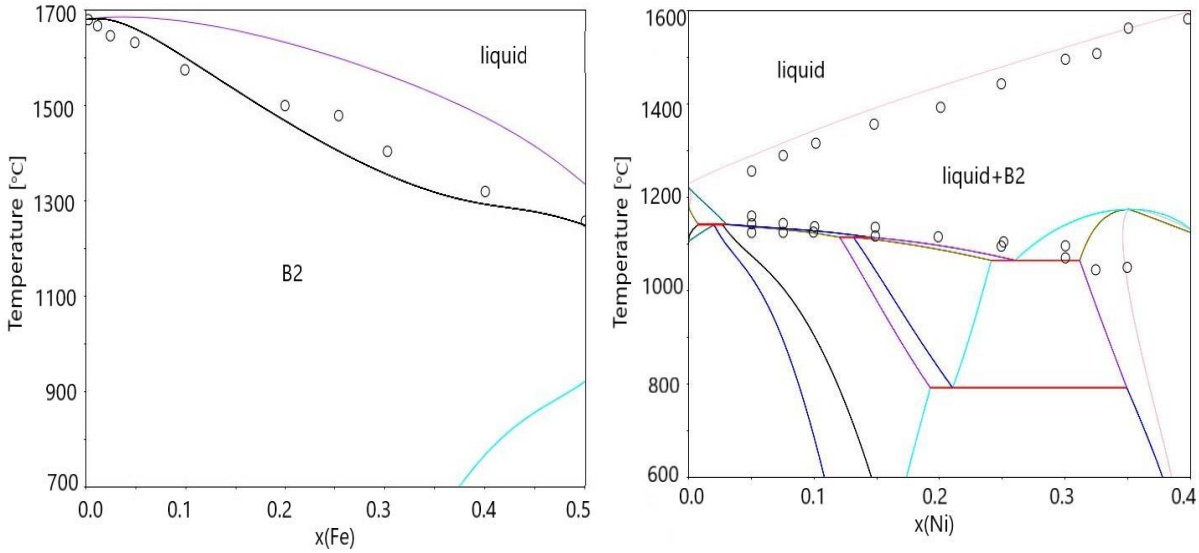

a) 50 at% Al [210] **b)** 60 at% Al [200]

Fig. 21 *Vertical sections calculated at a) 50 at% Al and b) 60 at% Al compared with experimental data regarding liquidus and solidus temperatures* [200,210].

3.5 Al-Fe-Ta

3.5.1. Literature review

Partial isothermal section at 1000 °C was first determined by Hunt and Raman [215]. Risanti and Sauthoff [216] measured tie-line compositions between A2, B2 and C14 phases at 800, 1000 and 1150 °C by means of SEM and XRD. Afterwards, Witusiewicz et al. [127] analyzed a series of equilibrated alloys containing around 13, 32, 52 at% Ta and 13 at% Fe by means of SEM, XRD, EDS, DTA and DSC measurements. The samples were annealed at various temperatures between 550 and 1700 °C. The tie lines compositions of the annealed samples as well as phase transition temperatures were determined.

Kaufman [217] described thermodynamically the system and calculated isothermal sections, however, at that time the experimental information was very limited. More recently Witusiewicz et al. [127] reassessed the system based on the available data and their own experiments.

3.5.2. Solid phases

There are three binary phases dissolving third element to a large extent: Laves phase C14 ($TaFe_2$) dissolves up to 52 at% Al, the μ phase dissolves up to 39 at% Al and the σ phase (Ta_2Al) up to 12 at% Fe. Several intermetallic phases are formed in the Al-rich corner. The bcc phase undergoes the ordering transformation on the Al-Fe side. The stable solid phases together with their crystallographic structures are reported in Table 11.

Table 11 *Stable solid phases in the Al-Fe-Ta system.*

Phase name	Struktur-bericht	Pearson symbol	Prototype	Space group
A1	A1	cF4	Cu	$Fm\bar{3}m$
A2	A2	cI2	W	$Im\bar{3}m$
B2	B2	cP2	CsCl	$Pm\bar{3}m$
$L1_2$	$L1_2$	cP4	Cu_3Au	$Pm\bar{3}m$
M_4Al_{13}_type		mS102	Fe_4Al_{13}	$C\,2/m$
Fe_2Al_5		oC24	Fe_2Al_5	$Cmcm$
$FeAl_2$_type		aP18	$FeAl_2$	$P1$
Fe_5Al_8 (γ-HT)	$D8_2$	cI52	Cu_5Zn_8	$I4\bar{3}m$
Fe_3Al	$D0_3$	cF16	BiF_3	$Fm\bar{3}m$
C14		hP12	$MgZn_2$	$P\,6_3/m\,mc$
μ		hR36	W_6Fe_7	$R\bar{3}m$
σ	$D8_b$	tP30	CrFe	$P4_2/mmm$
$Ta_{39}Al_{69}$_type		cF432	$Ta_{39}Al_{69}$	$F43m$
$Ta_{48}Al_{38}$_type		mP86	$Ta_{48}Al_{38}$	$P2_1/c$

3.5.3. Results and discussion

The thermodynamic description proposed by Witusiewicz et al. [127] required some modifications due to inconsistency with the present multicomponent database. Parameters of the Laves C14 phase had to be adjusted because of different values used for pure elements (Al, Fe and Ta), hence, the functions GHC14AL, GHC14FE and GHC14TA were introduced. The μ phase had to be completely reassessed and the parameters describing the σ phase were modified in order to improve the match with the experimental data.
The different bcc ordering structure, such as $D0_3$ and Heusler $L2_1$, are not included in this assessment, because they require the use of 4-sublattice model for the bcc phase, whereas in the present multicomponent database the 2-sublattice model is used in order to simplify calculations.

The results of this work juxtaposed with the experimental tie lines from [127,216] are presented in Fig. 22. The figure shows isothermal sections calculated at the various temperatures ranging from 800 up to 1700 °C with the corresponding tie lines.

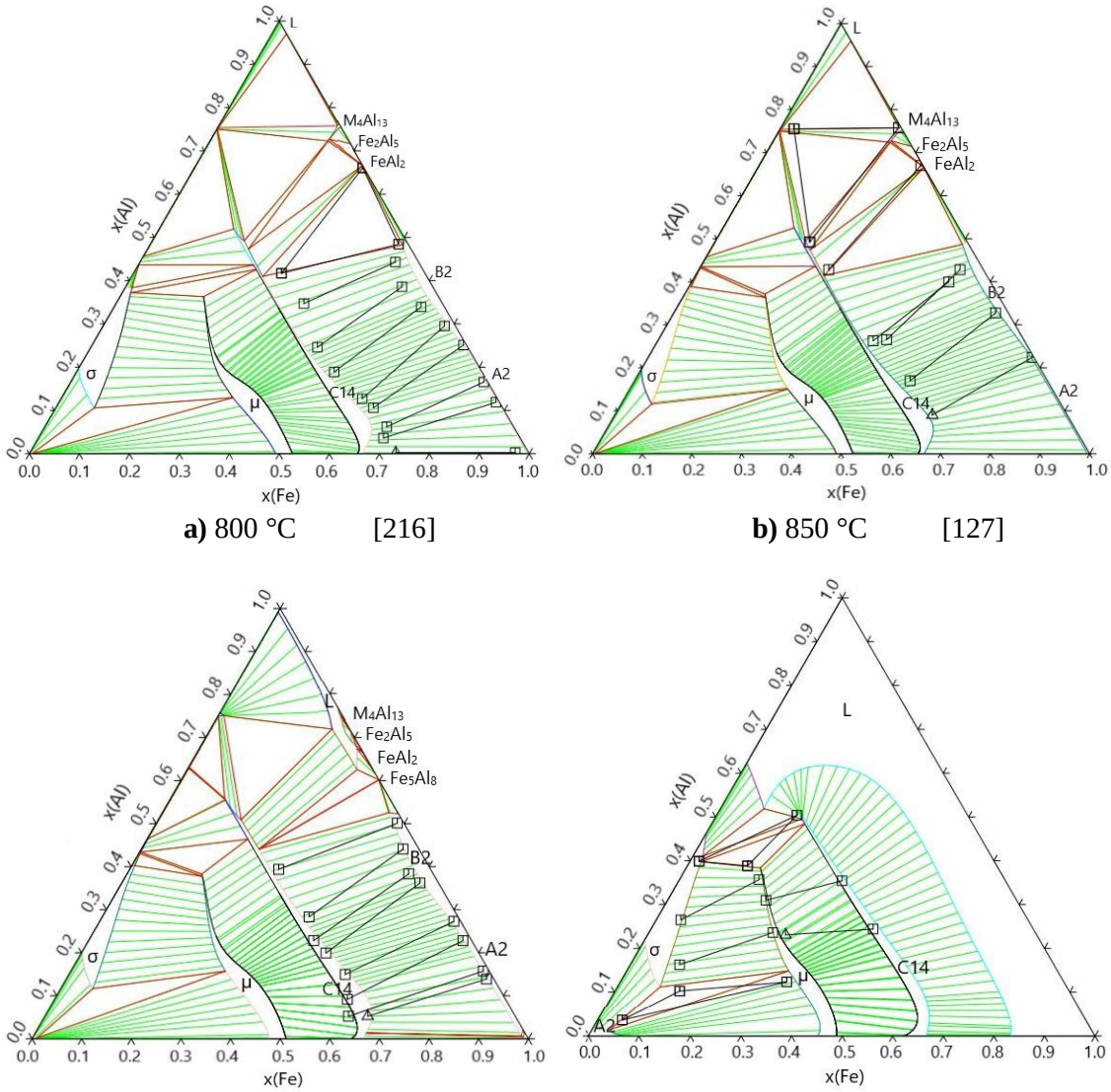

a) 800 °C [216] **b)** 850 °C [127]

c) 1150 °C [216] **d)** 1700 °C [127]

Fig. 22 *Isothermal section of Al-Fe-Ta system calculated at a) 800°C, b) 850 °C, c) 1150 °C and d) 1700 °C compared with the experimental data from* [127,216].

3.6 Co-Cr-Fe

3.6.1. Literature review

Among numerous experimental research on the Co-Cr-Fe system, the most significant in terms of phase equilibria was performed by Dombre et al. [145] by means of equilibrated alloys at temperatures ranging from 800 to 1300 °C. The annealed alloys were investigated by means of EPMA, DTA and XRD techniques. They established experimental isothermal sections at 6 different temperatures. Koester and Hofmann [218] measured the phase equilibria at lower temperatures (600 and 700 °C) using XRD technique.

Phase diagrams of the Co-Cr-Fe system were calculated by various authors using extrapolation from binary subsystems [145,219,220]. Choi et al. [12] evaluated ternary parameters in order to implement a multicomponent Co-Cr-Fe-Ni-V database. They used $(Co,Fe)_8(Cr)_4(Co,Cr,Fe)_{18}$ model and simple arithmetic relations of binary parameters to describe σ phase in the ternary system.

3.6.2. Solid phases

In the Co-Cr-Fe system equilibria between A1, A2 and σ phase are present. σ is stable in the Co-Cr binary side and dissolves significant amount of Fe. At 800 °C the σ phase creates a continuous phase between the Co-Cr and Cr-Fe systems. The A1 phase is stable on the Co-Fe side while the A2 phase stabilizes on the Cr-Fe side. All stable phases are summarised in Table **12**.

Table 12 *Stable solid phases in the Co-Cr-Fe system.*

Phase name	Struktur-bericht	Pearson symbol	Prototype	Space group
A1	A1	cF4	Cu	$Fm\bar{3}m$
A2	A2	cI2	W	$Im\bar{3}m$
A3	A3	hP2	Mg	$P6_3/mmc$
σ	$D8_b$	tP30	CrFe	$P4_2/mnm$
B2	B2	cP2	CsCl	$Pm\bar{3}m$

3.6.3. Results and discussion

In the present assessment the σ phase is described by 4 end-members. In this system Cr is the biggest element, therefore, it is more likely to occupy the first sublattice. Consequently, the most stable end-member is *G(σ,Cr:Fe:Co)=-2746.85+4.9620*T*. Three mixing parameters were added to reproduce the solubility, one allowing mixing between Co and Fe in the last sublattice *G(σ,Cr:Cr:Co,Fe)=+133914.45-267.6989*T* and another two with Co and Cr and all three elements in the second sublattice (*G(σ,Cr:Co,Cr:Fe)=+150000* and *G(σ,Cr:Co,Cr,Fe:Co)=+150000)*. Parameters describing fcc and bcc phases were also added.

The optimization process was performed using the experimental data from Dombre et al. [145] at the temperature ranging from 800 to 1300 °C. The calculated equilibria are compared with the experimental data in Fig. 23.

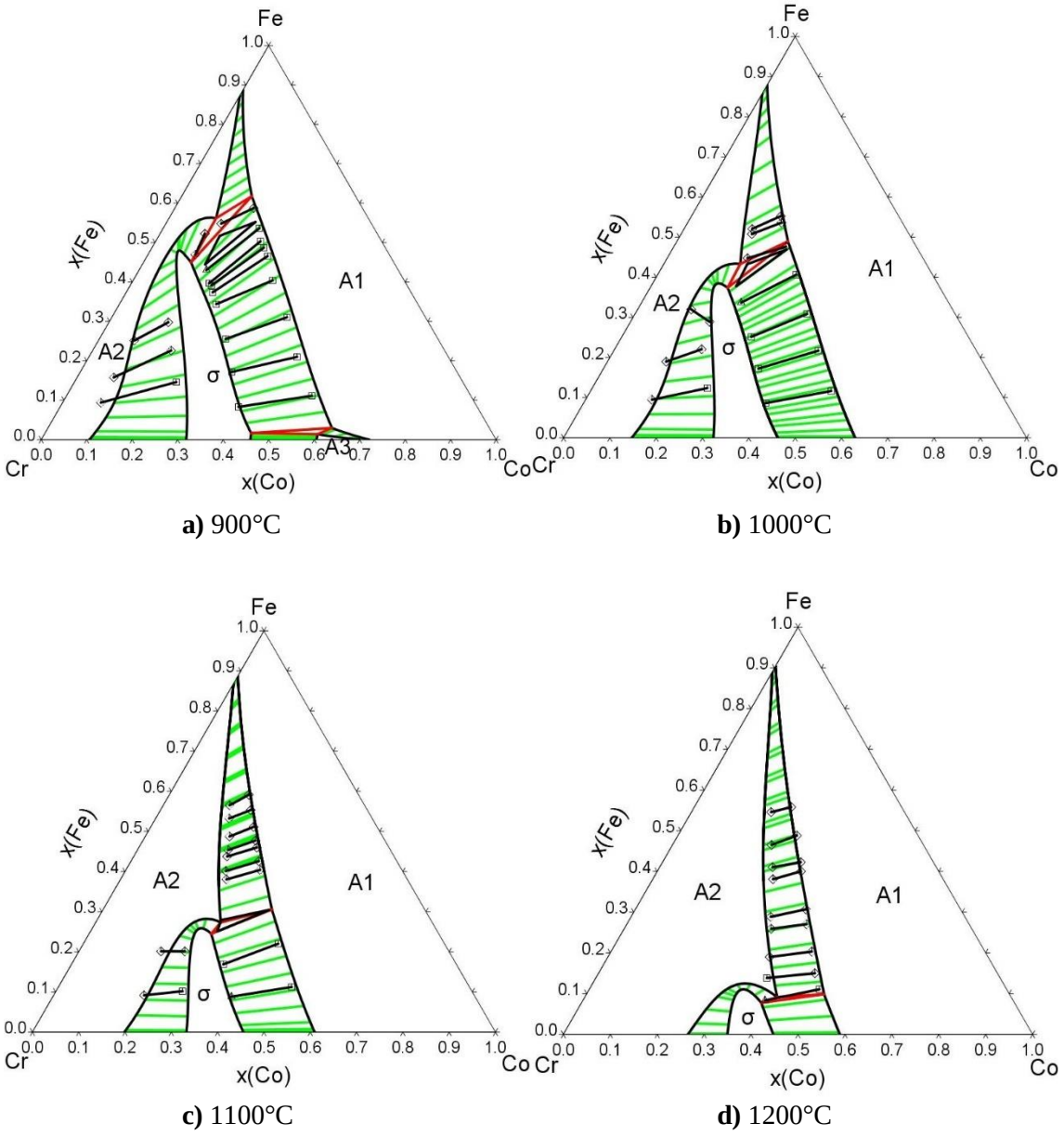

Fig. 23 *Isothermal section of Co-Cr-Fe system calculated at a) 900°C, b) 1000°C, c) 1100°C and d) 1200°C compared with the experimental data from[145].*

A slightly worse agreement between the experimental data from Ref. [145] and the calculated equilibria was obtained at 900 °C (Fig. 23a). This could be caused by the fact, that the samples have not reached the equilibrium state at lower temperatures due to the too short annealing time (150h at 900 °C). At higher temperatures, the experimental data from [145] are well reproduced by the calculations.

Additionally, the site occupancy in σ phase was calculated for each sublattice (4f, 8i'+8j and 2a+8i'') at 727 °C for the section $Co_xCr_{0.475+0.4x}Fe_{0.525-1.4x}$ (with x = 0 – 0.375). The calculations are compared in Fig. 24 to the experimental data reported by Cieślak et al. [221]. The calculated values match fairly well the data reported by Cieślak at al. A small discrepancy can be observed

only in the sublattice 4f, where Co and Cr occupancies qualitatively agree with the experiments but have opposite variation with composition.

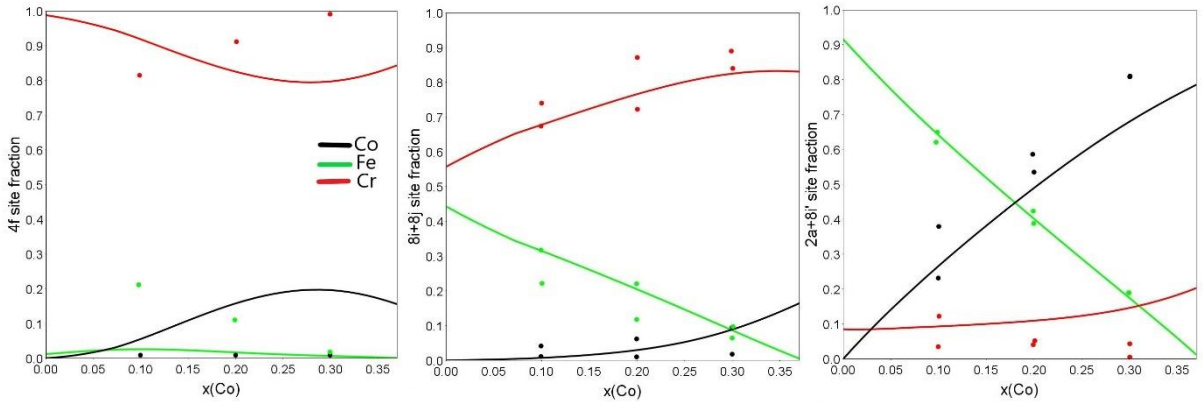

a) 4f **b)** 8i'+8j **c)** 2a+8''

Fig. 24 *Calculated site fractions for a) 4f, b) 8i'+8j and c) 2a+8i'' sites in σ phase at 727°C along composition* $Co_xCr_{0.475+0.4x}Fe_{0.525-1.4x}$ *compared with the experimental data from* [221].

3.7 Co-Cr-Mo

3.7.1. Literature review

Co-Cr-Mo system has been investigated by various authors. The method of equilibrated alloys was applied by Wang et al. [94], Rideout et al. [92] and Darby and Beck [222] to investigate equilibria present at 927, 1200 and 1300 °C, respectively. Zhao [223] used the diffusion-multiple technique to establish the isothermal section at 1100 °C.

The Co-Cr-Mo ternary phase diagram was first calculated by Rajan [81] as a simple extrapolation from binary parameters. In 2011 Lu [224] assessed the Co-Cr-Mo system using data available from the literature in a temperature range of 1100-1300 °C in addition to his own experimental results at 1300 °C. He described σ and μ phases using the same models adopted in the present database, however, the parameters describing the Co-Cr binary system were different and for that reason his parameters could not be implemented in the database. Afterwards, Wang et al. [94] improved the thermodynamic description of the system by adding their own experimental data at 927 °C. σ and μ phases were described in their work using $(Co,Cr,Mo)_8(Cr,Mo)_4(Co,Cr,Mo)_{18}$ and $(Co,Cr,Mo)_7(Cr,Mo)_2(Co,Cr,Mo)_4$ models, respectively.

3.7.2. Solid phases

In the Co-Cr-Mo system the equilibria between σ, μ and R phases are present. The σ phase extends significantly from the Co-Cr binary side and at 1300 °C creates a continuous solution between Co-Cr and Co-Mo systems, as observed by Darby and Beck [222]. It is worth noticing that close to the Co-Cr binary side the σ phase has very large solubility that further increases in

the centre of the phase diagram, whereas it becomes almost stoichiometric when it approaches the Co-Mo side. The μ phase is stable in the Co-Cr and Co-Mo binary subsystems. In the ternary it appears close to the Co-Mo side and extends to the centre of the ternary diagram, dissolving around 18at% Cr. Additionally, the ternary R phase stabilised between the σ and μ. The disordered bcc (A2) phase is formed along the Co-Mo side. The A1 (Co) phase dissolves a significant amount of Cr (~40at%) and lower amount of Mo, which is thermally dependent and reaches ~19at% at 1300°C. The stable solid phases present in the Co-Cr-Mo system are shown in Table 13.

Table 13 *Stable solid phases in the Co-Cr-Mo system.*

Phase name	Struktur-bericht	Pearson symbol	Prototype	Space group
A1	A1	cF4	Cu	$Fm\bar{3}m$
A2	A2	cI2	W	$Im\bar{3}m$
A3	A3	hp2	Mg	$P6_3/mmc$
σ	$D8_b$	tP30	CrFe	$P4_2/mnm$
μ	$D8_5$	hR36	W_6Fe_7	$R\bar{3}m$
R		*hR*159	$Co_5Cr_2Mo_3$	$R\bar{3}$
$D0_{19}$	$D0_{19}$	hP8	Ni_3Sn	$P6_3/mmc$

3.7.3. Results and discussion

In the present assessment, the parameters by Wang et al. [94] were adopted as a starting point. However, all parameters describing σ and μ phase were reassessed due to differences in models and consequently all the other parameters had to be adjusted.
The most stable end-member in σ phase is *G(σ,Mo:Cr:Co)=-293529+19.82*T*. Additionally, 6 mixing parameters were added allowing mixing between Cr and Mo in the first sublattice, Co with Cr and Mo in the second sublattice and Co and Cr in the last one. The μ phase is described using 24 end-members. Among them the most important are: *G(μ,Mo:Mo:Cr:Co)= -107000*, *G(μ,Mo:Cr:Mo:Co)=-120000* and *G(μ,Mo:Cr:Cr:Co)=-110000*. Moreover 7 mixing parameters were added to the description of the μ phase.

The experimental data taken from [92,94,223,225] were used in this work for the optimisation of parameters describing the σ and μ phases and they are added to the calculated isothermal sections in Fig. 25.

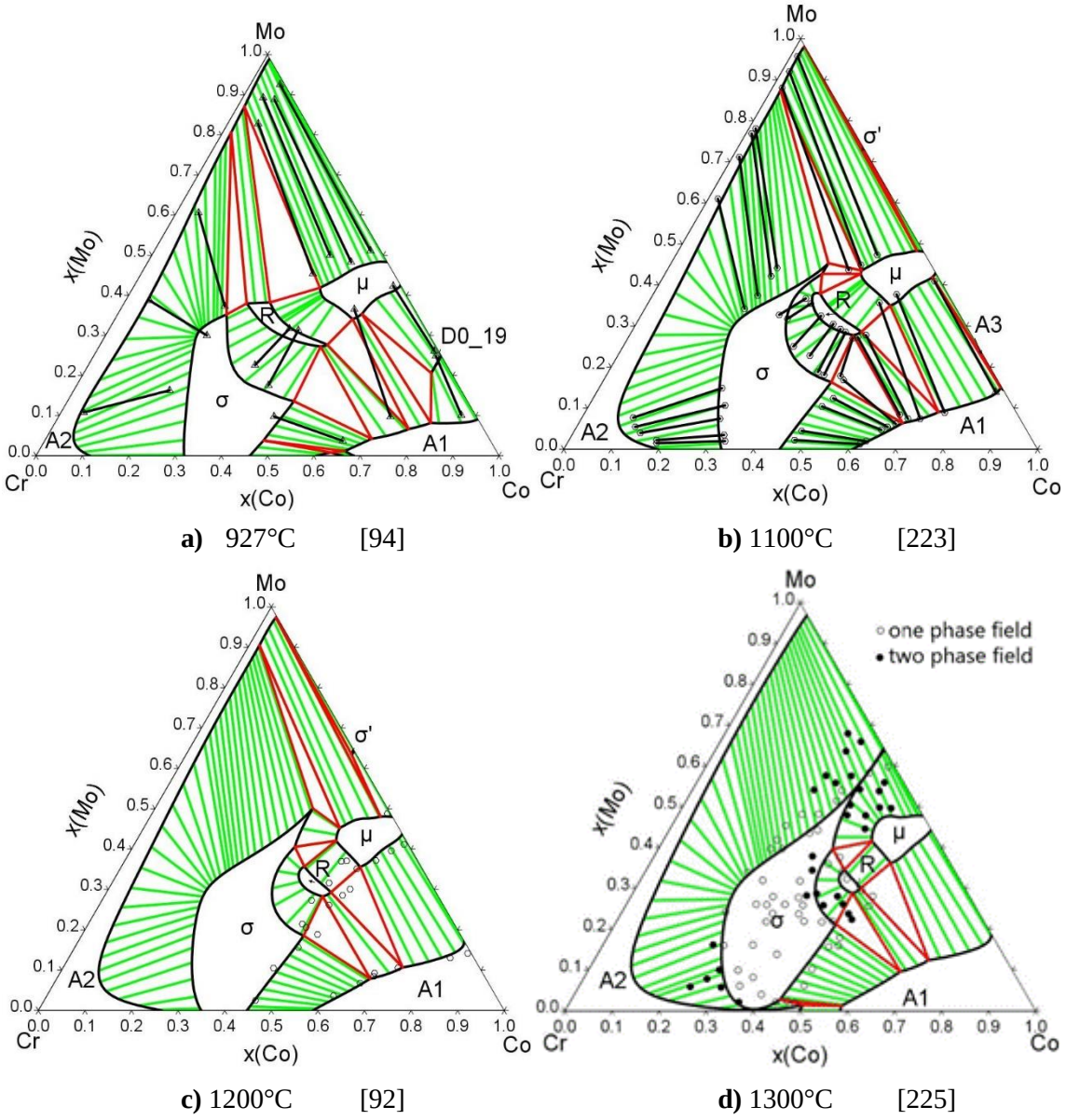

a) 927°C [94] **b)** 1100°C [223]

c) 1200°C [92] **d)** 1300°C [225]

Fig. 25 *Isothermal section of Co-Cr-Mo system calculated at a) 927°C , b) 1100°C, c) 1200°C and d) 1300°C compared with the experimental data from* [92,94,223,225].

The experimental data at each temperature were obtained by different authors, hence, there are some discrepancies between them. The best agreement of the calculations occurs with the data reported by Zhao [223] at 1100 °C. According to Wang et al. [94] μ phase dissolves up to 23.6 at% Cr, whereas σ phase up to 39.6 at% Mo which is slightly higher compared to the results of the present calculations (19% and 36%, respectively).

It is interesting to check how the site occupancy changes along the $CoCr_2 – CoMo_2$ composition at 1300 °C. The calculated site fractions are shown in Fig. 26. As expected, the first and the second sublattices are rather occupied by bigger elements (Cr,Mo), and Cr is gradually replaced by Mo. What is more, Co can also replace up to 18 at% Cr, whereas it cannot replace Mo

(probably due to larger atomic size difference). The last sublattice is mainly occupied by Co (the smallest element), however, on the Co-Cr side it contains around 30% of Cr, whereas on the Co-Mo side it is exclusively occupied by Co. Unfortunately, I did not find any experimentally measure site fraction that could be compared with the calculations.

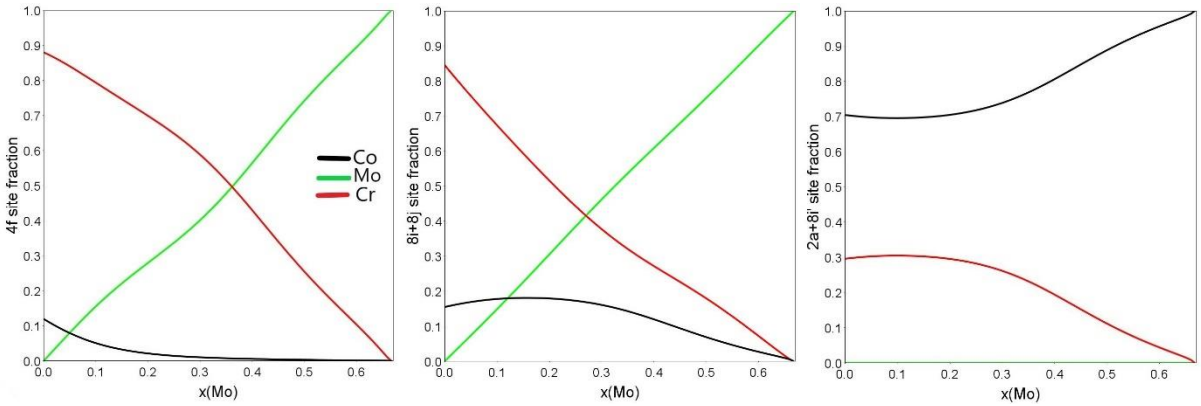

a) 4f **b)** 8i'+8j **c)** 2a+8''

Fig. 26 *Calculated site fractions of Co, Cr and Mo for a) 4f, b) 8i'+8j and c) 2a+8i'' sites in σ phase at 1300°C along $CoCr_2$-$CoMo_2$ composition.*

3.8 Co-Mo-W

3.8.1. Literature review

Ishchenko et al. [226] examined the phase equilibria present at 1000 °C by means of XRD and EPMA measurements. They observed that in the μ and $D0_{19}$ phases, Mo and W can replace each other forming a continuous phase in the ternary system. Wang et al. [164] performed a thorough examination of the system by annealing a series of specimens at the temperatures from 600 to 1300 °C for the time ranging from 1 week up to 3 months at lower temperature, followed by quenching in ice water. The tie lines compositions were measured using XRD and EPMA techniques.

Wang et al. [164] performed thermodynamic assessment of the system based on their own experimental data and the data reported by Ishchenko et al. [226]. Due to the lack of experimental information regarding liquid, this phase was not included in the assessment.

3.8.2. Solid phases

The two phases: μ and $D0_{19}$ that are present in the binary Co-Mo and Co-W sub-systems, exhibit a continuous solubility in the ternary Co-Mo-W in the large temperature range. The A1 phase (Co) has very limited solubility of other elements at 800 °C, however, it increases with the increasing temperature and at 1300 °C around 14 at% Mo and 13 at% W dissolve in the A1

phase. The stable solid phases in the Co-Mo-W are gathered in Table 14.

Table 14 *Stable solid phases in the Co-Mo-W system.*

Phase name	Struktur-bericht	Pearson symbol	Prototype	Space group
A1	A1	cF4	Cu	$Fm\bar{3}m$
A2	A2	cI2	W	$Im\bar{3}m$
A3	A3	hP2	Mg	$P6_3/mmc$
σ	$D8_b$	tP30	CrFe	$P4_2/mnm$
μ	$D8_5$	hR36	W_6Fe_7	$R\bar{3}m$
$D0_{19}$	$D0_{19}$	hP8	Ni_3Sn	$P6_3/mmc$

3.8.3. Results and discussion

In the present work the parameters regarding the Co-Mo-W system were adopted from [164]. The model applied for the μ phase was inconsistent with the one used in the present work, therefore, the description of this phase was modified. A few interaction parameters were inserted: *G(μ,Mo,W:W:Co:Co;0) = +30500+19*T*, *G(μ,W:Mo,W,Co:Co;0) = -34204-52*T* and *G(μ,W:Mo,W,Co:Co;1) = +70000*.

The isothermal section calculated at 800, 1000, 1200 and 1300 °C are presented in Fig. 27 with the experimental tie lines determined by Wang et al. [164].
The continuous solubility of the μ and $D0_{19}$ phases is well reproduced by the calculations. The experimental data suggest that the μ phase field should be slightly more extended. The σ phase does not dissolve W which is in agreement with the fact, that this phase was not observed experimentally by Wang et al.

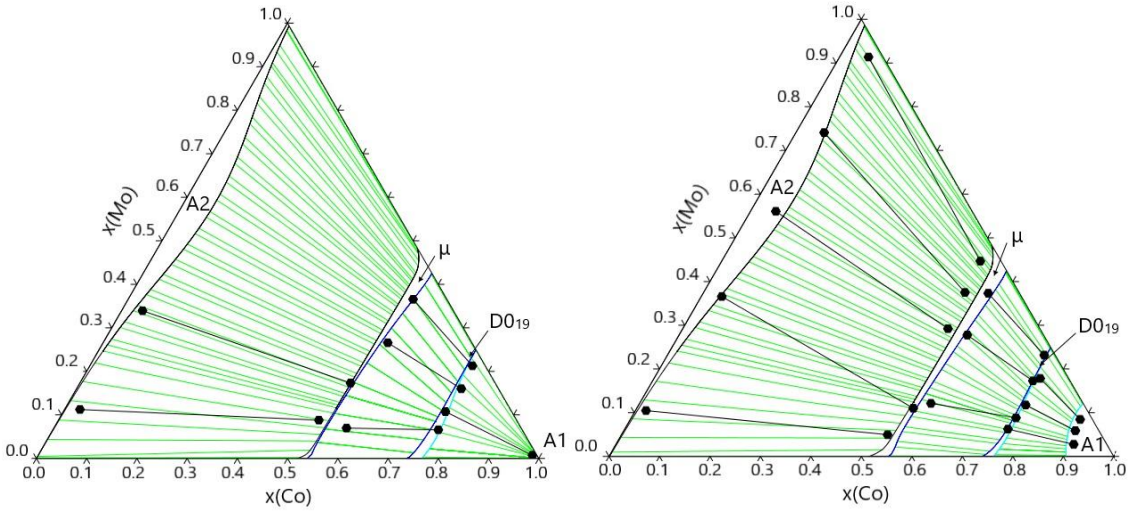

a) 800°C **b)** 1000°C

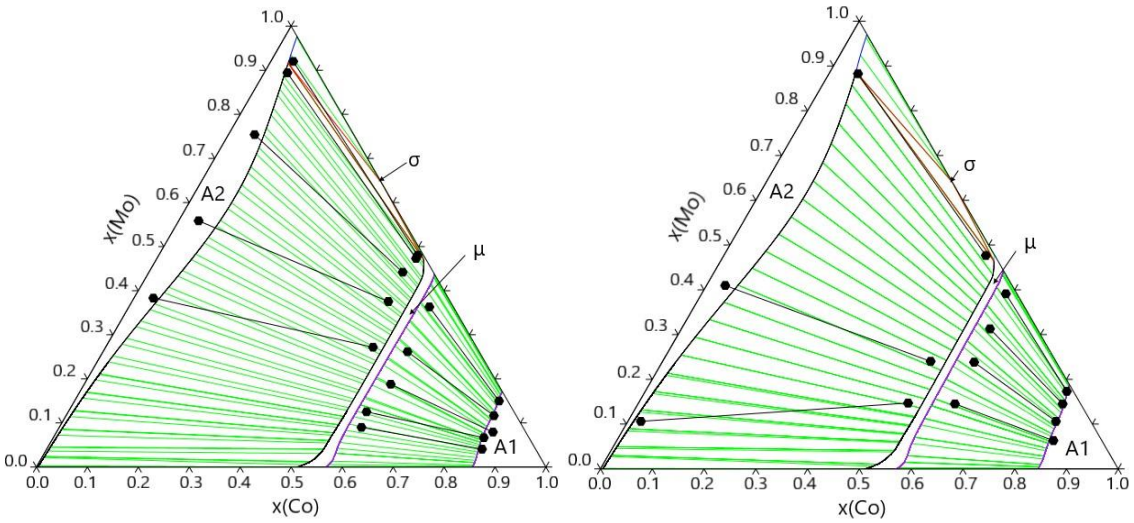

c) 1200°C **d)** 1300°C

Fig. 27 *Isothermal section of Co-Mo-W system calculated at a) 800 °C , b) 1000 °C, c) 1200 °C and d) 1300 °C compared with the experimental data from* [164].

3.9 Cr-Fe-Mo

3.9.1. Literature review

Main experimental investigations of the Cr-Fe-Mo phase equilibria have been conducted by Andersson and Lange [95] and, more recently, by Cao and Zhao [227]. Both of them used diffusion couples to determine isothermal sections at temperatures between 800 and 1200 °C.

The first thermodynamic assessment of the Cr-Fe-Mo system was published by Andersson and Lange [95]. Due to many disagreements in the previous literature they used for the parameters optimisation their own experimental results obtained at temperatures ranging from 950 to 1200 °C. They did not consider the stability of the fcc phase which was evaluated later by Qui [228]. Based on the available experimental data, Qui optimised a metastable fcc parameter in Cr-Mo subsystem. No ternary interaction parameter was needed.

3.9.2. Solid phases

In the Cr-Fe-Mo system several topologically close packed (TCP) phases are stable, such as σ, χ, μ and R. As reported in [227], in the Cr-Fe-Mo system, μ phase is stable up to 1370 °C, whereas σ decomposes at 1610 °C. σ phase is stable in the Cr-Fe and Fe-Mo binary subsystems and it has a very large solubility range in the centre of the ternary diagram. μ phase is stable in the binary Fe-Mo subsystem and dissolves a considerable amount of Cr. The R phase is formed at higher temperatures (~1000 °C) close to the Fe-Mo side. The ternary χ phase precipitates at around 18 at% Mo and it has a linear solubility, because Cr and Fe can replace each other on

the lattice sites. The Laves C14 phase is stable in the Fe-Mo binary system up to around 927 °C and dissolves Cr. The stable phases in the Cr-Fe-Mo are summarized in Table 15.

Table 15 *Stable solid phases in the Cr-Fe-Mo system.*

Phase name	Struktur-bericht	Pearson symbol	Prototype	Space group
A1	A1	cF4	Cu	$Fm\bar{3}m$
A2	A2	cI2	W	$Im\bar{3}m$
σ	$D8_b$	tP30	CrFe	$P4_2/mnm$
C14	C14	hP12	$MgZn_2$	$P6_3/mmc$
R		*hR*159	$Co_5Cr_2Mo_3$	$R\bar{3}$
μ	$D8_5$	hR36	W_6Fe_7	$R\bar{3}m$
χ	A12	cI58	α-Mn	$I\bar{4}3m$

3.9.3. Results and discussion

In the present work all stable phases have been reassessed. For the parameter optimisation both Parrot module in Thermo-Calc and ESPEI infrastructure have been used. In particular ESPEI allowed to improve the description of the σ phase.

σ phase is described using 4 ternary end-members: among them *G(σ,Mo:Fe:Cr)= -25071-72*T* and *G(σ,Mo:Cr:Fe)= -16208-70*T* have the biggest influence on phase equilibria. In order to reproduce its extensive solubility, a series of mixing parameters were added. Mo in the second sublattice can be replace by both, Cr and Fe, which was represented by following parameters: G(σ,Cr:Cr,Mo:Fe); G(σ,Mo:Cr,Mo:Fe); G(σ,Cr:Fe,Mo:Fe); G(σ,Mo:Fe,Mo:Cr). In the last sublattice Cr can replace Fe G(σ,Mo:Fe:Cr,Fe). Additionally, the parameter describing mixing between Cr and Fe in the second sublattice has a positive value to prevent formation of a miscibility gap *G(σ,Mo:Cr,Fe:Fe)= +155984*.
The μ phase is described by 12 end-members; among them, the most stable is: *G(μ,Mo:Cr:Fe:Fe)=-320000*. Fe in the last sublattice can be exchanged with Cr, hence one mixing parameter was added *G(μ,Mo:Mo:*:Cr,Fe)=-25000-200*T* in order to reproduce the solubility of Cr in the μ phase.

The isothermal sections computed according to the present assessment are compared with the experimental results used for the optimisation in Fig. 28.

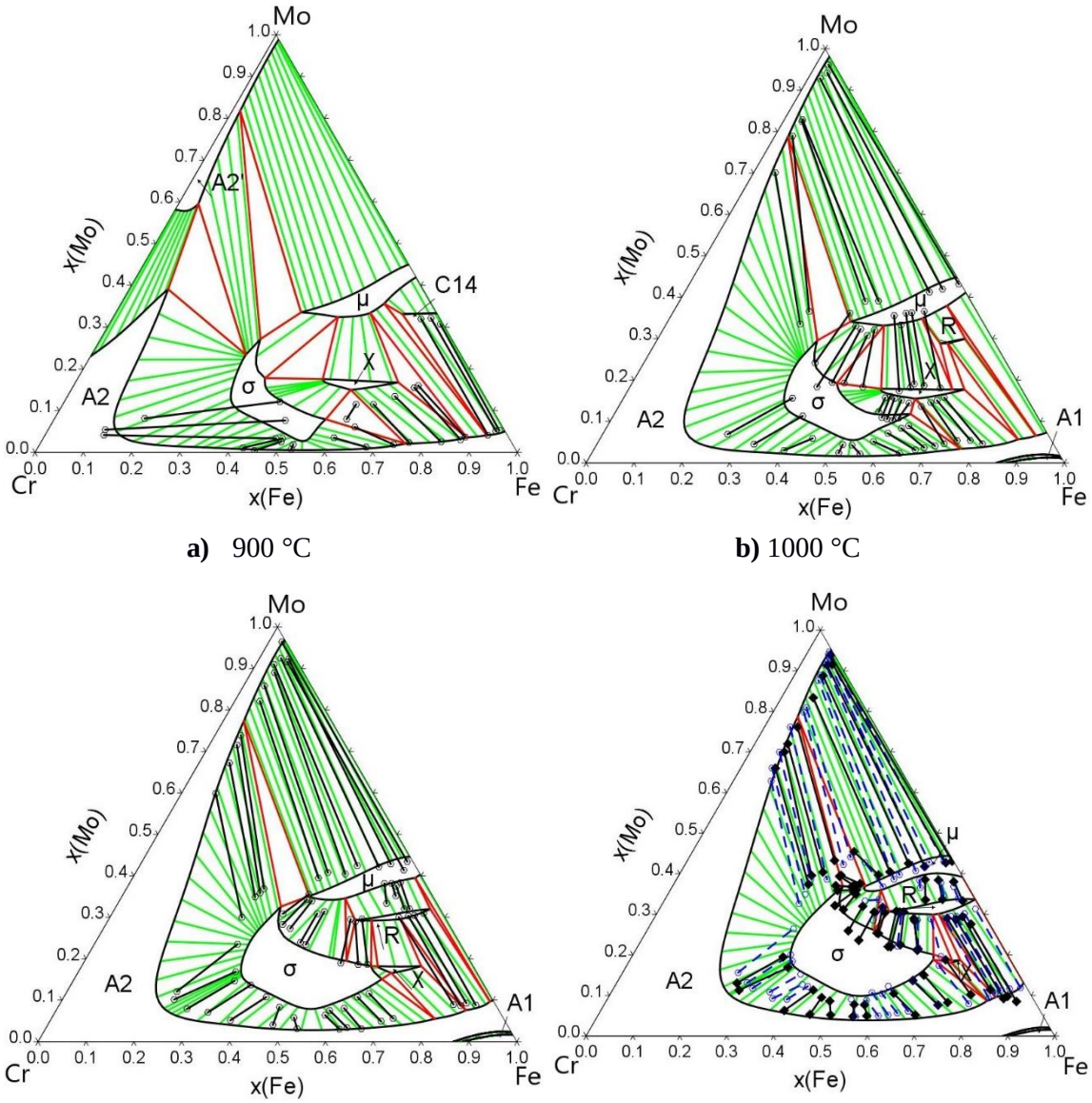

Fig. 28 *Isothermal section of Cr-Fe-Mo system calculated at a) 900°C, b) 1000°C, c) 1100°C and d) 1200°C compared with the experimental data from* [95] *(solid line) and* [227] *(dashed line).*

At 900 °C there is some disagreement between the experimental tie lines and the calculations. It can be explained considering that the samples were first annealed at higher temperature and then quenched and annealed again at 900 °C [227], which might result in a not complete attainment of equilibrium. For this reason, during assessment more attention was given to the data measured at higher temperature. The experimental data suggest that σ phase should extend more to the Cr-Mo side at temperatures above 900 °C. At 1200 °C it can be observed that some experimental data reported by different authors [95] and [227] are not in agreement with each other, especially the tie lines between μ and σ phases as well as those between bcc and μ (Andersson and Lange reported larger solubility of the μ phase than observed by Cao and Zhao).

Taking into account all of these discrepancies and the overall complexity of the system, a satisfactory good agreement was obtained.

Site occupancy of each element in each sublattice of the μ phase has been calculated at 1000 °C along $Fe_{58}Mo_{42}$-$Cr_{26}Fe_{42.92}Mo_{31.08}$ section (Fig. 29). Unfortunately, I did not find in literature any experimental data for a comparison. Nevertheless, it can be seen that the first and third sublattice are exclusively occupied by Mo and Fe, respectively. It results from the fact, that bigger elements (in this case Mo) tend to occupy the 6' and 6'' sites, whereas the smaller ones (here Fe), will rather fill the 3a and 18h sites. It is worth noticing that in the second sublattice (6''' site), Fe and Mo are gradually replaced by Cr (due to its medium size it can exchange with Fe as well as with Mo). What is more, Cr can also replace around 25% of Fe in the 18h site.

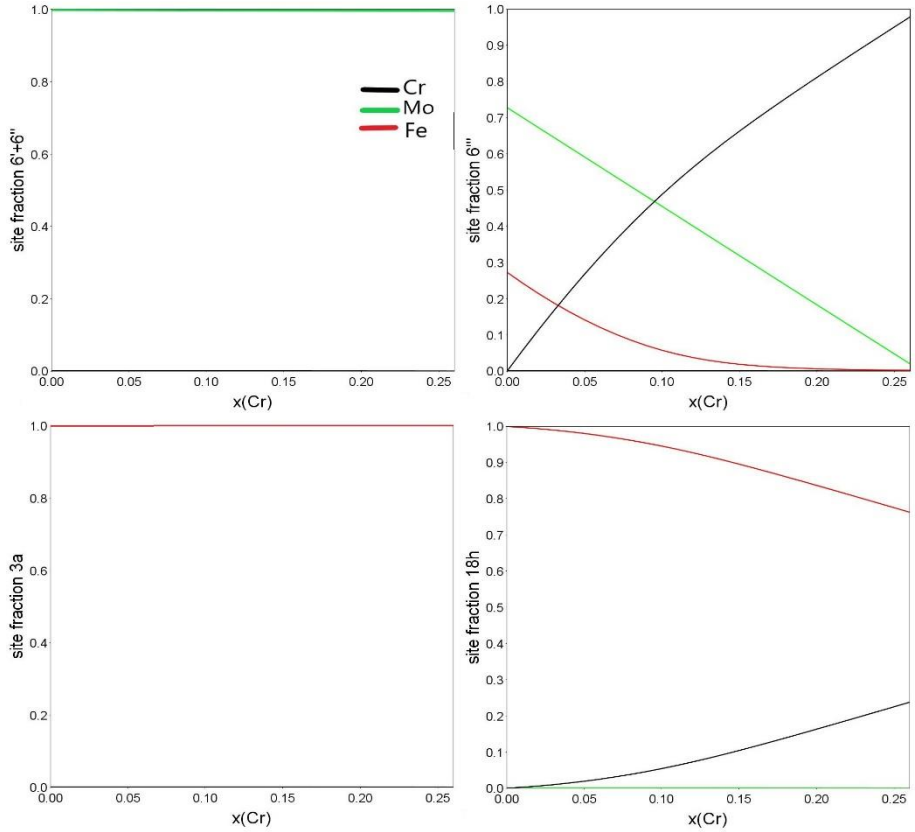

Fig. 29 *Calculated site fractions of Cr, Fe and Mo for 6'+6'', 6''', 3a and 18h sites in μ phase at 1000°C along the* $Fe_{58}Mo_{42}$-$Cr_{26}Fe_{42.92}Mo_{31.08}$ *section.*

3.10 Cr-Fe-W

3.10.1. Literature review

Gustafson [229] investigated the equilibria in the Cr-Fe-W system by means of a diffusion couple technique at temperatures ranging from 900 to 1400 °C.

In the assessment by Gustafson [229] the σ and μ phases were described using $(Fe)_8(Cr,W)_4(Cr,Fe,W)_{18}$ and $(Cr,Fe)_7(W)_2(Cr,Fe,W)_4$ models. The author noticed the presence of a high temperature ternary phase at 1400 °C (he referred to it as phase B), but it was not included in the assessment, due to problems with identifying its structure. Chvatalova et al. [230] performed the thermodynamic modelling of σ phase using a two-sublattice model based on the first-principle calculations (other parameters were taken from the Gustafson's assessment).

3.10.2. Solid phases

All stable phases are listed in Table 16. σ phase is stable in the binary Cr-Fe system below 827 °C. Even though it is metastable in the remaining binary systems (Cr-W and Fe-W), the presence of tungsten stabilises it at much higher temperature (up to about 1400 °C). The μ phase is stable in the binary Fe-W system and dissolves a considerable amount of Cr (up to around 40 at%). Analogously to the Cr-Fe-Mo system, the ternary χ phase stabilises at the constant amount of Mo (~20 at%) and has a linear solubility between Cr and Fe that decreases with temperature. This is also the case of the Laves C14 phase, which contains ~33 at% Mo. This phase was experimentally observed up to 1200 °C.

Table 16 *Stable solid phases in the Cr-Fe-W system.*

Phase name	Struktur-bericht	Pearson symbol	Prototype	Space group
A1	A1	cF4	Cu	$Fm\bar{3}m$
A2	A2	cI2	W	$Im\bar{3}m$
σ	$D8_b$	tP30	CrFe	$P4_2/mnm$
μ	$D8_5$	hR36	W_6Fe_7	$R\bar{3}m$
C14	C14	hP12	$MgZn_2$	$P6_3/mmc$
χ	A12	cI58	α-Mn	$I\bar{4}3m$

3.10.3. Results and discussion

Three ternary end-members were optimised to describe σ phase, namely *G(σ,Cr:W:Fe)=+94785-45*T*, *G(σ,W:Cr:Fe)= +54110-70*T* and *G(σ,W:Fe:Cr)=+460-20*T*. Additionally, 2 parameters were added allowing mixing between Cr and Fe in the second sublattice: *G(σ,W:Cr,Fe:Fe)=-240200-100*T* and *G(σ,W:Cr,Fe:Cr)=-270200-100*T* and 3 parameters allowing mixing of W with Cr and Fe (to reproduce the shift of the σ phase field towards W with increasing temperature). The μ phase is described by 12 end-members: among them *G(μ,W:Cr:Cr:Fe)= -80000* and *G(μ,W:Fe:Cr:Fe)= -40000* have the largest influence on the phase stability. The Gibbs energy of formation of two end-members with W in the last sublattice has a positive value, while for 5 end-members with no influence on the stable phase equilibria it is set to zero. Moreover, one mixing parameter *G(μ,W:W:Cr,Fe:*)= +73340- 108*T* was added. The χ phase is described by 4 ternary end-members, and the

*G(χ,Fe:W:Cr)=-68150-300*T* has the highest stability. Additionally, two parameters allowing mixing between Cr and Fe in the first and last sublattice were added. The C14 phase is described with a two-sublattice model and it was sufficient to add one interaction parameter *G(C14,W:Cr,Fe)=-17506-1.7*T* to reproduce the solubility of the C14 phase in the ternary system.
All the remaining phases were also evaluated during the assessment of this system.

The experimental data concerning σ and μ phases used for this optimisation come from the work of Gustafson [229] and they are shown in Fig. 30 together with the calculated diagrams.

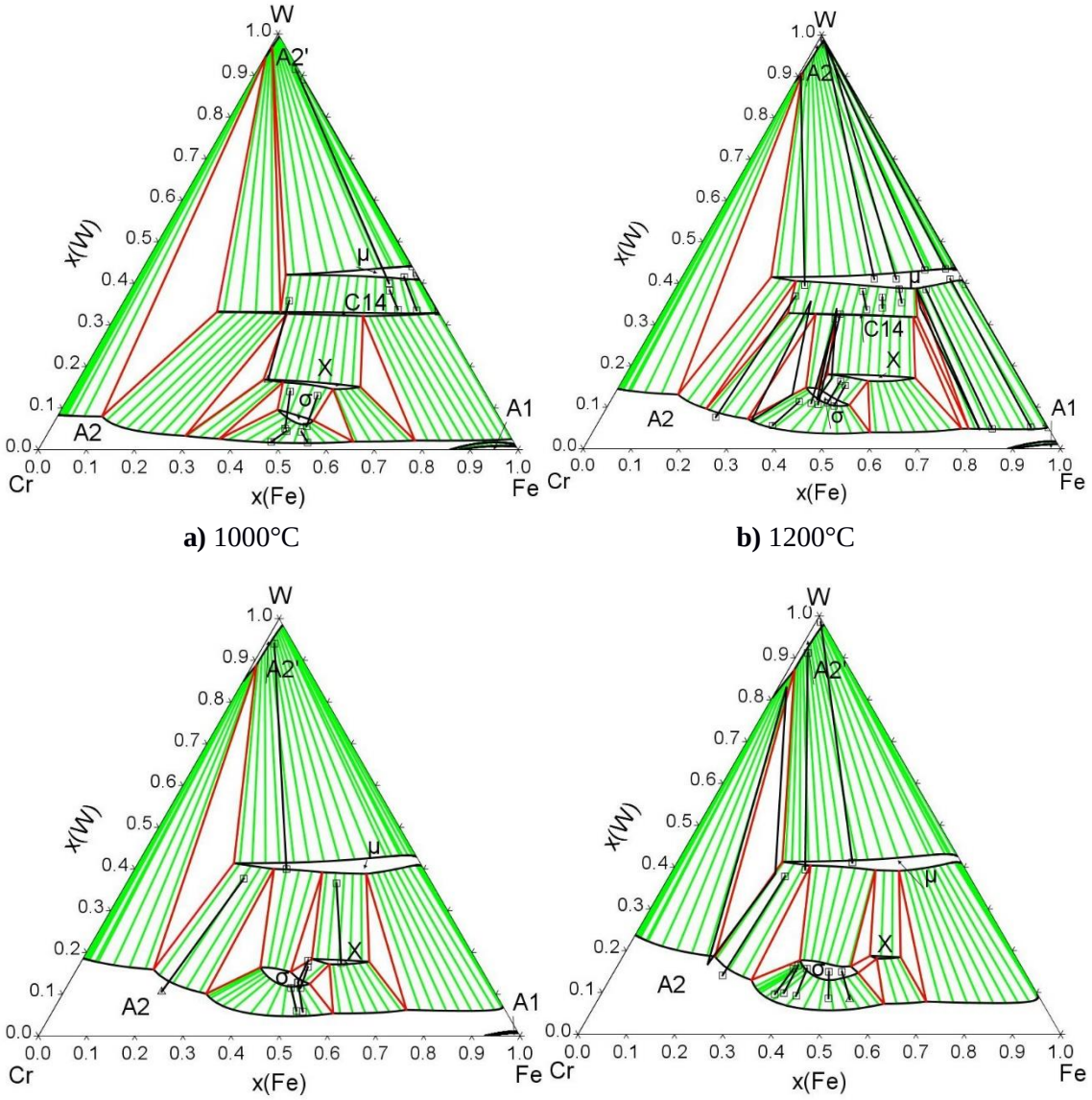

a) 1000°C **b)** 1200°C

c) 1300°C **d)** 1400°C

Fig. 30 *Isothermal section of Cr-Fe-W system calculated at a) 1000°C, b) 1200°C, c) 1300°C and d) 1400°C compared with the experimental data from* [229].

The experimental data are well reproduced by the calculated diagrams. According to the data reported by Gustafson [229], the σ phase should dissolve slightly higher amount of both Cr and Fe. At higher temperature (1400 °C) there is a small mismatch between tie lines connecting σ and A2, which is not observed at lower temperature.

3.11 Fe-Mo-W

3.11.1.Literature review

The Fe-Mo-W system was experimentally studied by Kirchner et al. [231], in particular, the equilibria between A2, μ and R phases. The samples were annealed at 1100 and 1305 °C for 720h. The compositions of stable phases were measured using EPMA. Ishchenko et al. [226] determined the phase equilibria present at 900 °C measured by XRD and EPMA techniques. They reported that the μ phase creates a continuous solid solution between Fe-Mo and Fe-W sides. Afterwards, this observation was confirmed by Meshkov et al. [232]. They studied the present stable phases of the specimens annealed at 900 °C for 2000h by means of XRD. Gustafson [137] determined the tie lines compositions at 1200, 1300 and 1400 °C by means of SEM equipped with EDS.

Gustafson [137] performed thermodynamic assessment of the Fe-Mo-W system. The parameters regarding liquid phase were not considered in his assessment due to the lack of the experimental information.

3.11.2.Solid phases

The μ and C14 phases create a continuous solid solution at lower temperature between Fe-Mo and Fe-W binary subsystems. The TCP σ and R phases are both present in the Fe-Mo system, but the presence of the third element (Mo) stabilizes them to the higher extent. The A1 phase is stable at lower temperatures close to the Fe-rich corner and the A2 phase is extended along the Mo-W binary side in the whole temperature range. All stable solid phases are collected in Table 17.

Table 17 *Stable solid phases in the Fe-Mo-W system.*

Phase name	Struktur-bericht	Pearson symbol	Prototype	Space group
A1	A1	cF4	Cu	$Fm\bar{3}m$
A2	A2	cI2	W	$Im\bar{3}m$
σ	$D8_b$	tP30	CrFe	$P4_2/mnm$
μ	$D8_5$	hR36	W_6Fe_7	$R\bar{3}m$
C14	C14	hP12	$MgZn_2$	$P6_3/mmc$
R		*h*R159	$Co_5Cr_2Mo_3$	$R\bar{3}$

3.11.3.Results and discussion

The models describing μ and σ phases applied by Gustafson in his assessment [137] are inconsistent with the models selected in the present database, therefore the Fe-Mo-W system was entirely reassessed in this work. The parameters describing A2, μ, σ and R phase were optimized. The A2 phase is described with positive interaction parameters *G(A2,Fe,Mo,W:Va)=+10000*. The most stable μ phase end-member parameter is *G(μ,W:Mo:Fe:Fe) = -257485-55*T*, other end-member parameters that had contribution to the phase stabilities were set to the value -300000. No interaction parameter was added. In σ phase, two end-member parameters were set to the negative value: *G(σ,Mo:W:Fe) = -222080-40*T* and *G(σ,W:Mo:Fe)=-100000*, additionally one interaction parameters was added, allowing exchange between Mo and W in the first sublattice *G(σ,Mo,W:Mo:Fe)=-110000*. The values are referred to the lattice stability of the pure elements in the μ and σ structure calculated ab-initio [109,117]. The R phase is described with two ternary end-members *G(R,Mo:W:Fe)=- 265000* and *G(R,W:Mo:Fe)=-255000*. The Mo and W can substitute each other in the first sublattice which was represented by addition of an interaction parameter: *G(R,Mo,W:Mo:Fe)=-25000*.

The isothermal sections calculated at 900, 1100, 1300 and 1400 °C are compared with the experimental data [137,231,232] in Fig. 31. As it can be seen, the continues solubility of the C14 and μ phases at lower temperature is reproduced by calculations as well as the formation of R and σ phases at higher temperatures (1300 and 1400 °C).

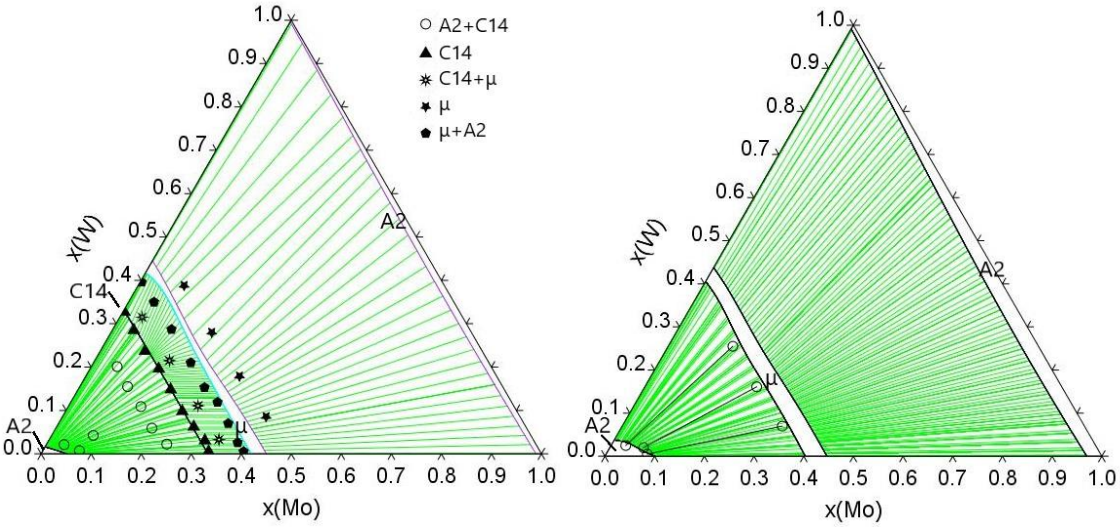

a) 900°C [232] **b)** 1100°C [137]

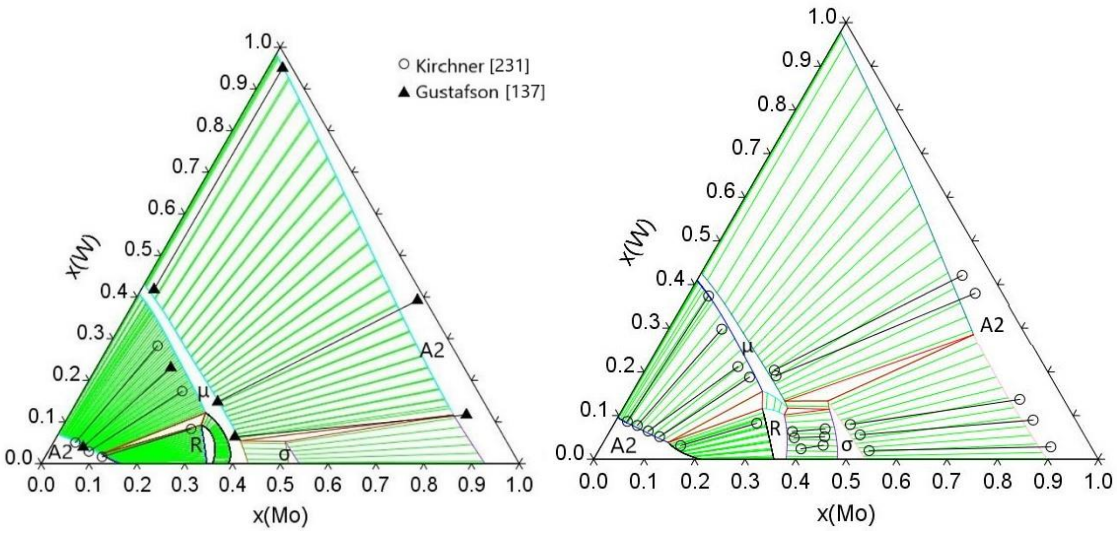

c) 1300°C [231], [137] **d)** 1400°C [137]

Fig. 31 *Isothermal section of Fe-Mo-W system calculated at a) 900 °C, b) 1100 °C, c) 1300 °C and d) 1400 °C compared with the experimental data from* [137,231,232],

3.12 Additional remarks

The stability of the σ phase can be related to the e/a ratio, as can be seen in Fig. 32a. The figure shows the homogeneity ranges at 1100 °C of the σ phase in the ternary systems assessed in this work. Cr is always in the lower left vertex, whereas the lower right vertex contains the element with the highest e/a value. The grey lines indicate constant e/a values. It can be observed that all reported homogeneity ranges extend into the ternary systems at constant e/a between 6.7 and 7.5. Tsai et al. [233] proposed a criterion to predict the existence of the σ phase in HEAs - a VEC value ranging from 6.88 to 7.84. The values reported by Tsai et al. are very close to the ones observed in this work.

In comparison, an analogous figure has been calculated for μ phase (Fig. 32b), where the grey lines indicate constant Mo or W concentration. It can be observed that while the σ phase is clearly stabilised by the valence electron concentration (it is stable along the constant e/a lines), it is not the case of μ phase which is stable in a wider range of e/a (between 6.5 and 8). Instead, the μ phase tends to occur at constant concentration of the biggest element, which indicates that the stability of the μ phase is mainly related to dimensional factors.

Then it can be concluded that the models selected in this work can satisfactorily reproduce solution ranges of both kind of phases: those extending at constant e/a as well as those extending at constant atomic concentration.

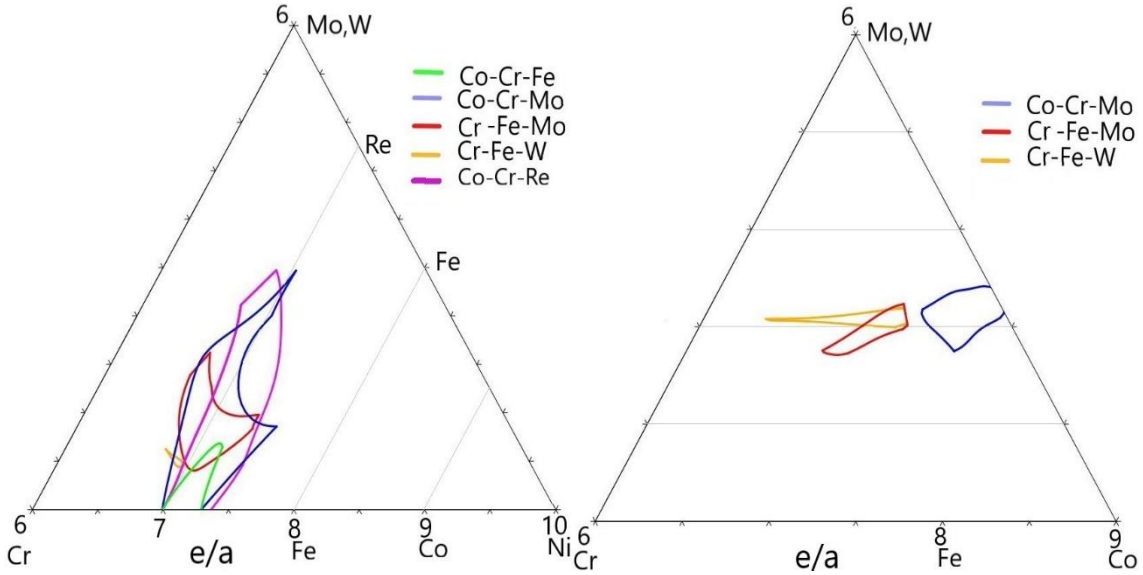

a) σ phase **b)** μ phase

Fig. 32 *Homogeneity ranges of the a) σ and b) μ phases at 1100 °C as a function of e/a in ternary systems assessed in this work.*

4. Experimental validation of quinary Al-Co-Cr-Fe-Ni system

While the influence of Al in the quinary system Al-Co-Cr-Fe-Ni has been profoundly investigated by various authors [234–242], the information about the impact of other elements on the microstructure of this alloys is very limited. In the present work, the equilibrated alloys with various amount of Co, Cr and Fe have been prepared in order to provide the missing information on phase compositions, that can be compared with the calculations and used for improvement of the database.

4.1. Materials and methods

4.1.1. Preparation of samples.

7 samples were prepared from a mixture of commercial purity metals (>99,99%). Their nominal compositions are reported in Table 18. They were melted several times in a vacuum arc-melting furnace under Ar atmosphere using Zr as a getter to capture the residual oxygen and impurities. In this method, an electric arc generated between two electrodes (a tungsten tip and a water-cooled Cu base) is used to melt the material. Ar does not interact with the material, but can be ionized allowing for the formation of the electric arc. This technique was chosen because of the high melting temperature of the prepared alloys. Multiple melting improved homogeneity of the samples. Each sample was approximately 1g and in all cases the weight loss after melting was less than 0.5mass%. The samples were placed inside tantalum crucibles, which were previously ultrasonically cleaned in petroleum ether for 15 minutes. They were sealed in quartz tubes under Argon atmosphere, and annealed for around 2160 h at 1050 ˚C followed by air cooling.

4.1.2. Characterization of the samples.

The polished sections of alloys were prepared following the standard metallographic procedure ASTM E3-11 (Standard Guide for Preparation of Metallographic Specimens). The samples cross-sections were abraded using SiC sandpapers with different grain size: 320-, 400, 600-, 800- and 1000-grit and then polished in a diamond suspension of 6, 3, and 1μm using polishing machine (Struers LaboPol-5) with the speed of 250 rpm and petroleum ether as a lubricant.

Microstructure of the samples was observed and the phase compositions were determined using Scanning Electron Microscope (Zeiss EVO 40, Carl Zeiss, Oberkochen, Germany) equipped with an Energy Dispersive X-ray spectroscope (EDX Pentafet, Oxford Instruments, Oxfordshire, U.K.). The high energy back-scattered electrons (BSE) signal was detected, which are the electrons coming from the incident beam reflected by the sample because of the elastic collision. The intensity of such signal is strongly related to the atomic number resulting in the

brighter (heavy elements) and darker (light elements) areas in the SEM image. There was no need for applying any conducting layers as all examined samples were electrically conducting. The BSE images were registered with magnification between 700 and 10000x. An acceleration voltage (EHT) was set to 20kV and working distance (WD) to 8mm.

The present phases were identified by X-Rays Diffraction using a vertical diffractometer (X'Pert MPD Philips, Almedo, Netherlands) with Cu Kα radiation. XRD patterns were registered with a step scan mode ranging from 10 to 100˚with the step size of 0.02˚and 4s time per step. The Match!3 software was used for the qualitative analysis of the obtained XRD patterns. The indexing of the reflections was done by superimposing reference diffraction patterns and the experimental ones. The reference diffraction patterns were taken from the Pearson's Crystal Data. The quantitative analysis was done by Rietveld refinement method by means of FullProf program.

Table 18 *Nominal composition of prepared samples.*

Name	Nominal composition [mol]
ARef	**Al-Co-Cr-Fe-Ni**
ACo0.5	**Al-$Co_{0.5}$-Cr-Fe-Ni**
ACo1.5	**Al-$Co_{1.5}$-Cr-Fe-Ni**
ACr0.5	**Al-Co-$Cr_{0.5}$-Fe-Ni**
ACr1.5	**Al-Co-$Cr_{1.5}$-Fe-Ni**
AFe0.5	**Al-Co-Cr-$Fe_{0.5}$-Ni**
AFe1.5	**Al-Co-Cr-$Fe_{1.5}$-Ni**

4.2. Experimental results

Fig. 33 and Fig. 34 show representative SEM images of the annealed samples. Two to three kinds of phases were identified in the samples. A uniform, coarse distribution of the brightest phase in a matrix (darkest phase). What is more, it can be seen that in some cases (Fig. 33, Fig. 34 d-f) there are grey precipitates within the brightest phase. The width of the brightest grains is around 4μm.

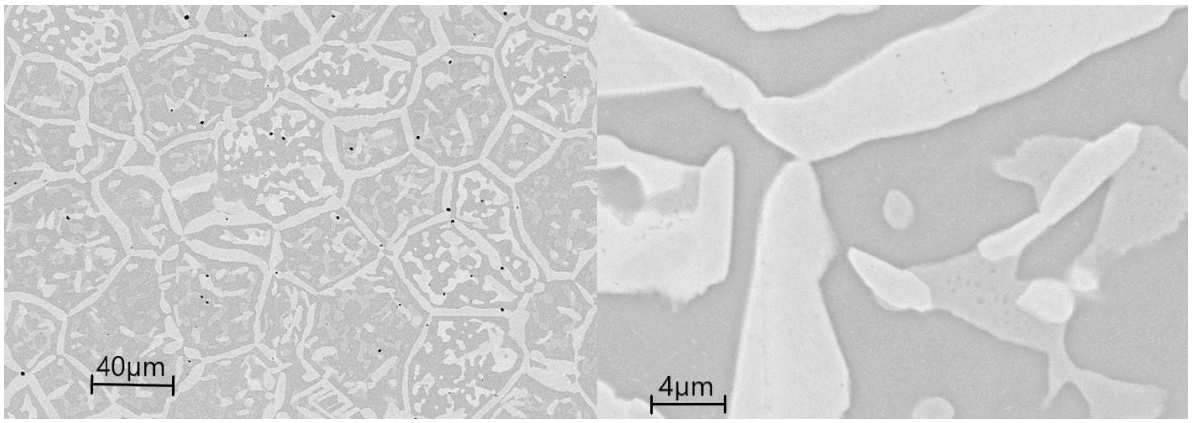

Fig. 33 *SEM images of the ARef sample with magnification 700x (left) and 6180x (right).*

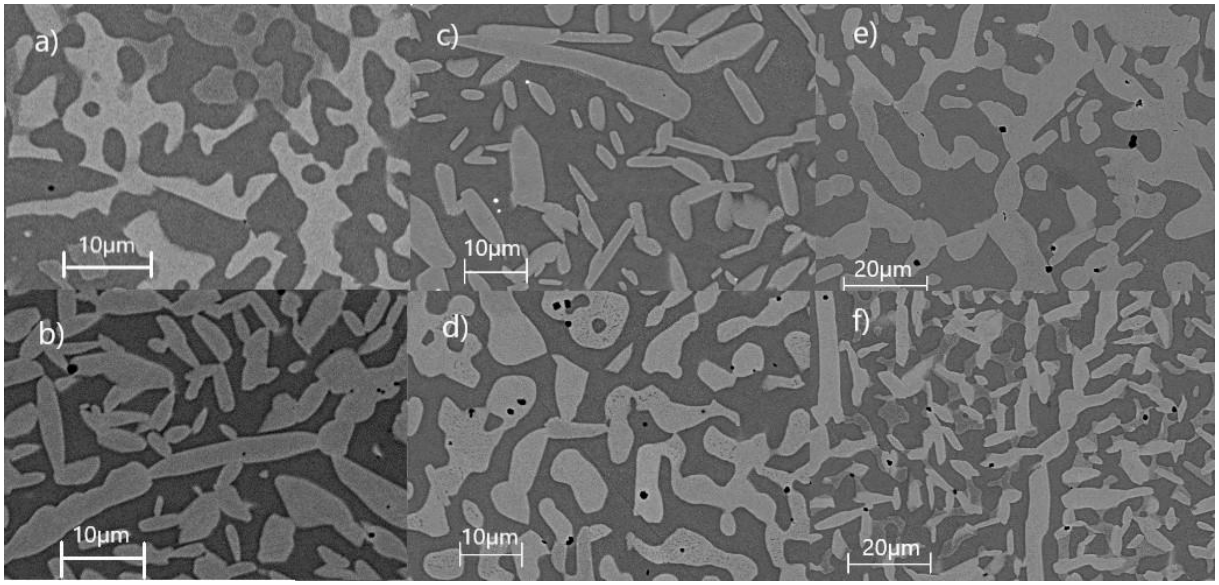

Fig. 34 *SEM images of the a) ACo0.5, b) ACo1.5, c) ACr0.5, d) ACr1.5, e) AFe0.5 and f) AFe1.5 samples.*

The XRD profiles with assigned phases are shown in Fig 35. The compositions of individual phases in the SEM images were estimated using EDX point analysis and are reported in Table 19. The matrix is rich in Al and Ni and is assigned as the ordered B2 phase. The bright regions consist of the brighter disordered A1 phase rich in Co, Cr and Fe and a less bright disordered bcc phase rich in Cr.

In two samples (ACr1.5 and AFe0.5), the σ phase was observed, which should not be stable at such high temperature. In fact, according to the calculations, the A2 phase transforms into σ phase at 887 ˚C for composition ACr1.5 and at 969 ˚C for composition AFe0.5 and the A2 and σ phases have very similar compositions. What is more, the data regarding phase stabilities of the Al-Co-$Cr_{1.5}$-Fe-Ni annealed specimen reported by Cieślak et al. [243] indicate that the A2 phase is stable at 1000 ˚C while the σ phase was not observed at such high temperature. Taking all of that into account it was assumed that the σ phase precipitated during cooling of the samples in the air.

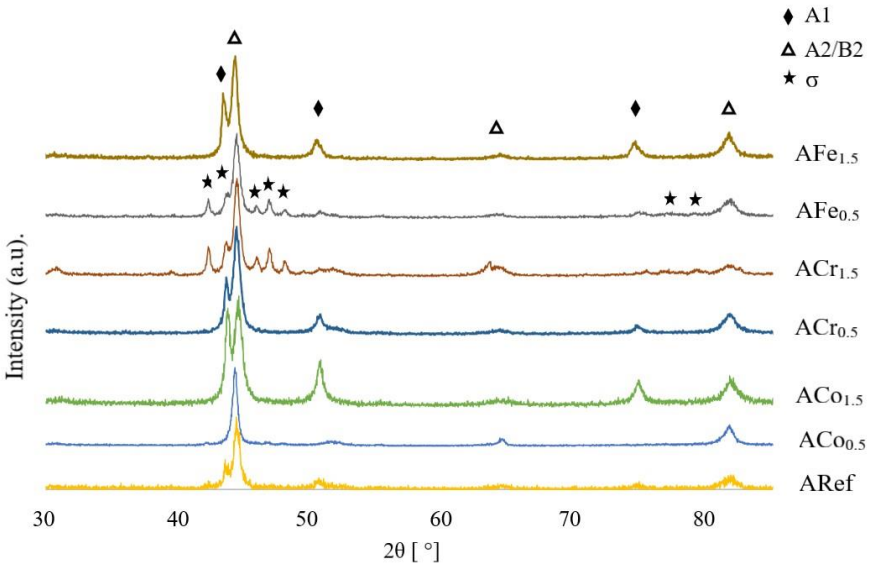

Fig 35 *XRD profiles of the samples annealed at 1050 ˚C for 2160 h*

Table 19 *Phase compositions (at%) measured by EDX point analysis.*

Sample	Phases identified using XRD	A1				A2				B2				σ			
		Al	Co	Cr	Fe	Al	Co	Cr	Fe	Al	Co	Cr	Fe	Al	Co	Cr	Fe
ARef	A1, A2, B2	5.6	23.8	28.3	29.2	2.0	16.6	49.2	28.2	32.3	18.9	7.2	12.5				
$ACo_{0.5}$	A2, B2					2.4	10.2	47.4	35.6	34.9	11.8	5.7	12.7				
$ACo_{1.5}$	A1, B2	5.6	30.1	28.2	24.1					31.5	23.5	8.4	11.3				
$ACr_{0.5}$	A1, B2	6.0	25.4	21.6	34.1					30.5	20.8	5.4	15.4				
$ACr_{1.5}$	A1, B2, σ	6.0	23.2	29.4	27.9					32.3	17.9	8.4	12.0	2.4	18.5	50.4	22.9
$AFe_{0.5}$	A1, B2, σ	6.1	29.0	30.0	15.5					33.4	19.6	8.0	7.7	2.7	23.6	52.7	13.7
$AFe_{1.5}$	A1, A2, B2	5.6	20.1	25.7	37.3	3.5	13.5	43.4	36.4	31.9	17.8	6.9	15.3				

4.3. Comparison with calculations

The presence of all phases observed in the samples have been correctly predicted by the calculations as it can be seen in Fig. 36, where the nominal compositions of the samples are marked in the calculated vertical sections $AlCo_xCrFeNi$, $AlCoCr_xFeNi$ and $AlCoCrFe_xNi$.

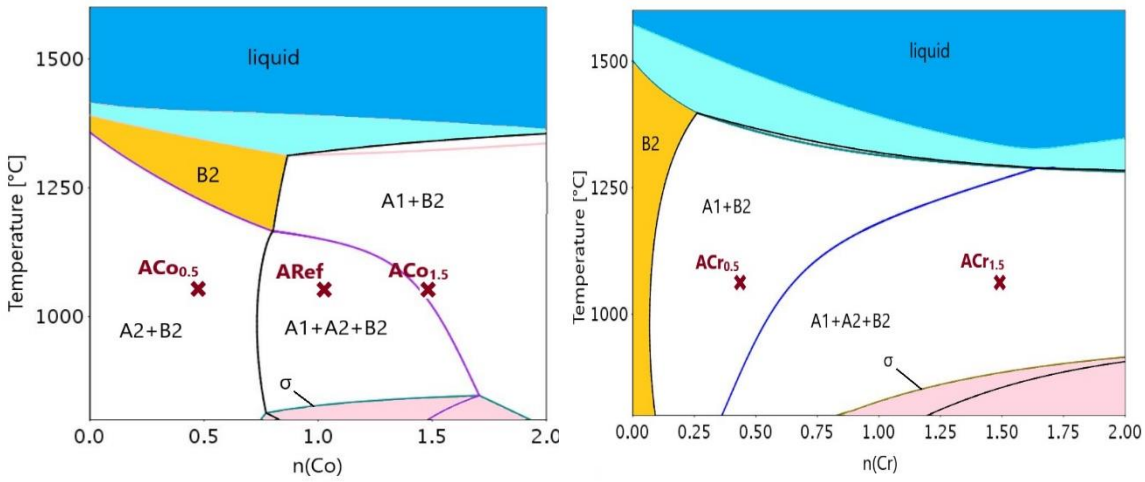

a) AlCoxCrFeNi **b)** AlCoCr$_x$FeNi

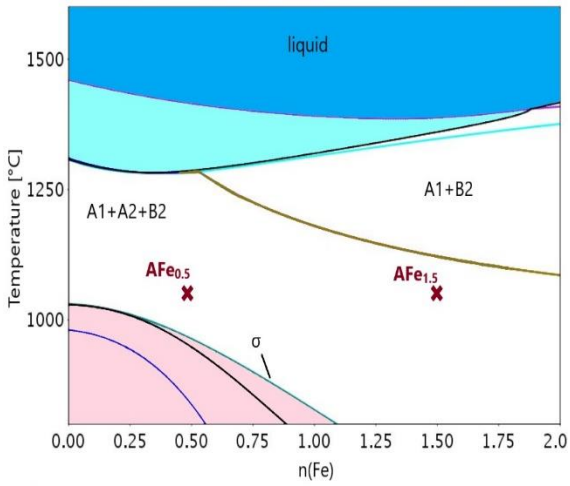

c) AlCoCrFe$_x$Ni.

Fig. 36 *Calculated vertical sections a) AlCoxCrFeNi, b) AlCoCr$_x$FeNi and c) AlCoCrFe$_x$Ni. The nominal compositions of the samples are added to the figures.*

At the beginning, the stability of the A2 phase was too low with respect to the experimental information, which required the addition of a metastable quaternary parameter: *G(A2,CO,CR,FE,NI:VA) = +482300-100*T*. As a consequence of the missing A2 phase, the mismatch between the calculated and measured composition of the B2 phase was quite high. Additionally, in order to improve the fit in the A1 phase composition the ternary A1 parameters were revised, in particular in the Al-Cr-Fe system. The corrections improved significantly the results. The experimentally measured average phase compositions reported in the previous sections are compared with the calculated values before (Calc1) and after the optimisation (Calc2) in Fig. 37 in order to check reliability of the multicomponent database. As mentioned before, the σ phase experimentally observed in the ACr1.5 and AFe0.5 samples has formed from the A2 phase during cooling in the air. Therefore, in Fig. 37 the experimentally determined compositions of the σ phase were compared with the calculated compositions of the A2 phase.

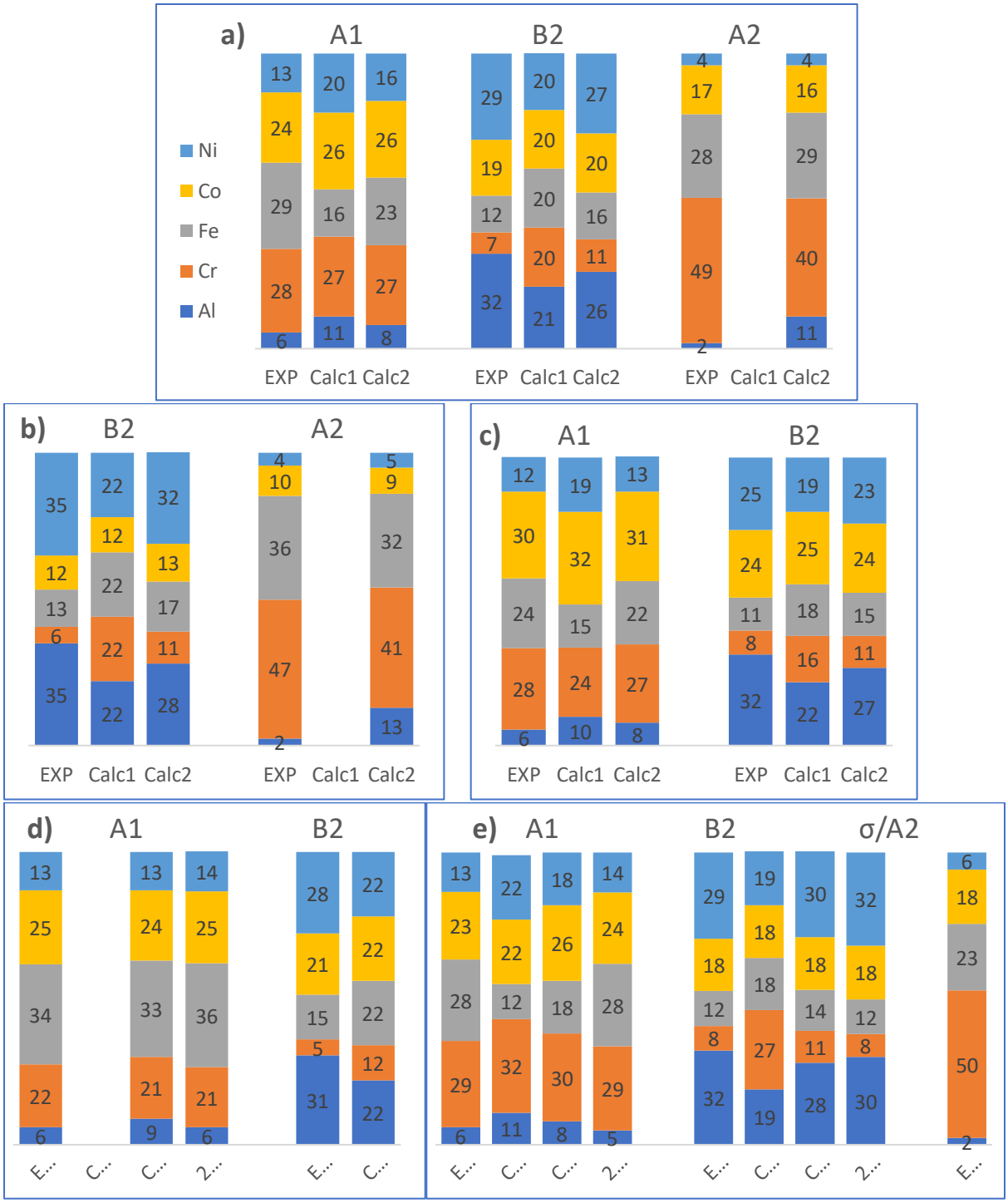
a)
A1
B2
A2
Ni
Co
Fe
Cr
Al
13 24 29 28 6
20 26 16 27 11
16 26 23 27 8
29 19 12 7 32
20 20 20 20 21
27 20 16 11 26
4 17 28 49 2
4 16 29 40 11
EXP Calc1 Calc2 EXP Calc1 Calc2 EXP Calc1 Calc2
b)
B2
A2
35 12 13 6 35
22 12 22 22 22
32 13 17 11 28
4 10 36 47 2
5 9 32 41 13
EXP Calc1 Calc2 EXP Calc1 Calc2
c)
A1
B2
12 30 24 28 6
19 32 15 24 10
13 31 22 27 8
25 24 11 8 32
19 25 18 16 22
23 24 15 11 27
EXP Calc1 Calc2 EXP Calc1 Calc2
d)
A1
B2
13 25 34 22 6
13 24 33 21 9
14 25 36 21 6
28 21 15 5 31
22 22 22 12 22
E... C... C... 2... E... C...
e)
A1
B2
σ/A2
13 23 28 29 6
22 22 12 32 11
18 26 18 30 8
14 24 28 29 5
29 18 12 8 32
19 18 18 27 19
30 18 14 11 28
32 18 12 8 30
6 18 23 50 2
E... C... C... 2... E... C... C... 2... E...

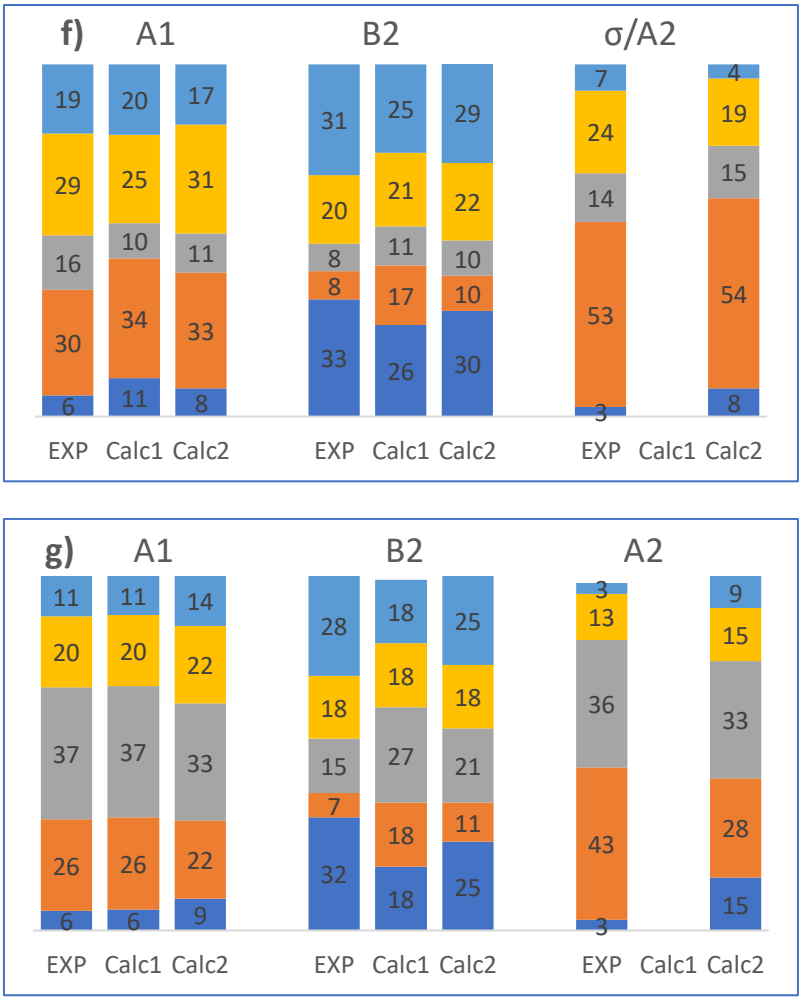

Fig. 37 *Experimentally obtained phase compositions of the samples a) ARef, b) $ACo_{0.5}$, c) $ACo_{1.5}$, d) $ACr_{0.5}$, e) $ACr_{1.5}$, f) $AFe_{0.5}$ and g) $AFe_{1.5}$ annealed at 1050 ˚C (EXP) compared with the calculated values before (Calc1) and after optimisation (Calc2).*

The overall agreement between the experimental and calculated data after the revision of the parameters is very good. The biggest discrepancy can be observed in the A2 phase, where the calculated amount of Al is significantly higher than the measured one.

The quantity of phases was determined from XRD profiles and SEM images. Micrographs were analysed with the freeware image processing programme ImageJ. Converting the image type to 8-bit and adjusting threshold allowed for the evaluation of the quantity of each phase. Such analysis gave preliminary information on phase quantities. However, it is important to underline, that it is linked to a large uncertainty. Firstly, the measurement registered in two dimensions not necessarily represents the volumetric values. Secondly, sometimes it was difficult to define the borders between different phases. It was especially the case when A2 phase was formed with intermediate colour, as it can be seen in Fig. 33 and Fig. 34. The quantitative analysis of the XRD profiles using Rietveld method allowed for obtaining the quantities of the identified phases, however, even this method has large uncertainty. The peaks related to the disordered and ordered bcc phases are overlapped making it difficult to evaluate the quantities of these phases correctly. For all these reasons, the quantities of A2 and B2 phases

are merged together and compared with the calculated values in Table 20.

Table 20 *Phase quantities experimentally obtained from micrographs (SEM) and from XRD profiles (XRD) compared with the calculated values (CALC).*

SAMPLE	**ARef**		**ACo$_{0.5}$**		**ACr$_{0.5}$**		**ACr$_{1.5}$**		**AFe$_{0.5}$**		**AFe$_{1.5}$**	
PHASE	**A1**	**A2+B2**	**A1**	**B2**	**A1**	**B2**	**A1**	**A2+B2**	**A1**	**A2+B2**	**A1**	**A2+B2**
SEM	*22*	*78*	*52*	*48*	*34*	*66*	*28*	*72*	*16*	*84*	*41*	*59*
XRD	*17.8*	*82.2*	*41.4*	*58.6*	*27.1*	*72.9*	*7.9*	*93.1*	*9.4*	*90.6*	*47.9*	*52.1*
CALC	*18*	*82*	*45.5*	*54.5*	*20.7*	*79.3*	*12.4*	*87.6*	*13.3*	*86.7*	*23*	*77*

5. Validation with the literature data

For the further verification of the database, the calculated values were compared with the chosen experimental data reported in the literature. The experimental data from the literature have been critically reviewed and carefully chosen for validation process, taking into account their reliability and usability. Due to the sluggish diffusion in HEAs it takes a long time to bring an alloy into equilibrium state, hence, many published results do not show the actual equilibrium compositions. The collected data were used to improve the quality of calculations by addition of parameters for metastable endmembers in lower order systems.

5.1. Al-Co-Cr-Fe-Ni

The Al-Co-Cr-Fe-Ni is the most frequently studied HEA. In 2009 Kao et al. [234] prepared a series of arc-melted samples with different Al content. They were annealed at 1100˚C for 24h and water quenched. The authors investigated the influence of Al on the microstructure of as-cast, annealed and deformed samples by means of SEM, EDS and XRD. The influence of Al was also studied by Chou et al. [235] in the same year. They prepared a series of AlxCoCrFeNi samples with x ranging from 0 to 2. They were kept at 1100 ˚C for 24h and water quenched. The present phases were identified using XRD measurement. Shun and Du [244] investigated samples with the $Al_{0.3}$CoCrFeNi composition by means of SEM, EDS and TEM techniques. The specimens underwent annealing at 700 and 900 ˚C for 72h and quenching in cold water. Wang et al. [237] examined the evolution of the structure of the AlxCoCrFeNi samples ($0<x<1.8$) using high temperature XRD, SEM and TEM. The samples for microstructural measurements were annealed at 900 and 1100 ˚C for 2h. Additionally, transition temperatures were determined by means of DTA. In 2015 Tang et al. [242] compared the microstructure and phase composition of as-cast samples and samples that underwent homogenizing treatment by applying hot isostatic pressure (HIP) and annealing at 1150˚C for 50h followed by cooling at 10˚C/min. The same fabrication method (HIP) was applied by Zhang et al. [239] at 1250 ˚C for 50h. Afterwards, the samples $Al_{0.3}$CoCrFeNi and $Al_{0.7}$CoCrFeNi were heat-treated at 700 and 1250 ˚C for 500 and 1000h, respectively. The present phases were analysed by means of XRD, SEM, EBSD, and APT techniques. Subsequently, Butler and Weaver [241] investigated the high temperature phases and compared the results with the predicted ones using the Thermo-Calc database TCNI8 [245]. A series of samples were annealed at 700 ˚C for 1000h and at 1050˚C for 520h, followed by water quenching. Rao et al. [240] studied 3 alloy compositions: $Al_{0.3}$CoCrFeNi, $Al_{0.5}$CoCrFeNi and $Al_{0.7}$CoCrFeNi by means of EBSD, TEM and APT. The samples were heated at 1250 ˚C for 50h followed by furnace cooling. The obtained data were compared with thermodynamic calculations in the same work. Wang et al. [246] examined the microstructure properties of the alloys with equimolar composition aged at 600, 800, 1000 and 1200 ˚C for 168h and water quenched. Sun et al. [247] prepared a set of samples with different Al to Co ratios. They were arc-melted, homogenized at 800˚C and 1000˚C for 30 days and quenched in cold water. Their phase constituents and microstructure were measured by SEM, EDS and XRD. A series of alloys with different Cr content were investigated by Cieslak et al.

[243]. They were prepared by two different synthesis methods: arc-melting and sintering from blended mixture of metallic powders. The first ones were then annealed at 1000˚C for 72h while the samples prepared from as-compacted metallic powder were annealed at the same temperature for 2 weeks. All samples underwent quenching. In addition to structural studies, the transition temperatures were identified using the Differential Scanning Calorimetry (DSC) technique. Stryzhyboroda et al. [248] investigated the transition temperatures of as-cast samples by means of DTA measurement with the heating rate of 20K/min. Additionally, the microstructural analysis was carried out on annealed samples by means of SEM equipped with EDS and EBSD detectors. Samples with different Al content were annealed at 1300, 1000 and 750 ˚C for 6, 24 and 48h, respectively. The summary of the annealing conditions applied by different authors is shown in Table 21.

Table 21 *Annealing and cooling conditions of Al-Co-Cr-Fe-Ni samples reported in the literature.*

Author	Annealing conditions	Cooling conditions
this work	1050˚C for 2160h	in the air
2009_Kao [234]	1100˚C for 24h	cold water
2009_Chou [235]	1100 ˚C for 24h	cold water
2009_Shun [244]	700 and 900 ˚C for 72h	cold water
2014_Wang [237]	900 and 1100 ˚C for 2h	cold water
2015_Tang [242]	1150˚C for 50h	10˚C/min
2016_Zhang [239]	700 ˚C for 500h 1250 ˚C for 1000h	
2017_Butler [241]	1050˚C for 520h	cold water
2017_Rao [240]	1250˚C for 50h	furnace cooling
2017_Wang [246]	800, 1000 and 1200 ˚C for 168h	cold water
2019_Sun[247]	800˚C for 720h 1000˚C for 720h	cold water
2019_Cieslak[243]	1000˚C for 336h	cold water
2020_ Stryzhyboroda [248]	750 ˚C for 48h 1000 ˚C for 24h 1300 ˚C for 6h	cold water

The average phase compositions measured in this work in the ARef sample with equimolar composition and the selected literature data for the equimolar AlCoCrFeNi alloy at the temperature ranging from 1000 to 1150˚C [234,241–243,247] are compared in Fig. 38 with the calculated values before (Calc1) and after (Calc2) the optimisation in order to check reliability of the multicomponent database.

The overall agreement between the experimental and calculated data for the AlCoCrFeNi composition after the revision of the parameters is very good. The biggest discrepancy can be observed in the A2 phase, where the calculated amount of Al is higher than the measured one.

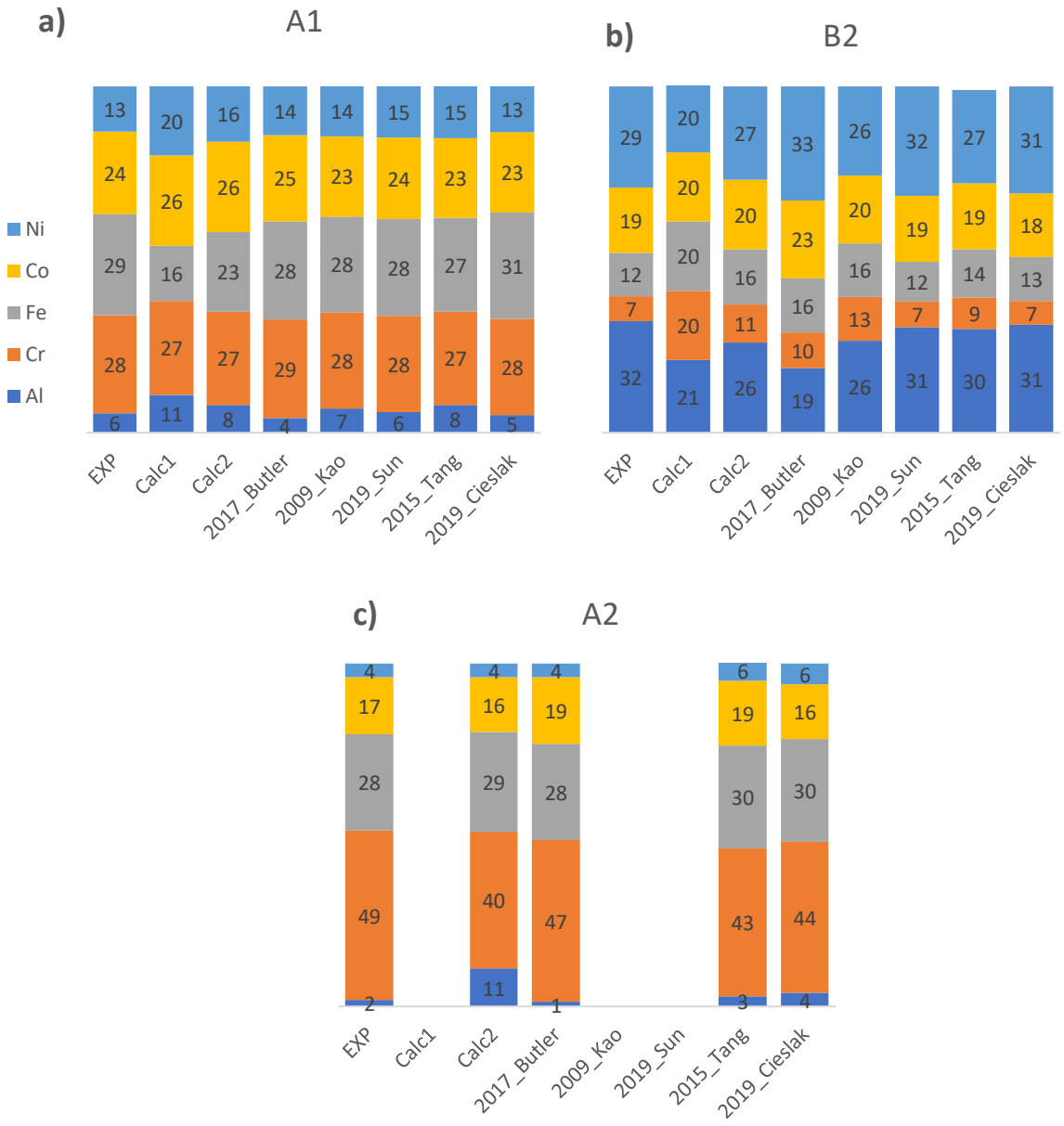

Fig. 38 *Experimentally obtained phase compositions in this work of the ARef sample annealed at 1050˚C (EXP) compared with the calculated values before (Calc1) and after optimisation (Calc2) and with various experimental results from the literature* [234,241–243,247] *for a) A1, b) B2 and c) A2 phase.*

The discrepancies between various authors may result from the fact that the samples were annealed at slightly different temperatures, as reported in Table 21 (between 1000 and 1150˚C). What is more, the annealing time varies significantly (from 24h to 720h). And finally, some sintered samples were quenched in cold water [234,241,243], whereas some were cooled at a control rate 10˚C/min [242] or in the air (this work). The A2 phase was not observed by some authors [234,247]. It can result from the fact that it is very difficult to distinguish between ordered and disordered bcc phases using only the XRD measurement, due to the vicinity of their peaks, especially, when the presence of the additional phase is not clear in the SEM images.

The influence of Al is presented in the calculated AlxCoCrFeNi vertical section (Fig. 39) with 0<x<2. The experimental datapoints are added. The data regarding stable phases were collected from several references [234,239–244,246–248], whereas the transformation temperatures were reported by Wang et al. [237] and Stryzhyboroda et al. [248]

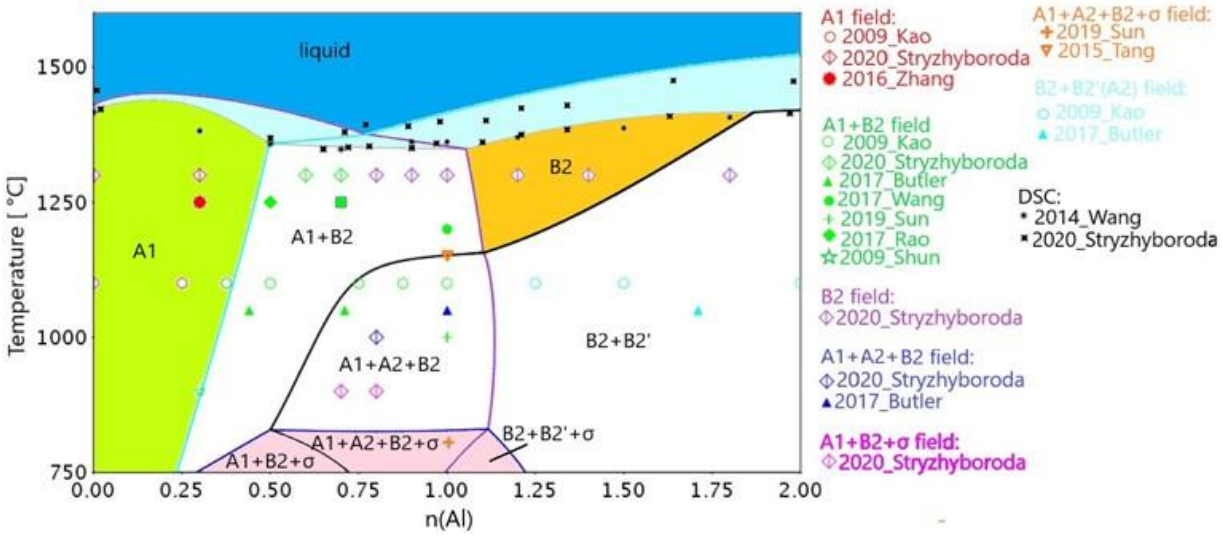

Fig. 39 *The calculated vertical section of the AlxCoCrFeNi system compared with the experimental data regarding stable phases* [234,235,237,239–243,247] *and solidus temperature* [237].

Some reported experimental results are not in agreement with each other. It is especially the case of the A2 and B2 phases. As already mentioned, this might be caused by the fact, that it is very difficult to correctly identify these phases using only the SED and XRD measurements. Additionally, Tang et al. [242] observed the σ phase at 1150 ˚C for the equimolar composition. It is highly unlikely that the σ phase stabilises at such high temperature in this quinary system and it is contrary to several other experimental data reported for this composition. The presence of the σ phase can be a result of the fact that the annealed samples were cooled at a controlled rate of 10˚C/min. During such slow cooling the phases that are stable at lower temperatures may precipitate. The σ phase was also observed in the $Al_{0.7}$CoCrFeNi and $Al_{0.8}$CoCrFeNi samples annealed at 900 ˚C by Stryzhyboroda et al. [248]. Additionally, the same authors report that a single phase B2 is stable at 1300 ˚C for the compositions above 0.8 mol Al, while according to our calculations the A1 phase is stable up to around 1.05 mol Al at that temperature. The solidus and liquidus temperatures measured by Stryzhyboroda et al. [248] and solidus temperatures reported by Wang et al. [237] are reproduced in a satisfactory way by the calculations, with the maximum difference of 40 ˚C.

5.2. Al-Co-Ni-W

Shiganawa et al. [249] investigated the phase equilibria between the A1 and $L1_2$ phases in the Al-Co-Ni-W system at 900˚C. They prepared a series of equilibrated alloys in the composition range: $Co\text{-}Ni_{0\text{-}80at\%}Al_{5.6\text{-}20at\%}W_{2.5\text{-}10at\%}$ which were annealed at 900˚C for 168h. The compositions of the A1 and $L1_2$ phases were examined by EPMA. Additionally, the phase transition temperatures were determined using Differential Scanning Calorimetry (DSC).

The calculated values of the solidus and $L1_2$ solvus temperatures for the $Co_{82.5-x}Al_{10}W_{7.5}Ni_x$ and $Co_{80-x}Al_{10}W_{10}Ni_x$ alloys were considerably higher than the experimentally measured by Shinagawa et al. [249]. In order to compensated the difference, the quaternary liquid and fcc parameters were inserted, namely: *G(liquid,Al,Co,Ni,W) = -120000* and G*(A1,Al,Co,Ni,W:Va) = -150000*. Furthermore, the value +135300-100*T was added to the ALCONIW function determining the relations between the parameters in the $L1_2$ phase introduced by Dupin and Sundman [106] are applied. These small modifications allowed to obtain much better agreement with the data from [249] as can be observed in Fig. 40.

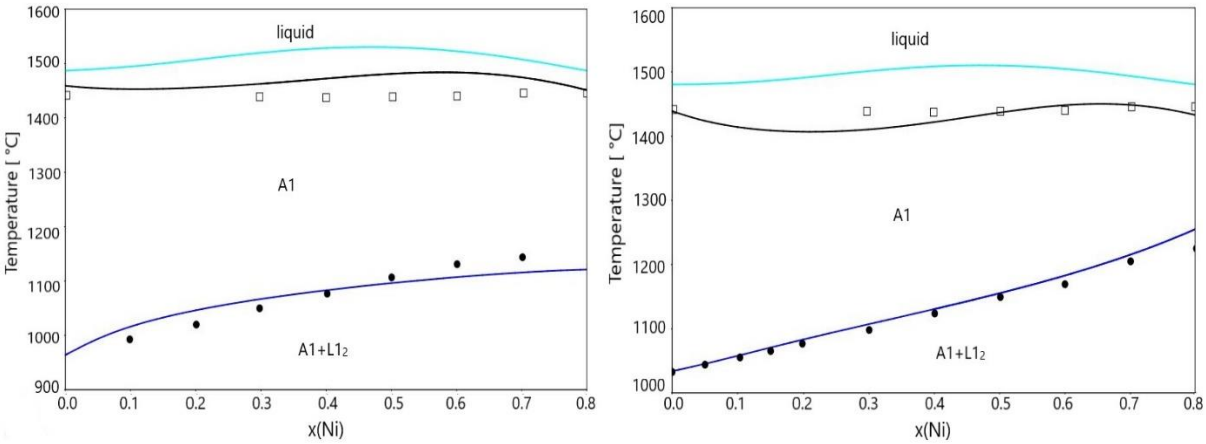

a) $Co_{82.5-x}Al_{10}W_{7.5}Ni_x$ **b)** $Co_{80-x}Al_{10}W_{10}Ni_x$

Fig. 40 *$L1_2$ solvus and solidus temperatures of the a) $Co_{82.5-x}Al_{10}W_{7.5}Ni_x$ and b) $Co_{80-x}Al_{10}W_{10}Ni_x$ alloys compared with the experimental data from* [249].

The compositions of the A1 and $L1_2$ phases of the $Co_{82.5-x}Al_{10}W_{7.5}Ni_x$ alloys calculated at 900˚C were compared with the experimentally measured compositions in Fig. 41. The data are in good agreement. The observations of Shinagawa et al. were confirmed by the calculations, Al has a tendency of concentrating in the $L1_2$ phase rather than in the A1 phase, and it is more evident when the Ni concentration is increasing.

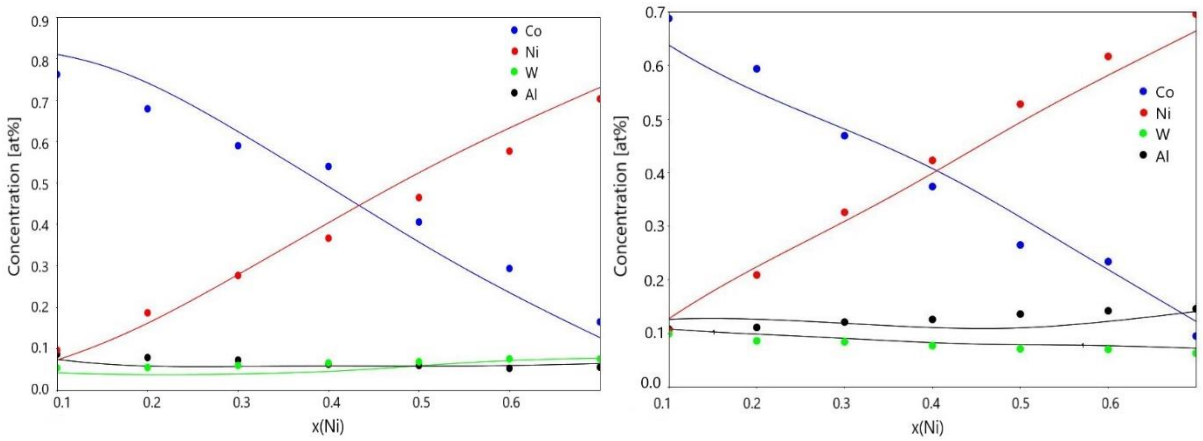

a) A1 **b)** $L1_2$

Fig. 41 *Variation of phase composition of the a) A1 and b) $L1_2$ phases in the alloys $Co_{82.5-x}Al_{10}W_{7.5}Ni_x$ at 900˚C compared with the experimental data from* [249].

5.3. Al-Cr-Mo-Ni

The experimental data regarding phase equilibria in the Al-Cr-Mo-Ni quaternary system is limited to the compositions rich in Ni (above 50 at%). Chakravorty and West [250] investigated alloys with 75at% Ni (A(75)1: $Ni_{75}Al_{20}Cr_{2.5}Mo_{2.5}$, A(75)2: $Ni_{75}Al_{15}Cr_5Mo_5$ and A(75)3 : $Ni_{75}Al_{10}Cr_{7.5}Mo_{7.5}$). The samples were annealed at 800, 1000 and 1250˚C for 168h followed by water quenching. The samples were then analysed by means of SEM and EDX. Based on the results the partial isothermal sections were constructed. Bursik and Svoboda [251] prepared samples with around 70 at% Ni. The samples annealed at 600 and 800˚C were analysed using SEM, TEM and EDX with focus on the formation of P and Ni_2Cr phases. Alloys containing 70 at% Ni with different (Mo+Cr)/Al and Mo/Cr ratios (A(70)1: $Ni_{70.3}Al_{2.1}Cr_{13}Mo_{14.6}$, A(70)2: $Ni_{71.3}Al_{4.1}Cr_{11.6}Mo_{12.7}$, A(70)3: $Ni_{71.2}Al_{6.3}Cr_{10.3}Mo_{12.2}$, A(70)4: $Ni_{71.2}Al_{11}Cr_{8.1}Mo_{9.7}$ and A(70)5: $Ni_{71.8}Al_{14.6}Cr_{6.5}Mo_{7.1}$) were also studied by Havrankova et al. [252] at 900˚C. In their work the measured phase compositions were compared with theoretical results. Chakravorty et al. determined partial isothermal sections at 50 and 60 at% Ni at 800, 1000 and 1250˚C [253,254]. The structural information of the samples (A(60)1: $Ni_{60}Al_{32}Cr_4Mo_4$, A(60)2: $Ni_{60}Al_{24}Cr_8Mo_8$, A(60)3: $Ni_{60}Al_{16}Cr_{12}Mo_{12}$, A(60)4: $Ni_{60}Al_8Cr_{16}Mo_{16}$ and A(50)1: $Ni_{50}Al_{10}Cr_{28}Mo_{12}$) was obtained by means of SEM, EDX, TEM and XRD.

The calculated phase compositions 900, 1000 and 1250˚C using the present multicomponent database are compared with the experimentally obtained values [250,252–254].
The comparisons are graphically shown in Fig. 42-Fig. 44 for samples where more than one phase is present.

5.3.1. Samples annealed at 1250˚C

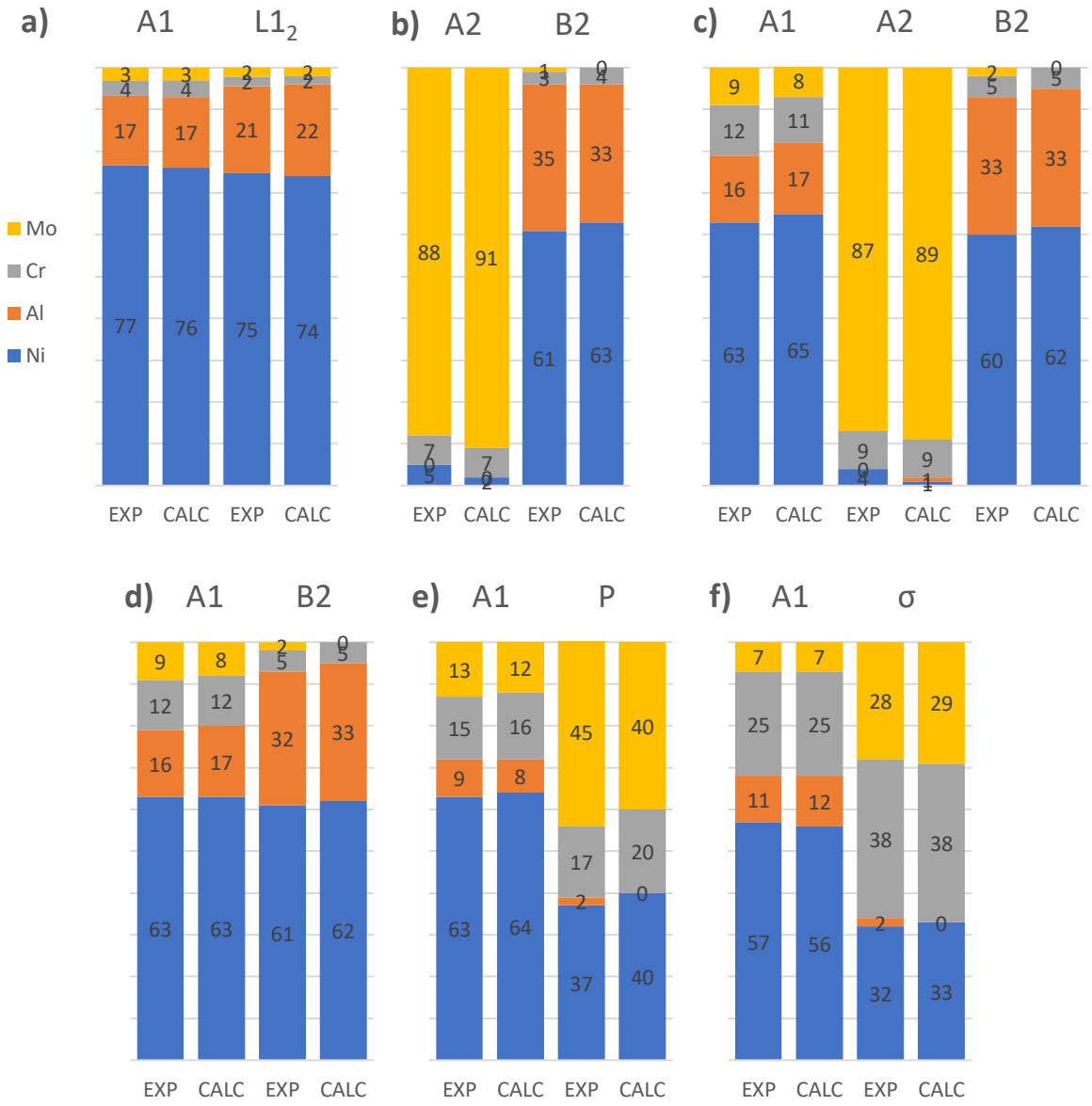

Fig. 42 *Phase composition measured experimentally (EXP) by* [250,253,254] *in samples (a) A(75)1, (b-e) A(60)1-4 and (f) A(50)1 annealed at 1250˚C compared with the calculated values (CALC) - see text for alloy compositions.*

A very good quantitative agreement has been obtained between experimental and theoretical values at 1250 ˚C. The only discrepancy is associated with the experimentally observed P phase in sample A(60)3 (Fig. 42d) whereas according to the calculations A2 phase resulted stable instead. The results are not shown for samples A(75)2 and A(75)3, where only A1 phase is present according to the calculations and experiments.

5.3.2. Samples annealed at 1000˚C

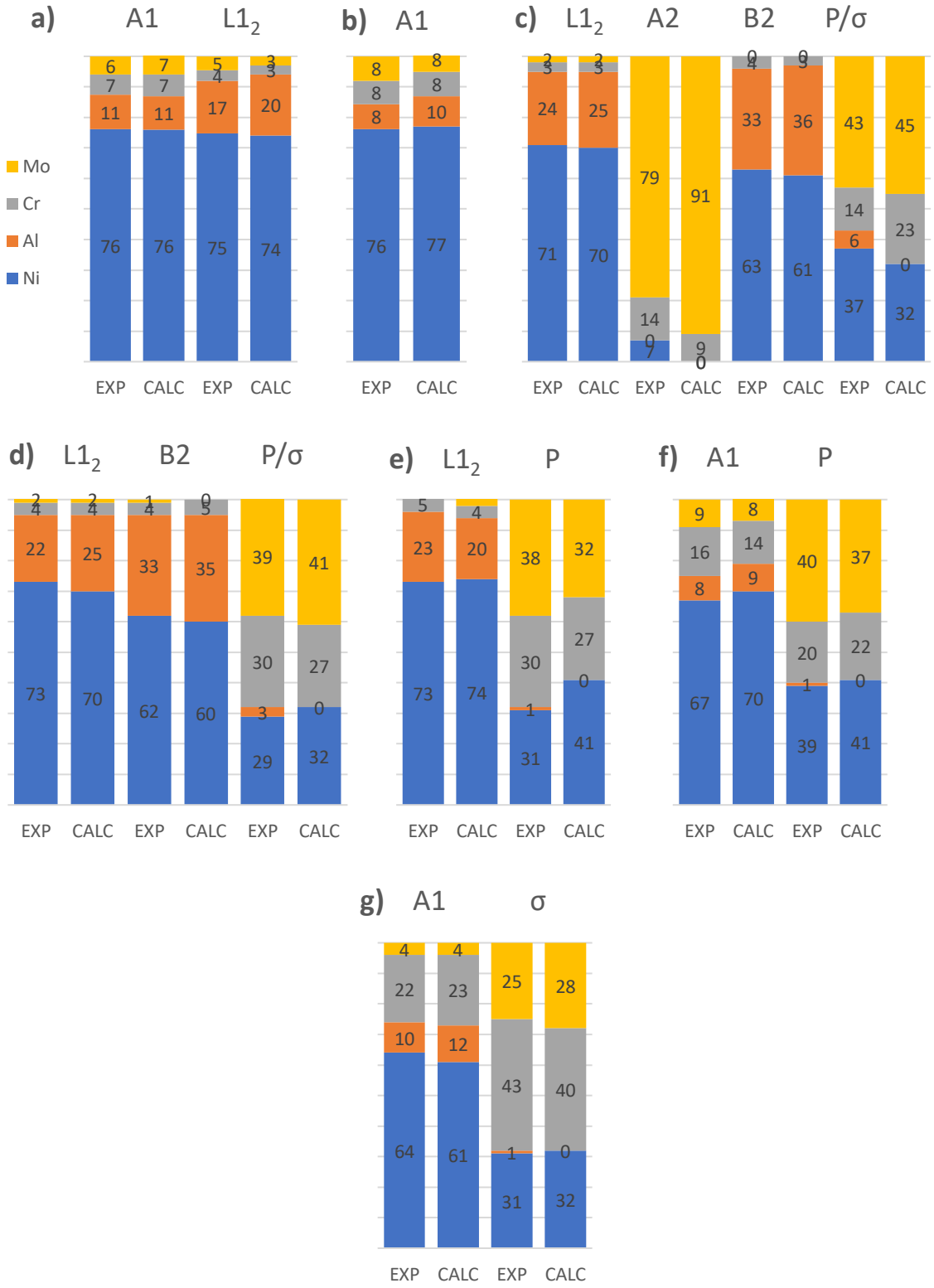

Fig. 43 *Phase composition measured experimentally (EXP) by* [250,253,254] *in samples (a) A(75)2, (b) A(75)3, (c-f) A(60)1-4 and (g) A(50)1 annealed at 1000˚C compared with the calculated values (CALC) - see text for alloy compositions.*

The presented experimetal phase compositions of samples annealed at 1000˚C show a general good agreement with these calculations. However, a few descrepancies have been noticed: in the sample A(75)3 (Fig. 43b), beside A1 phase also ordered $L1_2$ phase has been observed experimentally, which is not stable according to the present calculations.
In the A(60)1 sample (Fig. 43c) calculations indicate a significant higher amount of Mo in A2 phase. The experimentally measured P phase in samples A(60)1 and A(60)2 (Fig. 43c-d), has been identified as the σ phase in the calculations (with a very similar phase composition). The difference can result from the fact that during analysis of diffraction patterns it is very difficult to distinguish between peaks related to the P and σ phases, due to the high number of reflections and their possible overlapping. What is more, the additional $L1_2$ and B2 phases have been detected experimentally in the samples A(60)4 and A(50)1 (Fig. 43f-g), respectively. On the calculated phase diagrams their compositions are indeed placed in the vicinity of the fields where these phases are present, The presence of these phases in the samples can be related to the difference between the nominal and actual measured composition.
The results for the sample A(75)1 were not added, because only one phase – ordered fcc, has been detected for this composition in experimental measurements and in the calculations.

5.3.3. Samples annealed at 900˚C

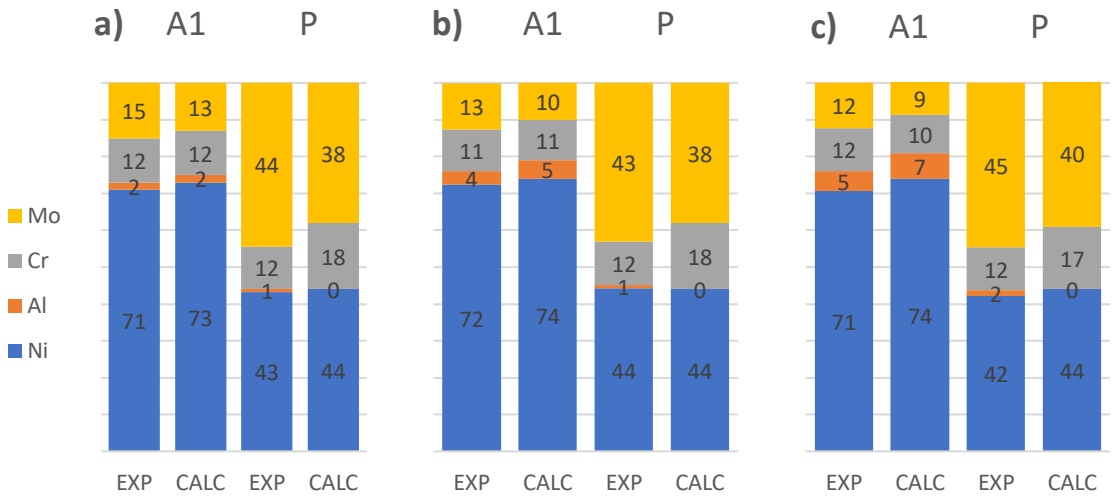

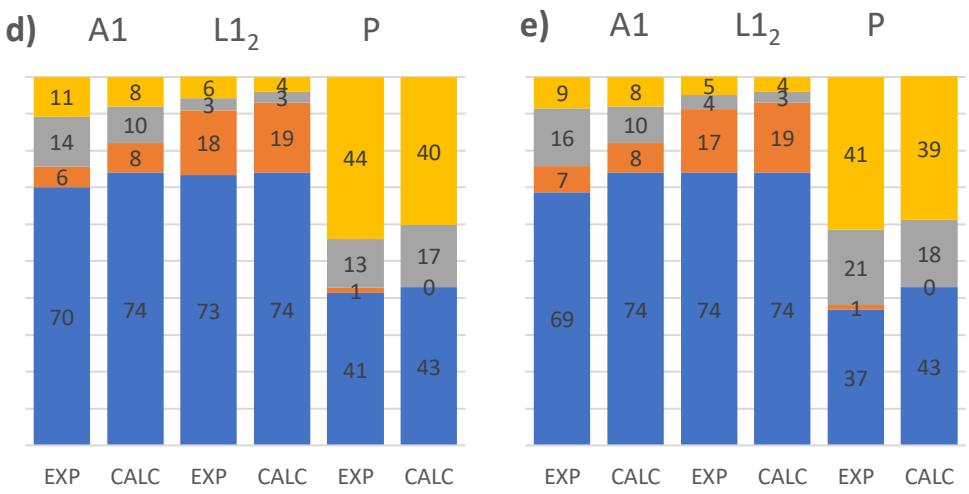

Fig. 44 *Phase composition measured experimentally (EXP) by Havrankova et al.* [252] *for A(70)1–5 (a-e) samples annealed at 900˚C compared with calculated values (CALC) - see text for alloy compositions.*

The overall good agreement has been obtained for experimentally measured and calculated phase compositions of the samples annealed at 900˚C. All phases detected experimentally have been reproduced by calculations with exception of the ordered $L1_2$ phase in the sample A(70)3. Similarly to the A(60)4 and A(50)1 samples, this composition is localised in the vicinity of the $L1_2$ field on the phase diagram and therefore the reason for this difference can be a small composition change during annealing process. With decreasing ratio (Mo+Cr)/Al (from Fig. 44a to e) the calculated amount of Cr in the A1 phase slightly decreases (from 12 to 10at%) whereas in the experimental measurements it increases (from 12 to 16at%).

A general tendency can be observed regarding the composition of P phase. The calculated amount of Mo is usually lower than experimentally observed, while the amount of Ni tends to be too high. However, in most of the cases the difference is not bigger than 5at%. Al has not been included in the present model, because this phase is not stable in any binary or ternary subsystem containing Al, nevertheless a small amount of Al (~1at%) has been detected in the P phase in different publications [251–254].

The primary solidification surface of NiAl-Cr-Mo system has been investigated by various authors [126,255–258]. Based on this data, Peng [126] optimised the liquid phase interaction parameter in Al-Cr-Mo in order to improve the liquid description in the quaternary system and reproduce available experimental data. Similar optimisation has been done in this work. The thermodynamic data regarding Al-Cr-Mo system are not available, therefore, the liquid interaction parameter has been optimised based purely on the quaternary data: *G(liquid,Al,Cr,Mo) = +40000*. The calculated partial liquidus surface of the NiAl-Cr-Mo system is shown in Fig. 45. The experimental data regarding primary phases and eutectic compositions [126,256–258] are added to the figure.

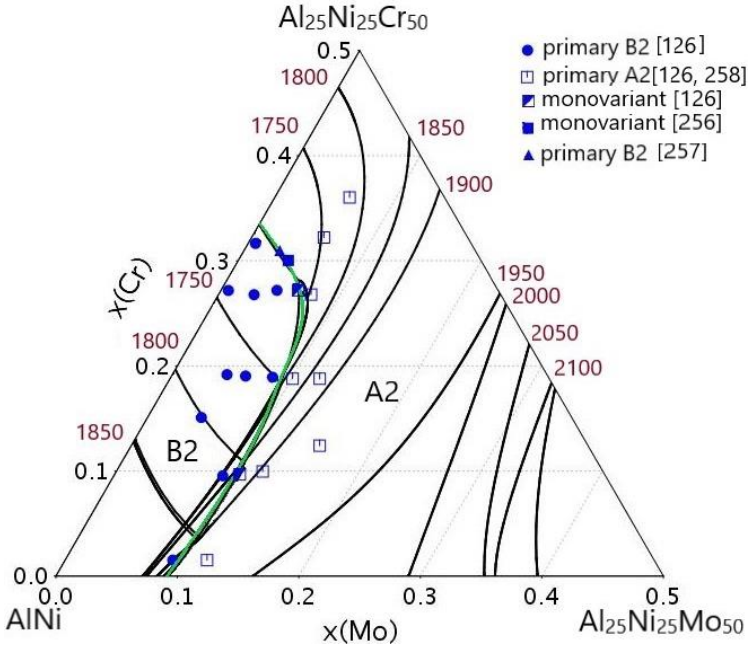

Fig. 45 *Partial liquidus surface of the AlNi-Mo-Cr system compared with the experimental data* [126,256–258].

5.4. Al-Cr-Ni-W

Chakravorty et al. [259] investigated the isothermal sections of the Al-Cr-Ni-W system at 75at% Ni. On this account, 4 samples with nominal compositions W1: $Ni_{75}Cr_{10}Al_{12.5}W_{2.5,}$ W2: $Ni_{75}Cr_4Al_{17}W_{4,}$ W3: $Ni_{75}Cr_{2.5}Al_{20}W_{2.5,}$ W4: $Ni_{75}Cr_{2.5}Al_{16.25}W_{6.25}$ were prepared and annealed at 800, 1000 and 1250 ˚C for 672, 1008 and 1344 h, respectively, followed by quenching in iced water. The structure of the annealed samples was examined by means of SEM and TEM, while the phase composition was measured with EPMA. The experimental information about the Al-Cr-Ni-W system was subsequently extended by the measurements of Bursik et al. [260]. They studied six quaternary compositions with around 70at% and 75at% Ni (M1: $Ni_{76.3}Cr_{7.3}Al_{15.6}W_{0.8,}$ M2: $Ni_{77.6}Cr_{3.1}Al_{17}W_{2.3,}$ M3: $Ni_{75.7}Cr_{4.3}Al_{15.6}W_{4.4,}$ M4: $Ni_{71.1}Cr_{12.5}Al_{14.5}W_{1.9,}$ M5: $Ni_{71.5}Cr_{8.7}Al_{16.7}W_{3.1,}$ M6: $Ni_{71.4}Cr_{4.6}Al_{16.4}W_{7.6}$). The samples were annealed at 900 and 1000 ˚C for 672 and 176 h, respectively. Their structure and phase compositions were reported.

The calculated phase compositions at 1250, 1000 and 900˚C using the present multicomponent database are compared with the experimentally obtained values [259,260]. The comparisons are graphically shown in Fig. 47, Fig. 49 and Fig. 51 for samples where more than one phase is present. Additionally, the isothermal sections were calculated for each temperature where the composition of each sample is shown (Fig. 46, Fig. 48, Fig. 50).

5.4.1. Samples annealed at 1250˚C

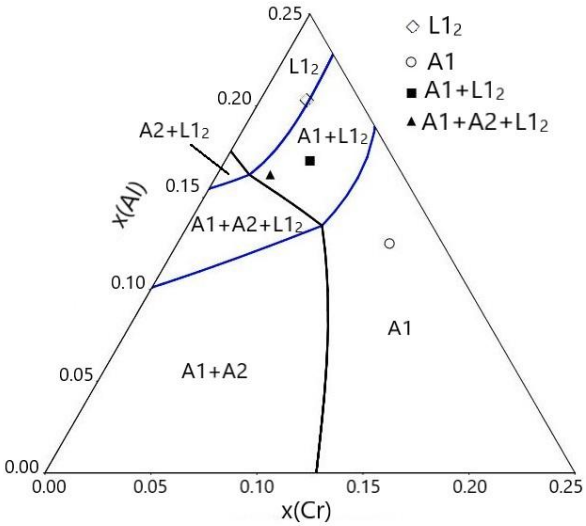

Fig. 46 *Isothermal section calculated at 75at%Ni at 1250˚C compared with the experimental data from* [259].

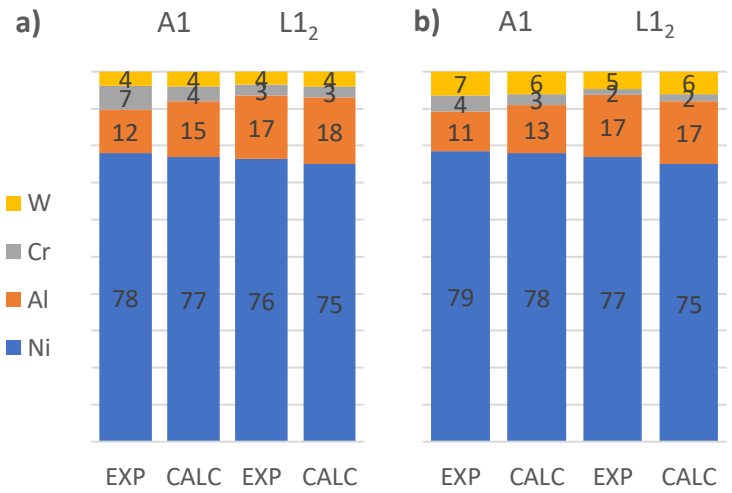

Fig. 47 *Phase composition measured experimentally (EXP) by Chakravorty et al.* [259] *for W2 (a) and W4 (b) samples annealed at 1250˚C compared with calculated values (CALC) - see text for alloy compositions.*

The stable phases were correctly predicted by calculations for samples W1-W3. In the sample W4, in addition to the $L1_2$ and A1 phases, also the A2 phase was experimentally observed, but did not result stable according to the calculations. The phase composition of ordered and disordered fcc phases ($L1_2$ and A1) are in agreement with the measured values.

5.4.2. Samples annealed at 1000˚C

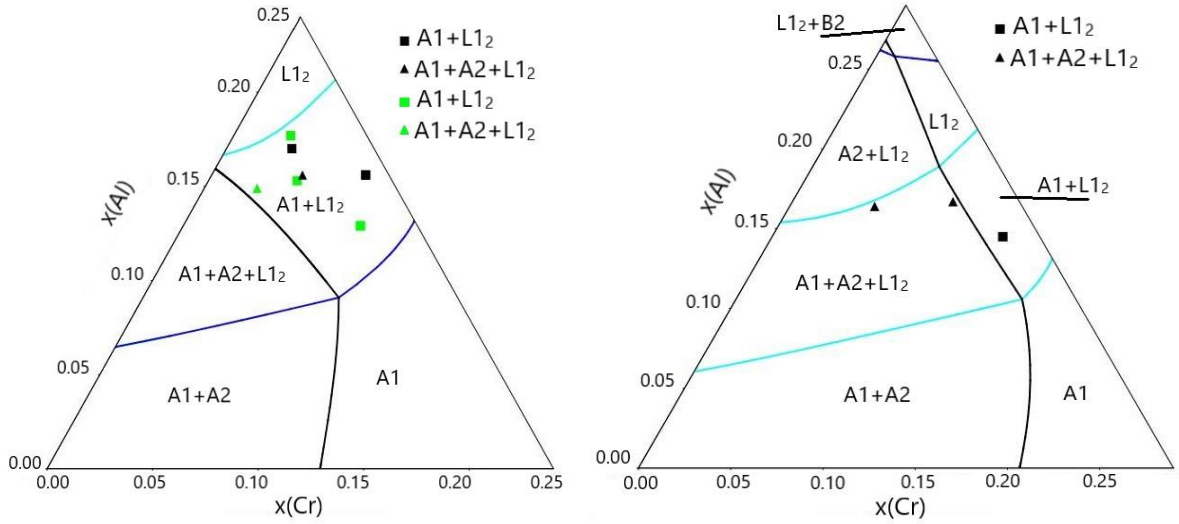

a) 76 at% Ni **b)** 71 at% Ni

Fig. 48 *Isothermal section calculated at 76 at% Ni (a) and 71 at% Ni (b) calculated at 1000˚C compared with the experimental data from* [259] *(green) and* [260]*(black).*

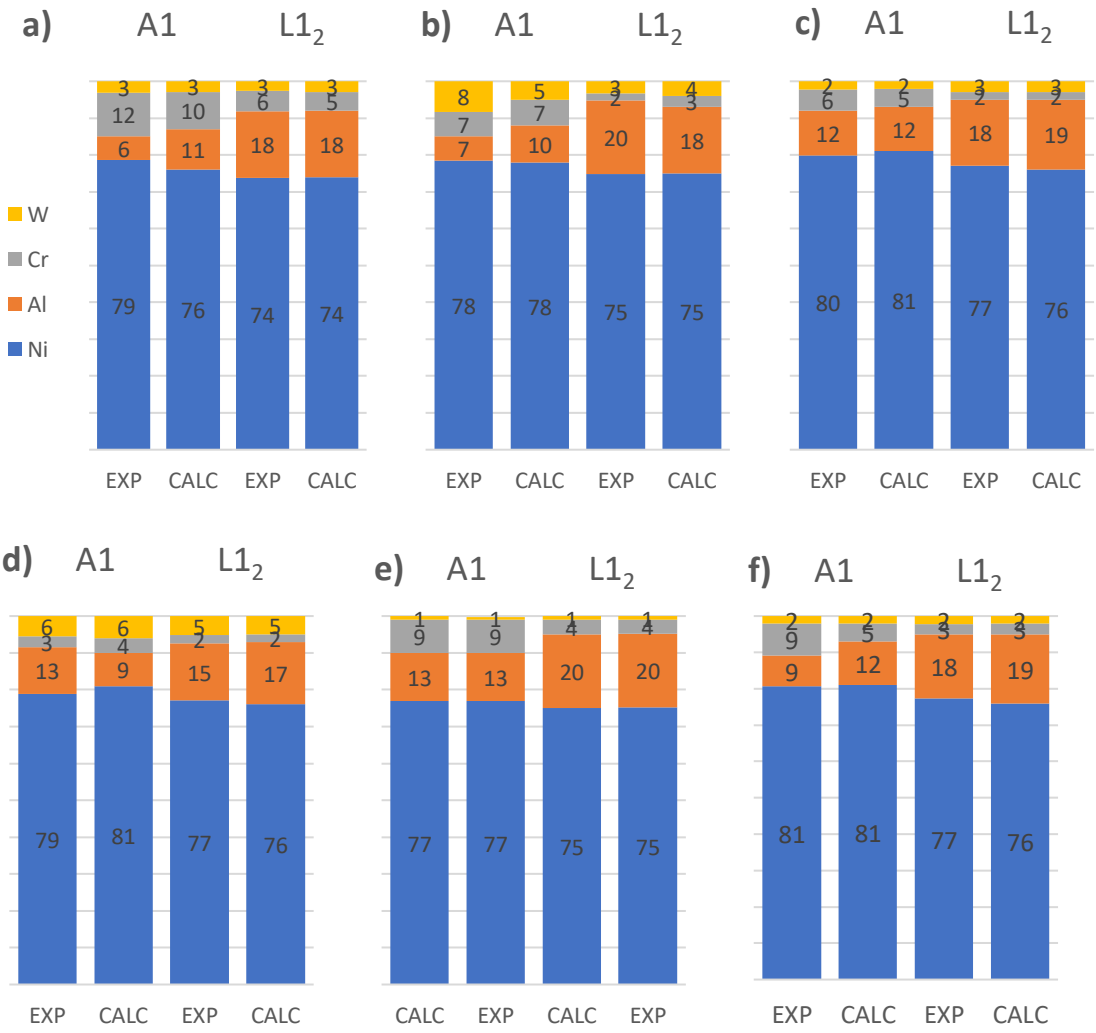

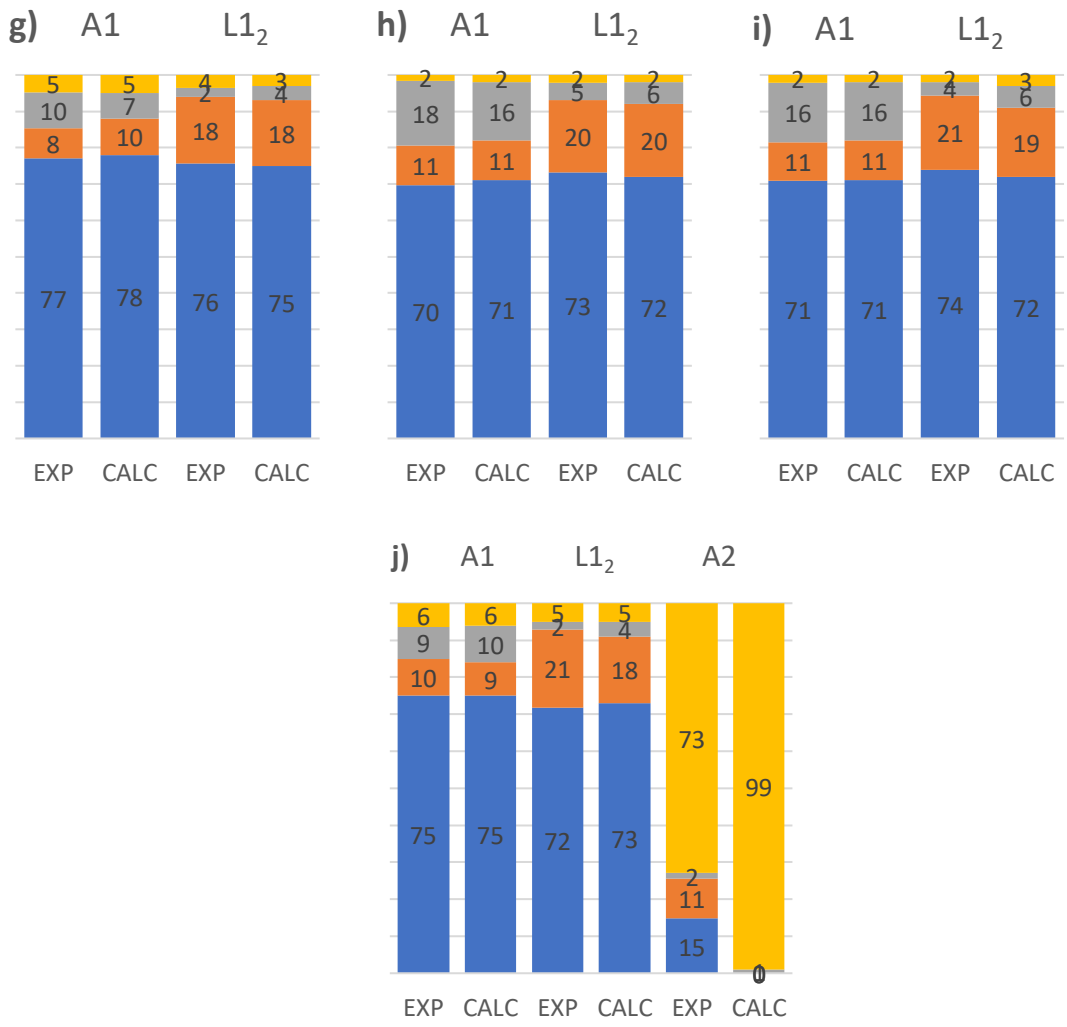

Fig. 49 *Phase composition measured experimentally (EXP) by Chakravorty et al.* [259] *for W1-W4 samples (a-d) and by Bursik et al.* [260] *for M1-M6 samples (e-j) annealed at 1000˚C compared with calculated values (CALC) - see text for alloy compositions.*

As it can be seen in Fig. 48, in case of 3 samples (W4, M3 and M5), the presence of the A2 phase was not predicted by the calculations. However, in the calculated isothermal sections the compositions of W4 and M5 samples are located very close to the field where the A2 phase is stable. The composition of the A2 phase in the M3 and M5 samples reported by Bursik et al. contains 70.1 and 21.4 at% Ni, respectively. Such high content of Ni in the A2 phase is very unlikely, taking into account that in the Ni-W binary system the A2 phase at 1000˚C contains only trace amount of Ni. What is more, the same authors report that the lattice parameter of the A2 phase is very close to that of αW. All of that indicates, that the data concerning A2 phase reported by Bursik et al. are not reliable. As expected, in the sample M6, where the presence of the A2 phases was correctly predicted, the phase composition differs considerably from the measured one. At the same time the calculated phase composition of ordered and disordered fcc phases ($L1_2$ and A1) are in agreement with the measured values.

5.4.3. Samples annealed at 900˚C

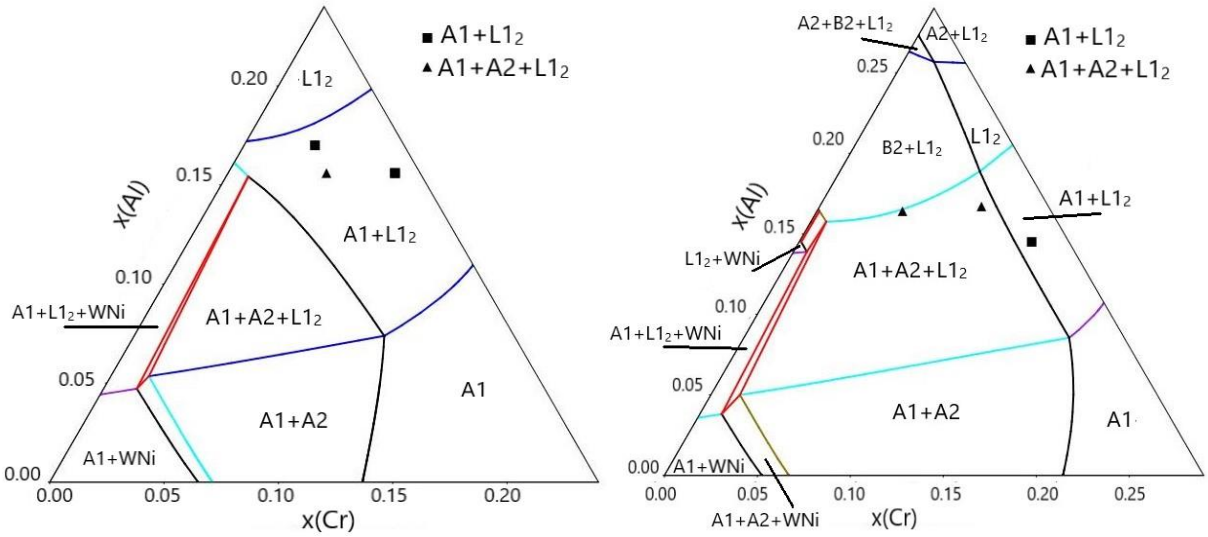

a) 76 at% Ni **b)** 71 at% Ni

Fig. 50 *Isothermal section calculated at a) 76 at% Ni and b) 71 at% Ni calculated at 900˚C compared with the experimental data from* [260].

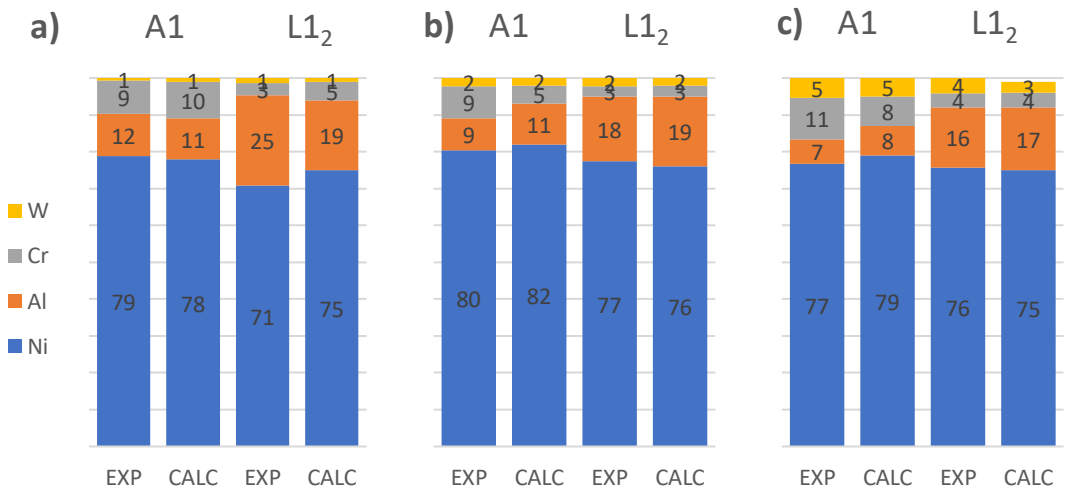

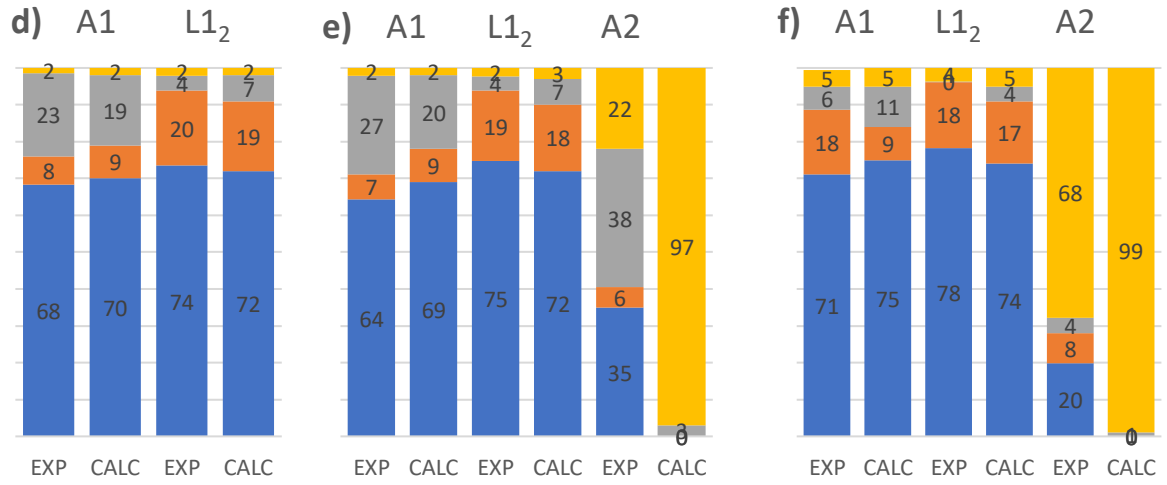

Fig. 51 *Phase composition measured experimentally (EXP) by Bursik et al.* [260] *for M1-M6 samples (a-f) annealed at 900˚C compared with calculated values (CALC) - see text for alloy compositions*

As shown in Fig. 50, the stable phases were correctly predicted by calculations, except for one sample – M3, for which the A2 phase did not result stable according to the calculations, but it was observed experimentally by Bursik et al. Additionally, as reported in Fig. 51e-f, the difference between experimentally measured (EXP) and calculated (CALC) phase compositions of the A2 phase is even more evident at 900˚C than at higher temperatures. As already noticed, such high content of Ni in the A2 phase (up to 35at%) determined by Bursik et al. is very improbable, therefore, the data regarding A2 phase are shown here for comparison, but they were not considered for revision of this system.

5.5. Cr-Fe-Mo-Ni

Yang et al. [101] investigated thermal stability of intermetallic phases, in particular the χ and C14 phases, in the Fe-rich Cr-Fe-Mo-Ni quaternary system. The samples $Fe_{69.75}Cr_{13.5}Mo_{7.75}Ni_9$ (C1) and $Fe_{63.25}Cr_{15}Mo_{8.75}Ni_{13}$ (C2) were annealed at 700, 850 and 1000˚C for 3795, 168 and 50 h, respectively. The samples were then investigated by SEM, EDX, XRD and TEM.
The calculated phase compositions using the present multicomponent database are compared with the experimentally obtained values [101] and shown in Fig. 52 and Fig. 53.

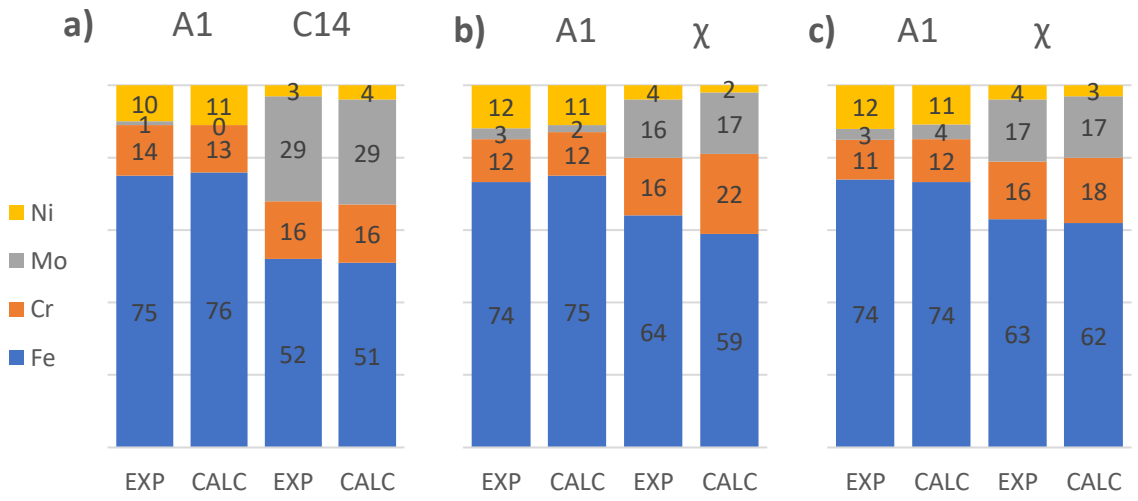

Fig. 52 *Phase compositions measured experimentally (EXP) by Yang et al.* [101] *for C1 sample annealed at a) 700, b) 850 and c) 1000˚C compared with calculated values (CALC).*

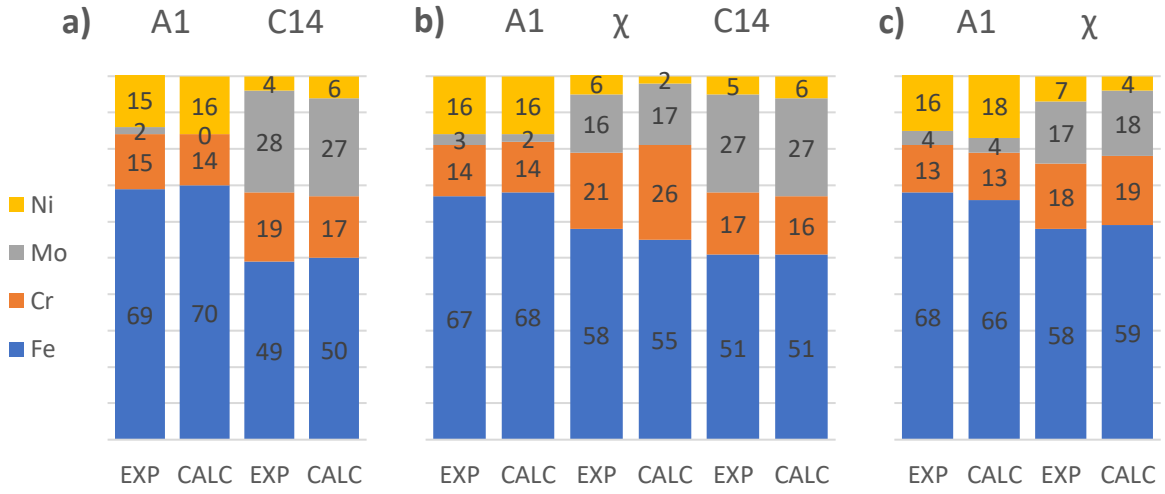

Fig. 53 *Phase compositions measured experimentally (EXP) by Yang et al.* [101] *for C2 sample annealed at a) 700, b) 850 and c) 1000˚C compared with calculated values (CALC).*

An overall good agreement has been obtained between experimental and calculated phase compositions. As shown in Fig. 54b and d, the C14 phase is stable at lower temperature and at around 800˚C it starts transforming into the χ phase. In fact, in C1 sample at 850˚C both phases C14 and χ resulted stable according to the calculations. Yang et al. noticed, that a weak XRD signal indicating the presence of C14 phase might be present, however, the volume fraction of the phase was too small to be detected, therefore the phase composition of the C14 could not be compared with the experimental results.

At the beginning μ and σ phases resulted too stable at the expense of χ and C14 phases (Fig. 54a and c), which created a need for revision of metastable parameters in the latter phases. The metastable end-member parameters describing χ phase were inserted in several binary and

ternary subsystems, namely Cr-Mo, Cr-Ni, Fe-Ni, Mo-Ni, Cr-Fe-Ni, Cr-Mo-Ni and Fe-Mo-Ni, whereas the metastable parameters related to the C14 phase were added to the binary systems: Cr-Fe, Cr-Mo, Cr-Ni, Fe-Ni and Mo-Ni.

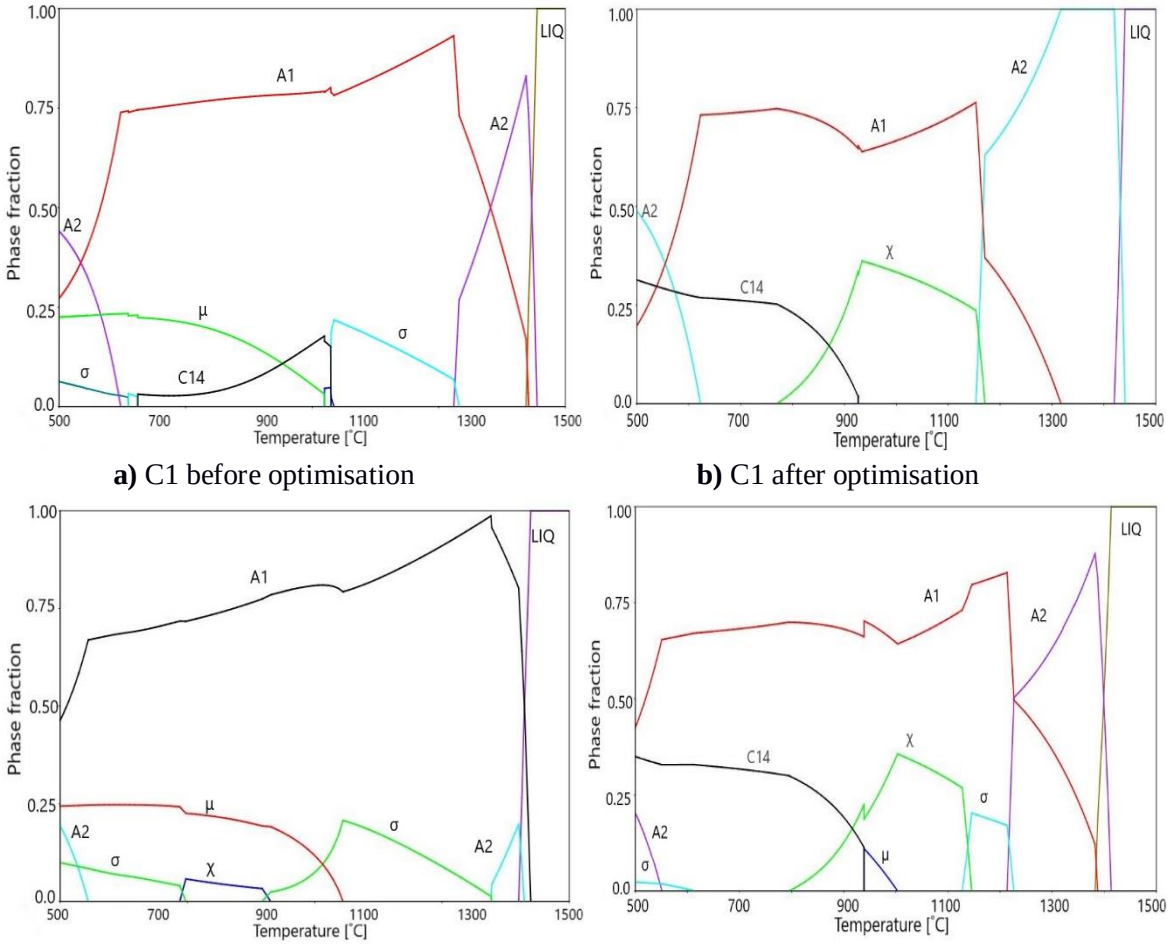

a) C1 before optimisation

b) C1 after optimisation

c) C2 before optimisation

d) C2 after optimisation

Fig. 54 *Calculated phase fractions as a function of temperature for a) C1 sample before optimisation, b) C1 sample after optimisation, c) C2 sample before optimisation and d) C2 sample after optimisation (see text for alloy compositions).*

6. Predictions in multi-component systems

In the previous chapter, the reliability of the present database have been verified with my own experiments and with the data reported in the critically selected literature. An overall good agreement between the measured and calculated compositional data have been obtained in case of the multicomponent systems containing Mo and W. The systems containing Ta could not be verified, due to the very scarce experimental information regarding multicomponent as well as ternary systems containing Ta. As many authors reported, a small addition of refractory metals to the alloys containing 3d metals can be beneficial for their mechanical properties, such as Vickers hardness and yield strength. In the present chapter, the effect of refractory metals on the phase stabilities in the Al-Co-Cr-Fe-Ni-X system (X=Mo, Ta or W) is analysed by means of CALPHAD simulations using the database developed in this work.

6.1. The influence of Mo

The isopleth of the $AlCoCrFeNiMo_x$ system is shown in Fig. 55. As it can be seen, both solidus and liquidus temperatures are slightly decreasing with increasing amount of Mo. Liquidus temperature drops from 1395 ˚C for the AlCoCrFeNi composition down to 1310˚C for AlCoCrFeMoNi, while the solidus temperature drops from 1302 to 1250˚C. Mo is a bcc former, it increases the stability range of the A2 phase and destabilizes the A1 phase, which disappears after an addition of 0.14 mol of Mo. The B2 is the primary phase in the whole composition range. As expected, the addition of Mo stabilizes the σ phase. It results stable up to the solidus temperature after addition of around 0.4 mol of Mo. It is rich in Mo and Cr. The other phase that is clearly stabilized by Mo is the μ phase. It forms at lower temperature and its stability reaches the maximum temperature for an equimolar composition (940 ˚C).

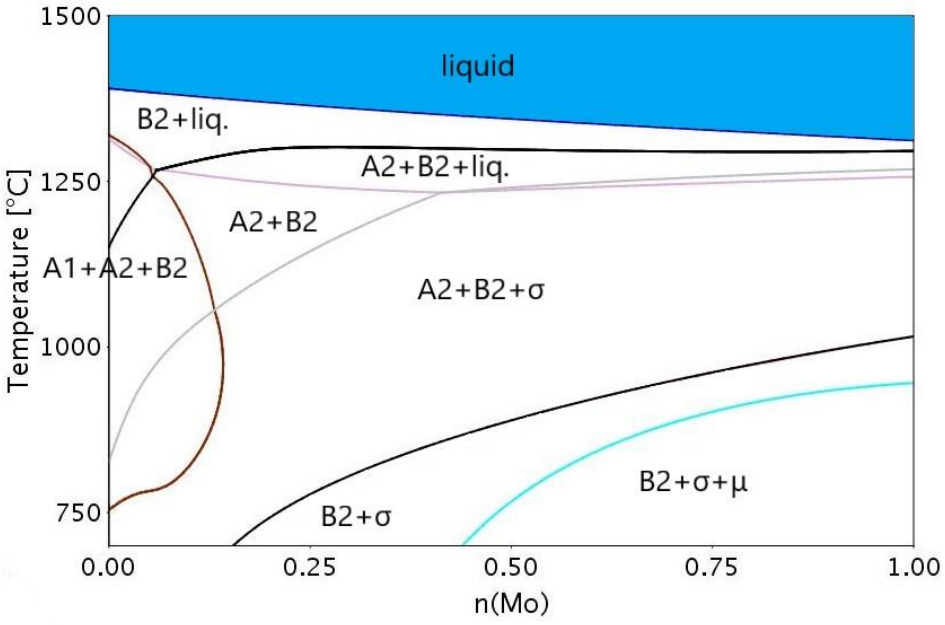

Fig. 55 *Isopleth showing the effect of Mo addition to the AlCoCrFeNi alloy calculated with the database developed in the present work.*

The formation of intermetallic phases such as the σ and μ phases is detrimental for the mechanical properties, therefore, it should be avoided, if application requires high strength. In Fig. 55 it can be seen that even a very small addition of Mo to the AlCoCrFeNi equimolar alloy, enhances the formation of the σ phase at high temperatures. In order to suppress the formation of the σ phase, the amount of other elements can be adjusted. An increase of the stability of bcc phases over the intermetallic phases can be achieved by increasing the amount of the bcc phase former such as Al. In Fig. 56 the phase stabilities are calculated as a function of Al:Mo ratio and the temperature.

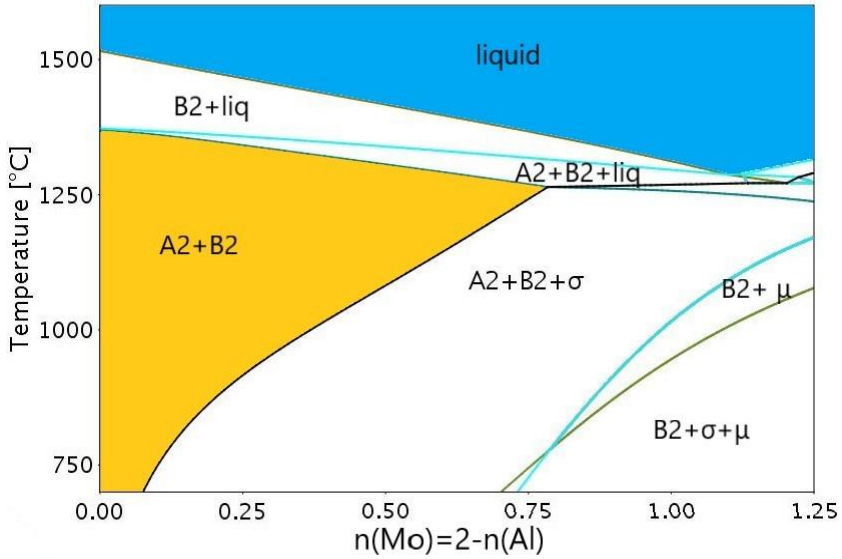

Fig. 56 *Isopleth of the $Al_{(2-x)}CoCrFeMo_xNi$ system calculated with the database developed in the present work.*

Indeed, it can be seen that in the Mo-free side only two bcc phases are stable (A2+B2) and after addition of around 0.25 mol of Mo, the σ phase precipitates at around 900 ˚C. The phase fractions as a function of temperature were analysed in Fig. 57 for 4 different compositions of the $Al_{(2-x)}CoCrFeMo_xNi$ alloys (x=0.1, 0.25, 0.4 and 0.55).

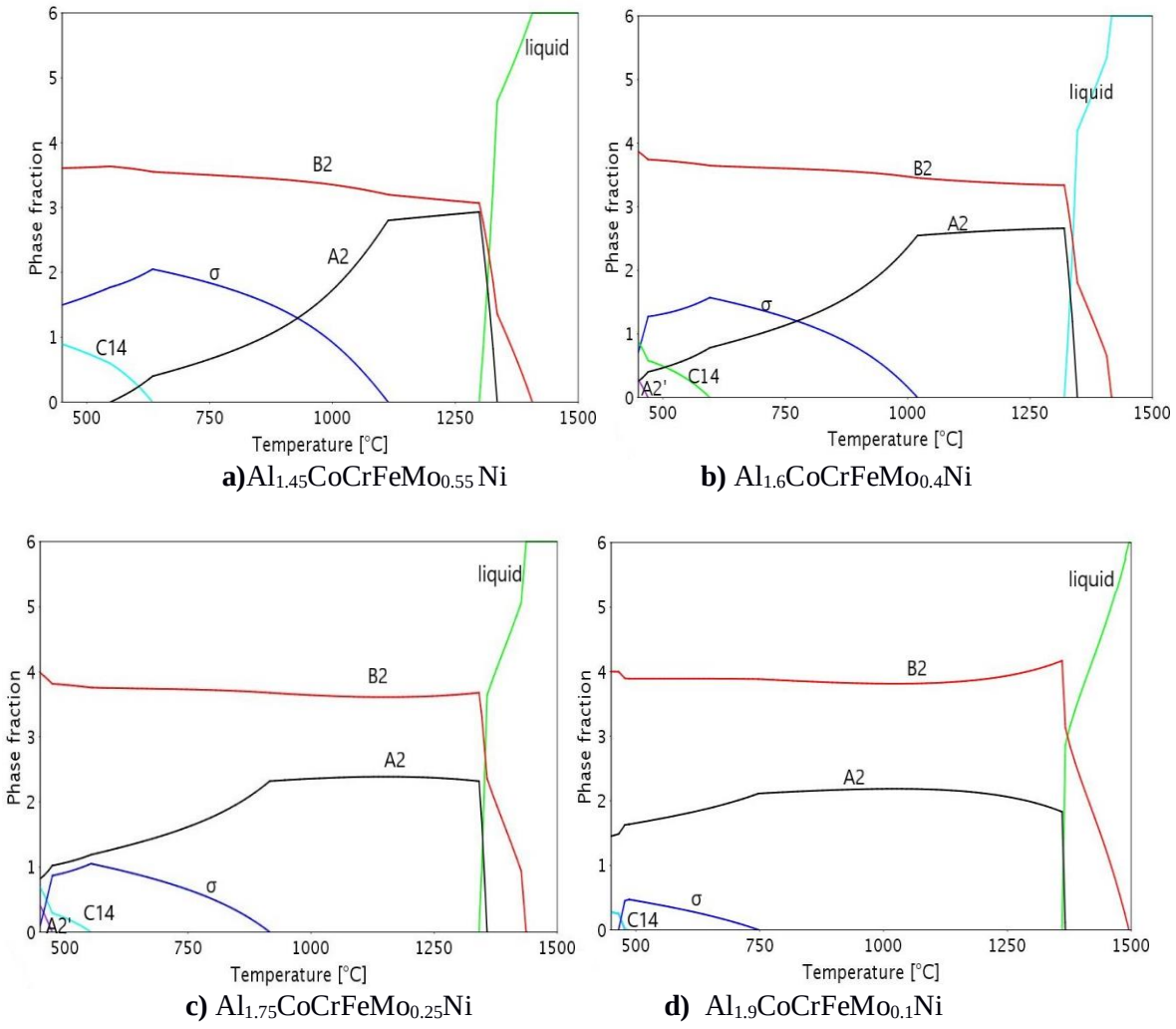

a) $Al_{1.45}CoCrFeMo_{0.55}Ni$ **b)** $Al_{1.6}CoCrFeMo_{0.4}Ni$

c) $Al_{1.75}CoCrFeMo_{0.25}Ni$ **d)** $Al_{1.9}CoCrFeMo_{0.1}Ni$

Fig. 57 Phase fractions as a function of the temperature for a)$Al_{1.45}CoCrFeMo_{0.55}Ni$, b)$Al_{1.6}CoCrFeMo_{0.4}Ni$, c) $Al_{1.75}CoCrFeMo_{0.25}Ni$ and d) $Al_{1.9}CoCrFeMo_{0.1}Ni$ calculated with the database developed in the present work.

Fig. 57 confirmed that the increasing ratio Al:Mo suppresses the formation of the σ phase at elevated temperature. For n(Mo)=0.55 and n(Al)=1.45 it is stable up to around 1120 ˚C , while for n(Mo)=.1 and n(Al)=1.9 it is stable up to 750 ˚C. It is important to notice, that not only the temperature range, but also the molar fraction of the σ phase is significantly decreased. The other observation is the increase of the solidus temperature by around 100 ˚C. Below the solidus temperature, two bcc phases are stable, A2 and B2. With the increase amount of Al, the amount of the latter phase increases. In Fig. 57a the amount of both phases is more or less equal, while in Fig. 57d. the amount of B2 phase is almost twice as high as the A2 phase.

As it can be seen in Fig. 55, if the amount of Mo is kept below 0.1 mol the formation of the σ phase is supressed above 1000 ˚C. In Fig. 58. the effect of other elements such as Co, Fe and

Ni on the phase equilibria in the alloys containing 0.1 mol of Mo is shown and compared with the isopleths calculated for the alloys without Mo.

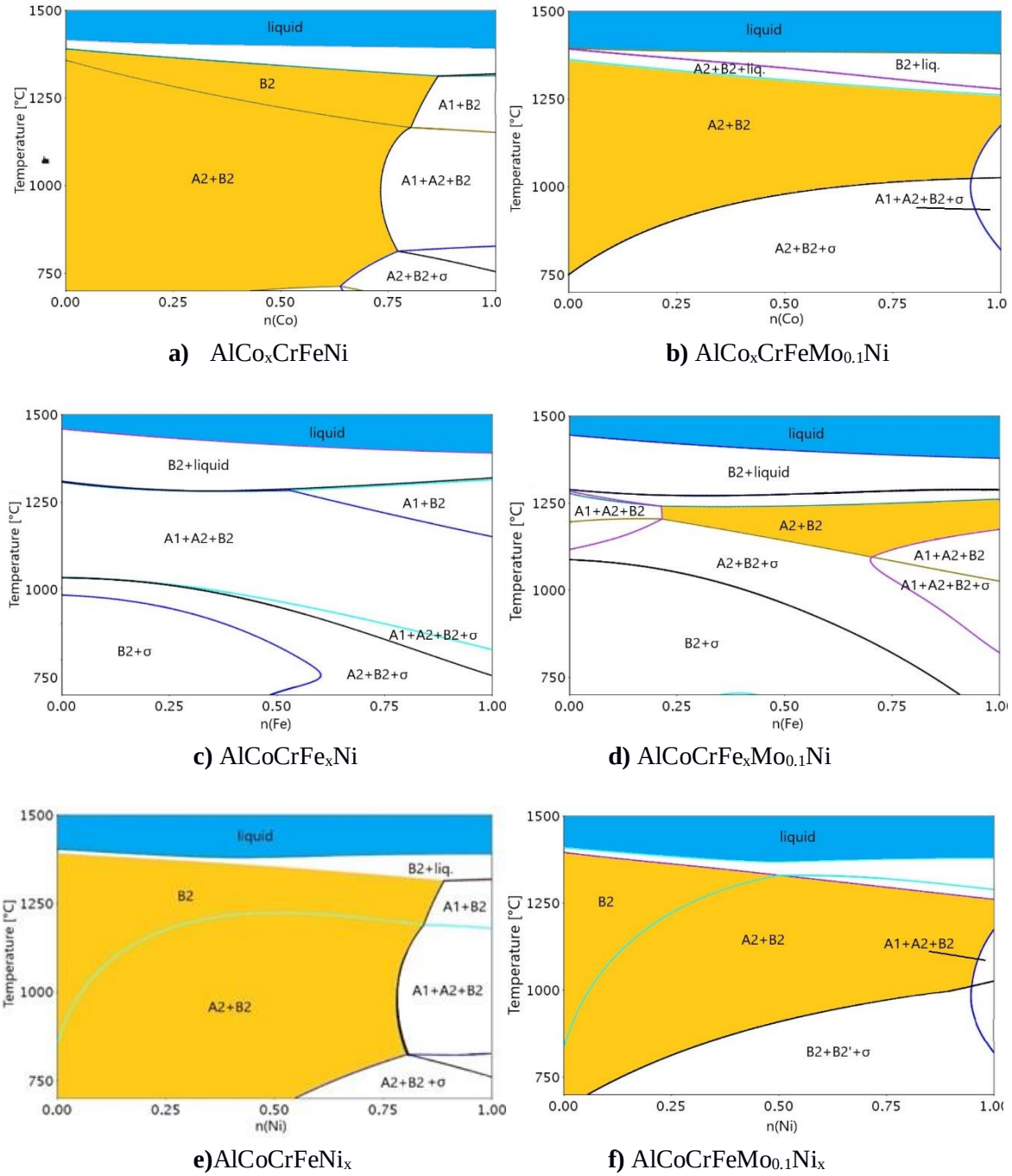

a) $AlCo_xCrFeNi$ **b)** $AlCo_xCrFeMo_{0.1}Ni$

c) $AlCoCrFe_xNi$ **d)** $AlCoCrFe_xMo_{0.1}Ni$

e) $AlCoCrFeNi_x$ **f)** $AlCoCrFeMo_{0.1}Ni_x$

Fig. 58 *Isopleths in the Al-Co-Cr-Fe-Ni (a, c, e) and Al-Co-Cr-Fe-Mo-Ni (b, d, f) systems: a) $AlCo_xCrFeNi$, b) $AlCo_xCrFeMo_{0.1}Ni$, c) $AlCoCrFe_xNi$, d) $AlCoCrFe_xMo_{0.1}Ni$, e) $AlCoCrFeNi_x$ and f) $AlCoCrFeMo_{0.1}Ni_x$ calculated using the database developed in the present work.*

The addition of 0.1 mol of Mo destabilizes the A1 phase, extending the B2 and A2+B2 homogeneity range. In all cases the B2 phase solidifies directly from the liquid in the whole composition range. When Mo is added, the A2 phase results stable up to much higher

temperature. Additionally, in the alloys with 0.1 mol of Mo (Fig. 58 b, d and f) the σ phase precipitates at temperatures around 150 ˚C higher with respect to the alloys without Mo (Fig. 58 a, c and e). In general the addition of Co, Fe and Ni do not have any significant effect on the liquidus temperature.

Fig. 59 shows isothermal sections calculated at 1000 ˚C around the equimolar composition AlCoCrFeMoNi, as a function of the molar amount of Mo and one of the other four elements Co, Cr, Fe, Ni.

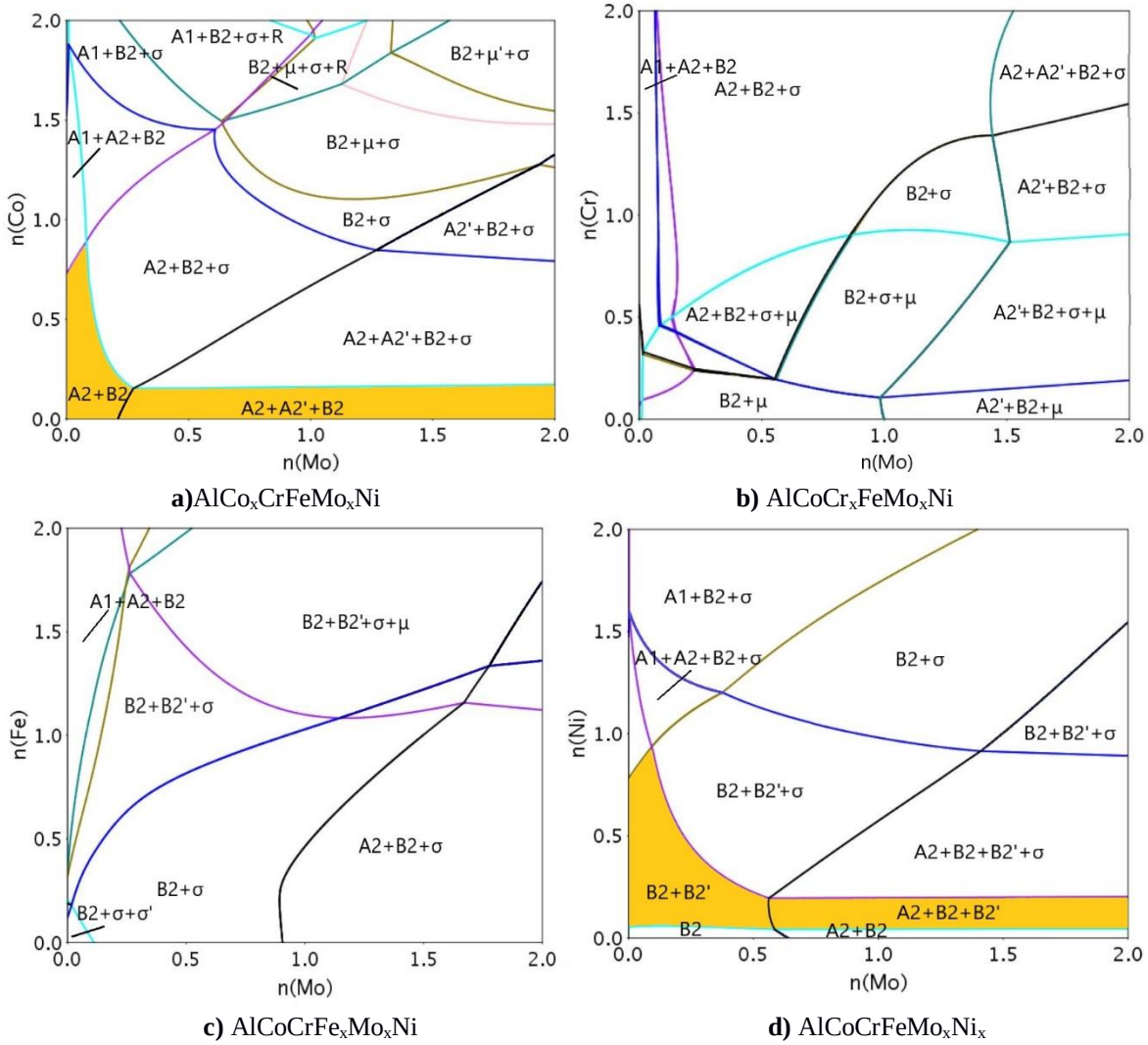

a) $AlCo_xCrFeMo_xNi$ **b)** $AlCoCr_xFeMo_xNi$

c) $AlCoCrFe_xMo_xNi$ **d)** $AlCoCrFeMo_xNi_x$

Fig. 59 *Al-Co-Cr-Fe-Ni isothermal sections calculated at 1000˚C around the equimolar composition as a function of the molar amounts of Mo and a second element: a) $AlCo_xCrFeMo_xNi$, b) $AlCoCr_xFeMo_xNi$, c) $AlCoCrFe_xMo_xNi$ and d) $AlCoCrFeMo_xNi_x$*

It can be seen that even a very small addition of Mo stabilizes the σ phase. It can be supressed by decreasing the amount of Co (<0.15 mol) or Ni (<0.2 mol). It is also worth noticing, that the minimum amount of Cr is needed to allow the σ phase formation and below that limit (~0.15mol), the μ phase would form instead.

In order to enhance the formation of fcc solid solution, Al can be removed from the alloy composition. The combined effect of Mo and a second element on the phase stabilities in the Co-Cr-Fe-Mo-Ni system calculated at 1100 ˚C is shown in Fig. 60.

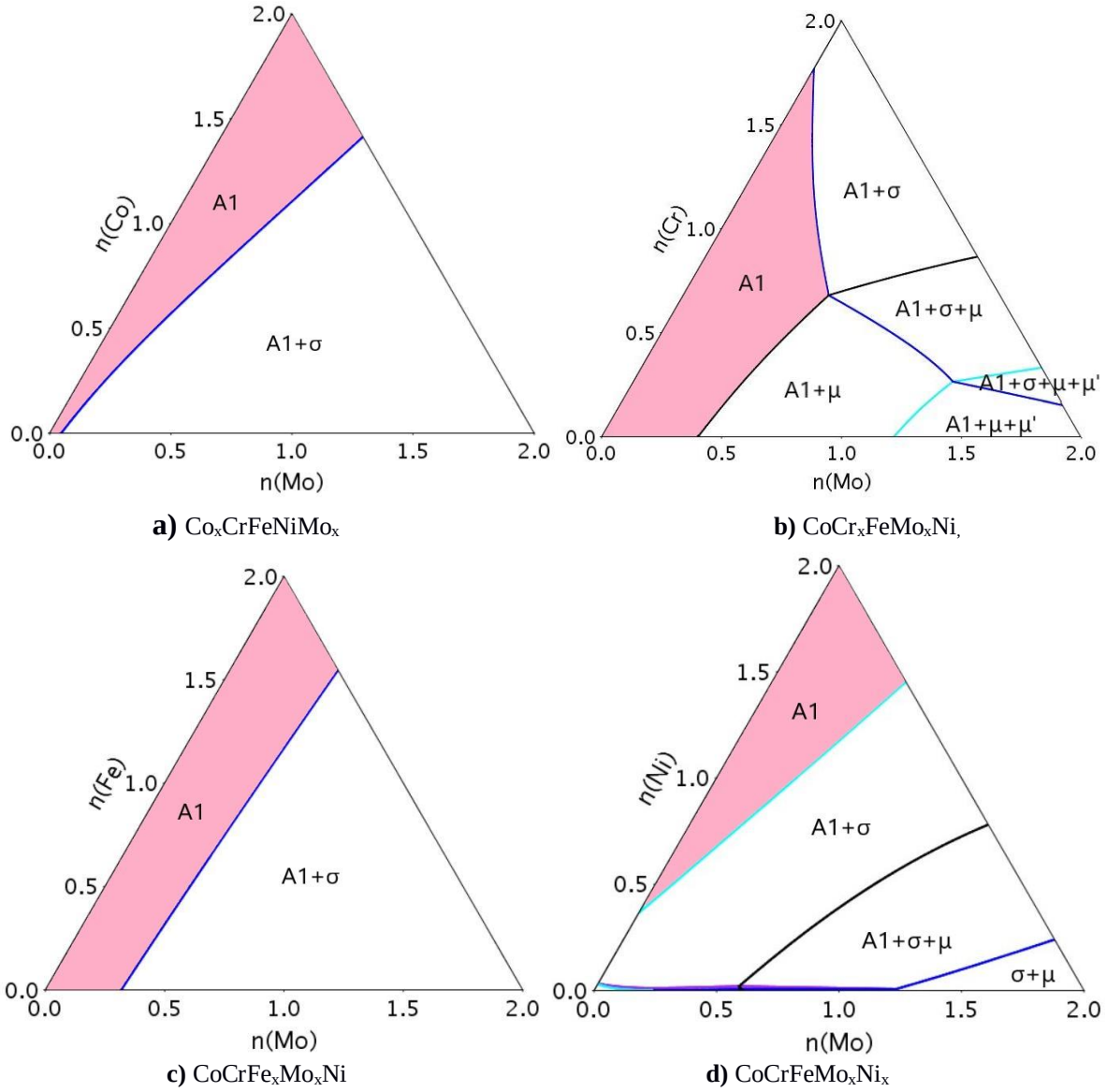

a) $Co_xCrFeNiMo_x$ **b)** $CoCr_xFeMo_xNi$, **c)** $CoCrFe_xMo_xNi$ **d)** $CoCrFeMo_xNi_x$

Fig. 60 *Co-Cr-Fe-Mo-Ni isothermal sections calculated at 1100 ˚C with the database developed in the present work: a) $Co_xCrFeMo_xNi$, b) $CoCr_xFeMo_xNi$, c) $CoCrFe_xMo_xNi$ and d) $CoCrFeMo_xNi_x$.*

Two intermetallic phases can be formed at 1100 ˚C in this system: σ and μ. The σ phase is stabilized by the addition of Cr and Mo, however, when the amount of Cr is lower than ~0.8 mol, the addition of Mo enhances the formation of the μ phase (Fig. 60b). What is more, by increasing the amount of Co and Ni, the solubility of Mo in the A1 phase increases, whereas Fe does not have any significant influence on that. The highest amount of Mo can be dissolved in the A1 phase at 0.75 mol of Cr. Taking all of that into account, the composition maximising the overall Mo solubility in the A1 phase was selected: $Co_{1.15}Cr_{0.75}FeNi_2$ and the effect of the temperature and Mo is presented in Fig. 61. If the amount of Mo is kept below 0.2 mol, the intermetallic phases do not form above 700 ˚C and the single fcc solid solution is obtained.

What is more, the addition of Mo decreases the solidus and liquidus temperatures.

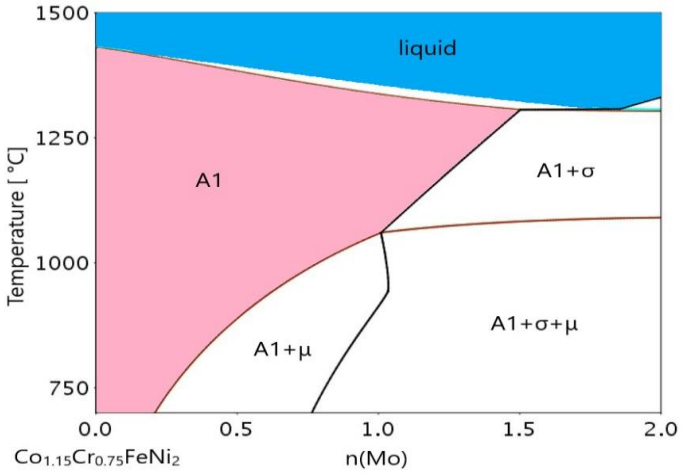

Fig. 61 *Isopleth $Co_{1.15}Cr_{0.75}FeNi_2Mo_x$ calculated with the database developed in the present work.*

6.2. The influence of Ta

As it can be seen in Fig. 62, the addition of Ta significantly increases the liquidus temperature (from 1390 for AlCoCrFeNi to 1560 ˚C for AlCoCrFeNiTa). Similarly to Mo, Ta is a bcc former, therefore it increases the stability of A2 phase and destabilizes A1 phase. The addition of 0.18 mol of Ta completely decomposes the A1 phase. A very small quantity of Ta is enough to stabilize the Laves C14 phase, which becomes stable in the very wide temperature range. The monovariant liquid in equilibrium with B2 and C14 takes place at 1355 ˚C and around 0.28 mol of Ta. When the quantity of Ta is higher, the C14 phase becomes the primary phase. The addition of Ta stabilizes also the ternary $TaCo_2Al$ phase, which at the equimolar AlCoCrFeNiTa composition decomposes at 1160 ˚C

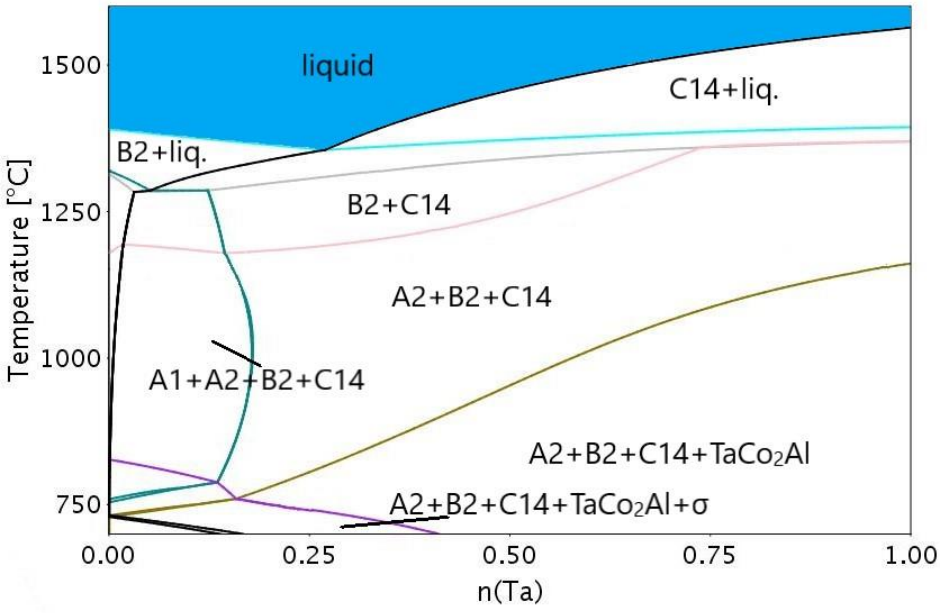

Fig. 62 *Isopleth showing the effect of Ta addition to the AlCoCrFeNi alloy calculated with the database developed in the present work.*

The addition of 0.1 mol of Ta does not have any significant influence on the solidus and liquidus temperatures (Fig. 63). However, even such small addition of Ta stabilizes the C14 phase up to the solidus temperature. As it can be seen in Fig. 63b, decreasing the amount of Al below 0.3 mol stabilizes the fcc structure over the bcc. Such structure consists of the fcc solid solution matrix with precipitates of the Laves C14 phase and could have a very attractive properties, if the precipitation of the Laves phase is controlled. On the other hand, by decreasing the amount of Co below 0.8 mol, the formation of the fcc phase is suppressed and the matrix consists of bcc phases (B2 and A2). The addition of Fe decreases stability of the σ phase, which results stable up to 1050 ˚C when no Fe is added, and up to 800 ˚C with addition of 1 mol of Fe.

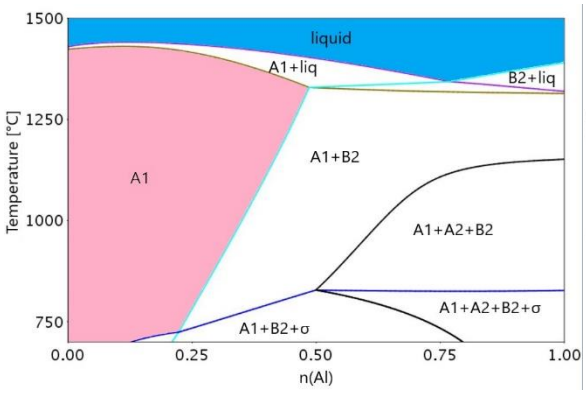

a)$Al_xCoCrFeNi$

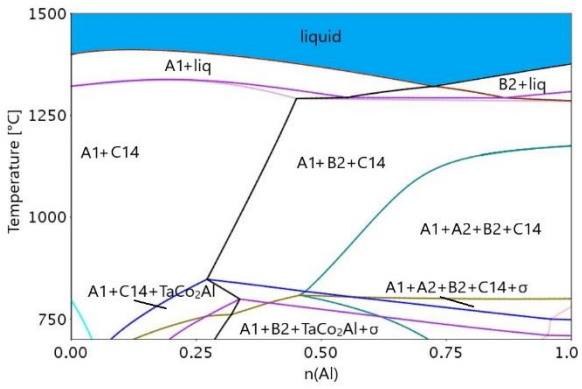

b) $Al_xCoCrFeNiTa_{0.1}$

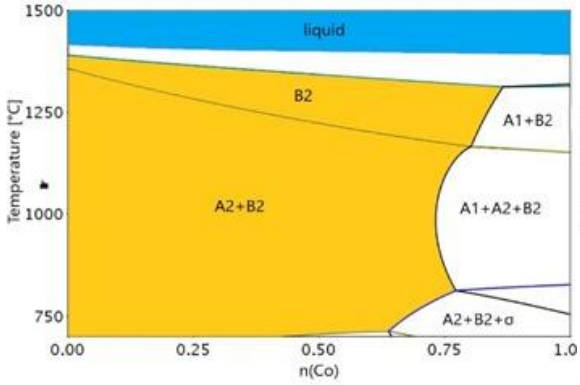

c) $AlCo_xCrFeNi$

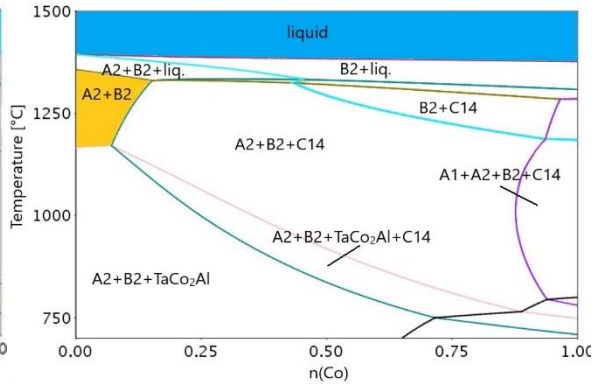

d) $AlCo_xCrFeNiTa_{0.1}$

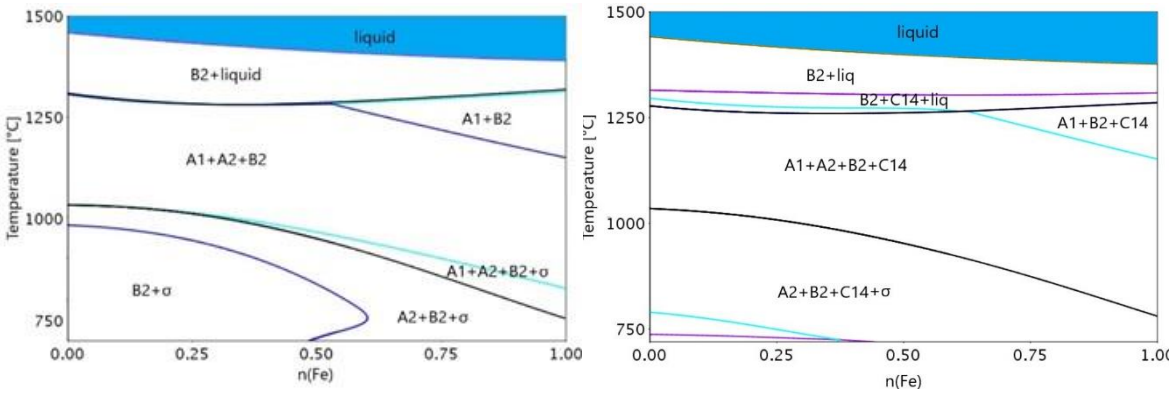

e)$AlCoCrFe_xNi$ **f)** $AlCoCrFe_xNiTa_{0.1}$

Fig. 63 *Isopleths in the Al-Co-Cr-Fe-Ni (a, c, e) and Al-Co-Cr-Fe-Ni-Ta (b, d, f) systems calculated with the database developed in the present work: a) $Al_xCoCrFeNi$, b) $Al_xCoCrFeNiTa_{0.1}$, c) $AlCo_xCrFeNi$, d) $AlCo_xCrFeNiTa_{0.1}$, e) $AlCoCrFe_xNi$ and f) $AlCoCrFe_xNiTa_{0.1}$.*

Analysing the influence of each element on the phase equilibria at 1000 ˚C (Fig. 64) it can be seen that even a very small addition of Ta is enough to form the Laves C14 phase. Such low solubility of Ta in fcc and bcc phases might result from the fact, that many important ternary systems containing Ta could not be assessed due to the lack of experimental and theoretical data. Therefore, ternary interaction parameters of such systems were not included in the present database and it can suffer from the inaccuracy of the predictions in the multicomponent systems containing Ta. Besides C14, also a ternary phase $TaCo_2Al$ results stable when n(Ta)>0.5 mol and the μ phase stabilizes when the Ta amount is father increased.

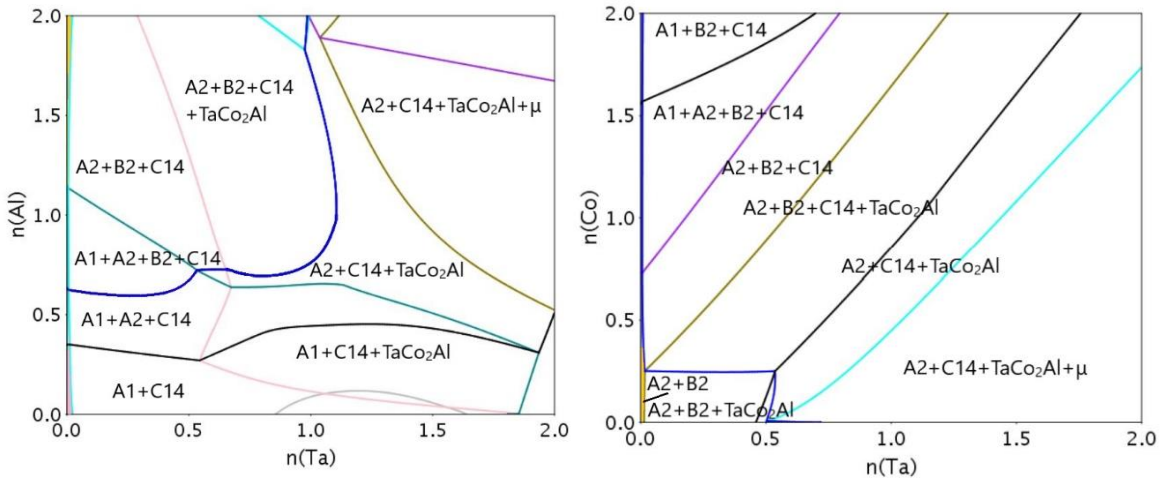

a)$Al_xCoCrFeNiTa_x$ **b)** $AlCo_xCrFeNiTa_x$

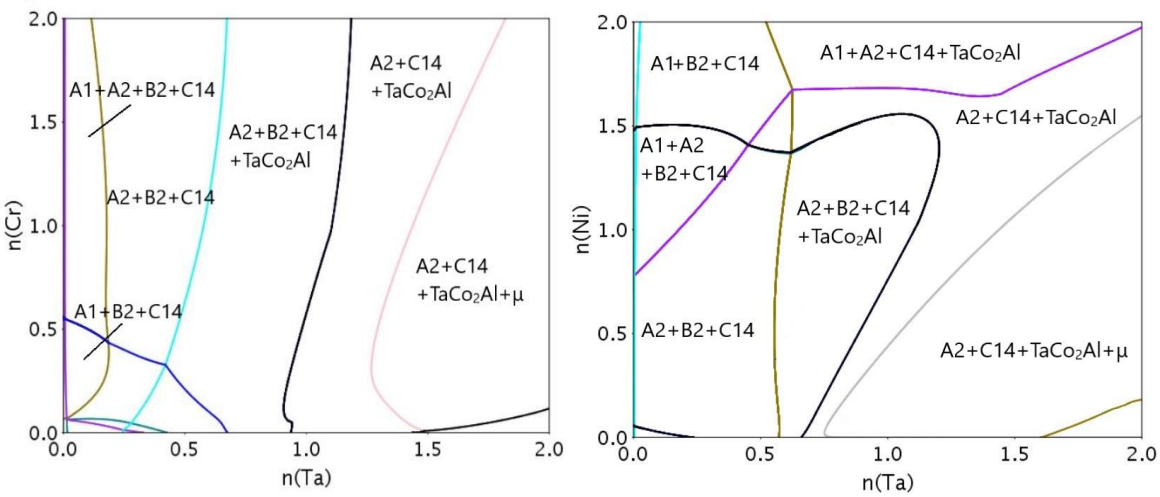

c) $AlCoCr_xFeNiTa_x$ **d)** $AlCoCrFeNi_xTa_x$

Fig. 64 *Al-Co-Cr-Fe-Ni-Ta isothermal sections calculated at 1000˚C around the equimolar composition as a function of the molar amounts of Ta and a second element: a) $Al_xCoCrFeNiTa_x$, b) $AlCo_xCrFeNiTa_x$, c) $AlCoCr_xFeNiTa_x$, and d) $AlCoCrFeNi_xTa_x$*

6.3. The influence of W

The effect of W addition to the equimolar alloy AlCoCrFeNi is shown by the isopleth $AlCoCrFeNiW_x$ presented in Fig. 65. The minimum of the liquidus curve takes place at 1340 ˚C and about 0.35 mol of W. The primary phases are B2 below 0.35mol of W and A2 when the amount of W is higher. The solidus temperature slightly decreases after the addition of W and then stabilizes at around 1250 ˚C. A very small addition of W is sufficient to stabilize the μ phase, which forms below 1120 ˚C. It is rich in W and contains also high quantity of Co, Cr and Fe. A1 phase is stable in the whole composition range at elevated temperatures.

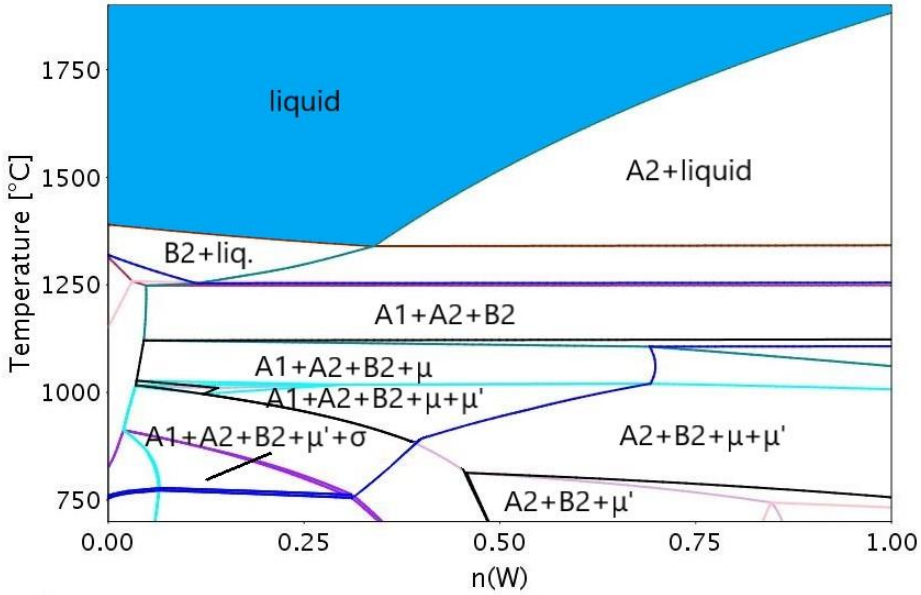

Fig. 65 *Isopleth showing the effect of W addition to the AlCoCrFeNi alloy calculated with the database developed in the present work.*

Fig. 66a shows phase fraction in the AlCoCrFeMoNi system as a function of the quantity of Mo, calculated at 900 ˚C. The principle phase is B2 and the addition of W does not influence its quantity. The formation of the fcc phase is suppressed when the amount of W is higher than 0.4 mol. As already noticed, the μ phase is stabilized by a very small addition of W, however, the amount of μ phase formed when 0.1 mol of W is added is very low (around 5%). For this reason the composition $AlCoCrFeMo_{0.1}Ni$ was selected for further investigation. In Fig. 66b, the phase fraction in the $AlCoCrFeMo_{0.1}Ni$ system are shown as a function of temperature. It can be seen that the amount of μ phase stays low in the whole temperature range. The σ phase precipitates below 920 ˚C. The B2 phase solidifies directly from the liquid and accounts for around 70% of all phase in the whole temperature range.

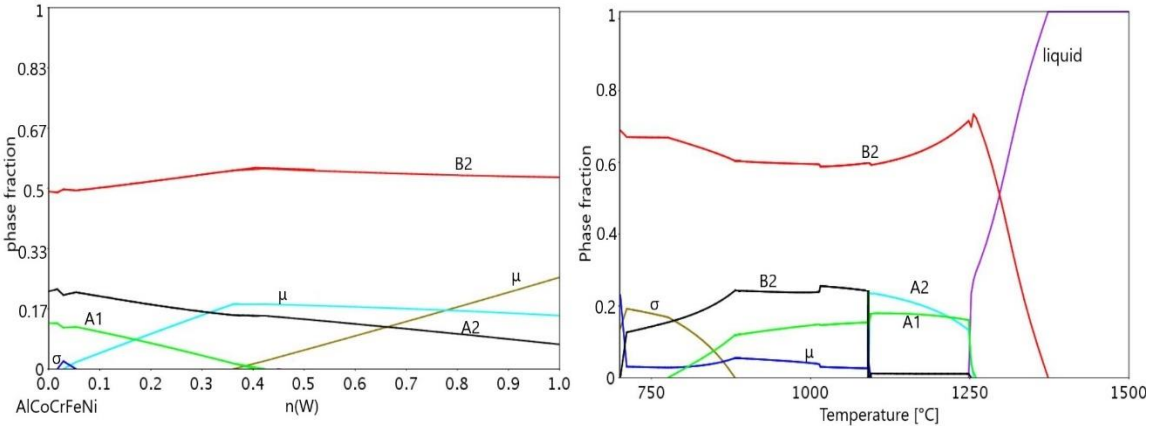

a) $AlCoCrFeW_xNi$ at 900 ˚C **b)** $AlCoCrFeW_{0.1}Ni$

Fig. 66 *Phase fractions calculated a) at 900 ˚C as a function of the quantity of W and b) at 0.1 mol of W as a function of the temperature for the composition* $AlCoCrFeNiW_{0.1}$ *calculated with the database developed in the present work.*

The comparison between a series of Al-Co-Cr-Fe-Ni and Al-Co-Cr-Fe-Ni-W vertical sections is presented in Fig. 67. The isopleths examine the effect of selected elements such as Co, Cr and Ni on the phase equilibria in the alloys containing 0.1 mol of W. The results are compared with the analogous isopleths without W. As it can be seen, the addition of W increases the stability of the μ phase. It can be controlled by decreasing the amount of Co (the μ phase does not results stable above 700 ˚C if the amount of Co is lower than 0.25 mol). What is more, removing Co significantly increases the solidus temperature, as it can be seen in Fig. 67b. By decreasing the amount of Cr, the μ phase is further stabilized and results stable up to the solidus temperature when the amount of Cr is below 0.2 mol, which is detrimental for the mechanical properties. On the other hand, if the amount of Ni is decreased, the σ phase increases its stability up to 1120 ˚C, which is also an undesired effect for the material's performance.

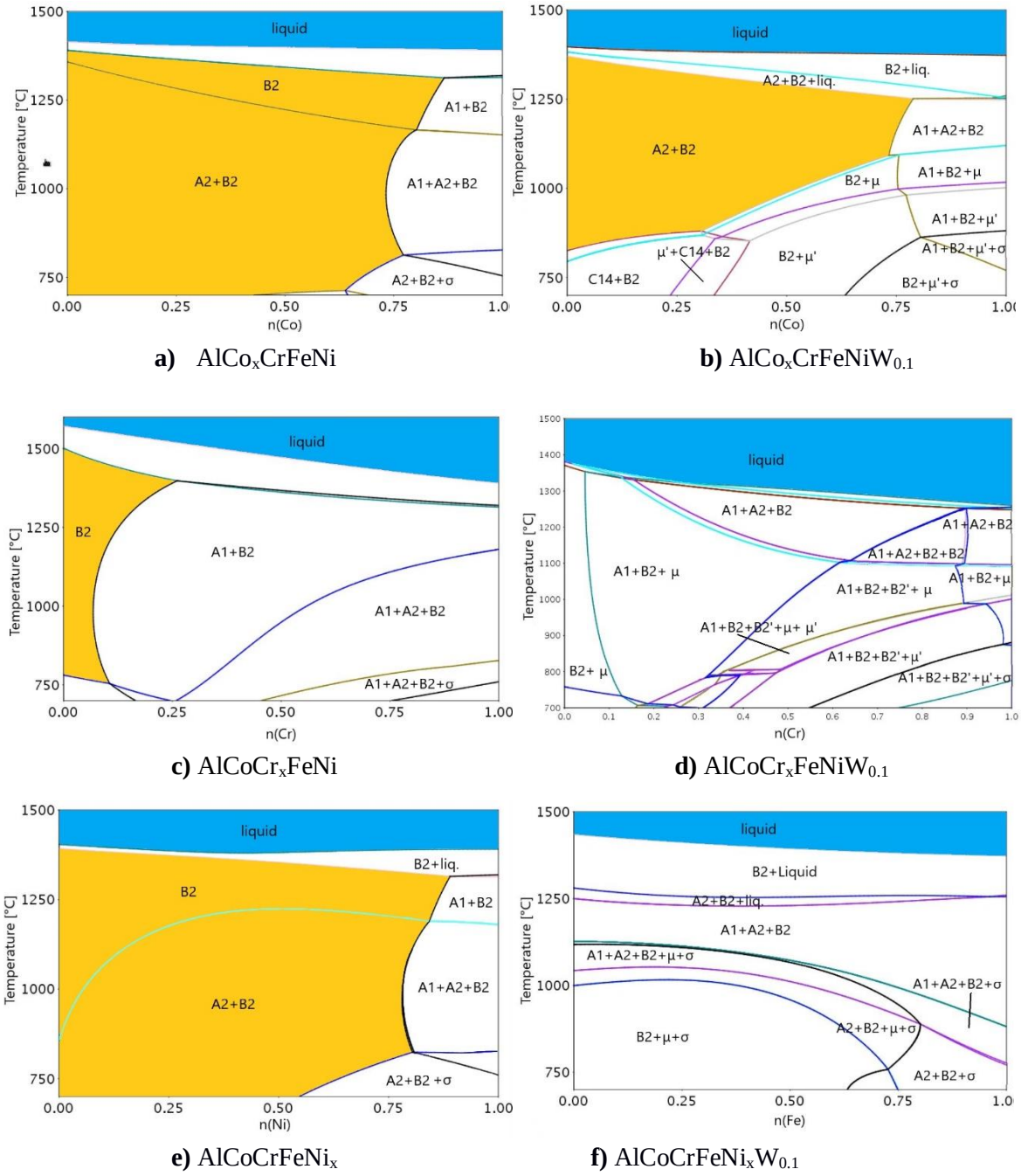

a) $AlCo_xCrFeNi$ **b)** $AlCo_xCrFeNiW_{0.1}$

c) $AlCoCr_xFeNi$ **d)** $AlCoCr_xFeNiW_{0.1}$

e) $AlCoCrFeNi_x$ **f)** $AlCoCrFeNi_xW_{0.1}$

Fig. 67 *Isopleths in the Al-Co-Cr-Fe-Ni (a, c, e) and Al-Co-Cr-Fe-Ni-W (b, d, f) systems calculated with the database developed in the present work: a) $AlCo_xCrFeNi$, b) $AlCo_xCrFeNiW_{0.1}$, c) $AlCoCr_xFeNi$, d) $AlCoCr_xFeNiW_{0.1}$, e) $AlCoCrFeNi_x$ and f) $AlCoCrFeNi_xW_{0.1}$.*

Fig. 68 shows the Al-Co-Cr-Fe-Ni-W isothermal section calculated at 1000˚C as a function of molar quantity of W and a second element. Notice that in all graphs of *Fig. 68* the equimolar composition is at the centre of the figure.

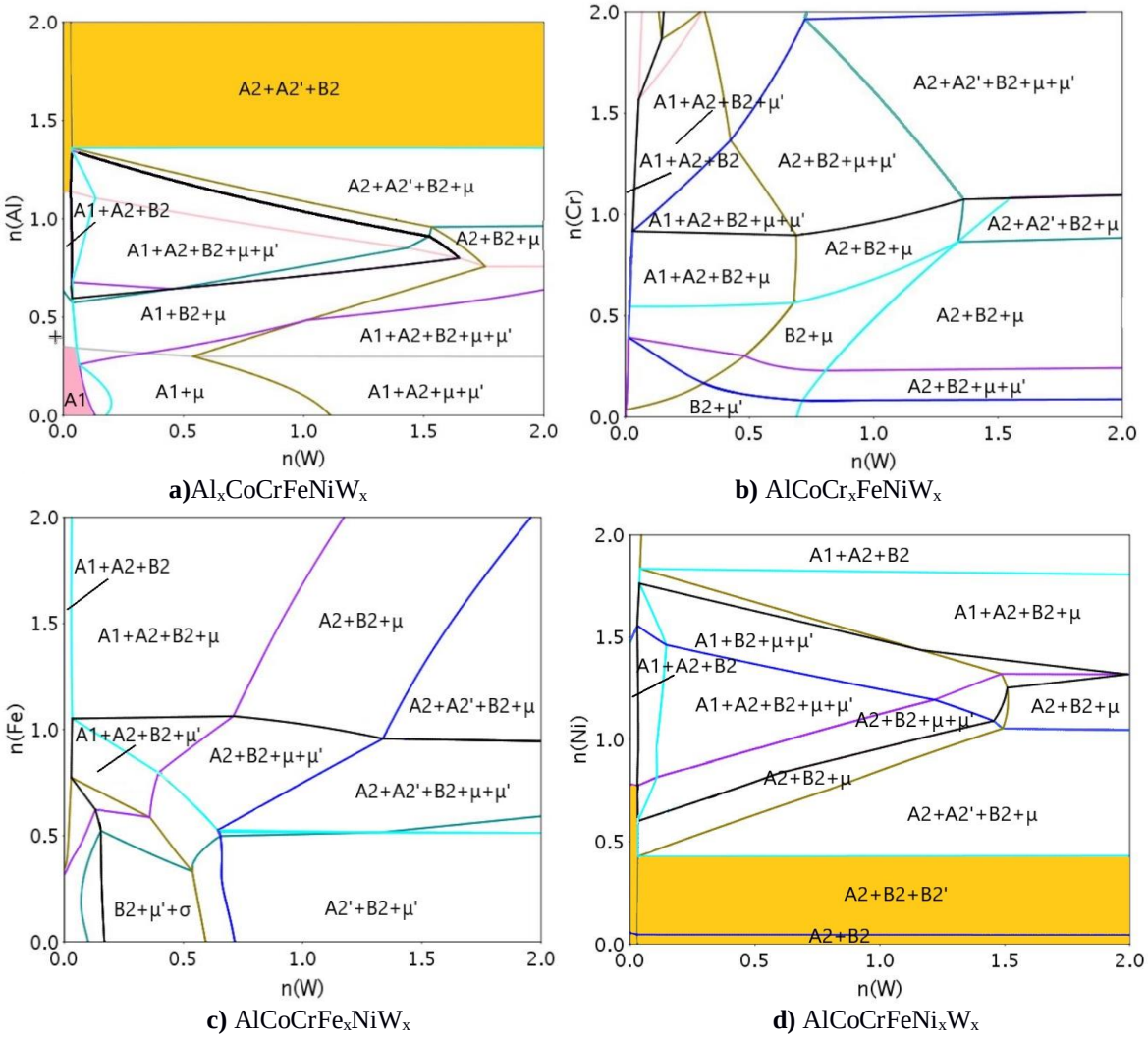

a) $Al_xCoCrFeNiW_x$ **b)** $AlCoCr_xFeNiW_x$

c) $AlCoCrFe_xNiW_x$ **d)** $AlCoCrFeNi_xW_x$

Fig. 68 *Al-Co-Cr-Fe-Ni-W isothermal sections calculated at 1000˚C around the equimolar composition as a function of the molar amounts of W and a second element: a) $Al_xCoCrFeNiW_x$ b) $AlCoCr_xFeNiW_x$, c) $AlCoCrFe_xNiW_x$ and d) $AlCoCrFeNi_xW_x$ systems using the database developed in the present work.*

As expected, even a small addition of W stabilizes the formation of the μ phase. It can be suppressed either by keeping the amount of Al above 1.4 mol (see Fig. 68a) or by decreasing the amount of Ni below 0.45 mol (see Fig. 68d).

The calculations and the considerations reported in this chapter are very useful in understanding the role of the addition of new elements to the quinary reference system and of the relationship between pairs of elements. It was shown that even a small amount of a refractory metal enhances the formation of intermetallic phases, such as σ (Mo), C14 (Ta) and μ (W). However, the adjustment of other elements and the fact that in HEAs the mobility of atoms in the solid state is sluggish, can inhibit the formation of intermetallics in real alloys.

The database developed during this thesis provides very valuable information such as phase transformation temperatures, melting temperature, primary solidified phases or solubility of

phases, which can be used for the design of new alloys and will significantly reduce the time needed to screen a broad range of compositions.

7. Summary and Outlook

7.1. Summary

During this thesis, a multicomponent thermodynamic database containing Al, Co, Cr, Fe, Mo, Ni, Ta and W was developed following the CALPHAD method in order to support the design of new high entropy alloys for high temperature applications.

Chapter 1 presents the motivation of my project and the introduction to high entropy alloys and the CALPHAD method. Beside the classic CALPHAD modelling, also the recently developed tools based on Bayesian probability and machine learning are shortly presented. The advantages of using thermodynamic modelling over a traditional trial and error method are underlined as well as the challenges that have to be overcome.

Different thermodynamic models applied in the CALPHAD method for calculation of Gibbs energy expressed according to the Compound Energy Formalism are described in chapter 2. The thermodynamic models for each phase were carefully chosen, according to their crystallographic structure and the available literature data on site occupation. It had to be taken into account that they are inserted in a large multicomponent database, therefore, some sublattices were merged together, consequently, reducing the number of end-member parameters to be optimised. The model selection for each phase is discussed in details in section 2.2. A special attention has been given to the σ and μ phases, because the models used by different authors to describe these phases are often incompatible with each other and the correct modelling of them is vital in this work, as they are stable at elevated temperatures in numerous systems included in this database.

In chapters 3 to 5, the results of this project are presented regarding thermodynamic assessments, experimental measurements and assessment of the Al-Co-Cr-Fe-Ni system, comparison between calculated and published phase compositions of several quaternary systems and simulations of phase stabilities in various multi-component systems.

Chapter 3 focuses on the thermodynamic assessment of binary and ternary sub-systems. Section 3.1 summarizes the assessment of 28 binary and 56 ternary systems which were inserted in the multi-component database, from which 14 systems were assessed during this thesis and 29 systems required certain modifications of parameters, mainly related to the incompatibility of models used for TCP phases, such as σ and μ. The optimisation of parameters was done by means of Parrot module in Thermo-Calc software or Python-based ESPEI software tool in case of more complex equilibria, for which the Parrot module was not sufficient to obtain satisfactory results. The principle difference between these two software is the algorithm applied for the optimisation, as described in section 1.3.1. It has been noticed that during optimisation of complex systems containing many ternary end-member and interaction parameters, Parrot module based on a simple least-squares method did not allow to obtain a good fit with the experimental data. Espei, on the other hand, obtained better results, when the

number of iterations was set to a sufficiently high number. The assessments of the most challenging ternary systems are described in sections 3.2-3.11. The most significant literature about each system is critically reviewed. The phase stabilities are discussed, and additionally, all stable solid phases in each ternary system are summarised in tables. The modifications of thermodynamic parameters done in this work are described. At the end of each system assessment, the isothermal sections calculated using the present database are compared with the available experimental data and shortly discussed. At the end of the chapter, in section 3.12, the stabilities of the σ and μ phases in several ternary systems are superimposed. It is interesting to notice that these two phases are stabilised by different mechanisms. The σ phase is mainly stabilised by the valence electron concentration (ranging from 6.88 to 7.84), while the stability of the μ phase is mainly related to the dimensional factors.

Chapter 4 concerns the experimental measurements regarding the effect of Co, Cr and Fe on the phase stabilities in the Al-Co-Cr-Fe-Ni system. Samples preparation and methods applied for the experimental investigation and the measurements set-up are shortly introduced. Prolonged annealing ensured the attainment of the equilibrium state. The results, such as SEM images and XRD profiles are presented. Two to three types of phases were identified in the samples, namely A1, A2 and B2. What is more, the σ phase precipitated in two samples, which is believed to be a consequence of slow cooling in the air after the annealing process. The obtained information is used for the improvement of the database, which was successfully optimised by adding a few essential metastable ternary and quaternary parameters. The phase compositions obtained by EDX measurement were compared with the calculations using the present database before and after optimisation. It can be seen that according to the database before optimisation, the A2 phase does not result stable in several samples, where this phase was observed experimentally. Additionally, due to the missing A2 phase, the mismatch of the calculated and measured composition of the B2 phase was quite big. This problem was solved after the optimisation, the stability of all observed phases was correctly predicted by the calculations and their phase compositions were in satisfactory agreement with experiments.

In chapter 5 the overall reliability of the multicomponent database has been validated with the critically selected theoretical and experimental data available in the literature regarding the quinary Al-Co-Cr-Fe-Ni and various quaternary systems containing Mo and W.
In case of the Al-Co-Cr-Fe-Ni system, the calculated phase compositions of the equimolar alloy were compared with a vast amount of data reported in the literature for the temperature ranging from 1000 to 1150˚C. Afterwards, the measured solidus temperatures and the phase stabilities with varying amount of Al were compared with the calculations. The Al-Co-Ni-W system was validated with the data regarding phase transition temperatures and composition of A1 and $L1_2$ phases of alloys containing 10 at% Al and 7.5-10 at% W. Quaternary liquid parameters were inserted and quaternary $L1_2$ parameters were modified to obtain a better agreement with the data. The experimentally measured phase compositions of the alloys of the Al-Cr-Mo-Ni system rich in Ni (at 50, 60, 70 and 75 at% Ni) were compared with the calculated values at 900, 1000 and 1250 ˚C. Additionally, the information on primary solidified phases and liquidus temperatures was used for the optimization of a ternary liquid parameter in the Al-Cr-Mo system. The calculated phase compositions of the Al-Cr-Ni-W alloys at 70-76 at% Ni were

compared with the reported experimental values at 900, 1000 and 1250 ˚C. The Cr-Fe-Mo-Ni system was optimized using compositional data of samples annealed at 700, 850 and 1000 ˚C. A series of metastable binary and ternary parameters of the χ and C14 phases were added to the database to reproduce the experimental information and a very good agreement was obtained.

Finally, in chapter 6, the database developed in this thesis was used for thermodynamic simulations. It provided information on the effect of refractory metals, such as Mo, W and Ta on the phase stabilities in 5- and 6-component systems. Homogeneity range of single phase solid solutions was identified, as well as the solidus and liquidus temperatures, eutectic reactions and stabilities of intermetallic phases. Afterwards, the effect of other elements on phase equilibria was examined in the systems containing a small addition of refractory metals (0.1 mol). A series of isopleths and isothermal sections was calculated and analysed.

7.2. Outlook

Taking into account that new experimental and theoretical data are constantly published, the database can be further improved in the future. A special attention should be paid to the systems containing Ta, due to the very scarce experimental information regarding such systems.

The cutting-edge solutions based on machine learning techniques could be implemented to improve the database quality, in particular, by predicting the formation energies of metastable endmembers.

A few compositions selected based on the calculations presented in chapter 6 should be synthesized and investigated experimentally in order to confirm the predicted structures by microscopic measurements. The mechanical properties of such materials should be tested, in particular, high temperature compressive strength and ductility at room temperature.

Finally, the database can be extended by other refractory metals, such as Nb or Ti, that could further increase solidus temperature and mechanical properties at elevated temperature of investigated alloys.

References:

[1] D.B. Miracle, O.N. Senkov, A critical review of high entropy alloys and related concepts, Acta Mater. 122 (2017) 448–511. doi:10.1016/j.actamat.2016.08.081.

[2] J. Chen, X. Zhou, W. Wang, B. Liu, Y. Lv, W. Yang, D. Xu, Y. Liu, A review on fundamental of high entropy alloys with promising high–temperature properties, J. Alloys Compd. 760 (2018) 15–30. doi:10.1016/j.jallcom.2018.05.067.

[3] Y.T. Chen, Y.J. Chang, H. Murakami, S. Gorsse, A.C. Yeh, Designing high entropy superalloys for elevated temperature application, Scr. Mater. 187 (2020) 177–182. doi:10.1016/j.scriptamat.2020.06.002.

[4] L. Qiao, Aorigele, Z. Lai, J. Zhu, A promising new class of multi-component alloys with exceptional mechanical properties, J. Alloys Compd. 847 (2020). doi:10.1016/j.jallcom.2020.155929.

[5] M. Pole, M. Sadeghilaridjani, J. Shittu, A. Ayyagari, S. Mukherjee, High temperature wear behavior of refractory high entropy alloys based on 4-5-6 elemental palette, J. Alloys Compd. 843 (2020). doi:10.1016/j.jallcom.2020.156004.

[6] M. Wang, Z.L. Ma, Z.Q. Xu, X.W. Cheng, Designing VxNbMoTa refractory high-entropy alloys with improved properties for high-temperature applications, Scr. Mater. 191 (2021) 131–136. doi:10.1016/j.scriptamat.2020.09.027.

[7] L. Kaufman, H. Bernstein, Computer calculation of phase diagrams with special reference to refractory metals, Academic Press New York, 1970.

[8] B. Bocklund, R. Otis, A. Egorov, A. Obaied, I. Roslyakova, Z.K. Liu, ESPEI for efficient thermodynamic database development, modification, and uncertainty quantification: Application to Cu-Mg, MRS Commun. 9 (2019) 618–627. doi:10.1557/mrc.2019.59.

[9] H. Mao, H.L. Chen, Q. Chen, TCHEA1: A Thermodynamic Database Not Limited for “High Entropy” Alloys, J. Phase Equilibria Diffus. 38 (2017) 353–368. doi:10.1007/s11669-017-0570-7.

[10] M. Wu, S. Wang, H. Huang, D. Shu, B. Sun, CALPHAD aided eutectic high-entropy alloy design, Mater. Lett. 262 (2020) 127175. doi:10.1016/j.matlet.2019.127175.

[11] O.N. Senkov, C. Zhang, A.L. Pilchak, E.J. Payton, C. Woodward, F. Zhang, CALPHAD-aided development of quaternary multi-principal element refractory alloys based on NbTiZr, J. Alloys Compd. 783 (2019) 729–742. doi:10.1016/j.jallcom.2018.12.325.

[12] W.M. Choi, Y.H. Jo, D.G. Kim, S.S. Sohn, S. Lee, B.J. Lee, A thermodynamic description of the Co-Cr-Fe-Ni-V system for high-entropy alloy design, Calphad Comput. Coupling Phase Diagrams Thermochem. 66 (2019) 101624. doi:10.1016/j.calphad.2019.05.001.

[13] M. Ostrowska, G. Cacciamani, Thermodynamic modelling of the σ and μ phases in several ternary systems containing Co, Cr, Fe, Mo, Re and W, J. Alloys Compd. 845 (2020) 156122. doi:10.1016/j.jallcom.2020.156122.

[14] J.W. Yeh, S.K. Chen, S.J. Lin, J.Y. Gan, T.S. Chin, T.T. Shun, C.H. Tsau, S.Y. Chang, Nanostructured high-entropy alloys with multiple principal elements: Novel alloy design concepts and outcomes, Adv. Eng. Mater. 6 (2004) 299-303+274. doi:10.1002/adem.200300567.

[15] J.W. Yeh, Recent progress in high-entropy alloys, Ann. Chim. Sci. Des Mater. 31 (2006) 633–648. doi:10.3166/acsm.31.633-648.

[16] W. Zhang, P.K. Liaw, Y. Zhang, Science and technology in high-entropy alloys, 61 (2018) 2–22.

[17] T.K. Chen, T.T. Shun, J.W. Yeh, M.S. Wong, Nanostructured nitride films of multi-element

high-entropy alloys by reactive DC sputtering, Surf. Coatings Technol. 188–189 (2004) 193–200. doi:10.1016/j.surfcoat.2004.08.023.

[18] C.-Y. HSU, J.-W. YEH, S.-K. CHEN, T.-T. SHUN, Wear resistance and high-temperature compression strength of Fcc CuCoNiCrAl, Metall. Mater. Trans. A, Phys. Metall. Mater. Sci. 35 (2004) 1465–1469.

[19] P.K. Huang, J.W. Yeh, T.T. Shun, S.K. Chen, Multi-principal-element alloys with improved oxidation and wear resistance for thermal spray coating, Adv. Eng. Mater. 6 (2004) 74–78. doi:10.1002/adem.200300507.

[20] J. Yeh, S. Chen, J. Gan, S. Lin, T. Chin, Communications: Formation of Simple Crystal Structures in Cu-Co-Ni-Cr-Al-Fe-Ti-V Alloys with Multiprincipal Metallic Elements, 35 (2010) 2533–2536.

[21] O.N. Senkov, G.B. Wilks, J.M. Scott, D.B. Miracle, Mechanical properties of Nb25Mo25Ta 25W25 and V20Nb20Mo 20Ta20W20 refractory high entropy alloys, Intermetallics. 19 (2011) 698–706. doi:10.1016/j.intermet.2011.01.004.

[22] Q. Wu, Z. Wang, F. He, J. Li, J. Wang, Revealing the Selection of σ and μ Phases in CoCrFeNiMox High Entropy Alloys by CALPHAD, J. Phase Equilibria Diffus. 39 (2018) 446–453. doi:10.1007/s11669-018-0659-7.

[23] X.L. Shang, Z.J. Wang, Q.F. Wu, J.C. Wang, J.J. Li, J.K. Yu, Effect of Mo Addition on Corrosion Behavior of High-Entropy Alloys CoCrFeNiMo x in Aqueous Environments, Acta Metall. Sin. (English Lett. 32 (2019) 41–51. doi:10.1007/s40195-018-0812-7.

[24] W. Wang, J. Wang, Z. Sun, J. Li, L. Li, X. Song, X. Wen, L. Xie, X. Yang, Effect of Mo and aging temperature on corrosion behavior of (CoCrFeNi)100-xMox high-entropy alloys, J. Alloys Compd. 812 (2020) 152139. doi:10.1016/j.jallcom.2019.152139.

[25] H. Gasan, A. Ozcan, New Eutectic High-Entropy Alloys Based on Co–Cr–Fe–Mo–Ni–Al: Design, Characterization and Mechanical Properties, Met. Mater. Int. 26 (2020) 1152–1167. doi:10.1007/s12540-019-00515-9.

[26] Y.F. Juan, J. Li, Y.Q. Jiang, W.L. Jia, Z.J. Lu, Modified criterions for phase prediction in the multi-component laser-clad coatings and investigations into microstructural evolution/wear resistance of FeCrCoNiAlMox laser-clad coatings, Appl. Surf. Sci. 465 (2019) 700–714. doi:10.1016/j.apsusc.2018.08.264.

[27] Y.X. Zhuang, X.L. Zhang, X.Y. Gu, Effect of molybdenum on phases, microstructure and mechanical properties of Al0.5CoCrFeMoxNi high entropy alloys, J. Alloys Compd. 743 (2018) 514–522. doi:10.1016/j.jallcom.2018.02.003.

[28] Y.X. Zhuang, X.L. Zhang, X.Y. Gu, Effect of annealing on microstructure and mechanical properties of Al0.5CoCrFeMoxNi high-entropy alloys, Entropy. 20 (2018). doi:10.3390/e20110812.

[29] B. Chanda, J. Das, An assessment on the stability of the eutectic phases in high entropy alloys, J. Alloys Compd. 798 (2019) 167–173. doi:10.1016/j.jallcom.2019.05.241.

[30] C. Ai, F. He, M. Guo, J. Zhou, Z. Wang, Z. Yuan, Y. Guo, Y. Liu, L. Liu, Alloy design, micromechanical and macromechanical properties of CoCrFeNiTax eutectic high entropy alloys, J. Alloys Compd. 735 (2018) 2653–2662. doi:10.1016/j.jallcom.2017.12.015.

[31] W. Huo, H. Zhou, F. Fang, X. Zhou, Z. Xie, J. Jiang, Microstructure and properties of novel CoCrFeNiTax eutectic high-entropy alloys, J. Alloys Compd. 735 (2018) 897–904. doi:10.1016/j.jallcom.2017.11.075.

[32] H. Jiang, K. Han, D. Qiao, Y. Lu, Z. Cao, T. Li, Effects of Ta addition on the microstructures and mechanical properties of CoCrFeNi high entropy alloy, Mater. Chem. Phys. 210 (2018) 43–48. doi:10.1016/j.matchemphys.2017.05.056.

[33] A.C. Fan, J.H. Li, M.H. Tsai, On the phase constituents of three CoCrFeNiX (X = V, Nb, Ta) high-entropy alloys after prolonged annealing, J. Alloys Compd. 823 (2020) 153524. doi:10.1016/j.jallcom.2019.153524.

[34] Z. Niu, J. Xu, T. Wang, N. Wang, Z. Han, Y. Wang, Microstructure, mechanical properties and corrosion resistance of CoCrFeNiWx (x = 0, 0.2, 0.5) high entropy alloys, Intermetallics. 112 (2019) 106550. doi:10.1016/j.intermet.2019.106550.

[35] Y. Dong, Y. Lu, Effects of Tungsten Addition on the Microstructure and Mechanical Properties of Near-Eutectic AlCoCrFeNi2 High-Entropy Alloy, J. Mater. Eng. Perform. 27 (2018) 109–115. doi:10.1007/s11665-017-3096-6.

[36] Y. Dong, Y. Lu, Microstructure and Mechanical Properties of CoCrFeNi 2Al 1-xW x High Entropy Alloys, Arab. J. Sci. Eng. 44 (2019) 803–808. doi:10.1007/s13369-018-3297-9.

[37] O.N. Senkov, D.B. Miracle, K.J. Chaput, J.P. Couzinie, Development and exploration of refractory high entropy alloys - A review, J. Mater. Res. 33 (2018) 3092–3128. doi:10.1557/jmr.2018.153.

[38] E.P. George, W.A. Curtin, C.C. Tasan, High entropy alloys: A focused review of mechanical properties and deformation mechanisms, Acta Mater. 188 (2020) 435–474. doi:10.1016/j.actamat.2019.12.015.

[39] K. Hack, The SGTE casebook. Thermodynamics at Work., 2nd ed., Woodhead Publishing, 2008.

[40] J. Van Laar, The melting and freezing curves of binary system when the solid phase is a mixture (amorphous or crystalline solid solusion) of both components, Zeitschrift Fuer Phys. Chemie. 63 (1908) 216–253.

[41] J.L. Meijering, Calculation of the nickel-chromium-copper phase diagram from binary data, Acta Metall. 5 (1957) 257–264. doi:10.1016/0001-6160(57)90099-8.

[42] L. Kaufman, M. Cohen, The Martensitic Transformation in the Iron-Nickel System, Jom. 8 (1956) 1393–1401. doi:10.1007/bf03377892.

[43] P.J. Spencer, A brief history of CALPHAD, Calphad Comput. Coupling Phase Diagrams Thermochem. 32 (2008) 1–8. doi:10.1016/j.calphad.2007.10.001.

[44] M. Perrut, Thermodynamic modeling by the calphad method and its applications to innovative materials, J. AerospaceLab. (2015) 1–11. doi:10.1276212015.AL09.10.

[45] H.-L. Lukas, S.G. Fries, B. Sundman, Computational Thermodynamics: The Calphad Method, Cambridge University Press, 2007.

[46] Z.K. Liu, First-principles calculations and CALPHAD modeling of thermodynamics, J. Phase Equilibria Diffus. 30 (2009) 517–534. doi:10.1007/s11669-009-9570-6.

[47] S.-L. Chen, S. Daniel, F. Zhang, Chang Y A, The Pandat software package and its applications, Calphad. 26 (2002) 175–188.

[48] J.O. Andersson, T. Helander, L. Höglund, P. Shi, B. Sundman, Thermo-Calc & DICTRA, computational tools for materials science, Calphad Comput. Coupling Phase Diagrams Thermochem. 26 (2002) 273–312. doi:10.1016/S0364-5916(02)00037-8.

[49] C.W. Bale, E. Bélisle, P. Chartrand, S.A. Decterov, G. Eriksson, A.E. Gheribi, K. Hack, I.H. Jung, Y.B. Kang, J. Melançon, A.D. Pelton, S. Petersen, C. Robelin, J. Sangster, P. Spencer, M.A. Van Ende, FactSage thermochemical software and databases, 2010-2016, Calphad Comput. Coupling Phase Diagrams Thermochem. 54 (2016) 35–53. doi:10.1016/j.calphad.2016.05.002.

[50] R. Otis, Z.-K. Liu, pycalphad: CALPHAD-based Computational Thermodynamics in Python, J. Open Res. Softw. 5 (2017) 1–11. doi:10.5334/jors.140.

[51] C. Zhang, F. Zhang, S. Chen, W. Cao, Computational Thermodynamics Aided High-Entropy Alloy Design, JOM. 64 (2012) 839–845. doi:10.1007/s11837-012-0365-6.

[52] F. Müller, B. Gorr, H.J. Christ, H. Chen, A. Kauffmann, S. Laube, M. Heilmaier, Formation of complex intermetallic phases in novel refractory high-entropy alloys NbMoCrTiAl and TaMoCrTiAl: Thermodynamic assessment and experimental validation, J. Alloys Compd. 842 (2020) 155726. doi:10.1016/j.jallcom.2020.155726.

[53] K. Kaufmann, K.S. Vecchio, Searching for high entropy alloys: A machine learning approach, Acta Mater. 198 (2020) 178–222. doi:10.1016/j.actamat.2020.07.065.

[54] S. Zomorodpoosh, B. Bocklund, A. Obaied, R. Otis, Z.K. Liu, I. Roslyakova, Statistical approach for automated weighting of datasets: Application to heat capacity data, Calphad Comput. Coupling Phase Diagrams Thermochem. 71 (2020) 101994. doi:10.1016/j.calphad.2020.101994.

[55] A.M. Krajewski, J.W. Siegel, J. Xu, Z.K. Liu, Extensible structure-informed prediction of formation energy with improved accuracy and usability employing neural networks, ArXiv. (2020) 1–36. doi:10.2139/ssrn.3721830.

[56] S. Kirklin, J.E. Saal, B. Meredig, A. Thompson, J.W. Doak, M. Aykol, S. Rühl, C. Wolverton, The Open Quantum Materials Database (OQMD): Assessing the accuracy of DFT formation energies, Npj Comput. Mater. 1 (2015). doi:10.1038/npjcompumats.2015.10.

[57] A. Gelman, H.S. Stern, J.B. Carlin, D.B. Dunson, A. Vehtari, D.B. Rubin, Bayesian data analysis, Chapman and Hall/CRC, 2013.

[58] M. Hillert, The compound energy formalism, J. Alloys Compd. 320 (2001) 161–176. doi:10.1016/S0925-8388(00)01481-X.

[59] A.T. Dinsdale, SGTE data for pure elements, Calphad. 15 (1991) 317–425. doi:10.1016/0364-5916(91)90030-N.

[60] O. Redlich, A.T. Kister, Algebraic Representation of Thermodynamic Properties and the Classification of Solutions, Ind. Eng. Chem. 40 (1948) 345–348. doi:10.1021/ie50458a036.

[61] G. Inden, Computer Calculation of the Free Energy Contributions Due to Magnetic Ordering, in: CALPHAD V, Max Planck Institut für Eisenforschung, Düsseldorf, Germany, 1976: pp. 1–13.

[62] M. Hillert, M. Jarl, A model for alloying in ferromagnetic metals, Calphad. 2 (1978) 227–238. doi:10.1016/0364-5916(78)90011-1.

[63] Y.M. Muggianu, M. Gambino, J.P. Bros, Enthalpies of formation of liquid alloys bismuth-gallium-tin at 723k-choice of an analytical representation of integral and partial thermodynamic functions of mixing for this ternary-system., J. Chim. Phys. Physico-Chimie Biol. 72 (1975) 83–88.

[64] A.T. Dinsdale, A. V. Khvan, A. Watson, Critical Assessment 5: Thermodynamic data for vacancies, Mater. Sci. Technol. 30 (2014) 1715–1718. doi:10.1179/1743284714Y.0000000589.

[65] F. Stein, C. He, N. Dupin, Melting behaviour and homogeneity range of B2 CoAl and updated thermodynamic description of the Al–Co system, Intermetallics. 39 (2013) 58–68. doi:10.1016/j.intermet.2013.03.011.

[66] P.W. Guan, Z.K. Liu, A physical model of thermal vacancies within the CALPHAD approach, Scr. Mater. 133 (2017) 5–8. doi:10.1016/j.scriptamat.2017.02.002.

[67] N. Dupin, I. Ansara, On Sublattice Formalism applied to B2 phase, Zeitschrift Für Met. 90.1 (1999) 76–85.

[68] J.-M. Joubert, N. Dupin, Mixed site occupancies in the μ phase, Intermetallics. 12 (2004) 1373–1380. doi:10.1016/j.intermet.2004.04.036.

[69] A. Bolcavage, U.R. Kattner, A reassessment of the calculated Ni-Nb phase diagram, J. Phase Equilibria. 17 (1996) 92–100. doi:10.1007/BF02665782.

[70] A. Davydov, U.R. Kattner, Thermodynamic Assessment of the Co-Mo System, 20 (1999) 5–16.

[71] J.-M. Joubert, J.-C. Crivello, Non-Stoichiometry and Calphad Modeling of Frank-Kasper Phases, Appl. Sci. 2 (2012) 669–681. doi:10.3390/app2030669.

[72] A.F. andez Guillermet, The Fe-Mo (Iron-Molybdenum) system, Bull. Alloy Phase Diagrams. 3 (1982) 359–367. doi:10.1007/BF02869315.

[73] K.C. Hari Kumar, I. Ansara, P. Wollants, Sublattice modelling of the μ- phase, Calphad. 22

(1998) 323–334.

[74] W. Treischke, G. Tamman, No Title, Zeitschrift Für Anorg. Und Allg. Chemie. 55 (1907).

[75] B.G. Bergman, D.P. Shoemaker, No Title, J. Chem. Phys. 19 (1951).

[76] S.M. Dubiel, J. Cieślak, Sigma-phase in Fe-Cr and Fe-V alloy systems and its physical properties, Crit. Rev. Solid State Mater. Sci. 36 (2011) 191–208. doi:10.1080/10408436.2011.589232.

[77] C. Berne, M. Sluiter, Y. Kawazoe, T. Hansen, A. Pasturel, Site occupancy in the Re-W sigma phase, Phys. Rev. B - Condens. Matter Mater. Phys. 64 (2001) 1441031–1441038. doi:10.1103/PhysRevB.64.144103.

[78] J.C. Crivello, A. Breidi, J.M. Joubert, χ and σ Phases in binary rhenium-transition metal systems: A systematic first-principles investigation, Inorg. Chem. 52 (2013) 3674–3686. doi:10.1021/ic302142w.

[79] J.-M. Joubert, Crystal chemistry and Calphad modeling of the σ phase, Prog. Mater. Sci. 53 (2008) 528–583. doi:10.1016/j.pmatsci.2007.04.001.

[80] L. Kaufman, H. Nesor, Coupled phase diagrams and thermochemical data for transition metal binary systems -I, Calphad. 2 (1978) 55–58. papers3://publication/uuid/6CC7EFA6-B6D3-4975-BDD0-E2BBB7286AEB.

[81] K. Rajan, Thermodynamic assessment of heat treatments for a Co-Cr-Mo alloy, J. Mater. Sci. 18 (1983) 257–264. doi:10.1007/BF00543833.

[82] J.-O. Andersson, B. Sundman, Thermodynamic properties of the Cr-Fe system, Calphad. 11 (1987) 83–92. doi:10.2138/am-2001-8-907.

[83] J.-O. Andersson, A.F. Guillermet, M. Hillert, B. Jansson, B. Sundman, The bond energy model for ordering in a phase with sites of different coordination numbers, Acta Metall. 34 (1986) 437–445. doi:10.1016/0364-5916(92)90040-5.

[84] C. Servant, I. Ansara, Thermodynamic assessment of the Al-Nb system, J. Chim. Phys. 94 (1997) 869–888.

[85] A. Watson, F.H. Hayes, Some experiences modelling the sigma phase in the Ni-V system, J. Alloys Compd. 320 (2001) 199–206. doi:10.1016/S0925-8388(00)01472-9.

[86] R. Ferro, G. Cacciamani, Remarks on crystallochemical aspects in thermodynamic modeling, Calphad Comput. Coupling Phase Diagrams Thermochem. 26 (2002) 439–458. doi:10.1016/S0364-5916(02)00056-1.

[87] S.A. Farzadfar, M. Levesque, M. Phejar, J.M. Joubert, Thermodynamic assessment of the Molybdenum-Rhenium system, Calphad Comput. Coupling Phase Diagrams Thermochem. 33 (2009) 502–510. doi:10.1016/j.calphad.2009.02.001.

[88] S.G. Fries, B. Sundman, Using Re-W σ-phase first-principles results in the Bragg-Williams approximation to calculate finite-temperature thermodynamic properties, Phys. Rev. B - Condens. Matter Mater. Phys. 66 (2002) 1–4. doi:10.1103/PhysRevB.66.012203.

[89] B. Hallstedt, N. Dupin, M. Hillert, L. Höglund, H.L. Lukas, J.C. Schuster, N. Solak, Thermodynamic models for crystalline phases. Composition dependent models for volume, bulk modulus and thermal expansion, Calphad. 31 (2007) 28–37. doi:10.1016/j.calphad.2006.02.008.

[90] M. Palumbo, T. Abe, C. Kocer, H. Murakami, H. Onodera, Ab initio and thermodynamic study of the CrRe system, Calphad Comput. Coupling Phase Diagrams Thermochem. 34 (2010) 495–503. doi:10.1016/j.calphad.2010.09.003.

[91] Z. Li, H. Mao, P.A. Korzhavyi, M. Selleby, Thermodynamic re-assessment of the Co-Cr system supported by first-principles calculations, Calphad. 52 (2016) 1–7. doi:10.1016/j.calphad.2014.11.002.

[92] S. Rideout, W.D. Manly, E.L. Kamen, B.S. Lement, P.A. Beck, Intermediate Phases in Ternary Alloy Systems of Transition Elements, Trans. AIME. 191 (1951) 872–876.

[93] Y. Komura, W.G. Sly, D.P. Shoemaker, The crystal structure of the R phase, Mo–Co–Cr, Acta Crystallogr. 13 (1960) 575–585. doi:10.1107/s0365110x60001394.

[94] W. Wang, F. Yin, M. Zhang, M. Zhao, Z. Li, Experimental Investigation and Thermodynamic Calculation of the Co-Cr-Mo System, J. Phase Equilibria Diffus. 35 (2014) 544–554. doi:10.1007/s11669-014-0317-7.

[95] J.-O. Andersson, N. Lange, An experimental study and a thermodynamic evaluation of the Fe-Cr-Mo system, Zeitschrift Fuer Met. Res. Adv. Tech. 19 (1988) 1385–1394.

[96] K. Frisk, An experimental and theoretical study of the phase equilibria in the Fe-Mo-Ni system, Metall. Trans. A. 23 (1992) 639–649. doi:10.1007/BF02801181.

[97] K.W. Andrews, P.E. Brookes, Metal Treatment and Drop Forging, 1951.

[98] J.S. Kasper, The ordering of atoms in the chi-phase of the iron-chromium-molybdenum system, Acta Met. (1954) 456–461.

[99] J.M. Joubert, M. Phejar, Crystal chemistry and Calphad modelling of the χ phase, Prog. Mater. Sci. 54 (2009) 945–980. doi:10.1016/j.pmatsci.2009.04.002.

[100] P. Gustafson, An experimental study and a thermodynamic evaluation of the Cr-Fe-W system, Metall. Trans. A. 19A (1988) 2531–3546. doi:10.1007/BF02674012.

[101] Y. Yang, L. Tan, J.T. Busby, Thermal Stability of Intermetallic Phases in Fe-rich Fe-Cr-Ni-Mo Alloys, Metall. Mater. Trans. A Phys. Metall. Mater. Sci. 46 (2015) 3900–3908. doi:10.1007/s11661-015-2997-y.

[102] F. Laves, H. Witte, Die Kristallstruktur des MgNi2 und seine Beziehungen zu den Typen MgCu2 und MgZn2, Metallwirtsch. 14 (1935) 645–649.

[103] S.R. Rideout, W.D. Manly, E.L. Kamen, B.S. Lement, P.A. Beck, Intermediate phases in ternary alloy systems of transition elements, JOM. 3 (1951) 872–876.

[104] C. Brink, D.P. Shoemaker, A variation on the sigma-phase structure; the crystal structure of the P phase, Mo-Ni-Cr, Acta Crystallogr. 8 (1955) 734–735.

[105] D.P. Shoemaker, C.B. Shoemaker, F.C. Wilson, The crystal structure of the P phase, Mo-Ni-Cr. II. Refinement of parameters and discussion of atomic coordination, Acta Crystallogr. 10 (1957) 1–14.

[106] N. Dupin, B. Sundman, A thermodynamic database for Ni-base superalloys, Scand. J. Metall. 30 (2001) 184–192. doi:10.1034/j.1600-0692.2001.300309.x.

[107] AFLOW, (n.d.). http://aflowlib.org/.

[108] M.H.F. Sluiter, Ab initio lattice stabilities of some elemental complex structures, Calphad Comput. Coupling Phase Diagrams Thermochem. 30 (2006) 357–366. doi:10.1016/j.calphad.2006.09.002.

[109] M.H.F. Sluiter, Lattice stability prediction of elemental tetrahedrally close-packed structures, Acta Mater. 55 (2007) 3707–3718. doi:10.1016/j.actamat.2007.02.016.

[110] M. Ostrowska, G. Cacciamani, Critical evaluation and thermodynamic modeling of the Al-Co-Fe system, J. Alloys Compd. 794 (2019) 553–568. doi:10.1016/j.jallcom.2019.04.170.

[111] P. Priputen, M. Kusý, M. Drienovský, D. Janičkovič, R. Čička, I. Černičková, J. Janovec, Experimental reinvestigation of Al–Co phase diagram in vicinity of Al13Co4 family of phases, J. Alloys Compd. 647 (2015) 486–497. doi:10.1016/j.jallcom.2015.05.248.

[112] P. Wang, M.C. Peters, U.R. Kattner, K. Choudhary, G.B. Olson, Thermodynamic analysis of the topologically close packed σ phase in the Co–Cr system, Intermetallics. 105 (2019) 13–20. doi:10.1016/j.intermet.2018.11.004.

[113] J. Wang, X.G. Lu, N. Zhu, W. Zheng, Thermodynamic and diffusion kinetic studies of the Fe-Co system, Calphad Comput. Coupling Phase Diagrams Thermochem. 58 (2017) 82–100. doi:10.1016/j.calphad.2017.06.001.

[114] I. Ohnuma, H. Enoki, O. Ikeda, R. Kainuma, H. Ohtani, B. Sundman, K. Ishida, Phase

equilibria in the Fe-Co binary system, Acta Mater. 50 (2002) 379–393. doi:10.1016/S1359-6454(01)00337-8.

[115] A.V. Davydov, U.R. Kattner, Revised thermodynamic description of the Co-Mo system, J. Phase Equilibria Vol. 24 (2003) 209–211.

[116] Z.-K. Liu, Y.A. Chang, Thermodynamic assessment of the Co-Ta system, Calphad Comput. Coupling Phase Diagrams Thermochem. 23 (1999) 339–356. doi:10.1016/S0364-5916(00)00005-5.

[117] V.B. Rajkumar, K.C. Hari Kumar, Thermodynamic modeling of the Fe-Mo system coupled with experiments and ab initio calculations, J. Alloys Compd. 611 (2014) 303–312. doi:10.1016/j.jallcom.2014.05.030.

[118] V.T. Witusiewicz, A.A. Bondar, U. Hecht, V.M. Voblikov, O.S. Fomichov, V.M. Petyukh, S. Rex, Experimental study and thermodynamic re-assessment of the binary Fe-Ta system, Intermetallics. 19 (2011) 1059–1075. doi:10.1016/j.intermet.2011.03.018.

[119] S.H. Zhou, Y. Wang, C. Jiang, J.Z. Zhu, L.Q. Chen, Z.K. Liu, First-principles calculations and thermodynamic modeling of the Ni-Mo system, Mater. Sci. Eng. A. 397 (2005) 288–296. doi:10.1016/j.msea.2005.02.037.

[120] S.H. Zhou, Y. Wang, L.Q. Chen, Z.-K. Liu, R.E. Napolitano, Solution-based thermodynamic modeling of the Ni-Ta and Ni-Mo-Ta systems using first-principle calculations, Calphad Comput. Coupling Phase Diagrams Thermochem. 33 (2009) 631–641. doi:10.1016/j.calphad.2009.06.006.

[121] A.F. Guillermet, L. Östlund, Experimental and theoretical study of the phase equilibria in the fe-ni-w system, Metall. Mater. Trans. A. 17 (1986) 1809–1823. doi:10.1007/BF02817278.

[122] C. Guo, C. Li, S. Shang, Z. Du, Thermodynamic description of the Ta-W-Zr system, Zeitschrift Fuer Met. 105 (2014) 1048–1056. doi:https://doi.org/10.3139/146.111125.

[123] L. Kaufman, P.E.A. Turchi, W. Huang, Z. Liu, Thermodynamics of The Cr-Ta-W System by Combining the, Calphad. 25 (2001) 419–433.

[124] Y. Wang, G. Cacciamani, Thermodynamic modeling of the Al-Cr-Ni system over the entire composition and temperature range, J. Alloys Compd. 688 (2016) 422–435. doi:10.1016/j.jallcom.2016.07.130.

[125] B. Sundman, I. Ohnuma, N. Dupin, U.R. Kattner, S.G. Fries, An assessment of the entire Al-Fe system including D03ordering, Acta Mater. 57 (2009) 2896–2908. doi:10.1016/j.actamat.2009.02.046.

[126] J. Peng, Experimental investigation and thermodynamic modeling of the Al-Cr-Mo-Ni system and its sub- systems z, (2016).

[127] V.T. Witusiewicz, A.A. Bondar, U. Hecht, V.M. Voblikov, N.I. Tsyganenko, O.S. Fomichov, M. V. Karpets, V.M. Petyukh, T.Y. Velikanova, Experimental study and thermodynamic modelling of the ternary Al-Fe-Ta system, J. Mater. Sci. 48 (2013) 377–412. doi:10.1007/s10853-012-6755-x.

[128] P. Wang, W. Xiong, U.R. Kattner, C.E. Campbell, E.A. Lass, O.Y. Kontsevoi, G.B. Olson, Thermodynamic re-assessment of the Al-Co-W system, Calphad Comput. Coupling Phase Diagrams Thermochem. 59 (2017) 112–130. doi:10.1016/j.calphad.2017.09.007.

[129] A.F. Guillermet, Assessment of the thermodynamic properties of the Ni-Co system, Zeitschrift Fuer Met. 78 (1987) 639–647.

[130] A. Jacob, E. Povoden-Karadeniz, E. Kozeschnik, Revised thermodynamic description of the Fe-Cr system based on an improved sublattice model of the σ phase, Calphad Comput. Coupling Phase Diagrams Thermochem. 60 (2018) 16–28. doi:10.1016/j.calphad.2017.10.002.

[131] K. Frisk, Internal report D60, Div, Stockholm, Sweden, 1984.

[132] P. Gustafson, A thermodynamic evaluation of the Cr-Ni-W system, 12 (1988) 277–292.

[133] N. Dupin, I. Ansara, Thermodynamic Assessment of the Cr-Ta system, J. Phase Equilib. 14

(1993) 451–456.

[134] P. Franke, H.J. Seifert, The influence of magnetic and chemical ordering on the phase diagram of CrFeNi, Calphad Comput. Coupling Phase Diagrams Thermochem. 35 (2011) 148–154. doi:10.1016/j.calphad.2010.10.006.

[135] A. Jacob, C. Schmetterer, L. Singheiser, A. Gray-Weale, B. Hallstedt, A. Watson, Modeling of Fe-W phase diagram using first principles and phonons calculations, Calphad Comput. Coupling Phase Diagrams Thermochem. 50 (2015) 92–104. doi:10.1016/j.calphad.2015.04.010.

[136] Y. Cui, L.U. Xiaogang, Z. Jin, Experimental study and thermodynamic assessment of the Ni-Mo-Ta ternary system, Metall. Mater. Trans. A Phys. Metall. Mater. Sci. 30 (1999) 2735–2744. doi:10.1007/s11661-999-0110-0.

[137] P. Gustafson, An experimental study and a thermodynamic evaluation of the Fe-Mo-W system, Zeitschrift Fuer Met. 79 (1988) 388–396.

[138] X.L. Liu, T. Gheno, B.B. Lindahl, G. Lindwall, B. Gleeson, Z.K. Liu, First-principles calculations, experimental study, and thermodynamic modeling of the Al-Co-Cr system, PLoS One. 10 (2015) 1–14. doi:10.1371/journal.pone.0121386.

[139] E.S. Moskvitina, V.N. Kuznetsov, L.S. Guzei, Refinement of the Co-Cr-Al Phase Diagram, Vestn. Mosk. Univ., Ser. Khim. 33 (1992) 373–374.

[140] K. Ishikawa, M. Ise, I. Ohnuma, R. Kainuma, K. Ishida, Phase equilibria and stability of the bcc aluminide in the Co-Cr-Al system, Berichte Der Bunsengesellschaft Für Phys. Chemie. 102 (1998) 1206–1210.

[141] L. Zhu, S. Soto-Medina, R.G. Hennig, M. V. Manuel, Experimental investigation of the Al–Co–Fe phase diagram over the whole composition range, J. Alloys Compd. 815 (2020) 152110. doi:10.1016/j.jallcom.2019.152110.

[142] Y. Wang, G. Cacciamani, Experimental investigation and thermodynamic assessment of the Al-Co-Ni system, Calphad Comput. Coupling Phase Diagrams Thermochem. 61 (2018) 198–210. doi:10.1016/j.calphad.2018.03.008.

[143] S. Wang, Z. Li, Z. Qin, S. Wang, X. Lu, C. Li, Thermodynamic modeling of Al-Fe-Cr ternary system, Miner. Met. Mater. Ser. (2017). doi:10.1007/978-3-319-51493-2_42.

[144] L. Zhang, J. Wang, Y. Du, R. Hu, P. Nash, X.G. Lu, C. Jiang, Thermodynamic properties of the Al-Fe-Ni system acquired via a hybrid approach combining calorimetry, first-principles and CALPHAD, Acta Mater. 57 (2009) 5324–5341. doi:10.1016/j.actamat.2009.07.031.

[145] M.A.X. Dombre, O.S. Campos, N. Valignat, C. Allibert, C. Bernard, J. Driole, Solid State Phase Equilibrium in the Ternary Fe-Co-Cr System: Experimental Determination of Isothermal Sections in the Temperature Range 800-1300C, J. Less Common Met. 66 (1979) 1–11.

[146] G. Cacciamani, G. Roncallo, Y. Wang, E. Vacchieri, A. Costa, Thermodynamic modelling of a six component (C-Co-Cr-Ni-Ta-W) system for the simulation of Cobalt based alloys, J. Alloys Compd. 730 (2018) 291–310. doi:10.1016/j.jallcom.2017.09.327.

[147] W. Köster, W.D. Haehl, The Real Constitution Diagram and the Obtention of Equilibrium in the Ternary System Iron-Cobalt-Nickel., Arch. Eisenhuettenwes. 40 (1969) 569–574.

[148] T. Kase, No Title, Sci. Repts. Tohoku Imp. Univ. 16 (1927) 491–513.

[149] J. Miettinen, Thermodynamic reassessment of Fe-Cr-Ni system with emphasis on the iron-rich corner, Calphad Comput. Coupling Phase Diagrams Thermochem. 23 (1999) 231–248. doi:10.1016/S0364-5916(99)00027-9.

[150] L. Zhu, C. Wei, H. Qi, L. Jiang, Z. Jin, J.C. Zhao, Experimental investigation of phase equilibria in the Co-rich part of the Co-Al-X (X = W, Mo, Nb, Ni, Ta) ternary systems using diffusion multiples, J. Alloys Compd. 691 (2017) 110–118. doi:10.1016/j.jallcom.2016.08.210.

[151] Z. Du, C. Guo, C. Li, W. Zhang, Thermodynamic description of the Al-Mo and Al-Fe-Mo systems, J. Phase Equilibria Diffus. 30 (2009) 487–501. doi:10.1007/s11669-009-9564-4.

[152] S.H. Zhou, Y. Wang, L.Q. Chen, Z.K. Liu, R.E. Napolitano, Solution-based thermodynamic modeling of the Ni-Al-Mo system using first-principles calculations, Calphad Comput. Coupling Phase Diagrams Thermochem. 46 (2014) 124–133. doi:10.1016/j.calphad.2014.03.002.

[153] E. Povoden-Karadeniz, E. Eidenberger, P. Lang, G. Stechauner, H. Leitner, E. Kozeschnik, Simulation of precipitate evolution in Fe-25 Co- 15 Mo with Si addition based on computational thermodynamics, J. Alloys Compd. 587 (2014) 158–170. doi:10.1016/j.jallcom.2013.10.166.

[154] C. Zhang, Y. Liu, Y. Du, Y. Peng, J. Wang, Thermodynamic assessment of the Co–Mo–Ni and Mo–Ni–W ternary systems, Calphad Comput. Coupling Phase Diagrams Thermochem. 55 (2016) 243–251. doi:10.1016/j.calphad.2016.10.001.

[155] K. Frisk, Study of the Phase Equilibria in Cr-Mo-Ni system, Stockholm, Sweden, 1990.

[156] J. Zhu, M.S. Titus, T.M. Pollock, Experimental Investigation and Thermodynamic Modeling of the Co-Rich Region in the Co-Al-Ni-W Quaternary System, J. Phase Equilibria Diffus. 35 (2014) 595–611. doi:10.1007/s11669-014-0327-5.

[157] B. Kaplan, A. Blomqvist, M. Selleby, S. Norgren, Thermodynamic analysis of the W-Co-Cr system supported by ab initio calculations and verified with quaternary data, Calphad Comput. Coupling Phase Diagrams Thermochem. 50 (2015) 59–67. doi:10.1016/j.calphad.2015.04.012.

[158] A.F. Guillermet, Thermodynamic Calculation of the Fe-Co-W Phase Diagram, Zeitschrift Fuer Met. 79 (1998) 633–642.

[159] M. Palm, W. Sanders, S. G., Phase equilibria in the Ni-Al-Ta system, Zeitschrift Fuer Met. 87 (1996) 390–398.

[160] H. Xu, Y. Du, Y. Tan, Y. He, S. Li, Z. Xiang, Phase equilibria of the Co–Ni–Ta system at 1100°C, J. Alloys Compd. 425 (2006) 153–158. doi:10.1016/j.jallcom.2006.01.018.

[161] V.A. Baheti, S. Santra, S. Roy, K. Perumalsamy, S. Prasad, R. Ravi, A. Paul, Phase evolutions, growth kinetics and diffusion parameters in the Co-Ni-Ta system, J. Alloys Compd. 622 (2015) 1033–1040. doi:10.1016/j.jallcom.2014.10.112.

[162] R.K. Shaipov, E.Y. Kerimov, E.M. Slyusarenko, Isothermal sections of the Co-Ni-Ta phase diagram at 1200 and 1375 K, J. Alloys Compd. 701 (2017) 262–278. doi:10.1016/j.jallcom.2016.12.397.

[163] L. Zhu, C. Wei, L. Jiang, Z. Jin, J.-C. Zhao, Experimental determination of the phase diagrams of the Co-Ni-X (X = W, Mo, Nb, Ta) ternary systems using diffusion multiples, Intermetallics. 93 (2018) 20–29. doi:10.1016/j.intermet.2017.11.005.

[164] C.P. Wang, J. Wang, S.H. Guo, X.J. Liu, I. Ohnuma, R. Kainuma, K. Ishida, Experimental investigation and thermodynamic calculation of the phase equilibria in the Co-Mo-W system, Intermetallics. 17 (2009) 642–650. doi:10.1016/j.intermet.2009.02.004.

[165] N. Asrar, L.L. Meshkov, E.M. Sokolovskaya, Phase equilibria in ternary alloys based on iron-group metals and containing refractory metals (Mo, W, Nb, Ta), J. Less-Common Met. 144 (1988) 41–52. doi:10.1016/0022-5088(88)90347-5.

[166] N. Dupin, I. Ansara, Thermodynamic assessment of the Cr-Ni-Ta system, Zeitschrift Fuer Met. 87 (1996) 555–561.

[167] C. Wang, Y. Liang, S. Yang, M. Yang, L. Li, J. Han, Y. Lu, X. Liu, Isothermal sections of the Ni-Cr-Ta ternary system at 1200 °c and 1300 °c, Metals (Basel). 9 (2019) 1–13. doi:10.3390/met9070770.

[168] C. Tang, M. Tong, H. Xu, Y. Du, J. Lee, Q. Yao, Y. He, H. Zhou, Isothermal section at 1100 °c of the Fe-Ni-Ta system, J. Alloys Compd. 504 (2010) 181–185. doi:10.1016/j.jallcom.2010.05.084.

[169] Y. Wang, J. Wang, H. Wang, X.G. Lu, L. Zhang, Thermodynamic description of the Ni-Mo-W system and interdiffusion study of its fcc phase, Calphad Comput. Coupling Phase Diagrams

Thermochem. 61 (2018) 165–172. doi:10.1016/j.calphad.2018.03.010.

[170] G. V. Raynor, M.B. Waldron, The Constitution of the Aluminium-Rich Aluminium-Cobalt-Iron Alloys, with Reference to the Role of Transitional Elements in Alloy Formation, Proc. R. Soc. A Math. Phys. Eng. Sci. 194 (1948) 362–374. doi:10.1098/rspa.1950.0110.

[171] T. Kozakai, R. Okamoto, T. Miyazaki, Phase equilibria in the Fe-Al-Co ternary system at 923 K, Zeitschrift Für Met. 90.4 (1999) 261–266.

[172] B. Grushko, W. Kowalski, M. Surowiec, On the constitution of the Al-Co-Fe alloy system, J. Alloys Compd. 491 (2010) 2009–2011. doi:10.1016/j.jallcom.2009.10.156.

[173] O.S. Edwards, An X-Ray Investigation of the Aluminium-Cobalt-Iron System, Inst. Met. 67 (1941) 67–77.

[174] H. Ackermann, Experimentelle Untersuchung und Monte-Carlo-Simulation chemischer Ordnungsreaktionen in den ternären kubisch raumzentrierten Fe-Co-Al-Legierungen, 1988.

[175] T. Kozakai, T. Shikama, T. Koyama, Metastable two-phase field (A2+ B2) in Co-Al-Fe and Co-Al alloy systems, in: Mater. Sci. Forum Trans Tech Publ., 2004: pp. 61–64.

[176] T. Kozakai, T. Koyama, M. Doi, Phase decomposition and precipitation of metastable A2 phase in B2 ordered Co-Al-Fe alloys, Int. J. Mater. Res. 97 (2006) 266–272.

[177] N. Kamiya, T. Sakai, R. Kainuma, I. Ohnuma, K. Ishida, Phase separation of BCC phase in the Co-rich portion of Co-Fe-Al system, Intermetallics. 12 (2004) 417–423. doi:10.1016/j.intermet.2003.12.005.

[178] T. Miyazaki, K. Isobe, T. Kozakai, M. Doi, The phase separations of Fe-Al-Co ordering alloys, Acta Metall. 35 (1987) 317–326. doi:10.1016/0001-6160(87)90240-9.

[179] T. Kozakai, N. T., Experimental and theoretical studies on phase separations in the Fe-AI-Co ordering alloy system, J. Mater. Sci. 29 (1994) 652–659. doi:10.1007/BF00445974.

[180] W. Köster, Das system Eisen-Kobalt_Aluminium.pdf, Arch. Für Das Eisenhüttenwes. 7.4 (1933) 263–264.

[181] M. Yin, S. Chen, P. Nash, Enthalpies of formation of selected Co2YZ Heusler compounds, J. Alloys Compd. 577 (2013) 49–56. doi:10.1016/j.jallcom.2013.04.136.

[182] M. Yin, P. Nash, Enthalpies of formation of selected Pd2YZ Heusler compounds, Intermetallics. 58 (2015) 15–19. doi:10.1016/j.intermet.2014.10.019.

[183] C. Colinet, G. Inden, R. Kikuchi, CVM calculation of the phase diagram of bcc Fe-Co-Al, Acta Metall. Mater. 41 (1993) 1109–1118.

[184] H. Ohtani, Y. Chen, M. Hasebe, Phase separation of the B2 structure accompanied by an ordering in Co-Al and Ni-Al binary systems. - ProQuest, Mater. Trans. 45 (2004) 1489–1498. doi:10.2320/matertrans.45.1489.

[185] K. Niitsu, T. Omori, M. Nagasako, K. Oikawa, R. Kainuma, K. Ishida, Phase transformations in the B2 phase of Co-rich Co-Al binary alloys, J. Alloys Compd. 509 (2011) 2697–2702. doi:10.1016/j.jallcom.2010.11.130.

[186] V.Y. Markiv, V.V. Burnashova, V.P. Ryabov, Investigation of Al-rich part of the Mo-Fe-Al system, Dopov. Akad. Nauk Ukr. RSR,,. 1 (1970) 69–72.

[187] P. Villars, A. Prince, H. Okamoto, Handbook of ternary alloy phase diagrams, 3rd ed., ASM International, Metals Park, 1995.

[188] E.M. Sokolovskaya, G.M. Cheldieva, E.F. Kazakova, N.I. Kaloev, An investigation of alloys in the AL-AL3Fe-Al12Mo system, Moskow Univ. Chem. Bull. 42 (1987) 108–109.

[189] G. Wang, D.L. Douglass, F. Gesmundo, High-temperature sulfidation of Fe-30Mo alloys containing ternary additions of Al, Oxid. Met. 35 (1991) 349–373. doi:10.1007/BF00664708.

[190] M. Eumann, G. Sauthoff, M. Palm, Phase equilibria in the Fe-Al-Mo system - Part I: Stability of the Laves phase Fe2Mo and isothermal section at 800 °C, Intermetallics. 16 (2008) 706–716. doi:10.1016/j.intermet.2008.02.006.

[191] M. Eumann, G. Sauthoff, M. Palm, Phase equilibria in the Fe-Al-Mo system - Part II: Isothermal sections at 1000 and 1150 °C, Intermetallics. 16 (2008) 834–846. doi:10.1016/j.intermet.2008.04.001.

[192] J. Stepien-Damm, P. Salamakha, K. Wochowski, W. Suski, Crystal structure of Mo9Fe4.75Al0.25, Alloy. Compd. 282 (1999) 182–182.

[193] L. Eleno, K. Frisk, A. Schneider, Assessment of the Fe-Ni-Al system, Intermetallics. 14 (2006) 1276–1290. doi:10.1016/j.intermet.2005.11.021.

[194] A. Bradley, A. Taylor, An X-ray study of the iron-nickel-aluminium ternary equilibrium diagram, Proc. R. Soc. London. Ser. A. Math. Phys. Sci. 166 (1938) 353–375.

[195] A. Bradley, A. Taylor, An X-ray Investigation of Aluminium-Rich Iron-Nickel-Aluminium Alloys After Slow Cooling., J. Inst. Met. 66 (1940) 53–65.

[196] A. Schrader, H. Hanemann, The Aluminium-Rich Region of the System Aluminium-Iron-Nickel, Aluminium. 25 (1943) 339–342.

[197] G.V. Raynor, P.C.L. Pfeil, THE CONSTITUTION OF THE ALUMINIUM-RICH ALUMINIUM IRON NICKEL ALLOYS., J. Inst. Met. 73 (1947) 397.

[198] M. Khaidar, No Title, National Polytechnique Institute of Grenoble, 1981.

[199] M. Khaidar, C.H. Allibert, J. Driole, PHASE EQUILIBRIA OF THE FE-NI-AL SYSTEM FOR AL CONTENT ABOVE 50 AT.-% AND CRYSTAL STRUCTURES OF SOME TERNARY PHASES, Z. Met. 73 (1982) 433–438.

[200] I. Chumak, K.W. Richter, H. Ipser, The Fe-Ni-Al phase diagram in the Al-rich (>50 at.% Al) corner, Intermetallics. 15 (2007) 1416–1424. doi:10.1016/j.intermet.2007.04.012.

[201] L. Zhang, Y. Du, H. Xu, C. Tang, H. Chen, W. Zhang, Phase equilibria of the Al-Fe-Ni system at 850 °C and 627 °C, J. Alloys Compd. 454 (2008) 129–135. doi:10.1016/j.jallcom.2006.12.042.

[202] S.M. Hao, T. Takayama, K. Ishida, T. Nishizawa, Miscibility Gap in Fe-Ni-Al and Fe-Ni-Al-Co Systems. Reply., Met. Trans. 15A (1984) 1819–1828.

[203] C.C. Jia, K. Ishida, T. Nishizawa, Partition of Alloying Elements between 3 ’ (A1), Metall. Mater. Trans. A. 25 (1994) 473–485.

[204] Y. Himuro, Y. Tanaka, I. Ohnuma, R. Kainuma, K. Ishida, Phase equilibria and γ′-L12 phase stability in the Ni-rich portion of Ni-Fe-Si and Ni-Fe-Al systems, Intermetallics. 13 (2005) 620–630. doi:10.1016/j.intermet.2004.10.009.

[205] B.L. Bramfitt, J.R. Michael, No Title, Mater. Res. Soc. Symp. Proc. 62 (1986) 201–208.

[206] N. Masahashi, H.H. Kawazoe, T. Takasugi, O. Izumi, PHASE RELATIONS IN THE SECTION Ni//3Al-Ni//3Fe OF THE Al-Fe-Ni SYSTEM., Zeitschrift Fuer Met. 78 (1987) 788–794.

[207] Y. Himuro, Y. Tanaka, N. Kamiya, I. Ohnuma, R. Kainuma, K. Ishida, Stability of ordered L12 phase in Ni3Fe-Ni 3X (X:Si and Al) pseudobinary alloys, Intermetallics. 12 (2004) 635–643. doi:10.1016/j.intermet.2004.03.008.

[208] I. Chumak, K.W. Richter, S.G. Fries, H. Ipser, Experimental phase diagram investigations in the Ni-rich part of Al-Fe-Ni and comparison with calculated phase equilibria, J. Phase Equilibria Diffus. 28 (2007) 417–421. doi:10.1007/s11669-007-9157-z.

[209] I. Chumak, K.W. Richter, H. Ipser, Isothermal sections in the (Fe, Ni)-rich part of the Fe-Ni-Al phase diagram, J. Phase Equilibria Diffus. 29 (2008) 300–304. doi:10.1007/s11669-008-9319-7.

[210] H. Bitterlich, W. Löser, L. Schultz, Reassessment of Ni-Al and Ni-Fe-Al solidus temperatures, J. Phase Equilibria. 23 (2002) 301–304. doi:10.1361/105497102770331541.

[211] L. Zhang, Y. Du, Thermodynamic description of the Al-Fe-Ni system over the whole composition and temperature ranges: Modeling coupled with key experiment, Calphad Comput. Coupling Phase Diagrams Thermochem. 31 (2007) 529–540.

doi:10.1016/j.calphad.2007.03.003.

[212] L. Zhang, J. Wang, Y. Du, R. Hu, P. Nash, X.G. Lu, C. Jiang, Thermodynamic properties of the Al-Fe-Ni system acquired via a hybrid approach combining calorimetry, first-principles and CALPHAD, Acta Mater. 57 (2009) 5324–5341. doi:10.1016/j.actamat.2009.07.031.

[213] A. Bradley, Bradley, A. J. "MICROSCOPICAL STUDIES ON THE IRON-NICKEL-ALUMINIUM SYSTEM. 1. ALPHA+ BETA-ALLOYS AND ISOTHERMAL SECTIONS OF THE PHASE EQUILIBRIUM DIAGRAM, J. Iron Steel Inst. 163 (1949) 19.

[214] A. Bradley, Microscopical studies on the iron nickel aluminium system. 2. The breakdown of the body-centred cubic lattice, J. Iron Steel Inst. 168 (1951) 233.

[215] C. Hunt, A. Raman, Alloy chemistry of β (σU)-related phases. I. Extension and occurrence of μ¢-phases in ternary systems Nb (Ta)–X–Al, Z. Met. 59 (1968) 701–707.

[216] D.D. Risanti, G. Sauthoff, Microstructures and mechanical properties of Fe-Al-Ta alloys with strengthening Laves phase, Intermetallics. 19 (2011) 1727–1736. doi:10.1016/j.intermet.2011.07.008.

[217] L. Kaufman, CALCULATION OF MULTICOMPONENT TANTALUM BASED PHASE DIAGRAMS, Calphad. 15 (1991) 261–282.

[218] W. Koester, G. Kofmann, About Equilibria in Ternary Iron-Cobalt-Chromium System, Arch. Eisenhuettenwes. 30 (1959) 249–251.

[219] L. Kaufman, H. Nesor, Calculation of superalloy phase diagrams: Part I, Metall. Trans. 5 (1974) 1617–1721.

[220] C. Allibert, C. Bernard, G. Effenberg, H.D. Nüssler, P.J. Spencer, A thermodynamic evaluation of the FeCoCr system, Calphad. 5 (1981) 227–237. doi:10.1016/0364-5916(81)90006-7.

[221] J. Cieślak, J. Tobola, S.M. Dubiel, Site occupancies in sigma-phase Fe-Cr-X (X = Co, Ni) alloys: Calculations versus experiment, Comput. Mater. Sci. 122 (2016) 229–239. doi:10.1016/j.commatsci.2016.05.008.

[222] J.B. Darby, P.A. Beck, Intermediate Phases in the Cr-Mo-Co System at 1300C, Trans. AIME. 203 (1955) 765–766.

[223] J. Zhao, Methods dor Phase Diagram Determination, Elsevier Ltd, 2007. doi:10.1016/B978-0-08-044629-5.50007-0.

[224] Y. Lu, Theoretical and Experimental Study of the Co-Cr-Mo System, 2011.

[225] J.B. Darby, P.A. Beck, Intermediate Phase in the Cr-Mo-Co System at 1300C, Trans. AIME. 203 (1955) 765–766.

[226] T. V. Ishchenko, L.L. Meshkov, Y.M. Sokolovskaya, On the interaction of μ phases in systems formed by transition metals, J. Less-Common Met. 97 (1984) 145–150. doi:10.1016/0022-5088(84)90018-3.

[227] S. Cao, J.C. Zhao, Determination of the Fe-Cr-Mo Phase Diagram at Intermediate Temperatures using Dual-Anneal Diffusion Multiples, J. Phase Equilibria Diffus. 37 (2016) 25–38. doi:10.1007/s11669-015-0423-1.

[228] C. Qiu, Thermodynamic calculation of the austenite/ferrite equilibrium in the CrFeMo system, Calphad. 16 (1992) 281–289. doi:10.1016/0364-5916(92)90026-T.

[229] P. Gustafson, Experimental study and a thermodynamic evaluation of the Cr-Fe-W system, Metall. Trans. A, Phys. Metall. Mater. Sci. 19 A (1988) 2531–2546. doi:10.1007/BF02645481.

[230] K. Chvátalová, J. Vřešťál, J. Houserová, M. Šob, First-principles calculations of energetics of sigma phase formation and thermodynamic modelling in the Cr-Fe-W system, Mater. Sci. Eng. A. 462 (2007) 153–158. doi:10.1016/j.msea.2006.02.474.

[231] G. Kirchner, H. Harvig, G. Kirchner, Experimental and Thermodynamic Study of the Equilibria Between Ferrite, Austenite and Intermediate Phases in the Fe-Mo, Fe-W and Fe-Mo-W Systems, Met. Trans. 4 (1973) 1059–1067.

[232] L.L. Meshkov, S.N. Nesterenko, T. V. Ishchenko, Structural features of phase diagrams formed by Mo, W with Fe-group Metals, Akad. Nauk. SSSR. Met. (1985) 205–208.

[233] M.H. Tsai, K.C. Chang, J.H. Li, R.C. Tsai, A.H. Cheng, A second criterion for sigma phase formation in high-entropy alloys, Mater. Res. Lett. 4 (2016) 90–95. doi:10.1080/21663831.2015.1121168.

[234] Y.F. Kao, T.J. Chen, S.K. Chen, J.W. Yeh, Microstructure and mechanical property of as-cast, -homogenized, and -deformed AlxCoCrFeNi ($0 \leq x \leq 2$) high-entropy alloys, J. Alloys Compd. 488 (2009) 57–64. doi:10.1016/j.jallcom.2009.08.090.

[235] H.P. Chou, Y.S. Chang, S.K. Chen, J.W. Yeh, Microstructure, thermophysical and electrical properties in AlxCoCrFeNi ($0 \leq x \leq 2$) high-entropy alloys, Mater. Sci. Eng. B Solid-State Mater. Adv. Technol. 163 (2009) 184–189. doi:10.1016/j.mseb.2009.05.024.

[236] W.R. Wang, W.L. Wang, S.C. Wang, Y.C. Tsai, C.H. Lai, J.W. Yeh, Effects of Al addition on the microstructure and mechanical property of AlxCoCrFeNi high-entropy alloys, Intermetallics. 26 (2012) 44–51. doi:10.1016/j.intermet.2012.03.005.

[237] W.L.W.W.W.R. Wang, W.L.W.W.W.R. Wang, J.W. Yeh, Phases, microstructure and mechanical properties of AlxCoCrFeNi high-entropy alloys at elevated temperatures, J. Alloys Compd. 589 (2014) 143–152. doi:10.1016/j.jallcom.2013.11.084.

[238] T. Yang, S. Xia, S. Liu, C. Wang, S. Liu, Y. Zhang, J. Xue, S. Yan, Y. Wang, Effects of AL addition on microstructure and mechanical properties of AlxCoCrFeNi High-entropy alloy, Mater. Sci. Eng. A. 648 (2015) 15–22. doi:10.1016/j.msea.2015.09.034.

[239] C. Zhang, F. Zhang, H. Diao, M.C. Gao, Understanding Phase Stability of Al-Co-Cr-Fe-Ni High Entropy Alloys, Mater. Des. 109 (2016) 425–433.

[240] J.C. Rao, H.Y. Diao, V. Ocelík, D. Vainchtein, C. Zhang, C. Kuo, Z. Tang, W. Guo, J.D. Poplawsky, Y. Zhou, P.K. Liaw, J.T.M. De Hosson, Secondary phases in Al x CoCrFeNi high-entropy alloys: An in-situ TEM heating study and thermodynamic appraisal, Acta Mater. 131 (2017) 206–220. doi:10.1016/j.actamat.2017.03.066.

[241] T. Butler, M. Weaver, Investigation of the phase stabilities in AlNiCoCrFe high entropy alloys, J. Alloys Compd. 691 (2017) 119–129.

[242] Z. Tang, O.N. Senkov, C.M. Parish, C. Zhang, F. Zhang, L.J. Santodonato, G. Wang, G. Zhao, F. Yang, P.K. Liaw, Tensile ductility of an AlCoCrFeNi multi-phase high-entropy alloy through hot isostatic pressing (HIP) and homogenization, Mater. Sci. Eng. A. 647 (2015) 229–240. doi:10.1016/j.msea.2015.08.078.

[243] J. Cieslak, J. Tobola, J. Przewoznik, K. Berent, U. Dahlborg, J. Cornide, S. Mehraban, N. Lavery, M. Calvo-Dahlborg, Multi-phase nature of sintered vs. arc-melted CrxAlFeCoNi high entropy alloys - experimental and theoretical study, J. Alloys Compd. 801 (2019) 511–519. doi:10.1016/j.jallcom.2019.06.121.

[244] T.T. Shun, Y.C. Du, Microstructure and tensile behaviors of FCC Al0.3CoCrFeNi high entropy alloy, J. Alloys Compd. 479 (2009) 157–160. doi:10.1016/j.jallcom.2008.12.088.

[245] ThermoCalc Ni-based Superalloys Database, TCNI8, (2015).

[246] R. Wang, K. Zhang, C. Davies, X. Wu, Evolution of microstructure, mechanical and corrosion properties of AlCoCrFeNi high-entropy alloy prepared by direct laser fabrication, J. Alloys Compd. 694 (2017) 971–981. doi:10.1016/j.jallcom.2016.10.138.

[247] Y. Sun, C. Wu, H. Peng, Y. Liu, J. Wang, X. Su, Phase Constituent and Microhardness of As-Cast and Long-Time Annealed AlxCo2−xCrFeNi Multicomponent Alloys, J. Phase Equilibria Diffus. 40 (2019) 706–714. doi:10.1007/s11669-019-00761-9.

[248] O. Stryzhyboroda, V.T. Witusiewicz, S. Gein, D. Röhrens, U. Hecht, Phase Equilibria in the Al–Co–Cr–Fe–Ni High Entropy Alloy System: Thermodynamic Description and Experimental Study, Front. Mater. 7 (2020) 1–13. doi:10.3389/fmats.2020.00270.

[249] K. Shinagawa, T. Omori, J. Sato, K. Oikawa, I. Ohnuma, R. Kainuma, K. Ishida, Phase

equilibria and microstructure on γ′ phase in Co-Ni-Al-W system, Mater. Trans. 49 (2008) 1474–1479. doi:10.2320/matertrans.MER2008073.

[250] S. Chakravorty, D.R.F. West, The Ni3AI-Ni3Cr-Ni3Mo section of the Ni-Cr-Al-Mo system, J. Mater. Sci. 19 (1984) 3574–3587.

[251] J. Buršík, M. Svoboda, The existence of P phase and Ni2Cr superstructure in Ni-Al-Cr-Mo system, Scr. Mater. 39 (1998) 1107–1112. doi:10.1016/S1359-6462(98)00277-2.

[252] J. Havránková, J. Buršík, A. Kroupa, P. Brož, Experimental study and thermodynamic assessment of the Ni-Al-Cr-Mo system at 1173 K, Scr. Mater. 45 (2001) 121–126. doi:10.1016/S1359-6462(01)01001-6.

[253] S. Chakravorty, S. Sadiq, D.R.F. West, Equilibria involving P- and sigma-phases in Ni-Cr-AI-Mo system, Mater. Sci. Technol. 2 (1986) 110–121.

[254] S. Chakravorty, S. Sadiq, D.R.F. West, Intermetallic compound precipitation in Ni-Cr-Al-Mo system, Mater. Sci. Technol. (United Kingdom). 3 (1987) 629–641. doi:10.1179/mst.1987.3.8.629.

[255] J.D. Whittenberger, S. V. Raj, L.E. Locci, J.A. Salem, Elevated temperature strength and room-temperature toughness of directionally solidified Ni-33Al-33Cr-1Mo, Met. Mat. Trans. 33 (2002) 1385–1397.

[256] Z. Zhang, X. Liu, S. Gong, H. Xu, Microstructure and properties of the β NiAl and its eutectic alloy with Cr and Mo addtions, Trans. Nonferrous Met. Soc. China. 16 (2006) 2046–2049.

[257] J. Wang, G. Zhang, S. Li, Investigation of microstructure and corrosive behavior of NiAl-31Cr-3Mo alloy at high temperature, Min. Met. Eng. 30 (2010) 93–96.

[258] Z. Shang, J. Shen, L. Wang, Y. Du, Y. Xiong, H. Fu, Investigations on the microstructure and room temperature fracture toughness of directionally solidified NiAl-Cr(Mo) eutectic alloy, Intermetallics. 57 (2015) 25–33.

[259] S. Chakravorty, S. Sadiq, D.R.F. West, Constitution of the Ni3Cr-Ni3AI-Ni3W system, 24 (1989) 577–583.

[260] J. Buršík, P. Brož, R. Picha, Microstructural and phase equilibria study in the Ni-Al-Cr-W system at 1173 and 1273 K, Intermetallics. 11 (2003) 483–490. doi:10.1016/S0966-9795(03)00023-2.

Appendix A Phase Diagrams of binary subsystems

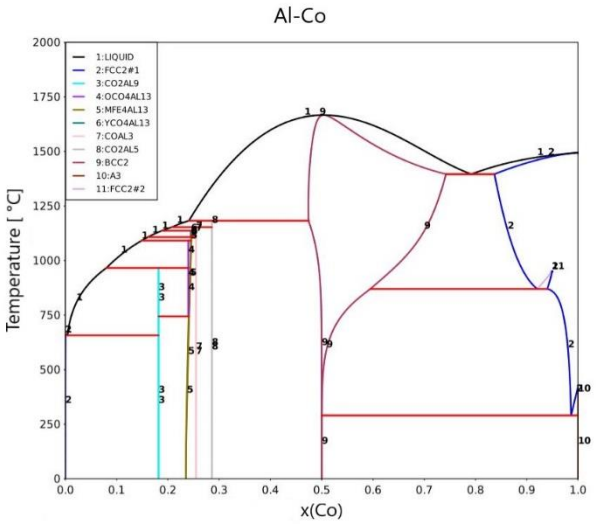

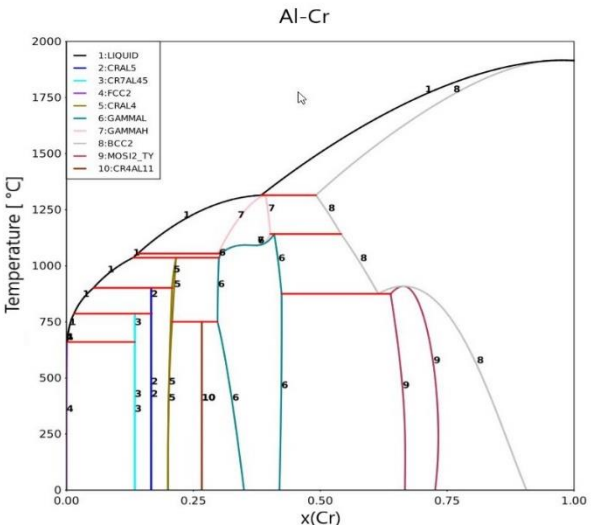

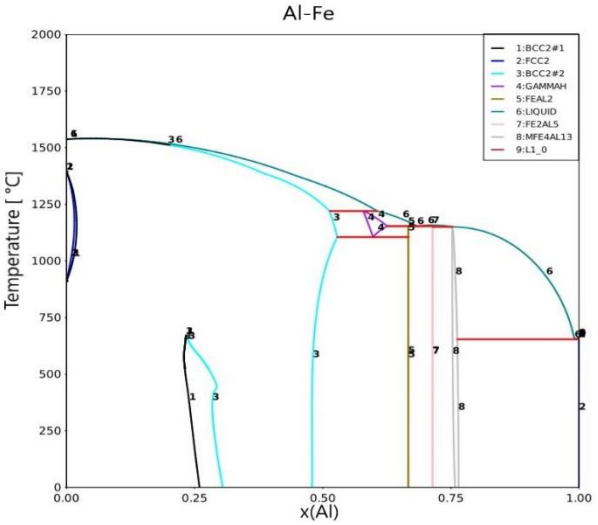

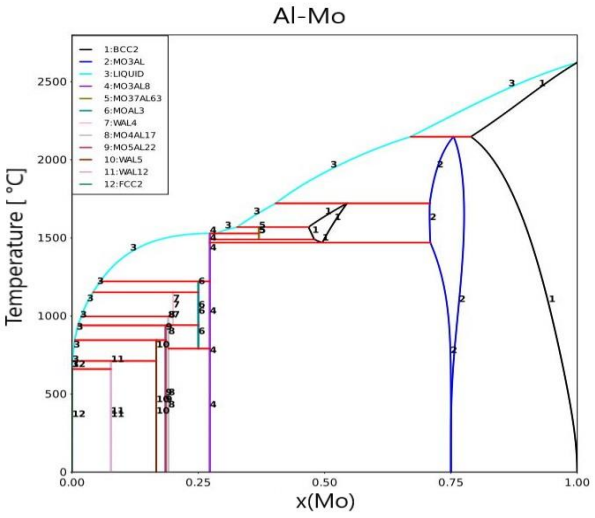

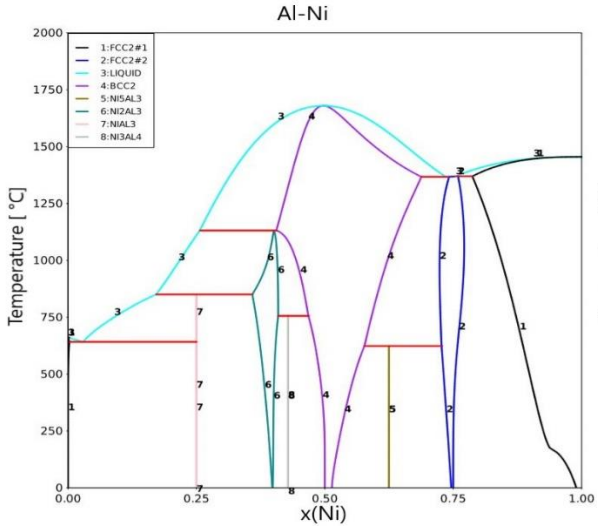

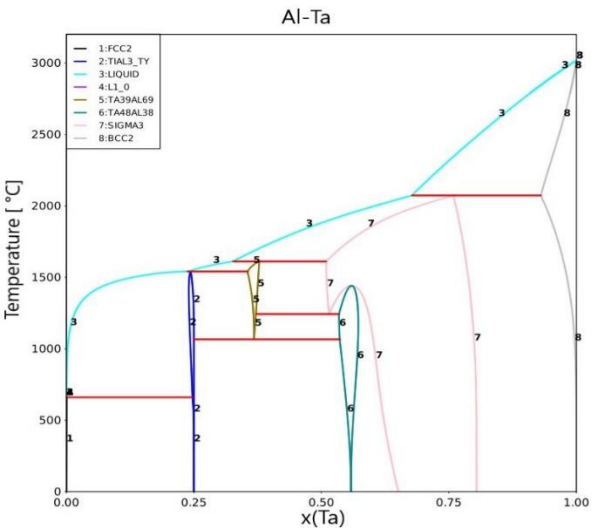

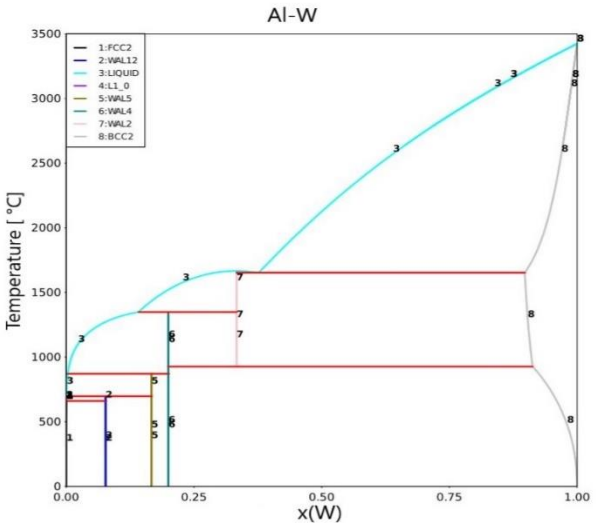
Al-W
1:FCC2
2:WAL12
3:LIQUID
4:L1_0
5:WAL5
6:WAL4
7:WAL2
8:BCC2
Temperature [°C]
x(W)

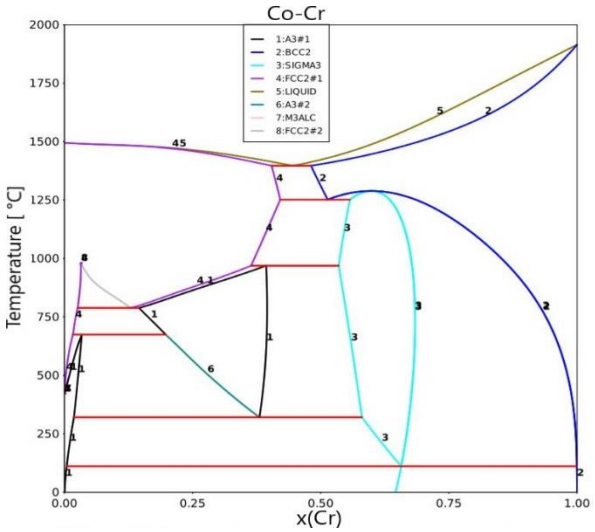
Co-Cr
1:A3#1
2:BCC2
3:SIGMA3
4:FCC2#1
5:LIQUID
6:A3#2
7:M3ALC
8:FCC2#2
Temperature [°C]
x(Cr)

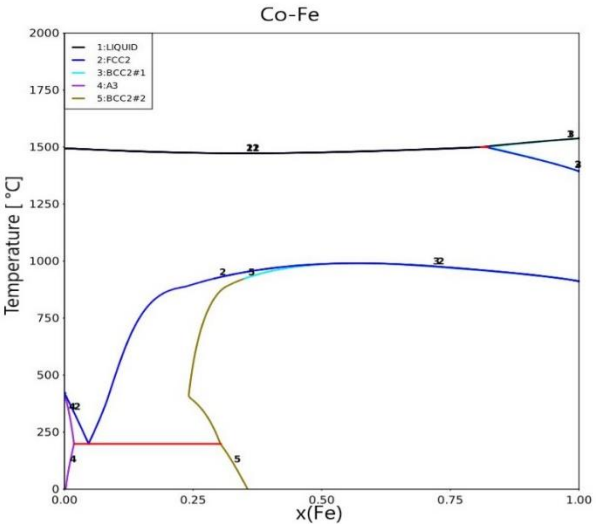
Co-Fe
1:LIQUID
2:FCC2
3:BCC2#1
4:A3
5:BCC2#2
Temperature [°C]
x(Fe)

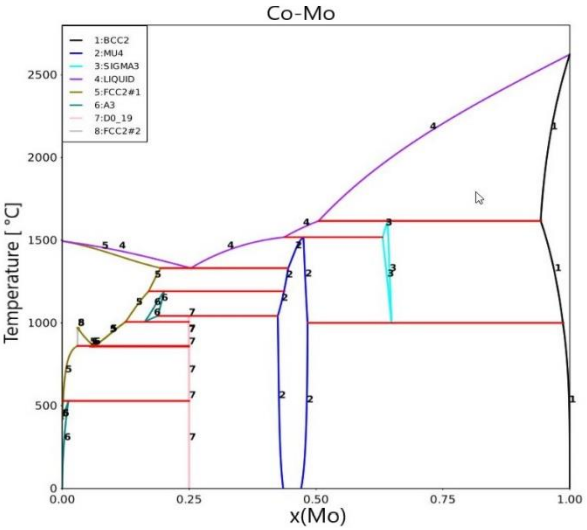
Co-Mo
1:BCC2
2:MU4
3:SIGMA3
4:LIQUID
5:FCC2#1
6:A3
7:D0_19
8:FCC2#2
Temperature [°C]
x(Mo)

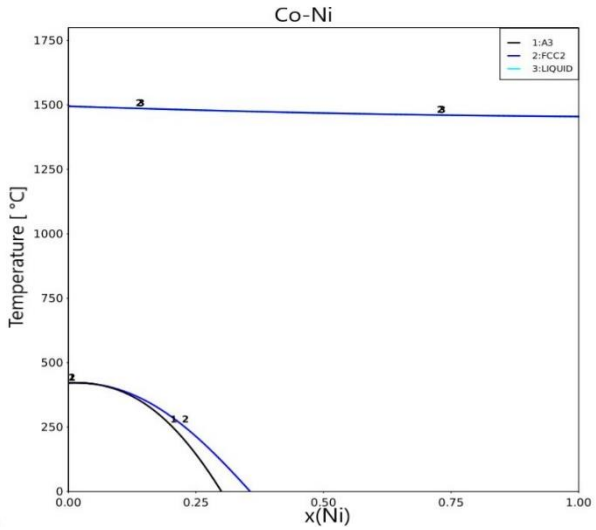
Co-Ni
1:A3
2:FCC2
3:LIQUID
Temperature [°C]
x(Ni)

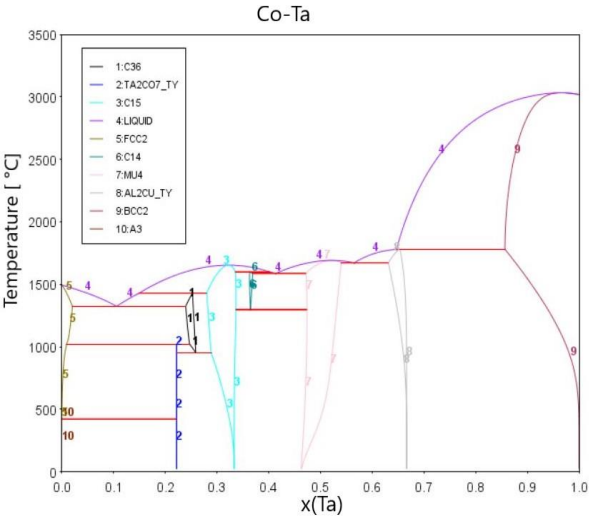
Co-Ta
1:C36
2:TA2CO7_TY
3:C15
4:LIQUID
5:FCC2
6:C14
7:MU4
8:AL2CU_TY
9:BCC2
10:A3
Temperature [°C]
x(Ta)

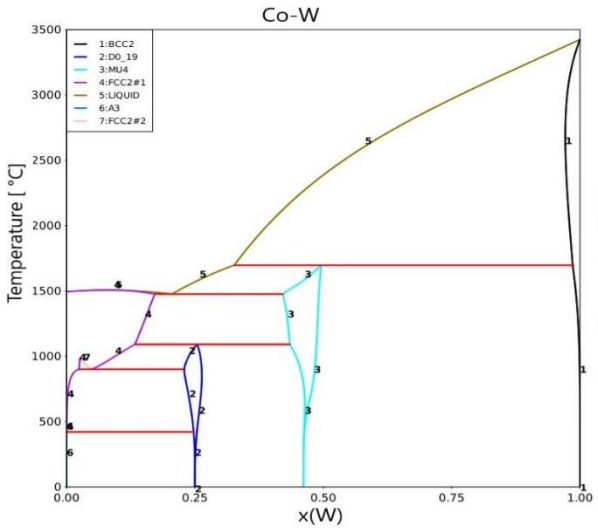
Co-W
1:BCC2
2:D0_19
3:MU4
4:FCC2#1
5:LIQUID
6:A3
7:FCC2#2
Temperature [°C]
x(W)

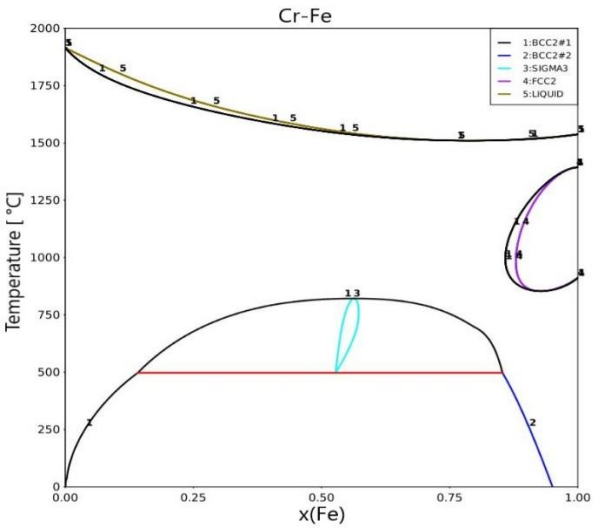
Cr-Fe
1:BCC2#1
2:BCC2#2
3:SIGMA3
4:FCC2
5:LIQUID
Temperature [°C]
x(Fe)

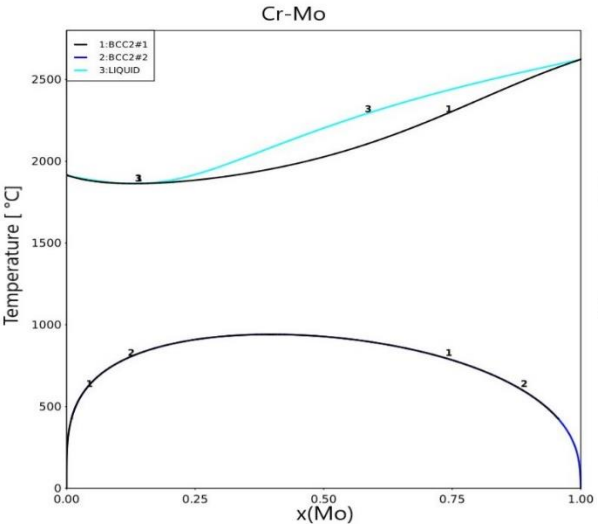
Cr-Mo
1:BCC2#1
2:BCC2#2
3:LIQUID
Temperature [°C]
x(Mo)

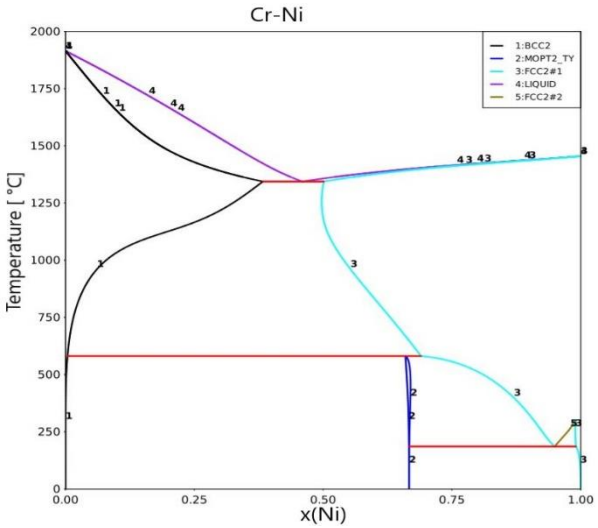
Cr-Ni
1:BCC2
2:MOPT2_TY
3:FCC2#1
4:LIQUID
5:FCC2#2
Temperature [°C]
x(Ni)

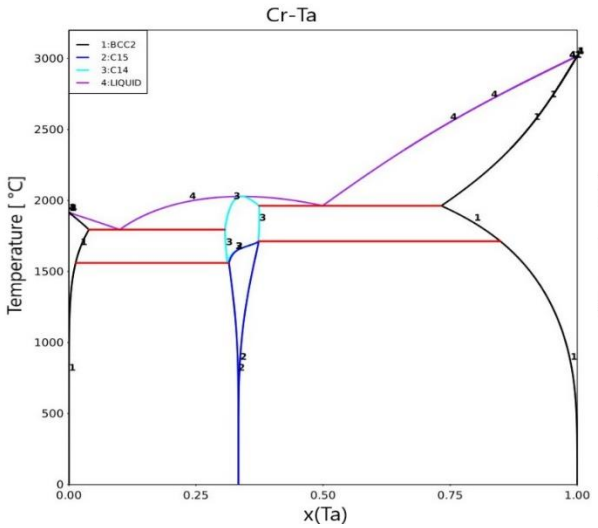
Cr-Ta
1:BCC2
2:C15
3:C14
4:LIQUID
Temperature [°C]
x(Ta)

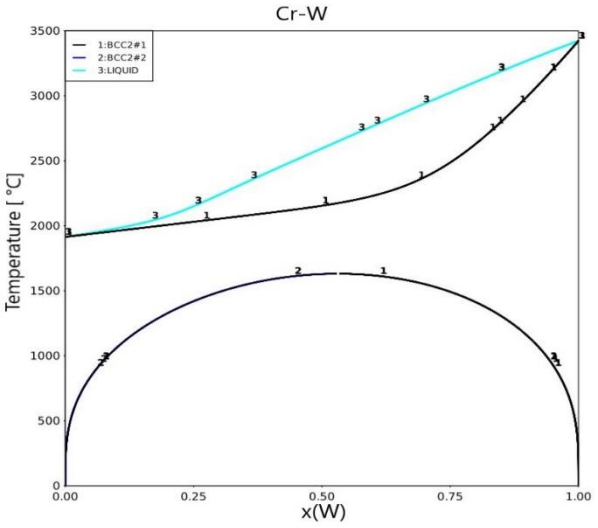
Cr-W
1:BCC2#1
2:BCC2#2
3:LIQUID
Temperature [°C]
x(W)

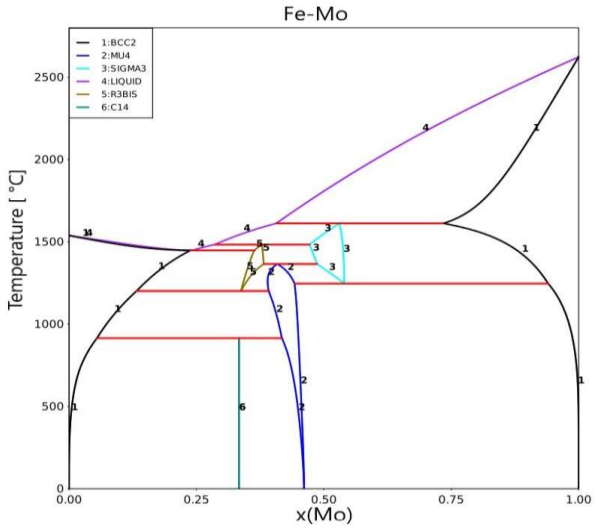
Fe-Mo
1:BCC2
2:MU4
3:SIGMA3
4:LIQUID
5:R3BIS
6:C14
Temperature [°C]
x(Mo)

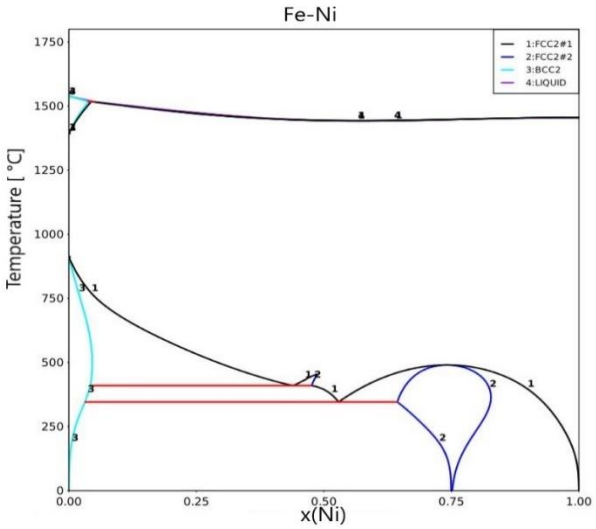
Fe-Ni
1:FCC2#1
2:FCC2#2
3:BCC2
4:LIQUID
Temperature [°C]
x(Ni)

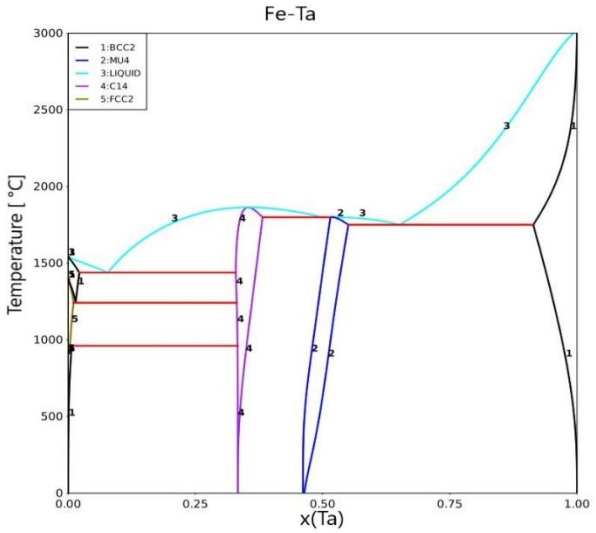
Fe-Ta
1:BCC2
2:MU4
3:LIQUID
4:C14
5:FCC2
Temperature [°C]
x(Ta)

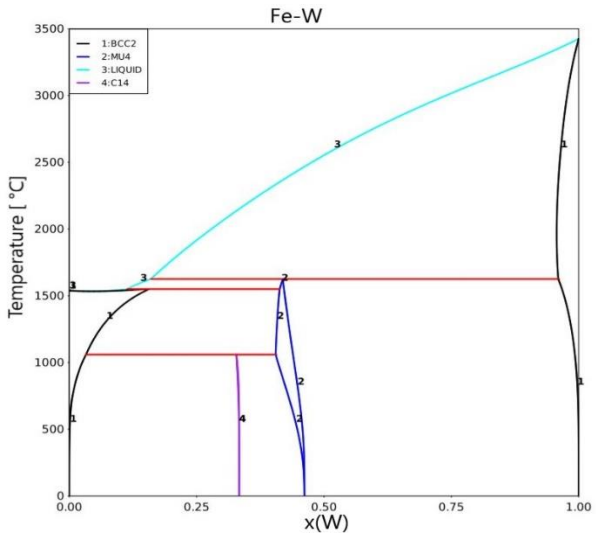
Fe-W
1:BCC2
2:MU4
3:LIQUID
4:C14
Temperature [°C]
x(W)

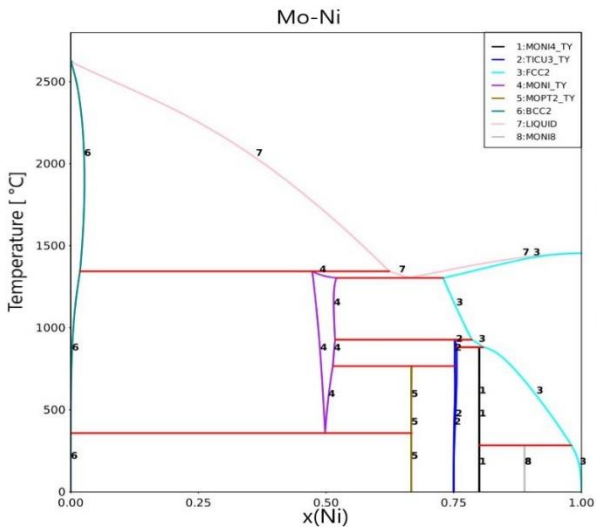
Mo-Ni
1:MONI4_TY
2:TICU3_TY
3:FCC2
4:MONI_TY
5:MOPT2_TY
6:BCC2
7:LIQUID
8:MONIB
Temperature [°C]
x(Ni)

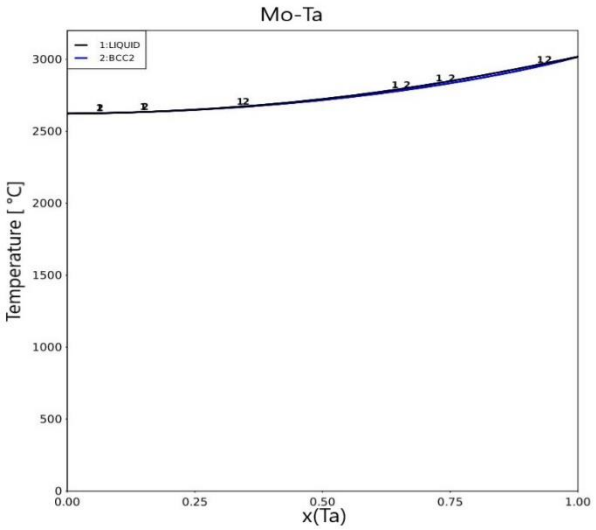
Mo-Ta
1:LIQUID
2:BCC2
Temperature [°C]
x(Ta)

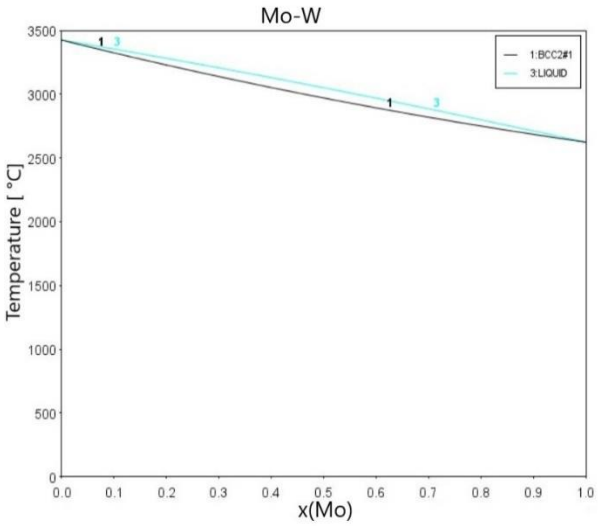
Mo-W
1:BCC2#1
3:LIQUID
Temperature [°C]
x(Mo)

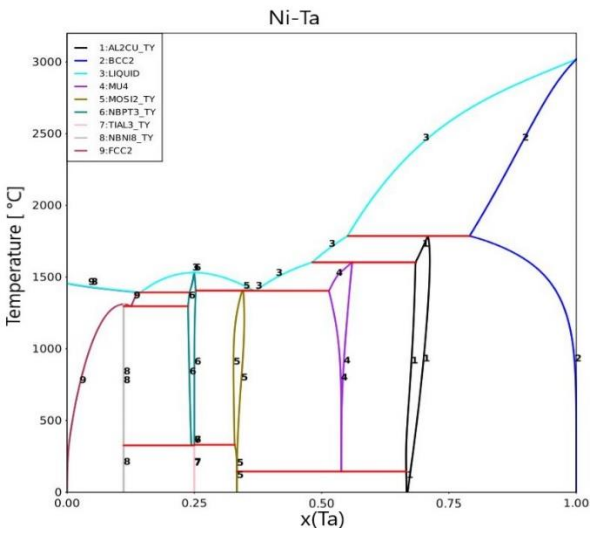
Ni-Ta
1:AL2CU_TY
2:BCC2
3:LIQUID
4:MU4
5:MOSI2_TY
6:NBPT3_TY
7:TIAL3_TY
8:NBNI8_TY
9:FCC2
Temperature [°C]
x(Ta)

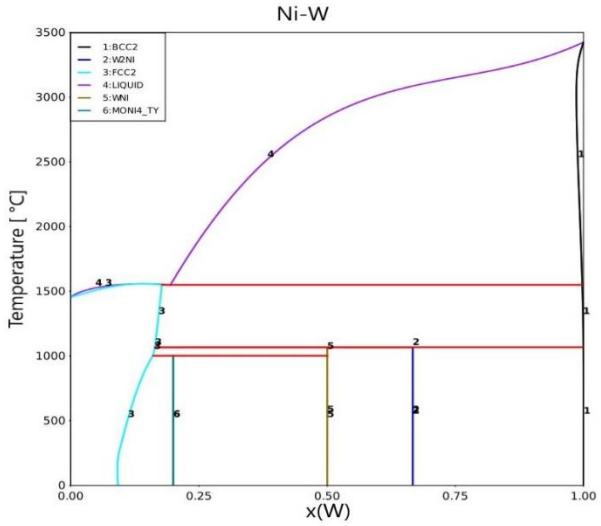
Ni-W
1:BCC2
2:W2NI
3:FCC2
4:LIQUID
5:WNI
6:MONI4_TY
Temperature [°C]
x(W)

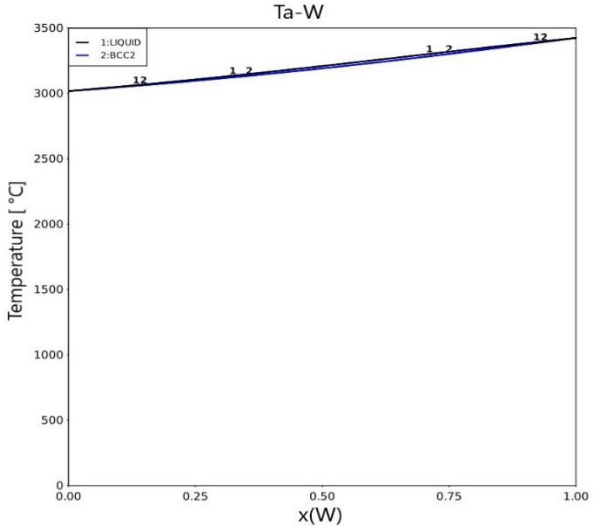
Ta-W
1:LIQUID
2:BCC2
Temperature [°C]
x(W)